

Analysis of the flow instabilities in the extrusion of polymeric melts

Citation for published version (APA):

Aarts, A. C. T. (1997). *Analysis of the flow instabilities in the extrusion of polymeric melts*. [Phd Thesis 1 (Research TU/e / Graduation TU/e), Mathematics and Computer Science]. Technische Universiteit Eindhoven. <https://doi.org/10.6100/IR475535>

DOI:

[10.6100/IR475535](https://doi.org/10.6100/IR475535)

Document status and date:

Published: 01/01/1997

Document Version:

Publisher's PDF, also known as Version of Record (includes final page, issue and volume numbers)

Please check the document version of this publication:

- A submitted manuscript is the version of the article upon submission and before peer-review. There can be important differences between the submitted version and the official published version of record. People interested in the research are advised to contact the author for the final version of the publication, or visit the DOI to the publisher's website.
- The final author version and the galley proof are versions of the publication after peer review.
- The final published version features the final layout of the paper including the volume, issue and page numbers.

[Link to publication](#)

General rights

Copyright and moral rights for the publications made accessible in the public portal are retained by the authors and/or other copyright owners and it is a condition of accessing publications that users recognise and abide by the legal requirements associated with these rights.

- Users may download and print one copy of any publication from the public portal for the purpose of private study or research.
- You may not further distribute the material or use it for any profit-making activity or commercial gain
- You may freely distribute the URL identifying the publication in the public portal.

If the publication is distributed under the terms of Article 25fa of the Dutch Copyright Act, indicated by the "Taverne" license above, please follow below link for the End User Agreement:

www.tue.nl/taverne

Take down policy

If you believe that this document breaches copyright please contact us at:

openaccess@tue.nl

providing details and we will investigate your claim.

**Analysis of the Flow Instabilities
in the Extrusion of
Polymeric Melts**

A.C.T. Aarts

**Analysis of the Flow Instabilities
in the Extrusion of
Polymeric Melts**

CIP-DATA KONINKLIJKE BIBLIOTHEEK, DEN HAAG

Aarts, Annemarie Catherine Theodora

Analysis of the flow instabilities in the extrusion of
polymeric melts / Annemarie Catherine Theodora Aarts.

Thesis Eindhoven University of Technology.

With references, and summaries in English and Dutch.

Subject headings: flow instabilities, polymeric melts, rheology, spurt.

ISBN 90-386-0269-3

Copyright ©1997 by A.C.T. Aarts, Eindhoven, The Netherlands.



Printed by Boek- en Offsetdrukkerij Letru, Helmond, (0492) 53 77 97.

Analysis of the Flow Instabilities in the Extrusion of Polymeric Melts

PROEFSCHRIFT

ter verkrijging van de graad van doctor aan de Technische
Universiteit Eindhoven, op gezag van de Rector Magnificus,
prof.dr. M. Rem, voor een commissie aangewezen door het
College van Dekanen in het openbaar te verdedigen op
woensdag 29 januari 1997 om 16.00 uur

door

Annemarie Catherine Theodora Aarts

geboren te Asten

Dit proefschrift is goedgekeurd door de promotoren:

prof.dr. J. Boersma

en

prof.dr.ir. M.L.J. Hautus

Copromotor: dr.ir. A.A.F. van de Ven

Preface

In this thesis mathematical analyses and numerical computations have been employed to study and to simulate flow instabilities that occur during an extrusion process of polymeric melts. In this way, a better insight into the various rheological aspects of extrusion processes can be obtained. This thesis makes clear that mathematical modelling provides excellent means to study physical phenomena, like the flow instabilities. The thesis is just one example of the large variety of applications of mathematics known. Hopefully, the practical use illustrated here, encourages more people to apply mathematics.

Although only my name appears on the cover of this thesis, I am indebted to many people who made this work possible. Therefore, I would like to express my gratitude towards them.

First of all, I would like to thank Fons van de Ven for his stimulating support, the pleasant collaboration, and the vivid and open-minded discussions. His positive encouraging helped me to get on very well in my research. Furthermore, his enthusiasm served me to experience the many interesting aspects of mechanics.

Secondly, I would like to express my gratitude to prof. J. Boersma. By carefully reading the drafts of this thesis, he pinpointed all inconsistencies and improved my English writing. Furthermore, his constructive criticism resulted in many improvements.

Next, I would like to thank prof. M.L.J. Hautus for the stimulating discussions and suggestions concerning the stability analyses.

I am also thankful to the people that are or have been involved with the project supported by DOW Chemical in Terneuzen, in particular to Jaap Molenaar, Rudy Koopmans, Marcel Grob and Jaap den Doelder. The discussions and suggestions about interesting aspects to study and checking the physical aspects of the problem, have always been very stimulating and useful to me. I would like to thank Rudy Koopmans also for providing me with some experimental data, and for the support of DOW Chemical.

Furthermore, I am grateful to prof. J.A. Nohel from 'Eidgenössische Technische Hochschule' in Zürich for his interest in my work and his valuable comments. To prof. G. Gripenberg from the University of Helsinki I render my thanks for his fast responses on several questions and his useful suggestions concerning the theory of Volterra integral equations. Prof. F. Verhulst from the University of Utrecht owes my thanks for the stimulating discussions about the theory of small parameter asymptotics.

Naturally, I would like to thank all colleagues of the group 'Toegepaste Analyse' for the pleasant work atmosphere during the last four years, and particularly prof. J.B. Alblas for his pleasant company and the interesting talks during the coffee breaks.

Finally, I would like to thank my family and friends for their continuing support and interest in my work. And most of all: Jacques Bruynen, whose care, encouragement and support have been very important to me.

Eindhoven, November 1996

Annemarie C.T. Aarts

Contents

Preface	i
1 Introduction	1
1.1 The extrusion process of polymers	1
1.2 The characteristic behaviour of polymer solutions and melts	2
1.3 Flow instabilities occurring in extrusion	4
1.4 Aim of this thesis	7
1.5 Modelling polymer flow instabilities: survey of the literature	8
1.6 Contents of this thesis	11
2 Pressure-driven shear flow of a KBKZ-fluid	15
2.1 Mathematical formulation	15
2.2 Steady state flow	21
2.3 Stability analysis	24
2.4 Transient flow behaviour	39
2.5 Spurt, shape memory and hysteresis	48
2.6 The influence of a relaxation spectrum	49
2.7 Conclusions	53
3 Piston-driven shear flow of a JSO-fluid	57
3.1 Mathematical formulation	57
3.2 Steady state flow	62
3.3 Transient flow behaviour	67
3.4 Stability analysis	84
3.5 Conclusions	89
4 Extrusion of a JSO-fluid, combined with compression	93
4.1 Mathematical formulation	93
4.2 Steady state flow	101
4.3 Transient flow behaviour	104
4.4 Stability analysis	117
4.5 Loading and unloading	123
4.6 Conclusions	127

5	Validation and perspective	133
5.1	Validation of the models	133
5.2	Perspective	141
A	Properties of $J(\omega)$ and $L(\omega)$	143
	Bibliography	145
	List of symbols	149
	Summary	151
	Samenvatting	153
	Curriculum Vitae	155

Chapter 1

Introduction

1.1 The extrusion process of polymers

Polymers are frequently used in many industrial applications because of their excellent material and mechanical properties. In the polymer manufacturing and shaping industry a variety of processes is employed to produce from polymeric feedstock all kinds of plastic products. One important production process for e.g. fibres is extrusion. The extrusion process is usually carried out in the liquid state of the polymer. The principle of extrusion is that a polymeric melt is forced to flow through a die, e.g. by the action of a moving plunger; see Figures 1.1 and 4.1 for a schematic representation of an extruder. This extruder consists of a wide barrel and a narrow die. The barrel is filled with polymeric melt and the plunger movement compresses the melt in the barrel and forces it through the die. When the melt leaves the die, the extrudate is formed by cooling down of the melt. The plunger velocity can be used to control the desired production rate, as this velocity determines the volumetric flow rate of the extrudate. By adapting the form of the cross-section of the die, one can extrude plastic products such as wires, pipes, fibres and plates. Wires are extruded from a circular die and pipes from an annular die. For the extrusion of plates one needs a flat die and to produce insulated cables a metal wire is enclosed by polymeric melt extruded from a circular die.

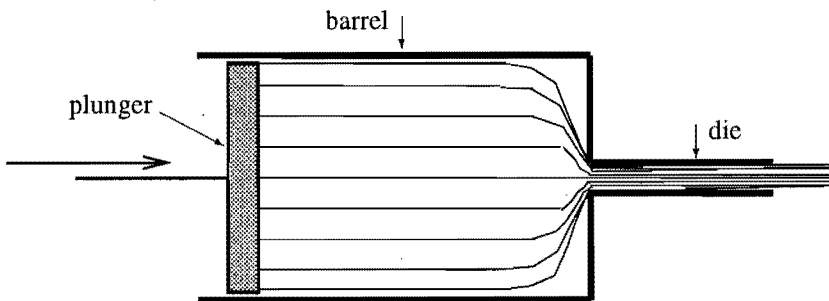


Figure 1.1 The flow in an extruder which consists of a wide barrel and a narrow die, controlled by a plunger moving to the right.

For the efficiency of the production process the polymeric melt is generally extruded at high flow rates. At these high flow rates, however, often surface distortions or fracture of the extrudate occur. Since the distortions make the product worthless, it is of commercial importance to know what causes the distortions and how they can be avoided. In this way, an optimal production rate, at which the extrudate flow rate is as high as possible and a smooth and regular extrudate forms, can be obtained. Since the ultimate extrudate properties will depend on the polymer used and on the processing conditions, it is important to know how the onset of the extrudate irregularities depends on the material properties of the polymeric melt and the dimensions of the extruder. In this way one can optimize the efficiency of the extrusion process.

1.2 The characteristic behaviour of polymer solutions and melts

The molecular weight of polymers, which is a measure for the length of the polymer chain, is about 10^4 - 10^6 gram per mol. The polymer chain exhibits a great diversity of orientations and conformations, e.g., fully stretched out, completely entangled or somewhere in between. As a result, fluids like polymer solutions and polymeric melts have a complex structure and behave in unexpected ways. In dilute solutions the concentration of polymers is so low that the chains do not interact. On the other hand, in concentrated solutions and molten polymers the molecular weight is so large that a gross interference between molecules is inevitable. In this thesis we consider flows of concentrated solutions and melts of flexible polymer molecules. Ferry [13, Chapter 17] showed that the rheology of concentrated solutions is similar in nature to the rheology of pure polymeric melts. Since the constituents of polymer solutions and melts differ in size, weight, and degrees of freedom, from small-molecule fluids like e.g. water and air, the microstructure of the materials has to be taken into account in order to describe typical features of non-Newtonian fluid behaviour, such as *shear-thinning* and *normal stress* effects.

The viscosity of a fluid is defined as the ratio of the shear stress and the shear strain-rate in a simple shear flow. For a Newtonian fluid the viscosity is constant. For a non-Newtonian fluid, however, the ratio depends on the shear strain-rate. Most of the concentrated polymer solutions and melts are shear-thinning which means that the viscosity decreases if the shear strain-rate increases. Another feature of a non-Newtonian fluid is that it exhibits normal stress differences in simple shear flow. With reference to a properly chosen orthogonal coordinate system (x_1, x_2, x_3) the normal stresses are equal to the diagonal terms T_{11} , T_{22} and T_{33} of the stress tensor. Here, the x_1 -direction is the flow direction, the x_2 -direction is the direction of the velocity gradient, and the x_3 -direction is the neutral direction. The two independent differences $N_1 := T_{11} - T_{22}$ and $N_2 := T_{22} - T_{33}$ are called the first and second normal stress differences, respectively. For a Newtonian fluid in a Poiseuille flow or Couette flow the normal stresses are equal, hence, the normal stress differences are exactly zero. For a polymer solution or melt, however, the first normal stress difference N_1 is positive and the second normal stress difference N_2 is negative, where N_2 is much smaller in magnitude than N_1 . Meissner et al. [37] experimentally found for a low-density polyethylene (LDPE)

the ratio $N_2/N_1 = -0.24$. A very close result ($N_2/N_1 = -0.22$) was found earlier by Meissner for an LDPE of a different molecular weight. In general, Weissenberg's hypothesis that the second normal stress difference is zero is an acceptable approximation for most polymer flows (cf. Tanner [50, p. 85]).

Another typical flow behaviour of polymeric melts and solutions is that they are *viscoelastic*, meaning that effects of both elasticity and viscosity are noticeable. In a purely viscous fluid the shear stress in a sheared body is proportional to the instantaneous *rate* of shear strain, whereas in a purely elastic material the shearing stress is proportional to the instantaneous *amount* of shear strain. After the applied force is removed, a viscous fluid remains unchanged in its deformed shape, whereas an elastic body retains its initial shape again. A material is called viscoelastic if the stress in a sheared body depends on the shear strain-rate as well as on the amount of shear strain. Moreover, the shear stress in a viscoelastic material also depends on the time elapsed since the strain has been applied. Hence, a viscoelastic material can be characterized by a positive, finite time λ^{-1} , during which it remembers its past deformations. For a purely elastic material the characteristic time $\lambda^{-1} = \infty$, i.e. the material never forgets its undeformed state, whereas for a purely viscous fluid $\lambda^{-1} = 0$, i.e. the fluid immediately forgets its initial state. This characteristic time is called the relaxation time, and λ is called the relaxation rate. Thus, a polymeric fluid has memory, and the entire temporal history of the deformation determines the stresses in the fluid. Typically the memory fades with time, meaning that applied forces or deformations in the distant past have less influence on the present stresses than those which occurred in the more recent past. The fading influence of the deformation history is governed by a memory function containing the characteristic relaxation rates of the polymer. Thus, polymeric materials are not described by the (linear) constitutive equation for Newtonian fluids; to describe the response of polymers adequately, a nonlinear viscoelastic constitutive model with fading memory is needed. These models must essentially be nonlinear, because the response of the very complex polymer solutions and melts is a highly nonlinear one.

Standard works on viscoelastic fluids are the books of e.g. Tanner [50], Bird et al. [5], Larson [28], Joseph [21], and Renardy et al. [48]. In these books various macroscopic constitutive models are derived from the microstructure of the polymers. To describe the nonlinear viscoelastic behaviour of a concentrated polymer solution or a polymeric melt with fading memory, we will use in this thesis two different constitutive models. The first model has been independently proposed by Kaye and by Bernstein, Kearsly and Zapas [4], and appears to have been inspired by the theory of rubberlike elasticity. The constitutive equation for the so-called KBKZ-model in its general form is given by an integral equation (cf. Tanner [50, p. 141] or (2.1.6)). Wagner modified this KBKZ-model into the so-called integral of Wagner (see Tanner [50, p. 209]; cf. (2.1.7) for simple shear flow). Since the second normal stress difference is small compared to the first normal stress difference (see Meissner et al. [37]), the integral of Wagner provides an adequate modification of the KBKZ-model. For the kernel in this integral various forms have been suggested by e.g. Wagner and Meissner (cf. Tanner [50, p. 212]) and by Papanastasiou et al. (cf. Tanner [50, p. 213]).

The second constitutive model we will use in this thesis is due to Phan-Thien and Tanner. This model is based on a relaxation of the hypothesis of affine deformation in the Lodge-Yamamoto network theory, and the constitutive equation is given by a differential equation

(see Tanner [50, p. 207]). Under neglect of the extensional flow response, the PTT-model is identical to the model of Johnson and Segalman which was deduced by an alternative (continuum) method; in this case the model becomes one of the Oldroyd family (cf. Tanner [50, p. 131] or (3.1.5)). Tas [51] showed that the constitutive PTT-model is the most satisfactory model to predict the stresses in a film blowing process. As for the capillary extrusion flow of polymeric melts and solutions, we will show that both Wagner's modification of the KBKZ-model and the Johnson-Segalman-Oldroyd (JSO)-model are qualitatively adequate to explain the various flow phenomena observed.

1.3 Flow instabilities occurring in extrusion

Flow instabilities are known to occur in a variety of commercially important polymer processing operations, including extrusion. The viscoelastic nature of polymeric fluids has many complex effects on the flow stability. Larson [29] has given an extended review of instabilities of many different categories, for example, instabilities in Taylor-Couette flows, in cone-plate and plate-plate flows, in parallel shear flows, in extensional flows, as well as thermohydrodynamical instabilities. We now summarize some of the instabilities that have been observed in the extrusion of polymeric fluids (cf. Larson [29, p. 236-242]).

When a polymeric melt leaves the die of the extruder, the formed extrudate becomes thicker than the die, the so-called *die-swell* (cf. Joseph [21, Chapter 13]). This die-swell is caused by the elastic elongation of the melt in the die which recovers in free space by contraction, so thickening. When choosing the die geometry one must take into account this die-swell. Especially in the case of a non-axisymmetric cross-section of the die, a deformation of the cross-section of the extrudate will occur along with the thickening.

One of the most dramatic phenomena observed in the flow of polymeric fluids is an instability commonly known as *melt fracture*. This instability is most easily observed in extrusion through a long die; see Kalika and Denn [23]. At high flow rates the elastic deformations often become extremely large, leading to distortions on the surface of the extrudate or to fracture of the extrudate. The distortions that occur can range from loss of gloss, small scratches, or slight roughness, to massive aperiodic and asymmetric variations in cross-sectional area and shape (cf. Kalika and Denn [23], Ramamurthy [46], El Kissi and Piau [12]). While the origins of extrudate distortions are still in dispute, there is agreement that the less severe distortions, called *sharkskin* or *surface melt fracture*, ought to be distinguished from the more severe distortions that are called *gross-melt fracture* or *wavy fracture*. As the name indicates, sharkskin is a surface roughness that usually modulates the extrudate diameter by no more than a few percent. Sharkskin consists of regular cracks or grooves that are narrowly spaced running perpendicular to the flow axis. Gross-melt fracture typically involves large variations of the diameter which at high flow rates are extremely irregular, even chaotic. In a piston-driven flow, Vinogradov et al. [52], Ramamurthy [46], Kalika and Denn [23], Durand [10] and El Kissi and Piau [12] found between sharkskin and gross-melt fracture a regime of alternating distorted and smooth extrudate, known in the literature as *stick-slip*, *spurt flow* or *cork flow*. In this thesis we shall refer to a flow that shows alternating distorted and smooth extrudate, as spurt flow.

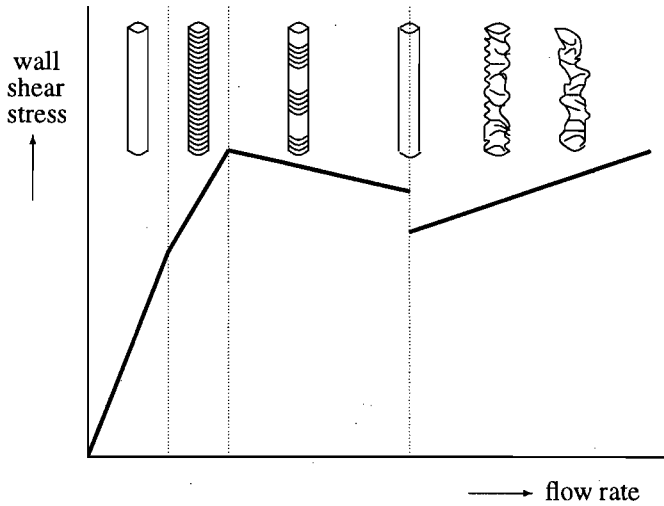


Figure 1.2 The different patterns of extrudate distortions delineated in the flow curve of the wall shear stress versus the flow rate for an LLDPE extruded under a constant plunger velocity.

Sharkskin, spurt flow and gross-melt fracture are distinguished not only by the appearance of the extrudate, but also by the critical conditions for onset. The most complete set of different forms of melt fracture is observed for a linear low density polyethylene (LLDPE) (Denn [9]; Kalika and Denn [23]). In Figure 1.2 the different patterns of extrudate distortions are shown coming up in the successive flow regimes of an LLDPE extruded under a constant plunger velocity. The patterns are delineated in a sketch of the flow curve of the wall shear stress versus the flow rate (cf. Kalika and Denn [23], Durand [10, p. 76]). The wall shear stress is a measure for the pressure drop in the die, whereas the flow rate is related to the plunger velocity. The figure shows that below some critical flow rate, the extrudate is smooth and glossy and no distortions are observed. At a first critical flow rate sharkskin occurs, observed as a regular pattern of small scratches on the extrudate. These scratches form a small-amplitude and narrowly spaced ribbing on the surface of the extrudate. Ramamurthy [46] and Kalika and Denn [23] found at the critical onset for sharkskin a small change in the slope of the flow curve (cf. Figure 1.2). At a second critical flow rate spurt flow occurs, observed as alternating smooth and distorted regions on the surface of the extrudate. The period of alternation roughly equals the time for the melt to traverse the die. The critical onset for spurt flow is characterized by a large change of the slope of the flow curve (see Figure 1.2). Spurt flow is accompanied with low-frequency, large-amplitude oscillations in the pressure (see Lim and Schowalter [31], El Kissi and Piau [12], Kalika and Denn [23]). The period of these oscillations is the same as the period of alternation of the extrudate. Due to the severe pressure oscillations, causing volume expansion and contraction of the melt, the flow rate at the die exit oscillates also with the same period. The spurt flow regime is apparently a consequence of the impossibility to operate at a volumetric flow rate on the 'forbidden' vertical part of the flow rate versus pressure gradient curve of Vinogradov et al. [52] (see Figure 1.3).

At a third critical flow rate the flow curve shows an apparent discontinuity (see Figure 1.2), indicating the onset of the gross-melt fracture regime. At this onset the oscillations in pressure and flow rate (as observed during the spurt flow regime) have disappeared, and the extrudate becomes severely and irregularly distorted. The degree of distortion at the onset of the gross-melt fracture regime depends on the die length. For longer dies there may be a narrow transition zone in which the extrudate is smooth and glossy again. The severity of the gross-melt distortions increases with increasing flow rate. Thus we conclude that sharkskin appears at a flow rate distinctly lower than that required for spurt flow or gross-melt fracture.

The critical conditions for the onset of the different flow instabilities are known to depend in some way on the polymeric fluid used and on the geometry of the extruder. Experimental observations indicate that sharkskin does not occur for all polymeric fluids (Denn [9]). For fluids for which it does occur, the critical wall shear stress at the onset of sharkskin is found to depend on the polymer concentration in the liquid (Pomar et al. [44]) and on the die material (Ramamurthy [46]). In particular, Ramamurthy [46] showed that the onset of sharkskin could be delayed to significantly larger values of the flow rate by a proper choice of the die material. The critical wall shear stress at the onset of spurt flow or gross-melt fracture, however, seems to depend little or not at all on the polymer concentration (Pomar et al. [44]), the length and diameter of the die, or on the material from which the die is made (Kalika and Denn [23], El Kissi and Piau [12], Ramamurthy [46]).

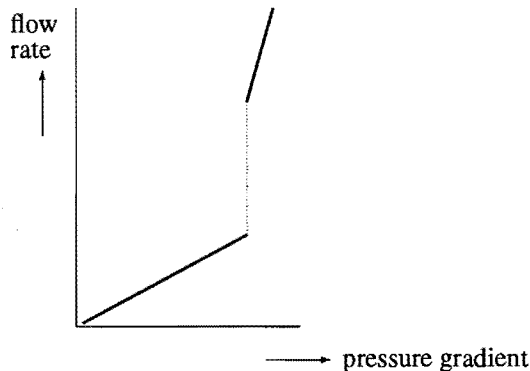


Figure 1.3 The flow rate versus pressure gradient curve of Vinogradov et al. [52] obtained from experiments involving pressure-driven flow.

A phenomenon related to the extrudate distortions described above is observed in experiments involving a pressure-driven flow. The phenomenon, called *spurt*, shows up through a discontinuity in the flow curve of the volumetric flow rate versus the driving pressure gradient (see Vinogradov et al. [52], [53], El Kissi and Piau [12], Figure 1.3). The discontinuity occurs at a critical pressure gradient which is independent of the molecular weight of the polymer and the temperature (Vinogradov et al. [52]; El Kissi and Piau [12]). Beyond this critical pressure gradient the volumetric flow rate increases substantially by a large amount. At the occurrence of the jump in the flow rate, the extrudate becomes irregularly distorted. Experiments by El Kissi and Piau [12] and Vinogradov et al. [53] involving a pressure-driven flow, have shown that the critical pressure gradient, or wall shear stress, at which the discontinuity

in the flow curve occurs, is also independent of the length and the diameter of the die. On the other hand, the jump in the flow rate becomes larger for larger molecular weight of the polymer. Moreover, in the experiments of El Kissi and Piau [12], *hysteresis* in the flow curve of the volumetric flow rate versus the driving pressure gradient has been observed. More specifically, when the pressure gradient is successively raised and lowered, the flow curve is found to consist of a loading path and an unloading path which do not coincide.

1.4 Aim of this thesis

The aim of this thesis is to get a better insight into the relation between the characteristic behaviour of polymeric melts and concentrated solutions, as described by the constitutive model chosen, and the particular flow phenomena discussed in Section 1.3. Die-swell has been analyzed in various papers (see e.g. Tanner [50, §§8.4-8.7], Goublomme et al. [14] and [15]). In this thesis we focus on spurt, observed in pressure-driven flow as well as in piston-driven flow. Specific questions are: What causes spurt, and how does spurt depend on the processing conditions and on the material parameters of the polymeric fluid? As a secondary topic we will validate some of our theoretical results in a comparison with experimental results described in the literature so far.

The investigation of a pressure-driven flow aims at an explanation of the spurt phenomenon observed in experiments of Vinogradov et al. [52], [53], and of the hysteresis loop in the flow curve obtained in experiments of El Kissi and Piau [12]. We will also explore the critical condition for the onset of spurt in its dependence on the flow parameters. The investigation of a piston-driven flow aims at an explanation of the spurt flow as observed in the experiments of Vinogradov et al. [52], Ramamurthy [46], Kalika and Denn [23], Durand [10], Lim and Schowalter [31], and El Kissi and Piau [12]. In particular, we go into the questions how the oscillations in the pressure observed during the spurt flow can be explained, and how the critical onset for the spurt regime is affected by the dimensions of the die and by the material parameters of the polymeric fluid used. As a third topic we will study the complete extrusion process of polymers, whereby the compression flow in the barrel is coupled to the capillary flow in the die. We will investigate in which way the critical onset for spurt flow depends on the input parameters: dimensions of the extruder, material parameters of the polymer, and plunger velocity. In essence, the ultimate aim of this thesis is to provide a theoretical basis for determining the input parameters such that an optimal extrusion rate is achieved at which no flow instabilities occur and the extrudate is smooth and glossy.

The irregularities of the extrudate that occur in the spurt flow regime, are assumed to be due to instabilities in the viscoelastic shear flow of the polymeric fluid inside the die. By using an adequate constitutive model and imposing the no-slip boundary condition at the wall of the die, we will provide a theoretical explanation for spurt and other related phenomena. To account for the unhindered motion of the polymer chains, we add a Newtonian viscous term to the stress tensor of the constitutive model employed. Further analysis leads to a non-monotone relation between the steady state shear stress and the steady state velocity gradient, or shear strain-rate. By integration of the velocity gradient under the no-slip boundary condition, we find that the flow is nearly plug flow, in accordance with the experiments of El Kissi

and Piau [12]. Moreover, we will show that the constitutive model does predict the hysteresis in the flow curve obtained in experiments of El Kissi and Piau [12], and the oscillations in the pressure during the spurt flow observed in experiments of Kalika and Denn [23], Lim and Schowalter [31], and El Kissi and Piau [12]. Indirectly, through the constitutive model which accounts for the memory of the polymeric melt, the deformation history and the different processing conditions also play an important role in the achieved flow behaviour.

In our approach the polymer properties (such as a nonlinear and nonmonotone viscoelastic behaviour and a fading memory) are crucial in explaining spurt, hysteresis and persistent oscillations in the pressure. Thus the flow instabilities are associated with internal properties of the melt, and are therefore referred to as *constitutive instabilities*. This is in contrast to the explanation of spurt as being due to *wall slip*, that is, the failure of the fluid to adhere to the wall (see e.g. Leonov [30], Piau and El Kissi [43], Greenberg and Demay [16]). Both explanations will be discussed in more detail in the next section. We just mention that true wall slip is experimentally difficult to distinguish from the nearly plug flow predicted by our theory. Finally, it is pointed out that our constitutive model does predict the flow instabilities as occurring in experiments. Furthermore, the dependence of the critical onset of the flow instabilities on the melt properties and on the dimensions of the extruder, agrees well with the experimentally observed dependence (cf. Chapter 5). We believe this agreement supports the explanation of spurt in terms of constitutive instabilities.

1.5 Modelling polymer flow instabilities: survey of the literature

In the previous section we have alluded to the explanation of spurt either in terms of constitutive instabilities (mechanical failure of the polymer itself), or in terms of wall slip (failure of the polymer to adhere to the wall of the capillary). A constitutive instability will occur when the constitutive relationship between the shear stress and the shear strain-rate is nonmonotone (Huseby [19], Malkus et al. [32]). Wall slip is modelled by replacing the conventional no-slip boundary condition by one that allows the fluid velocity at the wall to depend on the shear stress or strain history of the fluid at the wall (Piau and El Kissi [43], Renardy [47]). From experiments by El Kissi and Piau [12] it is known that for a sufficiently large pressure gradient the flow in the capillary is nearly plug flow, or intermittent plug flow. These experiments seem to support the hypothesis of wall slip. For the spurt flow regime various theories based on constitutive instabilities, however, predict that the flow will develop a thin layer (spurt layer) near the wall with large shear strain-rates, while the rest of the flow is nearly plug flow (see e.g. Malkus et al. [32], [33], Aarts and van de Ven [1], [2]). With respect to the two possible explanations of spurt, namely, constitutive instabilities or wall slip, Larson [29, p. 238] states that "although the two explaining mechanisms of extrudate distortion are different in principle, they are difficult to distinguish in practice, because both predict the same macroscopically observable phenomenon (namely, a sudden increase of the flow rate at a critical pressure gradient) and they both seem likely to lead to flow instabilities and extrudate distortion". Hence, both mechanisms provide a theoretical explanation for the flow instability spurt.

Theoretical explanations for the polymer flow instabilities, based on a nonmonotone constitutive relationship between the shear stress and the shear strain-rate and on the no-slip boundary condition, are given in many papers. Here, we mention some of these papers. Starting from Pao's molecular theory for viscoelastic polymeric melts combined with measurements of the relaxation spectrum of a linear polyethylene, Huseby [19] predicts the shear stress as a nonmonotone function of the shear rate. Malkus et al. [32], [33] and Nohel and Pego [41], [42] analyze the one-dimensional pressure-driven shear flow of a JSO-fluid through a slit die, in order to provide a theoretical explanation for the spurt phenomenon. The flow is governed by a quasilinear, singularly perturbed system of partial differential equations supplemented by a no-slip boundary condition and compatible initial data for the velocity and the stresses. The governing initial-boundary value problem is shown in [41] to be globally well-posed in time for smooth (even discontinuous) initial data of arbitrary size. The dynamics of the corresponding inertialess flow (obtained by putting the singular parameter α equal to zero) is governed by an autonomous quadratic system of ordinary differential equations. In [33], Malkus et al. determine the global dynamics of the inertialess flow by a phase-plane analysis and use the results to explain spurt, latency, shape memory and hysteresis under quasi-static loading and unloading of the pressure gradient, as well as flow reversal. Furthermore in [32], the flow parameters are fitted to experimental data for the onset of spurt obtained by Vinogradov et al. [52]. Subsequently, it is shown in [41] and [42] that the full governing system and its inertialess approximation display similar dynamics provided the singular parameter α (i.e., the ratio of Reynolds and Deborah numbers) is sufficiently small.

Corresponding results for the spurt phenomenon in the axisymmetric pressure-driven flow of a KBKZ-fluid through a capillary, have been found by Aarts and van de Ven [1], [2]. For the details we refer to Chapter 2 of this thesis, which comprises an expanded version of the papers [1] and [2]. Hunter and Slemrod [18] use a general (nonspecified) viscoelastic model with one relaxation rate to analyze the pressure-driven flow through a slit die. These authors show that the addition of a Newtonian viscous term is necessary to prove the existence of singular surfaces in the flow. Such singular surfaces are inherent to the spurt phenomenon. Kolkka et al. [24] analyze the shear flow of a JSO-fluid through a slit die by a numerical calculation of the dynamics of the spurt process by means of a finite-element solution technique.

One-dimensional piston-driven shear flow of a highly elastic and viscous JSO-fluid through a slit die at a prescribed volumetric flow rate, has been treated by Malkus et al. [35], [36]. The flow is governed by a quasilinear, singularly perturbed system of partial differential equations with a non-local constraint, supplemented by a no-slip boundary condition and compatible initial data for the velocity and the stresses. This system is globally well-posed in time but the asymptotic behaviour of its solutions as $t \rightarrow \infty$, and the stability of its possibly discontinuous steady states remain as open problems. The inertialess approximation of this flow is governed by a quadratic system of functional differential equations having all solutions bounded for $t \geq 0$. In [36], Malkus et al. use a spectral analysis of the linearization of this system about a piecewise smooth steady state solution with a single jump discontinuity to predict oscillations in the pressure gradient. These oscillations exhibit a transition to seemingly periodic oscillations at a critical prescribed volumetric flow rate. Although not established rigorously, the transition to persistent oscillations appears to be due to a Hopf bifurcation to a stable periodic orbit, in agreement with the occurrence of persistent oscillations

in the pressure observed in the experiments of Lim and Schowalter [31].

Molenaar and Koopmans [39] developed and analyzed a two-dimensional Lienard system that describes the extrusion of a polymeric fluid in a capillary by a plunger. The constitutive behaviour of the fluid determines the functional relationship between the global pressure and the flow rate fluctuation; this relationship is assumed to be nonmonotone. In [39], oscillations in the pressure and in the volumetric flow rate are predicted which are similar to the relaxation oscillations governed by Van der Pol's equation. Renardy [49] analyzes a two-dimensional Couette flow of a JSO-fluid between infinite parallel plates driven by the motion of the upper plate. For a given two-layer velocity profile the stability of the flow is examined by a numerical computation of the eigenvalue spectrum. Brunovsky and Sevcovic [8] provide a theoretical explanation for spurt by means of a constitutive model that is supplemented with a spatial diffusion term.

Theoretical explanations for the polymer flow instabilities, based on wall slip due to the failure of the polymer to adhere to the wall, are given in the following papers. On the basis of experimental measurements, Piau and El Kissi [43] propose a procedure for modelling polymer slip at the wall. The procedure makes use of a so-called friction curve that relates the shear stress at the wall to the fluid velocity at the wall (slip velocity). An empirical expression for the friction law is determined from experimental data. By combining the friction law with an equation for the compression of the melt in the barrel, Piau and El Kissi [43] succeed in modelling relaxation oscillations in the pressure. Leonov [30] employed a linear friction law, derived by a crude molecular approach, for a qualitative theoretical study of spurt flow phenomena.

Renardy [47] shows that the flow problem for an upper-convected Maxwell fluid becomes ill-posed if the no-slip boundary condition at the wall is replaced by a law of 'memory' slip which relates the slip velocity to the history of the shear stress. Greenberg and Demay [16] describe the extrusion process for a molten polymer in a capillary under the condition that the mean velocity at the capillary inlet is maintained at a constant value. The polymer is modelled as a linear (Newtonian) compressible fluid. As a boundary condition at the wall, a linear slip relation is postulated including an empirical piecewise linear switch rule that relates the wall shear stress to the slip velocity. The switch rule combined with the compressibility relation yields a global flow model exhibiting relaxation oscillations.

The discussion about the origins of extrudate distortions has not yet come to a conclusion. Even if there exists agreement about "slip" along the wall of the capillary, the interpretation and the modelling of this slip is still controversial. Joseph and Joe Liu [22] suggest that both explaining mechanisms of wall-slip and constitutive instabilities give rise to a lubricating layer of nearly inviscid material adjacent to the wall, as one observes in core-annular flows of heavy oils in water. These authors state that "the dynamics of lubricating layers in slipping polymer melts and solutions is such as to produce an asymmetric wavy extrudate in which the steep side of the wave advances". Kurtz [26], in his comment on the letter of Joseph and Joe Liu [22], states that "there are observations and experiments that do not fit with the Joseph/Liu model". Larson [29, p. 239] remarks that "one cannot decide conclusively between the mechanisms of wall slip and constitutive instabilities using data from a single fluid-die combination". Experiments (Ramamurthy [46], El Kissi and Piau [12], Vinogradov et al. [53]) have shown that the critical condition for the onset of spurt flow and gross-

melt fracture in cylindrical dies is little or not at all affected by changes in the die material or by the presence of lubricants, whereas the critical condition for the onset of sharkskin is affected in most cases. The difference in dependence for the onset suggests that different mechanisms may be responsible for sharkskin, for spurt flow, and for gross-melt fracture. Thus, following Larson [29, p. 239], wall slip may cause sharkskin instabilities, whereas it is possible that spurt flow and gross-melt fracture are nearly always caused by constitutive instabilities of the melt.

In Chapter 5 we present a validation of our theoretical results by a comparison with experimental results taken from the following papers. Vinogradov et al. [52], [53], and El Kissi and Piau [12] report on the spurt phenomenon observed in experiments involving pressure-driven flows. In these experiments the pressure gradient at the onset of spurt is found to be independent of the molecular weight, whereas the corresponding flow rate strongly depends on the molecular weight of the polymeric melt. Furthermore, spurt only occurs for polymeric melts that have a sufficiently large molecular weight. El Kissi and Piau [12] experimentally found that the hysteresis loop in the flow curve gets wider for a polymeric melt with a larger molecular weight.

Kalika and Denn [23], Lim and Schowalter [31], and El Kissi and Piau [12], report on spurt flow observed in experiments involving piston-driven flows. In these experiments persistent oscillations in the pressure are observed for a bounded range of flow rates. Lim and Schowalter [31] found that the span of the oscillations goes through a maximum with increasing flow rate. Furthermore, they observed that the persistent oscillations only occur for polymeric melts with sufficiently large molecular weight; the oscillations occur for a wider range of flow rates when the polymeric melt has a larger molecular weight. El Kissi and Piau [12] found that the flow rate at the onset of spurt flow is independent of the length of the capillary, whereas the flow rate gets larger for a wider capillary. Finally, both Kalika and Denn [23], and Lim and Schowalter [31] report that the frequency of the persistent oscillations increases with increasing flow rate. We shall return to the experimental observations of Vinogradov et al. [52], [53], Kalika and Denn [23], Lim and Schowalter [31], and El Kissi and Piau [12], in Chapter 5.

1.6 Contents of this thesis

At the end of Section 1.4 it was argued that the agreement with experimental results supports the explanation of spurt in terms of constitutive instabilities. The particular flow phenomena caused by constitutive instabilities are investigated in Chapters 2, 3 and 4.

In Chapter 2 we consider the axisymmetric flow of a polymeric melt through a cylindrical capillary driven by a pressure gradient. The characteristic behaviour of the viscoelastic melt is described by the KBKZ-model supplied with an extra Newtonian viscous term. For the simple shear flow considered the KBKZ-model is modified into the integral of Wagner. The Newtonian viscous term accounts for the response of a small-molecule solvent. We will show that the inclusion of this Newtonian term is essential in our further analysis, as it leads to a nonmonotone relationship between the steady state shear stress and the steady state shear strain-rate or velocity gradient. The inertialess approximation of the transient capillary flow

of the KBKZ-fluid is governed by an integrodifferential equation for the shear strain at a given radial coordinate (the governing equation (2.1.35) is obtained by putting $\alpha = 0$ in equation (2.1.29) for the full flow problem). The flow starts from rest by a suddenly applied constant pressure gradient. Numerical computations indicate that after the transient phase the flow approaches a steady state. Since the relation between the steady state shear stress and the steady state velocity gradient is nonmonotone, the steady state is not unique; depending on the prescribed pressure gradient, at most three distinct steady state solutions for the velocity gradient exist. We prove the asymptotic stability of two of the steady state states by a perturbation analysis of the nonlinear integral equation of non-convolution type that governs the inertialess flow, and we motivate why the third steady state is unstable. The question which of the two stable solutions for the velocity gradient is attained, has to be answered by numerical computations. These computations also confirm that the unstable state is not attained. Moreover, we show that the steady state velocity gradient is discontinuous as function of the radial coordinate, if the driving pressure gradient exceeds a certain critical value. As a result, the polymeric flow will develop a thin layer near the wall, called the spurt layer, in which the velocity gradient is very large compared to the velocity gradient in the rest of the capillary. Hence, in case of a supercritical pressure gradient, the bulk of the fluid contained in the central part of the capillary moves in a plug-like fashion. It is found that a slight increase of the driving pressure gradient beyond its critical value gives rise to a substantial increase of the flow rate, as observed in the experiments of Vinogradov et al. [52]. After a steady state has been attained, a subsequent small decrease of the driving pressure gradient results in *shape memory* of the fluid, that is, the spurt layer remains fixed. Shape memory is also instrumental in the explanation of the hysteresis loop in the flow curve obtained in experiments of El Kissi and Piau [12]. Finally, we show that the transient flow behaviour of a polymer solution containing a small-molecule solvent, is similar to the flow behaviour of a pure molten polymer. To that end, we establish that the KBKZ-model with one main relaxation rate and supplemented with a Newtonian viscous term, is a good approximation to the KBKZ-model with two widely spaced relaxation rates. Thus, the viscous Newtonian term accounts for the very fast relaxation rates of the polymeric liquid. The greater part of Chapter 2 has also been published in [1] and [2]. It should be mentioned that the results of Chapter 2 are very similar to those obtained by Malkus et al. [32], [33] for the pressure-driven flow of a JSO-fluid through a slit die.

In Chapter 3 we consider the flow of a polymeric melt through a cylindrical capillary, controlled by a moving piston that induces a constant volumetric flow rate. The pressure gradient is then unknown and adjusts itself to maintain the desired flow rate. The characteristic behaviour of the viscoelastic melt is described by the JSO-model supplied with an extra Newtonian viscous term. The extra term accounts either for the response of a small-molecule solvent, or for the unhindered polymer chain motions described by a very fast relaxation rate. Further analysis of the flow problem leads to a nonmonotone relationship between the steady state shear stress and the steady state shear strain-rate or velocity gradient (cf. Malkus et al. [32], [33]). Prescribing the constant volumetric flow rate of the capillary flow leads to an integral relation between the pressure gradient and the shear stress due to the polymer contribution. For a given radial coordinate this shear stress is coupled to the pressure gradient by a system of two ordinary differential equations derived from the constitutive JSO-model.

The flow starts from rest by a suddenly applied constant flow rate. Dependent on the prescribed flow rate, there exists a range of attainable steady state solutions for the pressure gradient and the velocity gradient, whereby the steady state velocity gradient is found to be discontinuous as function of the radial coordinate. Which steady state solution is attained, depends on the location of the discontinuity which has to be determined by numerical computations. Furthermore, we compare the dynamics of a piston-driven flow to the dynamics of a pressure-driven flow as considered in Chapter 2. One aspect of the piston-driven flow is the appearance of oscillations in the pressure gradient, if the prescribed flow rate is sufficiently large. For most flow rates these oscillations are damped and a steady state pressure gradient is attained. For a limited range of flow rates, however, the oscillations are not damped but persistent, and no steady state is attained. We will explain the occurrence of persistent oscillations by means of a linearized stability analysis of the steady state solution. In addition, we present conditions for the onset of persistent oscillations in terms of the material parameters of the polymeric melt and the radius of the capillary. In experiments spurt flow is accompanied by pressure oscillations, which corresponds very well with the persistent oscillations in the pressure gradient as predicted by our analysis. Furthermore, it is found that the flow curve of the attained steady state pressure gradient versus the prescribed flow rate is S-shaped and exhibits a nonmonotone behaviour, in accordance with experiments (cf. Kalika and Denn [23], El Kissi and Piau [12], and Durand [10]). Persistent oscillations in the pressure gradient have been found before by Malkus et al. [35], [36], in the piston-driven flow of a JSO-fluid through a slit die. In fact, Chapter 3 deals with the analogous problem of a piston-driven flow of a JSO-fluid through a cylindrical capillary. From a detailed study of this flow we find that the criterion for the onset of persistent oscillations depends both on the flow rate and on the material parameters of the polymeric melt.

In Chapter 4 we consider the complete extrusion process for a polymeric melt, combined with compression. The extruder is modelled by a wide barrel connected to a narrow cylindrical capillary. The melt is compressed in the barrel by a plunger, moving at constant speed, and is thus forced to flow into the capillary. The characteristic behaviour of the viscoelastic melt is described by the JSO-model supplied with an extra Newtonian viscous term. Both the pressure gradient and the flow rate are unknown. By coupling the compression flow in the barrel to the simple shear flow in the capillary, we are led to a system of differential equations supplemented with an integral relation to describe the whole extrusion process. As input parameters we have the constant plunger velocity driving the flow, the material parameters of the polymer (i.e. the compression modulus, the relaxation rate, the shear modulus and the solvent viscosity), and the dimensions of the extruder (i.e. length and radius of the barrel and of the capillary). Numerical computations disclose how these input parameters determine the pressure gradient and the flow rate as functions of time, if the flow starts from rest by a suddenly applied constant plunger velocity. In particular, the occurrence of persistent oscillations in the pressure gradient and in the flow rate will be demonstrated. Again, these oscillations provide a theoretical explanation for the spurt flow accompanied by pressure oscillations, as observed in the experiments of Kalika and Denn [23], Lim and Schowalter [31], El Kissi and Piau [12]. The occurrence of persistent oscillations is explained by means of a linearized stability analysis of the steady state solution, and the frequency of these oscillations is determined. The critical conditions for the onset of persistent oscillations are ex-

pressed in terms of three dimensionless input parameters. In this manner, the influence of parameters like length and radius of the capillary, and bulk modulus of the melt, on the onset of spurt flow accompanied by persistent oscillations, will be assessed. Finally, the influence of the deformation history is demonstrated in a study of some loading and unloading processes, whereby the prescribed inlet flow rate is successively raised and lowered. It is found that shape memory may occur and the transient flow behaviour may change drastically.

Different constitutive models are employed to describe the characteristic behaviour of the viscoelastic melt, namely, the integral KBKZ-model in case of a pressure-driven flow (Chapter 2), and the differential JSO-model in case of a piston-driven flow (Chapter 3) or an extrusion flow combined with compression (Chapter 4). We did not study the piston-driven flow or the extrusion flow of a KBKZ-fluid because the computation time would become prohibitive due to the time consuming evaluations of the hereditary integral in the KBKZ-model, and of the non-local constraint that fixes the volumetric flow rate. Neither did we investigate the pressure-driven flow of a JSO-fluid because that would duplicate the detailed analysis of Malkus et al. [32], [33].

In Chapter 5 we discuss the results of this thesis, and we will validate our theoretical analyses by a comparison with experimental results. Phenomena of spurt and hysteresis occurring in a pressure-driven flow (Chapter 2) are compared to their counterparts observed in experiments of Vinogradov et al. [52], [53], and El Kissi and Piau [12]. Spurt flow accompanied by persistent oscillations occurring in a piston-driven flow (Chapter 3) and in an extrusion flow combined with compression (Chapter 4) is compared to certain pressure oscillations observed in experiments of Kalika and Denn [23], Lim and Schowalter [31], and El Kissi and Piau [12]. Likewise, the critical conditions for the onset of flow instabilities predicted by our theory, are compared to the critical conditions found in experiments. To that end, we investigate the dependence of the (dimensional) critical conditions on the material parameters of the polymeric fluid and on the dimensions of the extruder. Here the material parameters in our KBKZ-model are estimated by a fit to the experimental data of Vinogradov et al. [52] for polyisoprene samples of different molecular weights. It will turn out that there is qualitative agreement between the theoretical results predicted by our models and the experimental results referred to. We conclude with some recommendations for further research.

Chapter 2

Pressure-driven shear flow of a KBKZ-fluid

In this chapter we consider the flow of a polymeric melt through a cylindrical capillary driven by a constant pressure gradient. Since the polymeric melt is strongly viscous, the inertia forces may be neglected. Due to the prescribed pressure gradient, the balance of linear momentum implies that the shear stress is a known function of the radial coordinate (see (2.1.34)). The constitutive equation to describe the characteristic behaviour of the viscoelastic melt with fading memory chosen here, is the Kaye-Bernstein-Kearsly-Zapas (KBKZ)-model supplied with an extra Newtonian viscous term. This extra term, which dominates the initial response of the fluid, is essential as it leads to a nonmonotone behaviour of the steady state shear stress as function of the steady state shear strain-rate or velocity gradient (see Figure 2.1).

2.1 Mathematical formulation

The flow of an incompressible viscoelastic fluid under isothermal conditions is governed by the conservation of mass

$$\nabla \cdot \mathbf{v} = 0 \quad (2.1.1)$$

and the balance of linear momentum

$$\nabla \cdot \mathcal{T} + \rho \mathbf{b} = \rho \left(\frac{\partial \mathbf{v}}{\partial t} + (\mathbf{v} \cdot \nabla) \mathbf{v} \right). \quad (2.1.2)$$

Here, ρ is the (constant) fluid density, \mathbf{b} the body force per unit of mass, \mathbf{v} the fluid velocity and \mathcal{T} the total (symmetric) stress tensor. Later on we shall show that for strongly viscous fluids the inertia forces, represented by the right-hand side of (2.1.2), can be neglected.

The characteristic response of the material to a deformation is described by the constitutive equation for the stress. For viscoelastic fluids with fading memory, the stress depends on the deformation history. If a polymer solution contains a small-molecule solvent, this solvent will generally respond in a viscous manner to any applied force or deformation, separately

from the elastic response due to the dissolved polymer; see Renardy et al. [48, p. 17]. Therefore, it is assumed that the extra stress tensor $S := \mathcal{T} + pI$ in the fluid consists of a Newtonian viscous component and an isotropic elastic one, namely

$$S = \mathcal{T} + pI = 2\eta_s \mathcal{D} + S_p. \quad (2.1.3)$$

Here, p is the pressure, I the unit tensor and \mathcal{D} is the rate-of-deformation tensor defined by

$$\mathcal{D} = \frac{1}{2}(\mathcal{L} + \mathcal{L}^T), \quad (2.1.4)$$

where \mathcal{L} is the gradient of the velocity, i.e.

$$\mathcal{L} = \text{grad } \mathbf{v} = \frac{\partial \mathbf{v}}{\partial \mathbf{x}} (\equiv (\nabla \mathbf{v})^T). \quad (2.1.5)$$

Furthermore, η_s is the solvent viscosity, and the elastic part S_p characterizes the polymer contribution.

In this chapter the elastic part S_p is assumed to be described by the KBKZ-model, which in its general form reads (see [50, p. 141] or [48, p. 23, p. 171])

$$S_p = \int_{-\infty}^t \left(\frac{\partial U}{\partial I_{C^{-1}}} C^{-1} - \frac{\partial U}{\partial I_C} C \right) d\tau. \quad (2.1.6)$$

Here, C is the strain tensor (see definition (2.1.12)), C^{-1} (the Finger tensor) is its inverse, I_C and $I_{C^{-1}}$ are the first invariants (traces) of these tensors, and the potential U is a scalar function of I_C , $I_{C^{-1}}$ and the time $t - \tau$. The term $\partial U / \partial I_C$ governs the second normal stress difference, which is small compared to the first normal stress difference (see Meissner et al. [37]). Accordingly, for simple shear flow Wagner modified the integral (2.1.6) by putting $\partial U / \partial I_C = 0$ and $\partial U / \partial I_{C^{-1}} = K(I_{C^{-1}})m(t - \tau)$, thus leading to (see [50, p. 209])

$$S_p = \int_{-\infty}^t K(I_{C^{-1}})m(t - \tau) C^{-1} d\tau. \quad (2.1.7)$$

The memory function m can be written as the derivative of the stress relaxation function G ,

$$m(t) = -G'(t). \quad (2.1.8)$$

The stress relaxation function G can be represented by a sum of n (≥ 1) exponential terms, i.e.

$$G(t) = \sum_{i=1}^n \mu_i e^{-\lambda_i t}, \quad (2.1.9)$$

where μ_i is the shear modulus corresponding to the relaxation rate λ_i . Henceforth we restrict ourselves to one relaxation rate λ , so that $G(t) = \mu e^{-\lambda t}$, and we use the kernel K explored by Papanastasiou et al. (see [50, p. 213]) given by

$$K(I_{C^{-1}}) = \frac{c}{c - 3 + I_{C^{-1}}}, \quad (2.1.10)$$

where c is a dimensionless material constant. Then the constitutive relation (2.1.7) becomes

$$S_p = \mu\lambda \int_{-\infty}^t \frac{c}{c-3+I_{C^{-1}}} C^{-1} e^{-\lambda(t-\tau)} d\tau, \quad (2.1.11)$$

where μ is the shear modulus of the material. The quotient μ/λ is also called the shear viscosity. When a material particle moves from position $\tilde{\mathbf{x}}$ at time τ to \mathbf{x} at time t ($\tau \leq t$), the strain tensor C is given by

$$C = \mathcal{F}^T \mathcal{F}, \quad \mathcal{F} = \frac{\partial \tilde{\mathbf{x}}}{\partial \mathbf{x}}, \quad (2.1.12)$$

and its inverse is

$$C^{-1} = \mathcal{F}^{-1} \mathcal{F}^{-T}. \quad (2.1.13)$$

We consider the axisymmetric shear flow in a cylindrical tube with radius R . Cylindrical coordinates (r, θ, z) are introduced with the z -axis along the centerline of the tube. With the flow aligned along the z -axis, the flow parameters are independent of the axial coordinate z and the azimuthal coordinate θ . Under the condition that the flow starts from rest at time $t = 0$, the velocity takes the form

$$\mathbf{v} = v(r, t)H(t)\mathbf{e}_z, \quad (2.1.14)$$

where H is the (Heaviside) step function and \mathbf{e}_z is a unit vector in the positive z -direction. The conservation of mass is now automatically satisfied, and the convective terms $\rho(\mathbf{v} \cdot \nabla)\mathbf{v}$ in (2.1.2) disappear. The no-slip boundary condition at the wall and the regularity of the velocity at the axis require

$$v(R, t) = 0, \quad (2.1.15)$$

and

$$\frac{\partial v}{\partial r}(0, t) = 0, \quad (2.1.16)$$

respectively. To determine the stress components we need the strain tensor C and its inverse. With the momentary position at time t represented in cylindrical coordinates by $(r, 0, z)$, the position of the same particle at an earlier time τ is $(r, 0, \tilde{z})$, where

$$\tilde{z} = z - \int_{\tau}^t v(r, s)H(s)ds. \quad (2.1.17)$$

Then (2.1.13) yields

$$C^{-1} = \begin{pmatrix} 1 & 0 & -\gamma \\ 0 & 1 & 0 \\ -\gamma & 0 & 1 + \gamma^2 \end{pmatrix} \quad (2.1.18)$$

with trace $I_{C^{-1}} = 3 + \gamma^2$, where

$$\gamma = \gamma(r, t, \tau) = - \int_{\tau}^t \frac{\partial v}{\partial r}(r, s)H(s)ds, \quad t \geq \tau, \quad (2.1.19)$$

is the shear strain from τ to t . For $\tau < 0$ no motion is observed, hence

$$\gamma(r, t, \tau) = \gamma(r, t, 0), \quad \tau < 0. \quad (2.1.20)$$

From (2.1.5) it follows that $L_{zr} = \partial v / \partial r$ is the only non-zero component of \mathcal{L} , implying that $D_{rz} = D_{zr} = \frac{1}{2} \partial v / \partial r$, whereas the remaining components of \mathcal{D} are zero. In terms of γ , the stress components T_{ij} determined from (2.1.3) and (2.1.11) become

$$\begin{aligned} T_{rr} &= T_{\theta\theta} = -p + \mu\lambda \int_{-\infty}^t \frac{c}{c + \gamma^2(r, t, \tau)} e^{-\lambda(t-\tau)} d\tau, \\ T_{zz} &= -p + \mu\lambda \int_{-\infty}^t \frac{c[1 + \gamma^2(r, t, \tau)]}{c + \gamma^2(r, t, \tau)} e^{-\lambda(t-\tau)} d\tau, \\ T_{rz} &= \eta_s \frac{\partial v}{\partial r} - \mu\lambda \int_{-\infty}^t \frac{c\gamma(r, t, \tau)}{c + \gamma^2(r, t, \tau)} e^{-\lambda(t-\tau)} d\tau, \\ T_{r\theta} &= T_{\theta z} = 0, \end{aligned} \quad (2.1.21)$$

where $p = p(r, z, t)$.

The balance of linear momentum (2.1.2), with $\rho \mathbf{b} = \mathbf{0}$, is satisfied if the stress components T_{ij} , given by (2.1.21), solve the following equations:

$$\frac{\partial T_{rr}}{\partial r} = 0, \quad \frac{\partial T_{rz}}{\partial r} + \frac{T_{rz}}{r} - \frac{\partial p}{\partial z} = \rho \frac{\partial v}{\partial t}. \quad (2.1.22)$$

Since T_{rz} and v are independent of z , the solution for the pressure p takes the form

$$p(r, z, t) = -f(t)z + p_0(r, t), \quad (2.1.23)$$

with

$$p_0(r, t) = \mu\lambda \int_{-\infty}^t \frac{c}{c + \gamma^2(r, t, \tau)} e^{-\lambda(t-\tau)} d\tau + P_0(t), \quad (2.1.24)$$

while the shear stress T_{rz} equals

$$T_{rz} = -\frac{1}{2}rf(t) + \frac{\rho}{r} \int_0^r y \frac{\partial v}{\partial t}(y, t) dy. \quad (2.1.25)$$

Here, f is the prescribed pressure gradient driving the flow, and P_0 is a further irrelevant pressure term. Substitution of (2.1.23) into (2.1.21)^{1,2} yields

$$\begin{aligned} T_{rr} &= T_{\theta\theta} = f(t)z - P_0(t), \\ T_{zz} &= f(t)z - P_0(t) + \mu\lambda \int_{-\infty}^t \frac{c\gamma^2(r, t, \tau)}{c + \gamma^2(r, t, \tau)} e^{-\lambda(t-\tau)} d\tau. \end{aligned} \quad (2.1.26)$$

By equating the expressions (2.1.25) and (2.1.21)³ for T_{rz} and using (2.1.20), we are led to the following relation between the velocity gradient and the pressure gradient:

$$\begin{aligned} \eta_s \frac{\partial v}{\partial r}(r, t) - \mu \frac{c\gamma(r, t, 0)}{c + \gamma^2(r, t, 0)} e^{-\lambda t} - \mu\lambda \int_0^t \frac{c\gamma(r, t, \tau)}{c + \gamma^2(r, t, \tau)} e^{-\lambda(t-\tau)} d\tau \\ = -\frac{1}{2}rf(t) + \frac{\rho}{r} \int_0^r y \frac{\partial v}{\partial t}(y, t) dy, \quad 0 \leq r \leq R, \quad t > 0. \end{aligned} \quad (2.1.27)$$

Equation (2.1.27) is made dimensionless by scaling length by R and time by λ^{-1} . Furthermore, we introduce dimensionless variables \hat{v} , $\hat{\gamma}$ and \hat{f} by writing $v = \lambda R \sqrt{c} \hat{v}$, $\gamma = \sqrt{c} \hat{\gamma}$, $f = \mu \sqrt{c} \hat{f}/R$, and the two dimensionless material parameters ε and α given by

$$\varepsilon = \frac{\eta_s \lambda}{\mu}, \quad \alpha = \frac{\rho R^2 \lambda^2}{\mu}. \quad (2.1.28)$$

Then equation (2.1.27) turns into its dimensionless form, reading (since no confusion will arise we omit the caret)

$$\begin{aligned} -\varepsilon \frac{\partial v}{\partial r}(r, t) + h(\Gamma(r, t))e^{-t} + \int_0^t h(\gamma(r, t, \tau))e^{-(t-\tau)} d\tau \\ = \frac{1}{2} r f(t) - \frac{\alpha}{r} \int_0^r y \frac{\partial v}{\partial t}(y, t) dy, \quad 0 \leq r \leq 1, \quad t > 0, \end{aligned} \quad (2.1.29)$$

where the function h is defined by

$$h(x) = \frac{x}{1+x^2}. \quad (2.1.30)$$

The variable Γ represents the shear strain from 0 to t , i.e.

$$\Gamma(r, t) = \gamma(r, t, 0) = - \int_0^t \frac{\partial v}{\partial r}(r, s) ds, \quad 0 \leq r \leq 1, \quad t \geq 0; \quad (2.1.31)$$

thus, γ can be expressed in terms of Γ as

$$\gamma(r, t, \tau) = \Gamma(r, t) - \Gamma(r, \tau), \quad 0 \leq r \leq 1, \quad 0 \leq \tau \leq t. \quad (2.1.32)$$

Notice that relation (2.1.19) between γ and $\partial v/\partial r$ remains the same after scaling, and also holds for the dimensionless variables $\hat{\gamma}$ and $\partial \hat{v}/\partial \hat{r}$. The velocity gradient, or shear strain-rate, w is defined by

$$w(r, t) = - \frac{\partial v}{\partial r}(r, t) = \frac{\partial \Gamma}{\partial t}(r, t). \quad (2.1.33)$$

The parameter ε represents the ratio of the solvent viscosity η_s and the shear viscosity μ/λ , and the quotient α/ε corresponds to the Reynolds number. For the strongly viscous polymers we consider, $\alpha \ll 1$. Thus, the last term in the right-hand side of (2.1.29) may be neglected. In the original equation (2.1.2) this amounts to the neglect of the inertia terms on the right. Consequently the shear stress T_{rz} in (2.1.25) reduces to

$$T_{rz} = - \frac{1}{2} r f(t), \quad (2.1.34)$$

which means that T_{rz} is a known function of r . With the inertia terms neglected ($\alpha = 0$) and with the notation (2.1.33), equation (2.1.29) takes the ultimate form

$$\begin{aligned} \varepsilon w(r, t) + h(\Gamma(r, t))e^{-t} + \int_0^t h(\gamma(r, t, \tau))e^{-(t-\tau)} d\tau = \frac{1}{2} r f(t), \\ 0 \leq r \leq 1, \quad t > 0. \end{aligned} \quad (2.1.35)$$

The boundary conditions pertinent to (2.1.35) read in dimensionless form

$$v(1, t) = 0, \quad w(0, t) = 0, \quad t > 0. \quad (2.1.36)$$

One integration by parts transforms (2.1.35) into

$$\varepsilon w(r, t) + \int_0^t w(r, \tau) h'(\gamma(r, t, \tau)) e^{-(t-\tau)} d\tau = \frac{1}{2} r f(t). \quad (2.1.37)$$

After division by $r/2$, the right-hand side of (2.1.37) becomes independent of r . Then, by letting $r \downarrow 0$ and using $h'(0) = 1$, we obtain the following expression for the pressure gradient $f(t)$:

$$f(t) = 2\varepsilon u(t) + 2 \int_0^t u(\tau) e^{-(t-\tau)} d\tau, \quad (2.1.38)$$

provided that

$$\lim_{r \downarrow 0} \frac{w(r, t)}{r} =: u(t) \quad (2.1.39)$$

exists. The inverse of (2.1.38) is

$$u(t) = \frac{1}{2\varepsilon} f(t) - \frac{1}{2\varepsilon^2} \int_0^t f(\tau) \exp\left[-\frac{1+\varepsilon}{\varepsilon}(t-\tau)\right] d\tau, \quad (2.1.40)$$

which can be used to calculate the function u when f is given.

We conclude this section by deriving an expression in terms of w for the volumetric flow rate Q defined by

$$Q(t) = 2\pi \int_0^R v(r, t) r dr, \quad (2.1.41)$$

or in dimensionless form

$$\hat{Q}(t) = 2 \int_0^1 \hat{v}(r, t) r dr, \quad (2.1.42)$$

where $\hat{Q} = Q/(\pi R^3 \lambda \sqrt{c})$. After one integration by parts with the aid of the no-slip boundary condition (2.1.36) at the wall, the volumetric flow rate can be expressed in terms of the velocity gradient by (omitting the caret)

$$Q(t) = \int_0^1 r^2 w(r, t) dr. \quad (2.1.43)$$

Since, according to (2.1.35), w is determined by f , the expression (2.1.43) provides a relationship between the volumetric flow rate Q and the pressure gradient f .

2.2 Steady state flow

In this section we investigate the asymptotic behaviour of the flow as $t \rightarrow \infty$, in case $\lim_{t \rightarrow \infty} f(t) = \bar{f}$ exists. It turns out that the flow reaches a steady state (in which the flow variables are independent of the time) as $t \rightarrow \infty$. This steady state plays an important role in the explanation of the spurt phenomenon. The steady state velocity profile is expressed in terms of the steady state velocity gradient ω , defined by

$$\omega(r) = \lim_{t \rightarrow \infty} w(r, t), \quad \omega(0) = 0. \quad (2.2.1)$$

From the stability analysis in Section 2.3 it follows that $\omega(r)$ exists under certain conditions; see the comment below Corollary 2.3.1. In this section we shall derive an equation for ω . Let the pressure gradient $f(t)$ be prescribed and tend to \bar{f} as $t \rightarrow \infty$. In the limit as $t \rightarrow \infty$, equation (2.1.35) turns into a relation between the steady state velocity gradient ω and the given pressure gradient \bar{f} .

Theorem 2.2.1 *If the steady state velocity gradient $\omega(r)$ exists, then it satisfies*

$$\varepsilon\omega(r) + \omega(r) \int_0^\infty \frac{\tau e^{-\tau}}{1 + \omega^2(r)\tau^2} d\tau = \frac{1}{2}r\bar{f}, \quad 0 \leq r \leq 1, \quad (2.2.2)$$

if

$$\bar{f} = \lim_{t \rightarrow \infty} f(t) \quad (2.2.3)$$

exists.

Proof: Given the existence of \bar{f} , we anticipate that $\omega(r)$, as defined by (2.2.1), exists (this will be justified below Corollary 2.3.1). Then for $t \rightarrow \infty$, the first and last terms of equation (2.1.35) tend to $\varepsilon\omega(r)$ and $r\bar{f}/2$, respectively. Since h is bounded, the function $h(\Gamma(r, t))e^{-t}$ vanishes for $t \rightarrow \infty$. Hence, to verify that equation (2.1.35) turns into equation (2.2.2) as $t \rightarrow \infty$, it remains to prove that

$$\lim_{t \rightarrow \infty} \int_0^t [h(\gamma(r, t, \tau)) - h(\omega(r)(t - \tau))] e^{-(t-\tau)} d\tau = 0. \quad (2.2.4)$$

Let $\delta > 0$, then there exists a time T_1 such that

$$|w(r, t) - \omega(r)| < \delta, \quad t > T_1. \quad (2.2.5)$$

Choose a fixed $t_0 > T_1$, then there exists a time T_2 such that

$$e^{-t} \int_0^{t_0} |h(\gamma(r, t, \tau)) - h(\omega(r)(t - \tau))| e^\tau d\tau < \delta, \quad t > T_2. \quad (2.2.6)$$

For all $t > t_0$ the remaining integral over $[t_0, t]$ is bounded by

$$\int_{t_0}^t |h(\gamma) - h(\omega(t - \tau))| e^{-(t-\tau)} d\tau \leq \int_{t_0}^t |\gamma(r, t, \tau) - \omega(r)(t - \tau)| e^{-(t-\tau)} d\tau < \delta, \quad (2.2.7)$$

since (2.1.19) and (2.2.5) imply that

$$|\gamma(r, t, \tau) - \omega(r)(t - \tau)| < \delta(t - \tau), \quad t_0 \leq \tau \leq t. \quad (2.2.8)$$

Thus, in view of (2.2.6) and (2.2.7), the integral in (2.2.4) is bounded by 2δ for all $t > \max\{t_0, T_2\}$. This completes the proof. \square

We introduce the integral J defined by

$$J(\omega) = \omega \int_0^\infty \frac{\tau e^{-\tau}}{1 + \omega^2 \tau^2} d\tau. \quad (2.2.9)$$

Then the steady state velocity gradient can be determined for each $r \in [0, 1]$ by solving $\omega = \omega(r)$ from the equation

$$\mathcal{F}(\omega(r)) = F(r), \quad (2.2.10)$$

where the function \mathcal{F} is defined by

$$\mathcal{F}(\omega) = \varepsilon \omega + J(\omega), \quad (2.2.11)$$

and the steady state shear stress F is given by (cf. (2.1.34))

$$F(r) = r \bar{f}/2. \quad (2.2.12)$$

The steady state velocity profile $\bar{v}(r) = \lim_{t \rightarrow \infty} v(r, t)$ is next obtained by integration of $\omega(r) = -\bar{v}'(r)$ using the boundary condition $\bar{v}(1) = 0$ at the wall.

In Appendix A it is shown that the function \mathcal{F} is nonmonotone in ω when $0 \leq \varepsilon < \varepsilon_1$, where $\varepsilon_1 = -J'(\omega^{**}) = 0.02886$. In Figure 2.1 the function $\mathcal{F}(\omega)$ is plotted for a specific value of ε with $0 < \varepsilon < \varepsilon_1$. Since the solvent viscosity η_s is small in comparison to the shear viscosity μ/λ , we will henceforth assume that $0 < \varepsilon < \varepsilon_1$ (cf. (2.1.28)). Then the function $\mathcal{F}(\omega)$ has two extreme values, a maximum $F_M = \varepsilon \omega_M + J(\omega_M)$ at $\omega = \omega_M$ and a minimum $F_m = \varepsilon \omega_m + J(\omega_m)$ at $\omega = \omega_m$; see Figure 2.1. If $\varepsilon \uparrow \varepsilon_1$, the two extreme values coalesce at the inflection point $\omega^{**} = 2.6255$. In addition to $\omega = \omega_M$ and $\omega = \omega_m$, both equations $\mathcal{F}(\omega) = F_M$ and $\mathcal{F}(\omega) = F_m$ have a second solution $\omega = \tilde{\omega}_M$ and $\omega = \tilde{\omega}_m$, respectively; see Figure 2.1. Numerical values of $\omega_M, F_M, \tilde{\omega}_M, \omega_m, F_m, \tilde{\omega}_m$ for $\varepsilon = 0.010, 0.020, 0.025$ are presented in Table A.1 of Appendix A.

Since $F(r) = r \bar{f}/2$ with constant \bar{f} , the function $F(r)$ reaches its maximum at the wall $r = 1$. This maximum, denoted by $F_W = \bar{f}/2$, remains below the minimum F_m , if $\bar{f} < 2F_m$. In that case equation (2.2.10) has a unique solution $\omega(r) < \tilde{\omega}_m$ for each radial coordinate r . Moreover, $\omega(r)$ is continuous in r , leading to a smooth steady state velocity profile $\bar{v}(r)$, and the flow is referred to as classical flow. The maximum F_W exceeds the maximum F_M , if $\bar{f} > 2F_M$. Denote the critical pressure gradient by $\bar{f}_{crit} := 2F_M$. Then in supercritical flow, i.e. if $\bar{f} > \bar{f}_{crit}$, equation (2.2.10) has

- one solution if $0 \leq F < F_m$,
- three solutions if $F_m < F < F_M$,
- one solution if $F_M < F \leq F_W$;

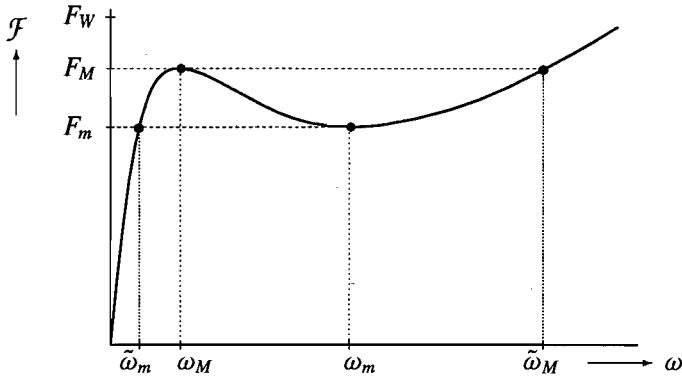


Figure 2.1 The function $\mathcal{F}(\omega) = \varepsilon\omega + J(\omega)$, when $0 < \varepsilon < \varepsilon_1$. In steady state flow the velocity gradient ω satisfies $\mathcal{F}(\omega) = F$, where $F = r\bar{f}/2$ is the steady state shear stress.

see Figure 2.1. Consequently, in supercritical flow the steady state velocity gradient ω has at least one jump at some radial coordinate. In case of exactly one jump we denote the radial coordinate at which the jump occurs by r^* ($r^* < 1$), and we refer to the flow as spurt flow. Hence, in spurt flow $\omega(r) < \omega_-^*$ for $0 \leq r < r^*$, whereas $\omega(r) > \omega_+^*$ for $r^* < r \leq 1$, where

$$\omega_-^* := \lim_{r \uparrow r^*} \omega(r) < \lim_{r \downarrow r^*} \omega(r) =: \omega_+^*, \tag{2.2.13}$$

with $\omega_-^* \leq \omega_M$ and $\omega_+^* \geq \omega_m$. The corresponding shear stress at which the jump occurs is denoted by $F^* := F(r^*) = r^*\bar{f}/2$, such that $\mathcal{F}(\omega_{\pm}^*) = F^*$, with $F_m \leq F^* \leq F_M$. As a result of the jump the velocity profile $\bar{v}(r)$ shows a kink at $r = r^*$; see Figure 2.2. If the velocity

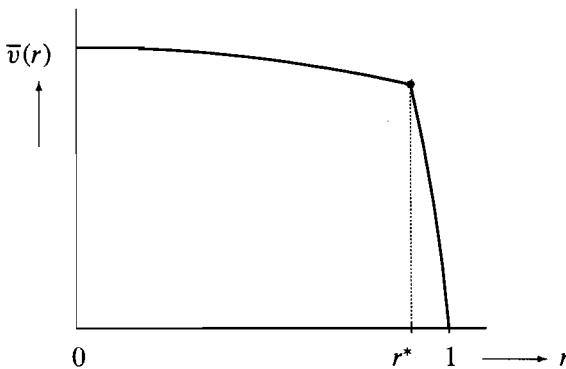


Figure 2.2 The steady state velocity profile $\bar{v}(r)$ in spurt flow showing a kink at $r = r^*$.

gradient jumps from $\omega_-^* = \omega_M$ to $\omega_+^* = \tilde{\omega}_M$ (i.e. if $F^* = F_M$), we call this top-jumping. If the velocity gradient jumps from $\omega_-^* = \tilde{\omega}_m$ to $\omega_+^* = \omega_m$ (i.e. if $F^* = F_m$), we call this bottom-jumping. Due to the jump in the velocity gradient profile, a layer with large velocity gradients

forms near the wall, the so-called spurt layer. The large velocity gradients near the wall give rise to an overall raise of the velocity in the capillary. As a result, the steady state volumetric flow rate \bar{Q} given by (cf. (2.1.42), (2.1.43))

$$\bar{Q} = 2 \int_0^1 \bar{v}(r) r dr = \int_0^1 r^2 \omega(r) dr, \quad (2.2.14)$$

will substantially increase when the pressure gradient is increased beyond \bar{f}_{crit} .

2.3 Stability analysis

In this section we first investigate the uniqueness and the existence of the solution of the integrodifferential equation (2.1.35). As the steady state equation (2.2.10) can have more than one solution ω , we next discuss the local stability of the different steady state solutions. This will be the main topic of this section.

The shear strain Γ and the velocity gradient w are related by

$$\Gamma(r, t) = \int_0^t w(r, s) ds; \quad (2.3.1)$$

see (2.1.31) and (2.1.33). Using (2.3.1) and (2.1.32) we rewrite the governing equation (2.1.35) as

$$\varepsilon \frac{\partial \Gamma}{\partial t}(r, t) + h(\Gamma(r, t)) e^{-t} + \int_0^t h(\Gamma(r, t) - \Gamma(r, \tau)) e^{-(t-\tau)} d\tau = \frac{1}{2} r f(t), \quad (2.3.2)$$

valid for $0 \leq r \leq 1$, $t > 0$. Equation (2.3.2) is a nonlinear integrodifferential equation for Γ . We integrate this equation with respect to t , suppress the variable r , and obtain

$$\Gamma(t) = \frac{r}{2\varepsilon} \int_0^t f(s) ds - \frac{1}{\varepsilon} \int_0^t h(\Gamma(s)) e^{-s} ds - \frac{1}{\varepsilon} \int_0^t \int_0^s h(\Gamma(s) - \Gamma(\tau)) e^{-(s-\tau)} d\tau ds. \quad (2.3.3)$$

Theorem 2.3.1 *The shear strain Γ depends continuously on the pressure gradient f .*

Proof: Let Γ_1 be a solution of (2.3.3) with $f = f_1$, and let Γ_2 be a solution of (2.3.3) with $f = f_2$. Then the difference $\Gamma_1 - \Gamma_2$ satisfies

$$\begin{aligned} |\Gamma_1(t) - \Gamma_2(t)| &\leq \frac{r}{2\varepsilon} \int_0^t |f_1(s) - f_2(s)| ds + \frac{1}{\varepsilon} \int_0^t |h(\Gamma_1(s)) - h(\Gamma_2(s))| e^{-s} ds \\ &\quad + \frac{1}{\varepsilon} \int_0^t \int_0^s |h(\Gamma_1(s) - \Gamma_1(\tau)) - h(\Gamma_2(s) - \Gamma_2(\tau))| e^{-(s-\tau)} d\tau ds, \quad t \geq 0. \end{aligned} \quad (2.3.4)$$

Since $|h(x) - h(y)| \leq |x - y|$ for $x, y \in \mathbb{R}$, it follows that

$$\begin{aligned}
 |\Gamma_1(t) - \Gamma_2(t)| &\leq \frac{r}{2\varepsilon} \int_0^t |f_1(s) - f_2(s)| ds + \frac{1}{\varepsilon} \int_0^t |\Gamma_1(s) - \Gamma_2(s)| e^{-s} ds \\
 &\quad + \frac{1}{\varepsilon} \int_0^t \int_0^s (|\Gamma_1(s) - \Gamma_2(s)| + |\Gamma_1(\tau) - \Gamma_2(\tau)|) e^{-(s-\tau)} d\tau ds \\
 &= \frac{r}{2\varepsilon} \int_0^t |f_1(s) - f_2(s)| ds + \frac{1}{\varepsilon} \int_0^t |\Gamma_1(s) - \Gamma_2(s)| (2 - e^{-(t-s)}) ds \\
 &\leq \frac{r}{2\varepsilon} \int_0^t |f_1(s) - f_2(s)| ds + \frac{2}{\varepsilon} \int_0^t |\Gamma_1(s) - \Gamma_2(s)| ds, \quad t \geq 0.
 \end{aligned} \tag{2.3.5}$$

By applying Gronwall's lemma (see Lakshmikantham et al. [27, Theorem 1.1.2]) to this inequality we obtain

$$|\Gamma_1(t) - \Gamma_2(t)| \leq \frac{r}{2\varepsilon} \int_0^t |f_1(s) - f_2(s)| e^{2(t-s)/\varepsilon} ds, \quad t \geq 0. \tag{2.3.6}$$

From (2.3.6) it is readily seen that Γ depends continuously on f . \square

In the same manner it can be shown that the shear strain $\Gamma(r, t)$ is a continuous function of r .

Theorem 2.3.2 *Let Γ_1 and Γ_2 be solutions of (2.3.3), then $\Gamma_1 \equiv \Gamma_2$.*

Proof. Put $f_1 \equiv f_2$ in (2.3.6). Then it immediately follows that $\Gamma_1(t) = \Gamma_2(t)$ for $t \geq 0$. \square

Theorem 2.3.3 *Let f be continuous on $[0, \infty)$. Then for each $T > 0$, equation (2.3.3) has a unique solution Γ on the interval $[0, T]$.*

Proof. The theorem is proved by applying the fixed point theorem for contraction mappings; see Kreyszig [25, p. 300] or Miller [38, p. 419]. Let $T > 0$. Let $C[0, T]$ be the Banach space of continuous functions defined on $[0, T]$, with norm

$$\|\phi\|_{[0, T]} = \sup_{0 \leq t \leq T} e^{-2t/\varepsilon} |\phi(t)|. \tag{2.3.7}$$

Then $C[0, T]$ is a complete metric space under the natural metric $d(\phi, \psi) = \|\phi - \psi\|_{[0, T]}$. For $\phi \in C[0, T]$ and $0 \leq t \leq T$, define the mapping \mathcal{M} by

$$\mathcal{M}(\phi)(t) = \Psi(t) - \frac{1}{\varepsilon} \int_0^t h(\phi(s)) e^{-s} ds - \frac{1}{\varepsilon} \int_0^t \int_0^s h(\phi(s) - \phi(\tau)) e^{-(s-\tau)} d\tau ds, \tag{2.3.8}$$

where

$$\Psi(t) = \frac{r}{2\varepsilon} \int_0^t f(s) ds. \tag{2.3.9}$$

Then equation (2.3.3) can be rewritten as $\Gamma(t) = \mathcal{M}(\Gamma)(t)$ for $0 \leq t \leq T$. Define $S = \{\phi \in C[0, T] \mid \|\phi - \Psi\|_{[0, T]} \leq 1\}$. Given $\phi \in S$ and $t \in [0, T]$, one has, since $|h(x)| \leq 1/2$ for $x \in \mathbb{R}$,

$$|\mathcal{M}(\phi)(t) - \Psi(t)| \leq \frac{1}{2\varepsilon} \int_0^t e^{-s} ds + \frac{1}{2\varepsilon} \int_0^t \int_0^s e^{-(s-\tau)} d\tau ds = \frac{t}{2\varepsilon}. \quad (2.3.10)$$

Hence,

$$\|\mathcal{M}(\phi) - \Psi\|_{[0, T]} \leq \sup_{0 \leq t \leq T} \frac{te^{-2t/\varepsilon}}{2\varepsilon} \leq \frac{e^{-1}}{4} < 1. \quad (2.3.11)$$

Furthermore, it is easily seen that if f is continuous, then Ψ is continuous. Consequently, $\mathcal{M}(\phi)$ is continuous, whenever ϕ is continuous. Therefore, \mathcal{M} maps S into S . Given $\phi_1, \phi_2 \in S$ and $0 \leq t \leq T$, one has

$$\begin{aligned} |\mathcal{M}(\phi_1)(t) - \mathcal{M}(\phi_2)(t)| &\leq \frac{1}{\varepsilon} \int_0^t |h(\phi_1(s)) - h(\phi_2(s))| e^{-s} ds \\ &\quad + \frac{1}{\varepsilon} \int_0^t \int_0^s |h(\phi_1(s) - \phi_1(\tau)) - h(\phi_2(s) - \phi_2(\tau))| e^{-(s-\tau)} d\tau ds \\ &\leq \frac{1}{\varepsilon} \int_0^t |\phi_1(s) - \phi_2(s)| e^{-s} ds \\ &\quad + \frac{1}{\varepsilon} \int_0^t \int_0^s (|\phi_1(s) - \phi_2(s)| + |\phi_1(\tau) - \phi_2(\tau)|) e^{-(s-\tau)} d\tau ds \\ &\leq \frac{1}{\varepsilon} \|\phi_1 - \phi_2\|_{[0, T]} \left(\int_0^t e^{(2/\varepsilon-1)s} ds + \int_0^t \int_0^s [e^{(2/\varepsilon-1)s+\tau} + e^{(2/\varepsilon+1)\tau-s}] d\tau ds \right) \\ &= \|\phi_1 - \phi_2\|_{[0, T]} \left(\frac{1+\varepsilon}{2+\varepsilon} e^{2t/\varepsilon} - 1 + \frac{e^{-t}}{2+\varepsilon} \right). \end{aligned} \quad (2.3.12)$$

Hence,

$$\begin{aligned} \|\mathcal{M}(\phi_1) - \mathcal{M}(\phi_2)\|_{[0, T]} &\leq \|\phi_1 - \phi_2\|_{[0, T]} \sup_{0 \leq t \leq T} \left\{ \frac{1+\varepsilon}{2+\varepsilon} - e^{-2t/\varepsilon} + \frac{e^{-(2/\varepsilon+1)t}}{2+\varepsilon} \right\} \\ &\leq \frac{1+\varepsilon}{2+\varepsilon} \|\phi_1 - \phi_2\|_{[0, T]}. \end{aligned} \quad (2.3.13)$$

Since $(1+\varepsilon)/(2+\varepsilon) < 1$ for $\varepsilon > 0$, the mapping $\mathcal{M} : S \rightarrow S$ is a contraction. By the Banach fixed point theorem it follows that \mathcal{M} has a unique fixed point in S . Since $\mathcal{M}(\Gamma) = \Gamma$, this fixed point is the unique solution Γ of (2.3.3) in S . \square

Next, we investigate the stability properties of the steady state solution ω , which satisfies (2.2.10). The pressure gradient $f = f_\omega$ is chosen such that the solution of (2.1.35) is given by $w(r, t) = \omega(r)$ for $t \geq 0$. Then the shear strain equals

$$\Gamma(r, t) = \omega(r)t, \quad t \geq 0, \quad (2.3.14)$$

and by substitution of (2.3.14) into (2.3.2) we find that f_ω is given by

$$f_\omega(t) = \frac{2}{r} \left[\varepsilon\omega(r) + h(\omega(r)t)e^{-t} + \int_0^t h(\omega(r)\tau)e^{-\tau} d\tau \right], \quad t \geq 0. \quad (2.3.15)$$

To investigate the stability properties of ω , we let $t_0 \geq 0$ and we assume that the system is in the steady state with $w(r, t) = \omega(r)$ for $t < t_0$; this is accomplished by choosing $f(t) = f_\omega(t)$ for $0 \leq t < t_0$. At $t = t_0$ the steady state is perturbed by a prescribed pressure gradient f of the form

$$f(t) = f_\omega(t) + \varphi(t), \quad t \geq t_0. \quad (2.3.16)$$

Here, φ denotes the perturbation of f_ω applied at time t_0 . From now on we consider only times $t \geq t_0$. The resulting perturbation of the steady state velocity gradient $\omega(r)$ is denoted by ξ , so that

$$w(r, t + t_0) = \omega(r) + \xi(r, t), \quad t \geq 0, \quad (2.3.17)$$

where $\xi(r, t) = 0$ for $t < 0$. Integration of (2.3.17) with respect to t yields

$$\Gamma(r, t + t_0) = \omega(r)t + \omega(r)t_0 + X(r, t), \quad t \geq 0, \quad (2.3.18)$$

where X is defined by

$$X(r, t) = \int_0^t \xi(r, \tau) d\tau, \quad t \geq 0. \quad (2.3.19)$$

The behaviour of the perturbation $\xi(r, t)$ for $t > 0$ determines the stability of the unperturbed steady state solution $\omega(r)$. As the dependence on r is irrelevant for our stability analysis, we suppress this variable and represent all functions as depending only on t .

In order to derive the equation for $\xi(t)$, we replace t by $t + t_0$ in (2.3.2), and obtain

$$\begin{aligned} \varepsilon \frac{\partial \Gamma}{\partial t}(t + t_0) + h(\Gamma(t + t_0))e^{-(t+t_0)} + \int_0^{t_0} h(\Gamma(t + t_0) - \Gamma(\tau))e^{-(t+t_0-\tau)} d\tau \\ + \int_{t_0}^{t+t_0} h(\Gamma(t + t_0) - \Gamma(\tau))e^{-(t+t_0-\tau)} d\tau = \frac{1}{2}r[f_\omega(t + t_0) + \varphi(t + t_0)], \end{aligned} \quad (2.3.20)$$

valid for $t > 0$. The two integrals in (2.3.20) are rewritten as

$$\begin{aligned} \int_0^{t_0} h(\Gamma(t + t_0) - \Gamma(\tau))e^{-(t+t_0-\tau)} d\tau &= \int_t^{t+t_0} h(\Gamma(t + t_0) - \Gamma(t + t_0 - \tau))e^{-\tau} d\tau, \\ \int_{t_0}^{t+t_0} h(\Gamma(t + t_0) - \Gamma(\tau))e^{-(t+t_0-\tau)} d\tau &= \int_0^t h(\Gamma(t + t_0) - \Gamma(\tau + t_0))e^{-(t-\tau)} d\tau. \end{aligned} \quad (2.3.21)$$

From (2.3.14) and (2.3.18) it follows that

$$\begin{aligned}\Gamma(t+t_0) - \Gamma(t+t_0-\tau) &= \omega\tau + X(t), \quad t \leq \tau \leq t+t_0, \\ \Gamma(t+t_0) - \Gamma(\tau+t_0) &= \omega t - \omega\tau + X(t) - X(\tau), \quad 0 \leq \tau \leq t.\end{aligned}\quad (2.3.22)$$

Substitution of (2.3.15), (2.3.18), (2.3.21) and (2.3.22) into (2.3.20) yields

$$\begin{aligned}\frac{dX}{dt} &= \frac{r}{2\varepsilon}\varphi(t+t_0) + \frac{1}{\varepsilon}h(\omega t + \omega t_0)e^{-(t+t_0)} + \frac{1}{\varepsilon}\int_0^{t+t_0} h(\omega\tau)e^{-\tau}d\tau \\ &\quad - \frac{1}{\varepsilon}h(\omega t + \omega t_0 + X(t))e^{-(t+t_0)} - \frac{1}{\varepsilon}\int_t^{t+t_0} h(\omega\tau + X(t))e^{-\tau}d\tau \\ &\quad - \frac{1}{\varepsilon}\int_0^t h(\omega t - \omega\tau + X(t) - X(\tau))e^{-(t-\tau)}d\tau, \quad t > 0.\end{aligned}\quad (2.3.23)$$

The latter equation is rewritten as the following integrodifferential equation for X :

$$\frac{dX(t)}{dt} = \Phi(t) - A(t+t_0)X(t) + \int_0^t a(t-\tau)X(\tau)d\tau + \mathcal{G}(X)(t, t_0), \quad t > 0, \quad (2.3.24)$$

with initial condition $X(0) = 0$. Here we introduced the notations

$$\Phi(t) = \frac{r}{2\varepsilon}\varphi(t+t_0), \quad a(t) = \frac{1}{\varepsilon}h'(\omega t)e^{-t}, \quad A(t) = a(t) + \int_0^t a(\tau)d\tau, \quad (2.3.25)$$

$$\begin{aligned}\mathcal{G}(X)(t, t_0) &= -\frac{1}{\varepsilon}R(X(t), \omega t + \omega t_0)e^{-(t+t_0)} - \frac{1}{\varepsilon}\int_t^{t+t_0} R(X(t), \omega\tau)e^{-\tau}d\tau \\ &\quad - \frac{1}{\varepsilon}\int_0^t R(X(t) - X(\tau), \omega t - \omega\tau)e^{-(t-\tau)}d\tau,\end{aligned}\quad (2.3.26)$$

where the function $R(X, \gamma)$ is given by

$$R(X, \gamma) = h(\gamma + X) - h(\gamma) - h'(\gamma)X. \quad (2.3.27)$$

Representing the function h by a Taylor expansion around γ , we observe that $R(X, \gamma) = h''(\gamma + \kappa X)X^2/2$ for some $\kappa \in (0, 1)$. Recalling that $dX(t)/dt = \xi(t)$ by (2.3.19), and performing one integration by parts in (2.3.24), we are led to the nonlinear integral equation

$$\xi(t) = \Phi(t) - c(t)X(t) - \int_0^t b(t-\tau)\xi(\tau)d\tau + \mathcal{G}(X)(t, t_0), \quad (2.3.28)$$

where b and c are given by

$$b(t) = \int_t^\infty a(\tau)d\tau, \quad c(t) = a(t+t_0) - b(t+t_0). \quad (2.3.29)$$

Finally, we rewrite (2.3.28) in the ultimate form

$$\xi(t) + \int_0^t k(t, \tau)\xi(\tau)d\tau = \Phi(t) + \mathcal{H}(\xi)(t), \quad t \geq 0, \quad (2.3.30)$$

where the kernel k is defined by

$$k(t, \tau) = c(t) + b(t - \tau), \quad 0 \leq \tau \leq t, \quad (2.3.31)$$

and the nonlinear term $\mathcal{H}(\xi)(t)$ is defined similar as $\mathcal{G}(X)(t, t_0)$ in (2.3.26), viz.

$$\mathcal{H}(\xi)(t) = \mathcal{H}_1(\xi)(t) + \mathcal{H}_2(\xi)(t) + \mathcal{H}_3(\xi)(t), \quad (2.3.32)$$

where

$$\begin{aligned} \mathcal{H}_1(\xi)(t) &= -\frac{1}{\varepsilon} R \left(\int_0^t \xi(s) ds, \omega t + \omega t_0 \right) e^{-(t+t_0)}, \\ \mathcal{H}_2(\xi)(t) &= -\frac{1}{\varepsilon} \int_t^{t+t_0} R \left(\int_0^t \xi(s) ds, \omega \tau \right) e^{-\tau} d\tau, \\ \mathcal{H}_3(\xi)(t) &= -\frac{1}{\varepsilon} \int_0^t R \left(\int_\tau^t \xi(s) ds, \omega t - \omega \tau \right) e^{-(t-\tau)} d\tau. \end{aligned} \quad (2.3.33)$$

By putting $k(t, \tau) = 0$ for $0 \leq t < \tau$, the kernel k is a Volterra kernel (see Gripenberg et al. [17, Definition 9.2.1]), and equation (2.3.30) is a nonlinear Volterra integral equation of nonconvolution type for ξ . Volterra integral equations are treated in e.g. the books of Miller [38] and of Gripenberg et al. [17].

The stability question for the steady state solution ω can now be reduced to the stability question for the zero solution $\xi \equiv 0$ of (2.3.30) with $\Phi \equiv 0$. Following Bownds and Cushing [6] we define the following stability criteria for the zero solution $\xi \equiv 0$.

Definition 2.3.1 *Let V be a normed space of functions defined for $t \geq 0$, with norm $\|\cdot\|_V$. Then the zero solution $\xi \equiv 0$ of (2.3.30) corresponding to $\Phi \equiv 0$ is called*

- *stable on V if for each $t_0 \geq 0$ and each $\eta > 0$ there exists a $\delta > 0$ (depending on t_0 and η) such that whenever $\Phi \in V$ with $\|\Phi\|_V \leq \delta$, the solution ξ of (2.3.30) exists and satisfies $|\xi(t)| \leq \eta$ for all $t \geq 0$;*
- *asymptotically stable on V if it is stable on V and if for each $t_0 \geq 0$ there exists a $\delta > 0$ (depending on t_0) such that whenever $\Phi \in V$ with $\|\Phi\|_V \leq \delta$, one has $\xi(t) \rightarrow 0$ as $t \rightarrow \infty$.*

As a proper function space to work with we choose the Banach space $V = BC_0 \cap L^1$, where

$$\begin{aligned} BC_0 &:= \{\phi : \mathbb{R}^+ \rightarrow \mathbb{R} \mid \phi \text{ is continuous, } \lim_{t \rightarrow \infty} \phi(t) = 0\}, \\ L^1 &:= \{\phi : \mathbb{R}^+ \rightarrow \mathbb{R} \mid \int_0^\infty |\phi(t)| dt < \infty\}, \end{aligned} \quad (2.3.34)$$

with the norm in $BC_0 \cap L^1$ given by

$$\|\phi\| = \sup_{t \geq 0} |\phi(t)| + \int_0^\infty |\phi(t)| dt. \quad (2.3.35)$$

Notice that a function in BC_0 is bounded, so that the norm (2.3.35) is finite in $BC_0 \cap L^1$. Then $BC_0 \cap L^1$ is a complete metric space under the natural metric $d(\phi, \psi) = \|\phi - \psi\|$.

We first present two preliminary lemmas on the operator \mathcal{H} introduced in (2.3.32) and (2.3.33).

Lemma 2.3.1 *The operator \mathcal{H} maps $BC_0 \cap L^1$ into $BC_0 \cap L^1$.*

Proof: Let $\xi \in BC_0 \cap L^1$. Since ξ is continuous, it is easily seen that $\mathcal{H}(\xi)$ is continuous. Hence, in order that $\mathcal{H}(\xi) \in BC_0 \cap L^1$, it remains to prove that

$$\sup_{t \geq 0} |\mathcal{H}(\xi)(t)| < \infty, \quad \lim_{t \rightarrow \infty} \mathcal{H}(\xi)(t) = 0, \quad \int_0^\infty |\mathcal{H}(\xi)(t)| dt < \infty. \quad (2.3.36)$$

Since $|h'(X)| \leq 1$ for $X \in \mathbb{R}$, the function R is bounded by

$$|R(X, \gamma)| \leq 2|X|, \quad X, \gamma \in \mathbb{R}. \quad (2.3.37)$$

From (2.3.37) we derive the following inequalities, valid for $t \geq 0$ and $t_0 \geq 0$:

$$|\mathcal{H}_1(\xi)(t)| \leq \frac{2}{\varepsilon} \|\xi\| e^{-t}, \quad |\mathcal{H}_2(\xi)(t)| \leq \frac{2}{\varepsilon} \|\xi\| e^{-t}, \quad |\mathcal{H}_3(\xi)(t)| \leq \frac{2}{\varepsilon} \|\xi\|. \quad (2.3.38)$$

These results prove (2.3.36)¹, and (2.3.36)^{2,3} for \mathcal{H}_1 and \mathcal{H}_2 . To prove (2.3.36)^{2,3} for \mathcal{H}_3 , we sharpen the estimate (2.3.38)³ to

$$\begin{aligned} |\mathcal{H}_3(\xi)(t)| &\leq \frac{2}{\varepsilon} \int_0^t \int_\tau^t |\xi(s)| e^{-(t-\tau)} ds d\tau \\ &\leq \frac{2}{\varepsilon} \int_0^{t/2} \|\xi\| e^{-(t-\tau)} d\tau + \frac{2}{\varepsilon} \int_{t/2}^t \int_\tau^t |\xi(s)| e^{-(t-\tau)} ds d\tau \\ &= \frac{2}{\varepsilon} \|\xi\| e^{-t/2} (1 - e^{-t/2}) + \frac{2}{\varepsilon} \int_{t/2}^t |\xi(s)| (e^{-(t-s)} - e^{-t/2}) ds. \end{aligned} \quad (2.3.39)$$

From (2.3.39) it easily follows that $\lim_{t \rightarrow \infty} \xi(t) = 0$ implies $\lim_{t \rightarrow \infty} \mathcal{H}_3(\xi)(t) = 0$. Finally, we use (2.3.39) to estimate

$$\begin{aligned} \int_0^\infty |\mathcal{H}_3(\xi)(t)| dt &\leq \frac{2}{\varepsilon} \|\xi\| \int_0^\infty e^{-t/2} dt + \frac{2}{\varepsilon} \int_0^\infty \int_{t/2}^t |\xi(s)| (e^{-(t-s)} - e^{-t/2}) ds dt \\ &= \frac{4}{\varepsilon} \|\xi\| + \frac{2}{\varepsilon} \int_0^\infty |\xi(s)| (1 + e^{-s} - 2e^{-s/2}) ds \leq \frac{6}{\varepsilon} \|\xi\|. \end{aligned} \quad (2.3.40)$$

This completes the proof of (2.3.36). □

Definition 2.3.2 *Let \mathcal{T} be an operator that maps $BC_0 \cap L^1$ into $BC_0 \cap L^1$. Then \mathcal{T} is of higher order with respect to $BC_0 \cap L^1$ if and only if $\mathcal{T}(0) = 0$, and for each $\eta > 0$ there exists a $\delta > 0$ such that $\|\mathcal{T}(\phi_1) - \mathcal{T}(\phi_2)\| \leq \eta \|\phi_1 - \phi_2\|$ whenever $\phi_1, \phi_2 \in BC_0 \cap L^1$ with $\|\phi_1\|, \|\phi_2\| \leq \delta$.*

Lemma 2.3.2 *The operator \mathcal{H} is of higher order with respect to $BC_0 \cap L^1$.*

Proof: In Lemma 2.3.1 it was shown that \mathcal{H} maps $BC_0 \cap L^1$ into $BC_0 \cap L^1$. From $R(0, \gamma) = 0$ for $\gamma \in \mathbb{R}$, it follows that $\mathcal{H}(0) = 0$. We start with some preliminaries. Since h'' is bounded, there exists a constant represented by εM such that

$$|R(X_1, \gamma) - R(X_2, \gamma)| \leq \varepsilon M(|X_1| + |X_2|)|X_1 - X_2|, \quad X_1, X_2, \gamma \in \mathbb{R}. \quad (2.3.41)$$

Let $\xi_1, \xi_2 \in BC_0 \cap L^1$. From (2.3.41) we derive the following inequalities, valid for $t_0 \geq 0$:

$$\begin{aligned} |\mathcal{H}_1(\xi_1)(t) - \mathcal{H}_1(\xi_2)(t)| &\leq M(\|\xi_1\| + \|\xi_2\|)\|\xi_1 - \xi_2\|e^{-t}, \quad t \geq 0, \\ |\mathcal{H}_2(\xi_1)(t) - \mathcal{H}_2(\xi_2)(t)| &\leq M(\|\xi_1\| + \|\xi_2\|)\|\xi_1 - \xi_2\|e^{-t}, \quad t \geq 0, \\ |\mathcal{H}_3(\xi_1)(t) - \mathcal{H}_3(\xi_2)(t)| &\leq M(\|\xi_1\| + \|\xi_2\|)\|\xi_1 - \xi_2\|, \quad t \geq 0. \end{aligned} \quad (2.3.42)$$

From (2.3.42) it readily follows that

$$\sup_{t \geq 0} |\mathcal{H}(\xi_1)(t) - \mathcal{H}(\xi_2)(t)| \leq 3M(\|\xi_1\| + \|\xi_2\|)\|\xi_1 - \xi_2\|. \quad (2.3.43)$$

Next, we sharpen the estimate (2.3.42)³ to

$$\begin{aligned} |\mathcal{H}_3(\xi_1)(t) - \mathcal{H}_3(\xi_2)(t)| &\leq M \int_0^{t/2} (\|\xi_1\| + \|\xi_2\|)\|\xi_1 - \xi_2\|e^{-(t-\tau)} d\tau \\ &\quad + M \int_{t/2}^t \int_{\tau}^t \|\xi_1 - \xi_2\|(|\xi_1(s)| + |\xi_2(s)|)e^{-(t-\tau)} ds d\tau \\ &= M(\|\xi_1\| + \|\xi_2\|)\|\xi_1 - \xi_2\|e^{-t/2}(1 - e^{-t/2}) \\ &\quad + M\|\xi_1 - \xi_2\| \int_{t/2}^t (|\xi_1(s)| + |\xi_2(s)|)(e^{-(t-s)} - e^{-t/2}) ds. \end{aligned} \quad (2.3.44)$$

By use of this estimate we find

$$\begin{aligned} \int_0^\infty |\mathcal{H}_3(\xi_1)(t) - \mathcal{H}_3(\xi_2)(t)| dt &\leq M(\|\xi_1\| + \|\xi_2\|)\|\xi_1 - \xi_2\| \int_0^\infty e^{-t/2} dt \\ &\quad + M\|\xi_1 - \xi_2\| \int_0^\infty \int_{t/2}^t (|\xi_1(s)| + |\xi_2(s)|)(e^{-(t-s)} - e^{-t/2}) ds dt \\ &= 2M\|\xi_1 - \xi_2\|(\|\xi_1\| + \|\xi_2\|) \\ &\quad + M\|\xi_1 - \xi_2\| \int_0^\infty (|\xi_1(s)| + |\xi_2(s)|)(1 + e^{-s} - 2e^{-s/2}) ds \\ &\leq 3M(\|\xi_1\| + \|\xi_2\|)\|\xi_1 - \xi_2\|. \end{aligned} \quad (2.3.45)$$

Let $\eta > 0$. Choose $\delta = \eta/16M$ and assume $\|\xi_1\|, \|\xi_2\| \leq \delta$. Combination of (2.3.42), (2.3.43) and (2.3.45) then yields

$$\begin{aligned} & \|\mathcal{H}(\xi_1)(t) - \mathcal{H}(\xi_2)(t)\| \\ &= \sup_{t \geq 0} |\mathcal{H}(\xi_1)(t) - \mathcal{H}(\xi_2)(t)| + \int_0^\infty |\mathcal{H}(\xi_1)(t) - \mathcal{H}(\xi_2)(t)| dt \quad (2.3.46) \\ &\leq 6M\delta\|\xi_1 - \xi_2\| + 4M\delta\|\xi_1 - \xi_2\| + 6M\delta\|\xi_1 - \xi_2\| = \eta\|\xi_1 - \xi_2\|. \end{aligned}$$

□

We now return to the stability question for the zero solution $\xi \equiv 0$ corresponding to $\Phi \equiv 0$. The stability is determined by the behaviour of the solution ξ of the Volterra integral equation (2.3.30). We introduce the (Volterra) resolvent $r(t, \tau)$ of the kernel $k(t, \tau)$ as the solution of

$$r(t, \tau) + \int_\tau^t k(t, s)r(s, \tau)ds = k(t, \tau), \quad 0 \leq \tau \leq t, \quad (2.3.47)$$

supplemented with $r(t, \tau) = 0$ for $0 \leq t < \tau$ (cf. Gripenberg et al. [17, p. 226]). By use of the variation of constants formula [17, Theorem 2.3.5]), equation (2.3.30) is transformed into

$$\xi(t) = \Phi(t) + \mathcal{H}(\xi)(t) - \mathcal{R}(\Phi)(t) - \mathcal{R}(\mathcal{H}(\xi))(t), \quad t \geq 0, \quad (2.3.48)$$

where the resolvent operator \mathcal{R} is defined by

$$\mathcal{R}(\phi)(t) = \int_0^t r(t, \tau)\phi(\tau)d\tau, \quad t \geq 0. \quad (2.3.49)$$

For latter use we need some concepts taken from [17, Section 9.2]. Let $\phi(t, \tau)$ be a continuous function defined for $0 \leq \tau \leq t$. Then ϕ is of type L^1 if and only if

$$\|\|\phi\|\|_{L^1} := \sup_{t \geq 0} \int_\tau^\infty |\phi(t, \tau)| dt < \infty, \quad (2.3.50)$$

whereas ϕ is of type L^∞ if and only if

$$\|\|\phi\|\|_{L^\infty} := \sup_{t \geq 0} \int_0^t |\phi(t, \tau)| d\tau < \infty; \quad (2.3.51)$$

see [17, Proposition 9.2.7]. Furthermore, we introduce the notation $g^*(z)$ for the Laplace transform of a function g defined on \mathbb{R}^+ , i.e.

$$g^*(z) = \int_0^\infty g(t)e^{-zt} dt, \quad (2.3.52)$$

defined for those $z \in \mathbb{C}$ for which the integral exists.

Theorem 2.3.4 *Let b satisfy the Paley-Wiener condition $1 + b^*(z) \neq 0$ for $\operatorname{Re} z \geq 0$. Then the resolvent operator \mathcal{R} maps $BC_0 \cap L^1$ into $BC_0 \cap L^1$, and the mapping is bounded (i.e. continuous).*

Proof: Since k is continuous, it follows from Gripenberg et al. [17, Theorem 9.5.7] that the resolvent r is continuous. The Volterra kernel $k(t, \tau) = b(t - \tau) + c(t)$ is of the form considered in [17, Theorem 9.3.19] with $b \in L^1$, while c is of both type L^1 and L^∞ , and

$$\lim_{T \rightarrow \infty} \int_T^\infty |c(t)| dt = 0, \quad \lim_{T \rightarrow \infty} \sup_{t \geq T} (t - T) |c(t)| = 0. \quad (2.3.53)$$

Furthermore, the resolvent r_c of the kernel c can be explicitly determined, viz.

$$r_c(t, \tau) = c(t) \exp\left(-\int_\tau^t c(s) ds\right), \quad 0 \leq \tau \leq t. \quad (2.3.54)$$

Clearly, r_c is of both type L^1 and L^∞ . Also the additional condition $1 + b^*(z) \neq 0$ for $\operatorname{Re} z \geq 0$ is satisfied. Then it follows from [17, Theorem 9.3.19] that k has a resolvent r of both type L^1 and L^∞ .

Let $\phi \in BC_0 \cap L^1$. By use of (2.3.50) and (2.3.51) we establish the inequalities

$$|\mathcal{R}(\phi)(t)| \leq \int_0^t |r(t, \tau)| |\phi(\tau)| d\tau \leq \| \|r\| \|_{L^\infty} \sup_{t \geq 0} |\phi(t)|, \quad (2.3.55)$$

$$\int_0^\infty |\mathcal{R}(\phi)(t)| dt \leq \int_0^\infty \int_0^t |r(t, \tau)| |\phi(\tau)| d\tau dt \leq \| \|r\| \|_{L^1} \int_0^\infty |\phi(t)| dt, \quad (2.3.56)$$

which are combined into

$$\| \mathcal{R}(\phi) \| \leq \max\{ \| \|r\| \|_{L^\infty}, \| \|r\| \|_{L^1} \} \| \phi \|. \quad (2.3.57)$$

Thus, \mathcal{R} induces a bounded mapping from $BC_0 \cap L^1$ into $BC \cap L^1$, where BC is the space of bounded continuous functions on \mathbb{R}^+ . It remains to verify that $\mathcal{R}(\phi) \in BC_0$. To that end consider the operator \mathcal{K} defined by

$$\mathcal{K}(\phi)(t) = \int_0^t k(t, \tau) \phi(\tau) d\tau, \quad t \geq 0. \quad (2.3.58)$$

Since k is of type L^∞ , and

$$\lim_{t \rightarrow \infty} \int_0^t |k(t, \tau)| d\tau = 0 \quad (2.3.59)$$

for each $T \geq 0$, it can easily be shown that \mathcal{K} maps BC_0 into BC_0 . Next it follows from a result of Pulyaev and Tsalyuk [45, Theorem 2] that also \mathcal{R} maps BC_0 into BC_0 . \square

To obtain the stability of the zero solution $\xi \equiv 0$ of the nonlinear Volterra integral equation (2.3.30) (equivalently of (2.3.48)) with $\Phi \equiv 0$, we require the following result:

Theorem 2.3.5 *Let $\Phi \in BC_0 \cap L^1$, and let b satisfy the Paley-Wiener condition $1 + b^*(z) \neq 0$ for $\operatorname{Re} z \geq 0$. Then for each $\eta > 0$ there exists a $\delta > 0$ such that whenever $\|\Phi\| \leq \delta$, equation (2.3.30) has a unique solution $\xi \in BC_0 \cap L^1$ with $\|\xi\| \leq \eta$.*

Proof: For $\phi \in BC_0 \cap L^1$, define the mapping \mathcal{M} by

$$\mathcal{M}(\phi)(t) = \Phi(t) - \mathcal{R}(\Phi)(t) + \mathcal{H}(\phi)(t) - \mathcal{R}(\mathcal{H}(\phi))(t), \quad t \geq 0. \quad (2.3.60)$$

Then equation (2.3.48) can be rewritten as $\xi(t) = \mathcal{M}(\xi)(t)$ for $t \geq 0$. From Lemma 2.3.1 and Theorem 2.3.4 it follows that the operator \mathcal{M} maps $BC_0 \cap L^1$ into $BC_0 \cap L^1$. Furthermore, the resolvent operator \mathcal{R} is bounded so that

$$\|\mathcal{R}\| := \sup_{\|\phi\|=1} \|\mathcal{R}(\phi)\| < \infty. \quad (2.3.61)$$

By Lemma 2.3.2 the operator \mathcal{H} is of higher order with respect to $BC_0 \cap L^1$. Hence, there exists a $\rho > 0$ such that

$$\|\mathcal{H}(\phi_1) - \mathcal{H}(\phi_2)\| \leq \frac{1}{2(1 + \|\mathcal{R}\|)} \|\phi_1 - \phi_2\|, \quad (2.3.62)$$

whenever $\phi_1, \phi_2 \in BC_0 \cap L^1$ with $\|\phi_1\|, \|\phi_2\| \leq \rho$. Let $\eta > 0$. Define $\rho_0 = \min\{\rho, \eta\}$ and $S = \{\phi \in BC_0 \cap L^1 \mid \|\phi\| \leq \rho_0\}$. Choose $\delta = \rho_0(1 + \|\mathcal{R}\|)^{-1}/2$. Assume $\|\Phi\| \leq \delta$. Given $\phi \in S$, one has

$$\begin{aligned} \|\mathcal{M}(\phi)\| &\leq \|\Phi\| + \|\mathcal{R}\| \|\Phi\| + \|\mathcal{H}(\phi)\| + \|\mathcal{R}\| \|\mathcal{H}(\phi)\| \\ &\leq \delta(1 + \|\mathcal{R}\|) + \frac{1}{2} \|\phi\| \leq \frac{\rho_0}{2} + \frac{\rho_0}{2} = \rho_0. \end{aligned} \quad (2.3.63)$$

Hence, \mathcal{M} maps S into S . Similarly, given $\phi_1, \phi_2 \in S$, one has

$$\|\mathcal{M}(\phi_1) - \mathcal{M}(\phi_2)\| \leq (1 + \|\mathcal{R}\|) \|\mathcal{H}(\phi_1) - \mathcal{H}(\phi_2)\| \leq \frac{1}{2} \|\phi_1 - \phi_2\|. \quad (2.3.64)$$

Thus, the mapping $\mathcal{M} : S \rightarrow S$ is a contraction. By the Banach fixed point theorem (see Kreyszig [25, p. 300]; Miller [38, p. 419]) it follows that \mathcal{M} has a unique fixed point in S . Since $\mathcal{M}(\xi) = \xi$, this fixed point is the unique solution ξ of (2.3.30) in S . \square

The result of Theorem 2.3.5 may be rephrased in terms of stability of the zero solution $\xi \equiv 0$ of (2.3.30) with $\Phi \equiv 0$.

Corollary 2.3.1 *Let b satisfy the Paley-Wiener condition $1 + b^*(z) \neq 0$ for $\operatorname{Re} z \geq 0$. Then the zero solution $\xi \equiv 0$ of (2.3.30) corresponding to $\Phi \equiv 0$ is asymptotically stable on $BC_0 \cap L^1$.*

Consequently, if b satisfies the Paley-Wiener condition $1 + b^*(z) \neq 0$ for $\operatorname{Re} z \geq 0$, then the steady state solution ω of (2.2.10) is asymptotically stable, and the limit (2.2.1) which is needed for achieving steady state flow exists provided the perturbation of the pressure gradient is sufficiently small.

Next, we investigate the stability of the steady state solution ω when the Paley-Wiener condition is not satisfied, i.e. when the equation

$$1 + b^*(z) = 0, \quad \operatorname{Re} z \geq 0, \quad (2.3.65)$$

has at least one root. To that end, we introduce the resolvent r_b of the Volterra kernel b . Since b is of convolution type, it is easily verified that r_b solves the integral equation

$$r_b(t) + \int_0^t b(t-\tau)r_b(\tau)d\tau = b(t), \quad t \geq 0. \quad (2.3.66)$$

From the latter equation the Laplace transform $r_b^*(z)$ of $r_b(t)$ is found as

$$r_b^*(z) = \frac{b^*(z)}{1 + b^*(z)}. \quad (2.3.67)$$

According to the Paley-Wiener theorem (cf. Gripenberg et al. [17, Theorem 2.4.1]) one has $r_b(t) \notin L^1$, if equation (2.3.65) has a root. Suppose now that equation (2.3.65) has precisely one root $z = z_0$, which is simple and satisfies $\operatorname{Re} z_0 > 0$. Then the Laplace transform r_b^* may be rewritten as

$$r_b^*(z) = \frac{\alpha}{z - z_0} + \rho_b^*(z), \quad (2.3.68)$$

where $\alpha = \operatorname{Res}_{z=z_0} r_b^*(z)$ and ρ_b^* is analytic in the half-plane $\operatorname{Re} z > 0$. Taking inverse Laplace transforms in (2.3.68), we find that $r_b(t)$ may be expressed as

$$r_b(t) = \alpha e^{z_0 t} + \rho_b(t). \quad (2.3.69)$$

Here, ρ_b is the so-called residual resolvent and it can be shown that $\rho_b(t) \in L^1$; for a proof see Jordan and Wheeler [20, Theorem 1.1].

We consider the solution ξ_l of equation (2.3.30) with $c \equiv 0$ and $\mathcal{H} \equiv 0$, i.e.

$$\xi_l(t) + \int_0^t b(t-\tau)\xi_l(\tau)d\tau = \Phi(t), \quad t \geq 0. \quad (2.3.70)$$

The latter equation is a linear Volterra integral equation of convolution type for ξ_l .

Lemma 2.3.3 *Let $1 + b^*(z) = 0$, $\operatorname{Re} z \geq 0$, have one root $z = z_0$, which is simple and satisfies $\operatorname{Re} z_0 > 0$. Then the solution ξ_l of (2.3.70) can be written as*

$$\xi_l(t) = -\alpha \Phi^*(z_0) e^{z_0 t} + \mathcal{N}(\Phi)(t), \quad (2.3.71)$$

where

$$\mathcal{N}(\phi)(t) = \phi(t) - \int_0^t \rho_b(t-\tau)\phi(\tau)d\tau + \alpha \int_t^\infty \phi(\tau)e^{-z_0(\tau-t)}d\tau. \quad (2.3.72)$$

Proof: By use of the variation of constants formula, equation (2.3.70) is transformed into

$$\xi(t) = \Phi(t) - \int_0^t r_b(t-\tau)\Phi(\tau)d\tau. \quad (2.3.73)$$

By substituting (2.3.69) into (2.3.73), and rearranging the terms, we obtain (2.3.71). \square

To obtain the instability of the zero solution $\xi_l \equiv 0$ of the linear Volterra integral equation of convolution type (2.3.70) with $\Phi \equiv 0$, we require the following result:

Theorem 2.3.6 *Let $1 + b^*(z) = 0$, $\operatorname{Re} z \geq 0$, have one root $z = z_0$, which is simple and satisfies $\operatorname{Re} z_0 > 0$. Then there exists a $t_0 \geq 0$ and an $\eta > 0$ such that for each $\delta > 0$ there exists a function $\Phi \in BC_0 \cap L^1$ with $\|\Phi\| \leq \delta$, for which the solution ξ_l of (2.3.70) satisfies $|\xi_l(t)| > \eta$ for some $t \geq 0$.*

Proof: We start from the representation (2.3.71) of the solution ξ_l . Choose $t_0 \geq 0$ and $\eta > 0$ arbitrarily. Let $\delta > 0$. Choose $\Phi \in BC_0 \cap L^1$ such that $\|\Phi\| \leq \delta$ and $|\Phi^*(z_0)| > 0$. Assume $\xi_l \in BC_0 \cap L^1$ with $\|\xi_l\| \leq \eta$. Since $\rho_b(t) \in L^1$, one has the estimate

$$|\mathcal{N}(\Phi)(t)| \leq M\|\Phi\| \leq M\delta, \quad (2.3.74)$$

where M is given by

$$M = 1 + \int_0^\infty |\rho_b(t)|dt + \frac{|\alpha|}{\operatorname{Re} z_0}. \quad (2.3.75)$$

From (2.3.71) it then follows that

$$|\xi_l(t)| \geq |\alpha| |\Phi^*(z_0)| e^{t \operatorname{Re} z_0} - M\delta, \quad t \geq 0. \quad (2.3.76)$$

This contradicts the assumption $\|\xi_l\| \leq \eta$. \square

The result of Theorem 2.3.6 may be rephrased in terms of instability of the zero solution $\xi_l \equiv 0$ of (2.3.70) with $\Phi \equiv 0$.

Corollary 2.3.2 *Let $1 + b^*(z) = 0$, $\operatorname{Re} z \geq 0$, have one root $z = z_0$, which is simple and satisfies $\operatorname{Re} z_0 > 0$. Then the zero solution $\xi_l \equiv 0$ of (2.3.70) corresponding to $\Phi \equiv 0$ is unstable on $BC_0 \cap L^1$.*

We conjecture that also the zero solution $\xi \equiv 0$ of (2.3.30) corresponding to $\Phi \equiv 0$ is unstable on $BC_0 \cap L^1$, if the equation $1 + b^*(z) = 0$, $\operatorname{Re} z \geq 0$, has one root $z = z_0$, which is simple and satisfies $\operatorname{Re} z_0 > 0$. We have not been able to prove the conjecture, not even in the linear case of the integral equation (2.3.30) with $\mathcal{H} \equiv 0$. To properly describe the state of affairs we introduce the following modified instability criterion:

Definition 2.3.3 *The steady state solution ω of (2.2.10) is called l -unstable if the zero solution $\xi_l \equiv 0$ of (2.3.70) corresponding to $\Phi \equiv 0$ is unstable on $BC_0 \cap L^1$.*

Thus as a consequence of Corollary 2.3.2 one has: If the equation $1 + b^*(z) = 0$, $\operatorname{Re} z \geq 0$, has one root $z = z_0$, which is simple and satisfies $\operatorname{Re} z_0 > 0$, then the steady state solution ω of (2.2.10) is l -unstable.

We now present a necessary and sufficient condition for stability of the steady state solution ω in terms of the function G_ω , defined by

$$G_\omega(z) = \varepsilon + \frac{1}{\omega z} \left(J(\omega) - J\left(\frac{\omega}{1+z}\right) \right), \quad \operatorname{Re} z > -1, \quad (2.3.77)$$

where the function J is given by (2.2.9).

Theorem 2.3.7

- If $G_\omega(z) \neq 0$ for $\operatorname{Re} z \geq 0$, then the steady state solution ω is asymptotically stable.
- If $G_\omega(z)$, $\operatorname{Re} z \geq 0$, has one zero $z = z_0$, which is simple and satisfies $\operatorname{Re} z_0 > 0$, then the steady state solution ω is l -unstable.

Proof. Since $b'(t) = -a(t)$, the Laplace transform of the function b is equal to $b^*(z) = (-a^*(z) + b(0))/z$. Calculating $b(0) = J(\omega)/\varepsilon\omega$ and the Laplace transform a^* of the function a as

$$a^*(z) = \int_0^\infty a(t)e^{-zt} dt = \frac{1}{\varepsilon} \int_0^\infty h'(\omega t)e^{-(z+1)t} dt = \frac{1}{\varepsilon\omega} J\left(\frac{\omega}{1+z}\right), \quad \operatorname{Re} z > -1, \quad (2.3.78)$$

we obtain

$$1 + b^*(z) = \frac{G_\omega(z)}{\varepsilon}, \quad \operatorname{Re} z > -1. \quad (2.3.79)$$

Next, translation of the conditions of Corollaries 2.3.1 and 2.3.2 in terms of G_ω completes the proof. \square

We investigate the zeros of $G_\omega(z)$ in the half-plane $\operatorname{Re} z \geq 0$, using the argument principle. This principle is formulated as (cf. Nehari [40, Chapter IV, Sec. 7])

Theorem 2.3.8 *Let the function $F(z)$ be analytic inside and on a simple closed contour K in the complex z -plane, and let $F(z) \neq 0$ on K . Then the total number N of zeros of $F(z)$ inside K , counted according to their multiplicities, is given by*

$$N = \frac{1}{2\pi} [\arg F(z)]_C, \quad (2.3.80)$$

where $[\arg F(z)]_C$ denotes the increase in $\arg F(z)$ as z goes once around K in anticlockwise direction.

As an equivalent formulation we have: N equals the number of times that the closed contour $F(K)$ goes around the origin in anticlockwise direction.

To determine the number N of zeros of $G_\omega(z)$ in $\operatorname{Re} z \geq 0$, we apply the argument principle to the function $G_\omega(z)$ and the closed contour K consisting of the semi-circle $C_R: |z| = R$, $R \rightarrow \infty$, $\operatorname{Re} z \geq 0$, and the imaginary axis $z = iy$, $y \in \mathbb{R}$. Since

$$\lim_{R \rightarrow \infty} G_\omega(Re^{i\phi}) = \varepsilon, \quad -\frac{\pi}{2} \leq \phi \leq \frac{\pi}{2}, \quad \lim_{y \rightarrow \pm\infty} G_\omega(iy) = \varepsilon, \quad (2.3.81)$$

the image $G_\omega(K)$ is the closed curve $G_\omega(iy)$, $\infty \geq y \geq -\infty$, with coinciding end points ε . Furthermore, for $z = 0$ one has

$$G_\omega(0) = \varepsilon + J'(\omega) = \mathcal{F}'(\omega), \quad (2.3.82)$$

with $\mathcal{F}'(\omega) > 0$ if $0 \leq \omega < \omega_M$ or $\omega > \omega_m$, while $\mathcal{F}'(\omega) < 0$ if $\omega_M < \omega < \omega_m$; see Figure 2.1. Further points of the contour $G_\omega(iy)$, $\infty \geq y \geq -\infty$, are found through numerical integration of

$$\begin{aligned} \operatorname{Re} G_\omega(iy) &= \varepsilon + \int_0^\infty \frac{1 + y^2 - \omega^2 \tau^2}{(1 + y^2)^2 + 2(1 - y^2)\omega^2 \tau^2 + \omega^4 \tau^4} \tau e^{-\tau} d\tau, \\ \operatorname{Im} G_\omega(iy) &= \frac{1}{y} \left(\int_0^\infty \frac{1 + y^2 + \omega^2 \tau^2}{(1 + y^2)^2 + 2(1 - y^2)\omega^2 \tau^2 + \omega^4 \tau^4} \tau e^{-\tau} d\tau - \frac{J(\omega)}{\omega} \right), \end{aligned} \quad (2.3.83)$$

for various values of y . Since $G_\omega(\bar{z}) = \overline{G_\omega(z)}$, it is sufficient to evaluate $G_\omega(iy)$ for $y > 0$. In Figure 2.3 the numerically computed contours $G_\omega(iy)$, $y \in \mathbb{R}$, are plotted for $\varepsilon = 0.02$, and three typical values of ω , namely, $\omega = 1 \in [0, \omega_M)$, $\omega = 3 \in (\omega_M, \omega_m)$, and $\omega = 6 \in (\omega_m, \infty)$; the values $\omega_M = 1.7063$ and $\omega_m = 5.2439$ for $\varepsilon = 0.02$ are given in Table A.1 of Appendix A. We observe that $G_\omega(iy) \rightarrow \varepsilon$ as $y \rightarrow \pm\infty$, for all three ω -values, in accordance with (2.3.81). Furthermore, we observe that $G_\omega(0) > 0$ for $\omega = 1 < \omega_M$ or $\omega = 6 > \omega_m$, whereas $G_\omega(0) < 0$ for $\omega = 3 \in (\omega_M, \omega_m)$, in correspondence to (2.3.82). From Figure 2.3 it is seen that the origin is outside the contours $G_\omega(iy)$ with $\omega = 1$ or $\omega = 6$, whereas the contour $G_\omega(iy)$ with $\omega = 3$ goes around the origin once in anticlockwise direction. Thus, we find $N = 0$ for $\omega = 1$ or $\omega = 6$ (when $G_\omega(0) > 0$), while $N = 1$ for $\omega = 3$ (when $G_\omega(0) < 0$). Supported by additional computations of $G_\omega(iy)$, $y \in \mathbb{R}$, for other ε - and ω -values, we conclude that the total number N of zeros of $G_\omega(z)$ in $\operatorname{Re} z \geq 0$, is given by

$$N = \begin{cases} 0, & 0 \leq \omega < \omega_M \text{ or } \omega_m < \omega, \\ 1, & \omega_M < \omega < \omega_m. \end{cases} \quad (2.3.84)$$

For $\text{Re } z = 0$, the computations reveal that $G_\omega(iy) \neq 0$ for $y \in \mathbb{R}$, if $\omega \neq \omega_M$ and $\omega \neq \omega_m$, whereas $G_\omega(0) = 0$ if $\omega = \omega_M$ or $\omega = \omega_m$. Notice that for $\omega = 0$, the function $G_0(z) = \varepsilon + 1/(1+z)$ has no zeros in $\text{Re } z \geq 0$. For $\omega_M < \omega < \omega_m$, the single zero of $G_\omega(z)$ in $\text{Re } z > 0$ is real because of $G_\omega(\bar{z}) = \overline{G_\omega(z)}$.

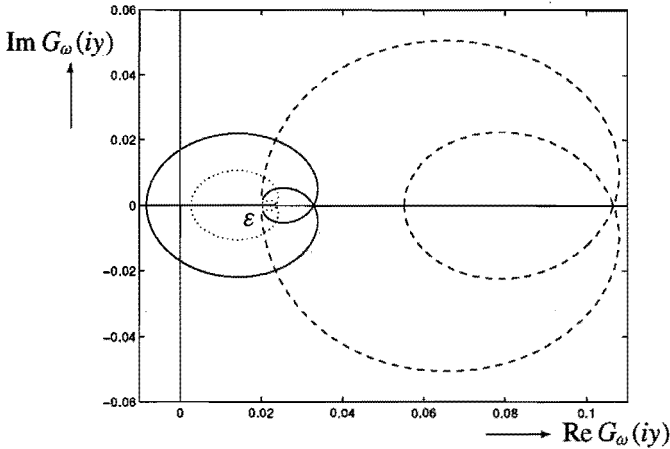


Figure 2.3 The contours $G_\omega(iy)$, $-\infty \leq y \leq \infty$, in the complex plane for $\varepsilon = 0.02$, and $\omega = 1$ (dashed curve), $\omega = 3$ (solid curve), and $\omega = 6$ (dotted curve).

The results for the zeros of $G_\omega(z)$ are now used in Theorem 2.3.7. Thus we arrive at the following Corollary on the stability of the steady state solution ω .

Corollary 2.3.3

- *Steady state solutions ω with $0 \leq \omega < \omega_M$ or $\omega > \omega_m$ are asymptotically stable.*
- *Steady state solutions ω with $\omega_M < \omega < \omega_m$ are l -unstable.*

Again it is conjectured that steady state solutions ω with $\omega_M < \omega < \omega_m$ are unstable (without the prefix l -). The conjecture is supported by the numerical calculations in Section 2.4 which disclose that steady states with $\omega_M < \omega < \omega_m$ are not attained.

2.4 Transient flow behaviour

In this section we present some results of numerical calculations based on the integrodifferential equation (2.3.2). These results will confirm the conclusions of our stability analysis and will provide extra information on such phenomena as spurt, shape memory and hysteresis. We first consider the loading process in which the flow is started up from rest, driven by a constant pressure gradient $f(t) = \bar{f}_0$. After a sufficiently long time, the velocity gradient will attain a steady state value $\omega(r)$, where either $0 \leq \omega < \omega_M$ or $\omega > \omega_m$; steady states with $\omega_M < \omega < \omega_m$ are l -unstable and accordingly such states are not attained. Next, after the steady state has been reached, the pressure gradient is suddenly decreased

to $f(t) = \bar{f}_0 + \Delta \bar{f}$, where $\Delta \bar{f} < 0$. The decrease of the stationary pressure gradient corresponds to an unloading process. We shall demonstrate the influence of the deformation history by exploring the flow during the loading and unloading processes.

At $t = 0$ the velocity gradient equals $w(r, 0) = rf(0+)/2\varepsilon$, as can be found by letting $t \downarrow 0$ in (2.1.37). Integration with respect to r and use of the no-slip boundary condition at the wall yield that the velocity profile is parabolic, namely

$$v(r, 0) = \frac{f(0+)}{4\varepsilon}(1 - r^2), \quad 0 \leq r \leq 1. \quad (2.4.1)$$

For $t > 0$ the velocity gradient $w = \partial\Gamma/\partial t$ is obtained by computing the shear strain $\Gamma(r, t)$ as solution of equation (2.3.2) for a fixed value of r and the pressure gradient $f(t)$ prescribed. We solve this integrodifferential equation by using Euler's forward discretisation method with fixed time step Δt . Under the initial conditions $\Gamma(r, 0) = 0$ and $w(r, 0) = rf(0+)/2\varepsilon$, the flow variables Γ and w at time $t = t_n := n\Delta t$ are computed according to

$$\begin{aligned} \Gamma(r, t_n) &= \Gamma(r, t_{n-1}) + \Delta t w(r, t_{n-1}), \\ w(r, t_n) &= \frac{1}{\varepsilon} \left[\frac{1}{2} r f(t_n) - h(\Gamma(r, t_n)) e^{-t_n} - \int_0^{t_n} h(\Gamma(r, t_n) - \Gamma(r, \tau)) e^{-(t_n - \tau)} d\tau \right]. \end{aligned} \quad (2.4.2)$$

The integral in (2.4.2)² is approximated by the trapezoidal rule. The governing equation (2.3.2) is stiff because of the term $\varepsilon \partial\Gamma/\partial t$ with small ε , and for an accurate numerical solution the time step must be sufficiently small ($\Delta t \ll \varepsilon$). Because of the hereditary effect we have to use all values of $\Gamma(r, \tau)$, $0 \leq \tau \leq t$, to compute $\Gamma(r, t)$. However, for t sufficiently large ($t > T$) the integral can be approximated by the integral over the interval $[t - T, t]$, since

$$\int_0^t h(\gamma) e^{-(t-\tau)} d\tau = \int_{t-T}^t h(\gamma) e^{-(t-\tau)} d\tau + O(e^{-T}), \quad T \rightarrow \infty. \quad (2.4.3)$$

In our calculations we have chosen $T = 20$.

During the loading process, the shear strain Γ and the velocity gradient w are computed for a prescribed pressure gradient of the form

$$f(t) = \bar{f}_0 H(t). \quad (2.4.4)$$

To let the flow be supercritical, we take $\varepsilon = 0.02$ ($< \varepsilon_1$) and $\bar{f}_0 = 0.8 > \bar{f}_{crit} = 2F_M = 0.7546$. In Figure 2.4 the computed velocity gradient $w(r, t)$ as a function of t is plotted for some values of r . We observe that $w(r, t)$ approaches a steady state value, equal to the solution ω numerically computed from $\varepsilon\omega + J(\omega) = r\bar{f}/2$ and represented by the dotted lines in Figure 2.4. As long as $0 \leq r < r_M := 2F_M/\bar{f}_0$ ($= 0.9432$ for $\varepsilon = 0.02$ and $\bar{f}_0 = 0.8$), the steady state value $\omega(r)$ is found to lie between 0 and ω_M . At $r = r_M$, the steady state velocity gradient jumps from a value below ω_M to a value that exceeds $\tilde{\omega}_M$ ($> \omega_m$); see Figure 2.1. Hence, for $r < r_M$ the steady state solution ω satisfies $\omega(r) < \omega_M = 1.7063$, whereas for $r > r_M$ it satisfies $\omega(r) > \tilde{\omega}_M = 9.0094$, which corresponds to top-jumping; see also Figure 2.7a. Due to the jump in the steady state velocity gradient $\omega(r)$ at $r = r_M$, a spurt layer in the steady state velocity profile $\bar{v}(r)$ forms for $r_M < r \leq 1$.

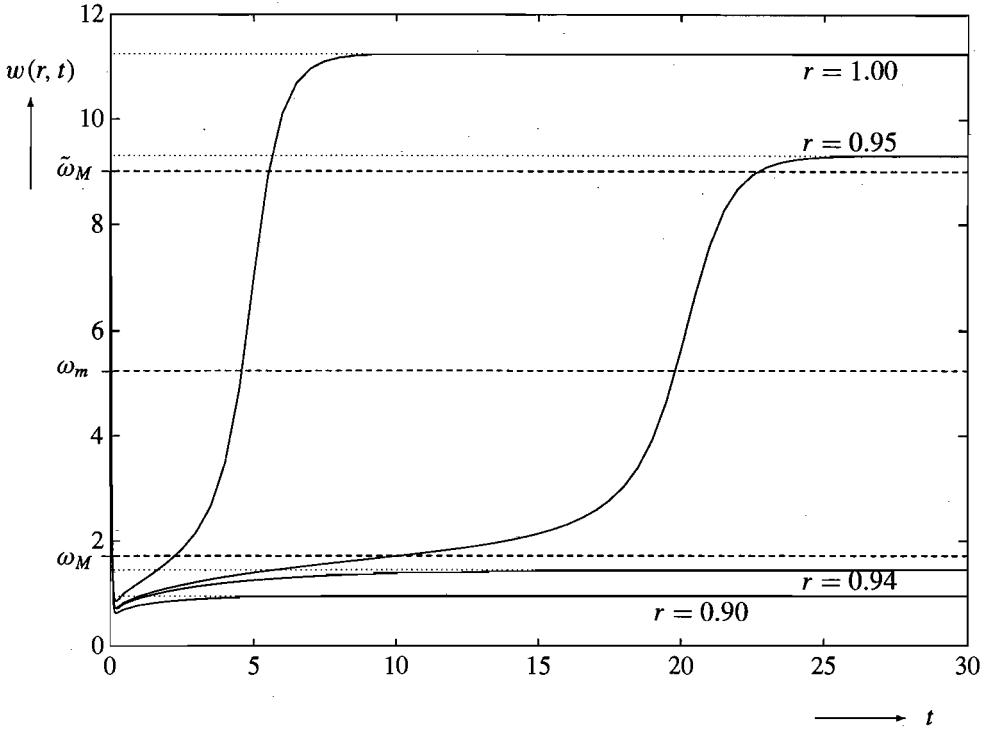


Figure 2.4 The velocity gradient $w(r, t)$ for $\varepsilon = 0.02$ and $f(t) = \bar{f}_0 H(t)$, $\bar{f}_0 = 0.8$, computed by Euler's forward discretisation method with time step $\Delta t = 0.005$. The steady state velocity gradient jumps at $r = r_M = 0.9432$, corresponding to top-jumping.

The process of unloading is numerically implemented by prescribing the pressure gradient as

$$f(t) = \bar{f}_0 H(t) + (\bar{f}_1 - \bar{f}_0) H(t - t_0), \quad \bar{f}_1 < \bar{f}_0, \quad (2.4.5)$$

where t_0 is sufficiently large to achieve a steady state at $t = t_0$ and $\Delta \bar{f} = -(\bar{f}_0 - \bar{f}_1)$. We take $\varepsilon = 0.02$, $\bar{f}_0 = 0.80$ and $t_0 = 27$. We choose $\bar{f}_1 = 0.78 > F_m \bar{f}_0 / F_M = 0.7605$ and plot the numerically computed solution following from this change of load in Figure 2.5. We observe that after the load has changed from $\bar{f}_0 = 0.80$ to $\bar{f}_1 = 0.78$, the jump in the steady state velocity gradient still occurs between $r = 0.94$ and $r = 0.95$, suggesting that the boundary of the spurt layer remains fixed at the position $r = r^* = 2F_M / \bar{f}_0 = 0.9432$. This phenomenon is called shape memory, because the spurt layer remains unchanged, regardless of the change in loading. The set of $\omega(r)$ -values (for $r \in [0, 1]$) can be read off from Figure 2.7b.

Next we choose $\bar{f}_1 = 0.75$, which lies between $2F_m = 0.7173$ and $F_m \bar{f}_0 / F_M = 0.7605$. The solution for this particular unloading step is presented in Figure 2.6. We observe that when the load has changed to $\bar{f}_1 = 0.75$, the jump in the steady state velocity gradient occurs between $r = 0.95$ and $r = 0.96$, suggesting that the boundary of the spurt layer lies at

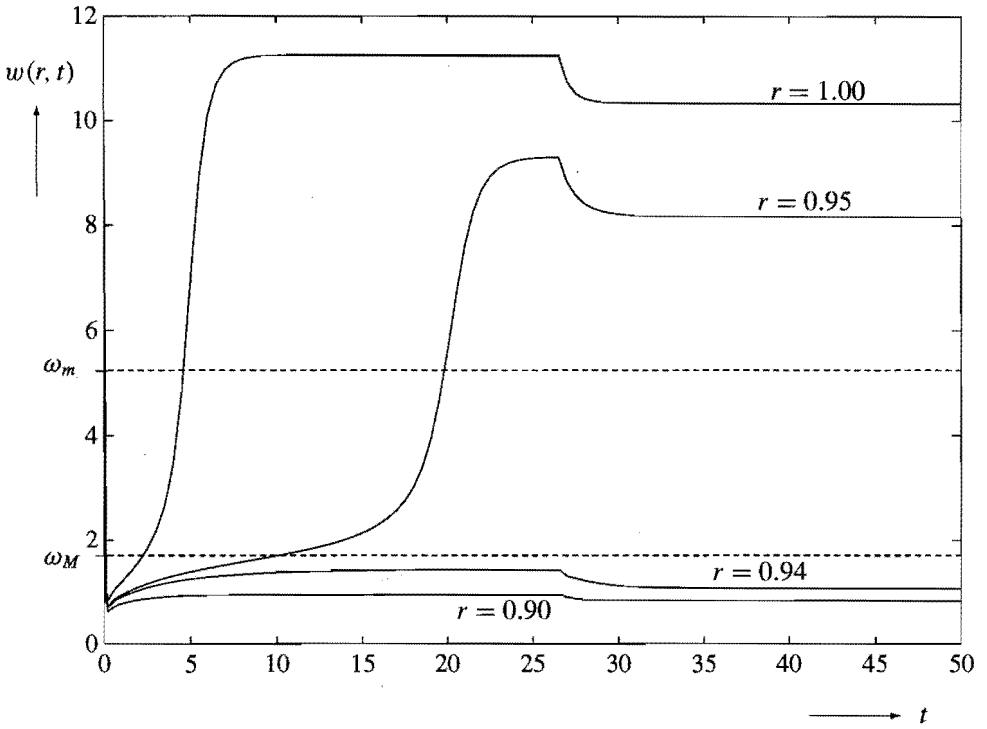


Figure 2.5 The velocity gradient $w(r, t)$ for $\varepsilon = 0.02$ under the changing load $f(t) = \bar{f}_0 H(t) - (\bar{f}_0 - \bar{f}_1) H(t - t_0)$, $\bar{f}_0 = 0.80$ and $\bar{f}_1 = 0.78$, at $t_0 = 27$, computed by Euler's forward discretisation method with time step $\Delta t = 0.005$. The steady state velocity gradient after change of load jumps at $r = r^* = 0.9432$.

$r = r_m := 2F_m/\bar{f}_1 = 0.9564$, which corresponds to bottom-jumping. Hence, the spurt layer boundary is closer to the wall than its position for $\bar{f}_0 = 0.80$, indicating that the spurt layer boundary has moved back to the wall. This corresponds to the loss of shape memory. As shown in Figure 2.7c, the velocity gradient now jumps from the value $\tilde{\omega}_m < \omega_M$ to ω_m .

If we choose $\bar{f}_1 < 2F_m = 0.7173$, then numerical computations show that the jump in the steady state velocity gradient has disappeared after the unloading step: for each radial coordinate $r \in [0, 1]$ the steady state velocity gradient satisfies $\omega(r) < \tilde{\omega}_m = 0.9242$.

We conclude that the numerical calculations confirm that in supercritical flow the steady state velocity gradient profile has one jump. If the loading is supercritical top-jumping occurs. Which particular steady state is achieved during the unloading process, depends on the deformation history. If the unloading $\Delta\bar{f}$ is smaller than a critical value, shape memory occurs. This shape memory causes hysteresis in a loading-unloading cycle, as will be shown in Section 2.5.

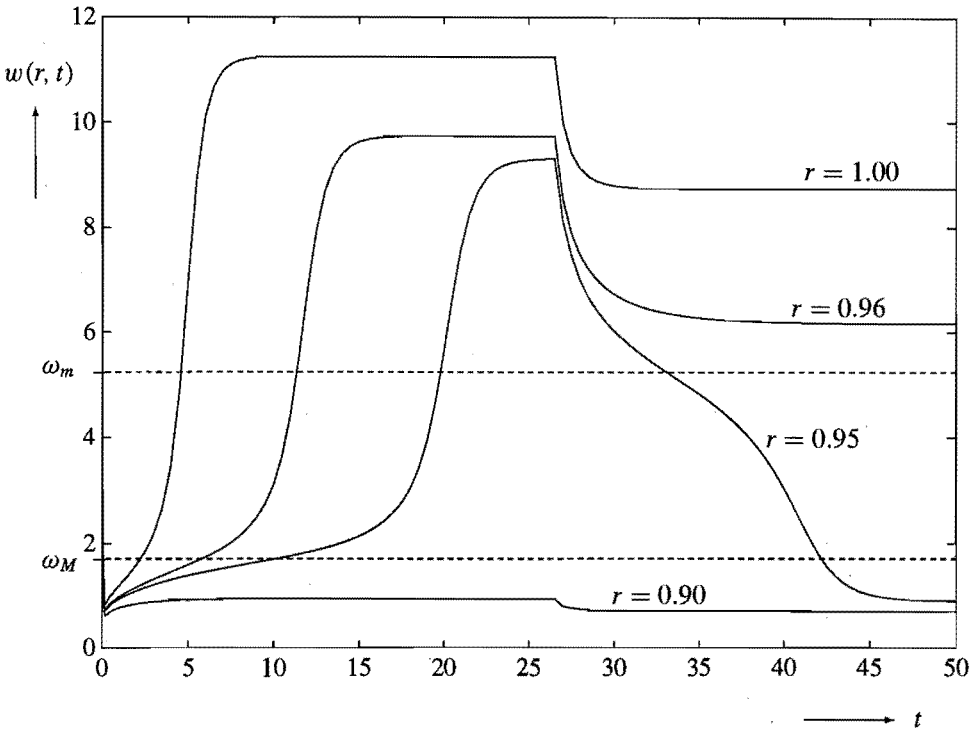
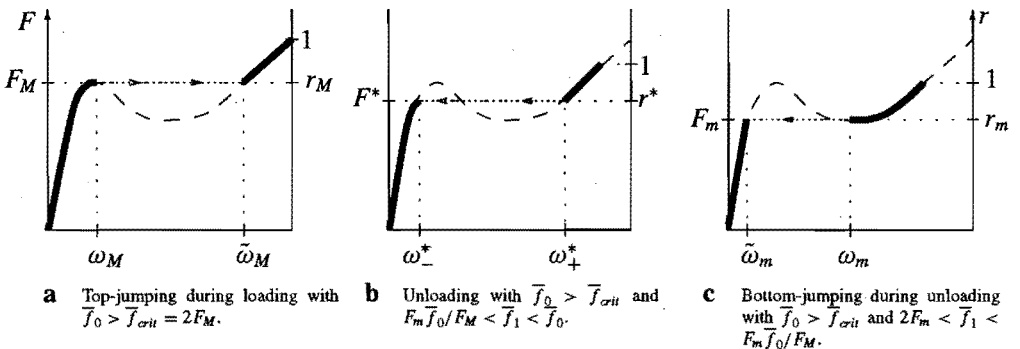


Figure 2.6 The velocity gradient $w(r, t)$ for $\varepsilon = 0.02$ under the changing load $f(t) = \bar{f}_0 H(t) - (\bar{f}_0 - \bar{f}_1) H(t - t_0)$, $\bar{f}_0 = 0.80$ and $\bar{f}_1 = 0.75$, at $t_0 = 27$, computed by Euler's forward discretisation method with time step $\Delta t = 0.005$. The steady state velocity gradient after change of load jumps at $r = r_m = 0.9564$, corresponding to bottom-jumping.



a Top-jumping during loading with $\bar{f}_0 > \bar{f}_{crit} = 2F_M$. **b** Unloading with $\bar{f}_0 > \bar{f}_{crit}$ and $F_m \bar{f}_0 / F_M < \bar{f}_1 < \bar{f}_0$. **c** Bottom-jumping during unloading with $\bar{f}_0 > \bar{f}_{crit}$ and $2F_m < \bar{f}_1 < F_m \bar{f}_0 / F_M$.

Figure 2.7 The set of ω -values for different values of the stationary pressure gradient \bar{f} .

Next, we reconsider the transient flow behaviour in some more detail for the loading process with $\varepsilon = 0.02$, $f(t) = \bar{f}H(t)$ and $\bar{f} = 0.80$; see Figure 2.4. In the development of the velocity gradient $w(r, t)$ for this loading process we distinguish, dependent on the radial coordinate r , two or three distinct time phases. These phases are characterized as follows:

- A Newtonian phase in which $w(r, t)$ decreases on an $O(\varepsilon)$ -time scale from its initial value $w(r, 0) = r\bar{f}/2\varepsilon$ to a value $w(r, t) = O(\varepsilon^0)$, $\varepsilon \rightarrow 0$.
- A latency phase in which $w(r, t) = O(\varepsilon^0)$, $\varepsilon \rightarrow 0$. If $r < r_M$, the latency phase is the final phase during which $w(r, t)$ tends to a steady state $\omega(r) < \omega_M$.
- If $r > r_M$, the latency phase is followed by a spurt phase during which $w(r, t)$ suddenly increases to a value larger than $\tilde{\omega}_M$, and then tends to a steady state $\omega(r) > \tilde{\omega}_M$.

We shall analyze these phases in terms of the dimensionless stresses S and N , defined by

$$S(r, t) = h(\Gamma(r, t))e^{-t} + \int_0^t h(\gamma(r, t, \tau))e^{-(t-\tau)} d\tau, \quad (2.4.6)$$

$$N(r, t) = g(\Gamma(r, t))e^{-t} + \int_0^t g(\gamma(r, t, \tau))e^{-(t-\tau)} d\tau, \quad (2.4.7)$$

where the function g is given by $g(\gamma) = \gamma h(\gamma)$. With the use of (2.1.21), we find that S and N equal

$$S = -\frac{1}{\mu\sqrt{c}}(T_{rz} - \eta_s \frac{\partial v}{\partial r}), \quad N = \frac{1}{\mu c}(T_{zz} - T_{rr}). \quad (2.4.8)$$

Hence, $-S$ corresponds to the (dimensionless) shear stress component S_{rz} of S_p , and N corresponds to the first normal stress difference. From (2.1.35) with $f(t) = \bar{f}$, $t \geq 0$, it follows that

$$\varepsilon w(r, t) + S(r, t) = F(r) = \frac{1}{2}r\bar{f}, \quad 0 \leq r \leq 1, \quad t \geq 0. \quad (2.4.9)$$

In the proof of Theorem 2.2.1 it has been derived that for $t \rightarrow \infty$ the function S tends to the stationary value $\bar{S}(r) = J(\omega(r))$, where the function J is defined by (2.2.9) and ω is a solution of (2.2.10). Analogously, it can be shown that the normal stress difference N tends to the stationary value $\bar{N}(r) = 1 - L(\omega(r))$, where the function L is defined by the integral

$$L(\omega) = \int_0^\infty \frac{e^{-\tau}}{1 + \omega^2 \tau^2} d\tau = 1 - \int_0^\infty g(\omega\tau)e^{-\tau} d\tau. \quad (2.4.10)$$

By letting $t \rightarrow \infty$ in (2.4.9) we find $\omega = (F - \bar{S})/\varepsilon$, from which we infer

$$\bar{N} = N_0(\bar{S}) := 1 - L\left(\frac{F - \bar{S}}{\varepsilon}\right). \quad (2.4.11)$$

On the other hand, $\omega = L^{\text{inv}}(1 - \bar{N})$, so that

$$\bar{S} = S_0(\bar{N}) := J(L^{\text{inv}}(1 - \bar{N})), \quad (2.4.12)$$

where L^{inv} is the inverse of the function L . Notice that L^{inv} exists, since L is a strictly decreasing function. Hence, in an (S, N) -plane the stationary values \bar{S} and \bar{N} correspond to the intersection points of the two curves $S = S_0(N)$ and $N = N_0(S)$.

In the Figures 2.8 and 2.9 the solid curves are plots of points $(S(r, t), N(r, t))$, with parameter t and fixed $r = 0.9$ and $r = 1.0$, respectively, for the loading process of Figure 2.4, i.e. for $\varepsilon = 0.02$, $f(t) = \bar{f}H(t)$ and $\bar{f} = 0.80 > \bar{f}_{crit}$. For $r = 0.9$ one has $F = r\bar{f}/2 = 0.36$ with $F_m < F < F_M$, while for $r = 1.0$ one has $F = r\bar{f}/2 = 0.4 > F_M$. Also shown in Figures 2.8 and 2.9 are the two curves $S = S_0(N)$ and $N = N_0(S)$, plotted as dashed-dotted and dotted curves, respectively. In Figure 2.8, where $F_m < F < F_M$, we observe that the curves $S = S_0(N)$ and $N = N_0(S)$ have three distinct intersection points, denoted by a dot (\circ), and corresponding to the three distinct steady state solutions. In Figure 2.9, where $F > F_M$, we observe that there is just one intersection point, denoted by a dot (\circ), and corresponding to the single steady state solution. Notice that the function $S = S_0(N)$ is independent of F , whereas $N = N_0(S)$ depends on F .

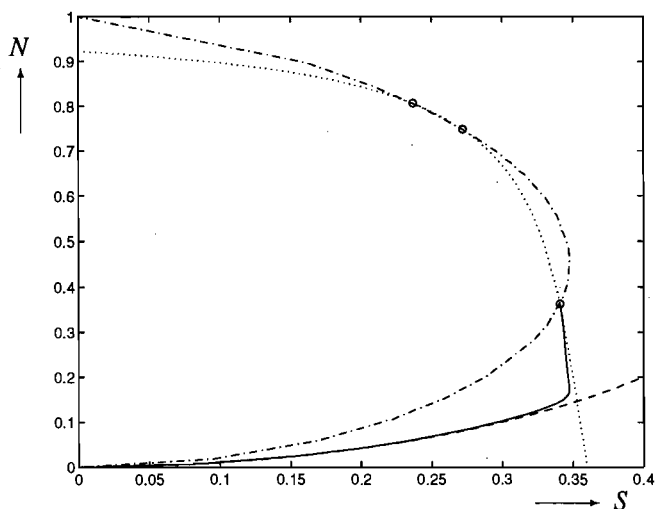


Figure 2.8 (S, N) -plot (solid curve) of points $(S(r, t), N(r, t))$ with parameter t and fixed $r = 0.9$, for $\varepsilon = 0.02$ and $\bar{f} = 0.8$. Dashed-dotted curve $S = S_0(N)$ of (2.4.12), dotted curve $N = N_0(S)$ of (2.4.11), and dashed curve $N = N_{New}(S)$ of (2.4.15). The dots (\circ) correspond to the three distinct steady state solutions.

Next, we derive some analytical approximations for S and N during the three distinct time phases, valid when $\varepsilon \ll 1$. At $t = 0$ the stresses S and N start at $S(r, 0) = N(r, 0) = 0$, because of $\Gamma(r, 0) = 0$. Then, by (2.4.9), the velocity gradient starts at $w(r, 0) = F(r)/\varepsilon$. During the Newtonian phase $0 \leq t < t_N$, say, $w(r, t)$ decreases on an $O(\varepsilon)$ -time scale to the value $w(r, t_N) = O(\varepsilon^0)$. Assuming that $t_N = O(\varepsilon)$ and setting $t = \varepsilon\tilde{t}$, we start from the formal expansions

$$\Gamma(r, t) = \Gamma_0(r, \tilde{t}) + \varepsilon\Gamma_1(r, \tilde{t}) + \dots, \quad w(r, t) = \frac{w_0(r, \tilde{t})}{\varepsilon} + w_1(r, \tilde{t}) + \dots, \quad (2.4.13)$$

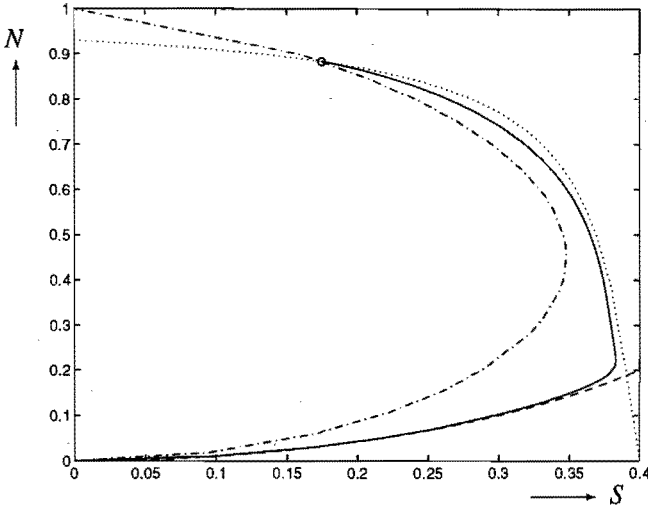


Figure 2.9 (S, N) -plot (solid curve) of points $(S(r, t), N(r, t))$ with parameter t and fixed $r = 1.0$, for $\varepsilon = 0.02$ and $\bar{f} = 0.8$. Dashed-dotted curve $S = S_0(N)$ of (2.4.12), dotted curve $N = N_0(S)$ of (2.4.11), and dashed curve $N = N_{New}(S)$ of (2.4.15). The dot (\circ) corresponds to the single steady state solution.

in which $w_i = \partial \Gamma_i / \partial \tilde{t}$. These expansions are supposed to be valid during the Newtonian phase, that is, till $t = O(\varepsilon)$ or $\tilde{t} = O(1)$. The initial values are $\Gamma_i(r, 0) = 0$, $i = 0, 1, 2, \dots$, $w_0(r, 0) = F(r)$ and $w_i(r, 0) = 0$, $i = 1, 2, \dots$. Substitution of (2.4.13) into (2.4.6) and (2.4.7) yields for the stresses during the Newtonian phase:

$$S = h(\Gamma_0) + O(\varepsilon), \quad N = g(\Gamma_0) + O(\varepsilon). \quad (2.4.14)$$

Neglecting the $O(\varepsilon)$ -term, we may eliminate Γ_0 to obtain the relationship

$$N = N_{New}(S) := \frac{1}{2}(1 - \sqrt{1 - 4S^2}), \quad 0 \leq t \leq t_N. \quad (2.4.15)$$

The function $N = N_{New}(S)$ is plotted as the dashed curve in the Figures 2.8 and 2.9. We observe that this curve approximates the calculated (S, N) -plot very well during the Newtonian phase. Substitution of the leading terms of the expansions for w and S into (2.4.9) results in the equation

$$w_0(r, \tilde{t}) \equiv \frac{\partial \Gamma_0(r, \tilde{t})}{\partial \tilde{t}} = F(r) - h(\Gamma_0(r, \tilde{t})). \quad (2.4.16)$$

The solution of (2.4.16) can implicitly be represented by \tilde{t} as a function of Γ_0 , viz.

$$\begin{aligned} \tilde{t} = & \frac{\Gamma_0}{F} + \frac{1}{2F^2} \ln \left(1 + \Gamma_0^2 - \frac{\Gamma_0}{F} \right) + \frac{1}{2F^2 \sqrt{1 - 4F^2}} \ln \left(\frac{1 - \sqrt{1 - 4F^2}}{1 + \sqrt{1 - 4F^2}} \right) \\ & - \frac{1}{2F^2 \sqrt{1 - 4F^2}} \ln \left(\frac{1 - 2F\Gamma_0 - \sqrt{1 - 4F^2}}{1 - 2F\Gamma_0 + \sqrt{1 - 4F^2}} \right), \end{aligned} \quad (2.4.17)$$

valid for $0 \leq \Gamma_0 < (1 - \sqrt{1 - 4F^2})/2F$, provided that $0 < F < 1/2$.

The Newtonian phase ends at $t = t_N$, determined by $w(r, t_N) = O(\varepsilon^0)$. Consequently, $S(r, t_N) = F(r) + O(\varepsilon)$ by (2.4.9). Since also $S(r, t_N) = h(\Gamma(r, t_N)) + O(\varepsilon)$, it follows that

$$\Gamma(r, t_N) = \Gamma_N(r) := \frac{1 - \sqrt{1 - 4F^2(r)}}{2F(r)}, \quad (2.4.18)$$

under neglect of the $O(\varepsilon)$ -terms. By setting $t = t_N = \varepsilon \tilde{t}_N$ in the expansion (2.4.13)² we find that $w_0(r, \tilde{t}_N) = \varepsilon p$ must hold for a certain $p = p(r)$. By use of (2.4.16) we are led to the equation

$$w_0(r, \tilde{t}_N) = F(r) - h(\Gamma_0(r, \tilde{t}_N)) = \varepsilon p, \quad (2.4.19)$$

which has the solution

$$\begin{aligned} \Gamma_0(r, \tilde{t}_N) &= \frac{1 - \sqrt{1 - 4(F(r) - \varepsilon p)^2}}{2(F(r) - \varepsilon p)} \\ &= \Gamma_N(r) \left(1 - \frac{\varepsilon p}{F(r)\sqrt{1 - 4F^2(r)}} + O(\varepsilon^2) \right). \end{aligned} \quad (2.4.20)$$

On inserting the latter value of Γ_0 into (2.4.17) we obtain, under neglect of the $O(\varepsilon)$ -terms,

$$\begin{aligned} \tilde{t}_N &= -\frac{1 - \sqrt{1 - 4F^2}}{2F^2\sqrt{1 - 4F^2}} \ln(\varepsilon p) + \frac{1 - \sqrt{1 - 4F^2}}{2F^2} + \frac{1}{2F^2} \ln \left(\frac{1 - \sqrt{1 - 4F^2}}{2F^3} \right) \\ &\quad - \frac{1}{2F^2\sqrt{1 - 4F^2}} \ln \left(\frac{2F}{(1 - 4F^2)(1 - \sqrt{1 - 4F^2})} \right). \end{aligned} \quad (2.4.21)$$

Thus, $\tilde{t}_N = O(\ln \varepsilon)$, implying that $t_N = O(\varepsilon \ln \varepsilon)$ rather than $t_N = O(\varepsilon)$.

In the Figures 2.8 and 2.9 the end $t = t_N$ of the Newtonian phase corresponds to the point where the (S, N) -plot starts to deviate from the curve $N = N_{New}(S)$. The Newtonian phase is followed by a latency phase in which $w(r, t) = O(\varepsilon^0)$ and consequently $S(r, t) = F(r) + O(\varepsilon)$, $\varepsilon \rightarrow 0$. In the Figures 2.8 and 2.9 we observe that after $t = t_N$ the (S, N) -plots run upwards with $S \approx F = 0.36$ and $S \approx F = 0.40$, respectively. Hence, S is almost constant, and the latency phase is referred to as a pseudo steady state; the first normal stress difference N still increases. For $F < F_M$ or $r < r_M$, as in Figure 2.8, we observe that during the latency phase the stationary value $\bar{S}(r) = F(r) + O(\varepsilon)$, $\varepsilon \rightarrow 0$, is reached. For $F > F_M$ or $r > r_M$, as in Figure 2.9, the latency phase is followed by a spurt phase during which S decreases and tends to the stationary value \bar{S} . For small ε we use the asymptotic expansions of the functions J and L (see Appendix A), to express the stationary values in the spurt phase by

$$\begin{aligned} \omega &= \frac{F}{\varepsilon} - \frac{1}{F} \ln \frac{F}{\varepsilon} + \frac{C}{F} + O(\varepsilon \ln^2 \varepsilon), \quad \varepsilon \rightarrow 0, \\ \bar{S} &= \frac{\varepsilon}{F} \ln \frac{F}{\varepsilon} - \frac{\varepsilon C}{F} + O(\varepsilon^2 \ln^2 \varepsilon), \quad \bar{N} = 1 - \frac{\varepsilon \pi}{2F} + O(\varepsilon^2 \ln \varepsilon), \quad \varepsilon \rightarrow 0, \end{aligned} \quad (2.4.22)$$

where $C = 0.57721\dots$ is Euler's constant. Finally, we observe in both Figures 2.8 and 2.9 that the (S, N) -plot starts in the origin and lies inside the region bounded by the three curves $N = N_{New}(S)$, $N = N_0(S)$ and $S = S_0(N)$.

2.5 Spurt, shape memory and hysteresis

Consider experiments in which the flow is in a steady state, reached at time $t = t_0$, corresponding to a pressure gradient $f(t) = \bar{f}_0 H(t)$, and the pressure gradient is suddenly changed to $\bar{f} = \bar{f}_0 + \Delta \bar{f}$. If $\Delta \bar{f} > 0$, we call this process loading, otherwise unloading. As the numerical calculations reveal, the outcome of the experiments depends on the initial loading \bar{f}_0 and the change of loading $\Delta \bar{f}$. On the basis of our numerical results, we shall discuss the quasi-static loading-unloading cycle, whereby the load is gradually increased from $\bar{f} = 0$ up to $\bar{f}_{max} > \bar{f}_{crit}$, followed by an unloading sequence until the initial load $\bar{f} = 0$ is reached again.

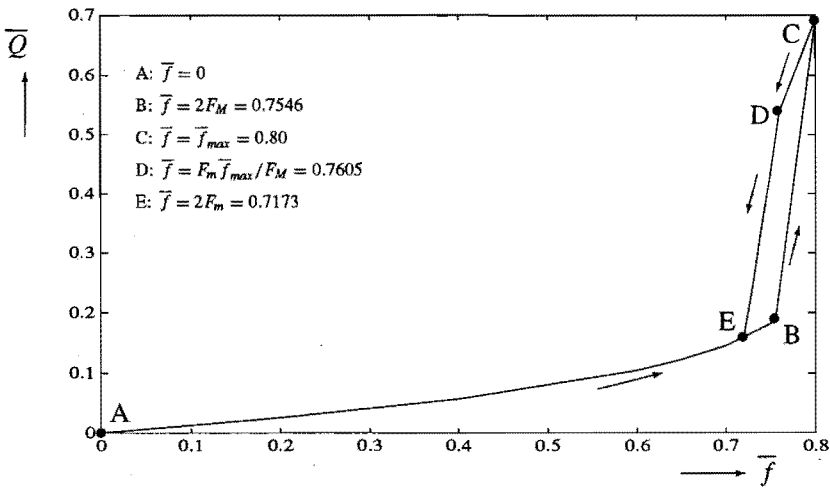


Figure 2.10 Hysteresis under cyclic load. The steady state volumetric flow rate \bar{Q} versus the loading \bar{f} , for $\varepsilon = 0.02$ and $\bar{f}_{max} = 0.80$.

During the first part of the loading, where $\bar{f} < \bar{f}_{crit} = 2F_M$ (subcritical flow), the entire flow is classical: The steady state velocity gradient satisfies $\omega(r) < \omega_M$ and is continuous in r for all $r \in [0, 1]$. In Figure 2.10 the steady state volumetric flow rate \bar{Q} (defined by (2.2.14)) is depicted as a function of \bar{f} . The curve AB corresponds to classical flow, where the point A corresponds to $\bar{f} = 0$ and the point B to $\bar{f} = \bar{f}_{crit}$. When the flow becomes supercritical ($\bar{f} \geq \bar{f}_{crit}$), a kink in the velocity profile forms at the wall, moving away from the wall to a position $r = r_M = 2F_M / \bar{f}$. The large values of the velocity gradient near the wall cause a substantial increase of the volumetric flow rate (curve BC in Figure 2.10). For $\bar{f} = \bar{f}_{max}$, corresponding to point C in Figure 2.10, the spurt layer $r^* \leq r \leq 1$, where $r^* = 2F_M / \bar{f}_{max}$, is of maximum thickness. From this point we start to unload and as a result \bar{Q} decreases. At first the spurt layer remains fixed between $r = r^* = 2F_M / \bar{f}_{max}$ and $r = 1$; this phenomenon called shape memory corresponds to the path from C to D in Figure 2.10. During this unloading the magnitude of the shear stress $T_{rz} = -F$ at r^* decreases according to $F^* = F(r^*) = r^* \bar{f} / 2 = F_M \bar{f} / \bar{f}_{max}$. If F^* falls below F_m , i.e. if $\bar{f} < F_m \bar{f}_{max} / F_M$, the boundary $r = r_m = 2F_m / \bar{f}$ of the spurt layer moves back towards the wall for further decreasing \bar{f} . This loss of shape

memory occurs on the path from D to E in Figure 2.10, where the point D corresponds to $\bar{f} = F_m \bar{f}_{max} / F_M$. The spurt layer disappears for $\bar{f} = 2F_m$, i.e. for $r_m = 1$, which corresponds to point E in Figure 2.10. After that (for $\bar{f} < 2F_m$), the flow becomes entirely classical again. In the final unloading path EA, the flow is classical and this path coincides with the initial part of the loading curve. The phenomenon that no part of the loading curve in Figure 2.10 is retraced until the flow has become entirely classical again, is typical for hysteresis.

2.6 The influence of a relaxation spectrum

In general, the characteristic response of molten polymers and polymer solutions to a deformation is described by a constitutive equation that involves a continuous spectrum of relaxation rates. This spectrum can be approximated by choosing a set of $n \geq 1$ discrete relaxation rates λ_i , whereupon the corresponding shear moduli μ_i are adjusted such that a satisfactory fit to experimental data is obtained. In this manner, the stress relaxation function G is represented by a sum of exponential terms $\mu_i \exp(-\lambda_i t)$ as in (2.1.9). The constitutive KBKZ-model employed thus far, describes the characteristic response of a concentrated polymer solution; the response of the polymer is characterized by one main relaxation rate λ , whereas the response of the small-molecule solvent with viscosity η_s is described by the Newtonian viscous term. For molten polymers, however, the Newtonian viscous term is obsolete ($\eta_s = 0$), because there is no solvent. Instead the response of molten polymers is characterized by at least two relaxation rates. In this section we will show that the KBKZ-model with two widely spaced relaxation rates λ_1 and λ_2 can be reduced to the KBKZ-model with only the dominant relaxation rate λ_1 retained and supplied with a Newtonian viscous term involving a fictitious solvent viscosity $\eta_s = \mu_2 / \lambda_2$.

We start from the stress relaxation function

$$G(t) = \mu_1 e^{-\lambda_1 t} + \mu_2 e^{-\lambda_2 t}, \quad (2.6.1)$$

with two widely spaced relaxation rates $\lambda_1 \ll \lambda_2$, and corresponding shear moduli μ_1 and μ_2 . The corresponding expression for $m(t) = -G'(t)$ and Papanastasiou's kernel K from (2.1.10) are inserted into (2.1.7). As a result we find that the polymer contribution S_p to the extra stress tensor S is given by

$$S_p = \int_{-\infty}^t \frac{c}{c - 3 + I_{c-1}} [\mu_1 \lambda_1 e^{-\lambda_1(t-\tau)} + \mu_2 \lambda_2 e^{-\lambda_2(t-\tau)}] C^{-1} d\tau, \quad (2.6.2)$$

similar to (2.1.11). We omit the Newtonian viscous term by putting $\eta_s = 0$ in (2.1.3), so that the extra stress tensor S reads

$$S = \mathcal{T} + pI = S_p. \quad (2.6.3)$$

The stress tensor \mathcal{T} thus determined, is substituted into the balance of linear momentum (2.1.2) without body forces ($\rho \mathbf{b} = \mathbf{0}$) and with the inertia forces neglected ($\rho(\partial \mathbf{v} / \partial t + (\mathbf{v} \cdot \nabla) \mathbf{v}) = \mathbf{0}$). The balance is satisfied if $T_{rz} = -rf(t)/2$ (cf. (2.1.34)), where f is the pressure

gradient $-\partial p/\partial z$ driving the flow (see (2.1.23)). Combined with the representation (2.1.21)³ for T_{rz} , properly modified, we obtain the governing equation (similar to (2.1.27))

$$\begin{aligned} & \frac{c\gamma(r, t, 0)}{c + \gamma^2(r, t, 0)} [\mu_1 e^{-\lambda_1 t} + \mu_2 e^{-\lambda_2 t}] + \mu_1 \lambda_1 \int_0^t \frac{c\gamma(r, t, \tau)}{c + \gamma^2(r, t, \tau)} e^{-\lambda_1(t-\tau)} d\tau \\ & + \mu_2 \lambda_2 \int_0^t \frac{c\gamma(r, t, \tau)}{c + \gamma^2(r, t, \tau)} e^{-\lambda_2(t-\tau)} d\tau = \frac{1}{2} r f(t), \quad 0 \leq r \leq R, \quad t > 0, \end{aligned} \quad (2.6.4)$$

in which the shear strain γ is defined by (2.1.19).

By scaling time by the dominant relaxation time λ_1^{-1} , length by the radius R , and by introducing the dimensionless variables $\hat{v} := v/\lambda_1 R\sqrt{c}$, $\hat{\gamma} := \gamma/\sqrt{c}$ and $\hat{f} := Rf/\mu_1\sqrt{c}$, we transform equation (2.6.4) into its dimensionless form (since no confusion will arise we omit the caret)

$$\begin{aligned} & h(\Gamma(r, t))e^{-t} + \int_0^t h(\gamma(r, t, \tau))e^{-(t-\tau)} d\tau + mh(\Gamma(r, t))e^{-\beta t} \\ & + m\beta \int_0^t h(\gamma(r, t, \tau))e^{-\beta(t-\tau)} d\tau = \frac{1}{2} r f(t), \quad 0 \leq r \leq 1, \quad t > 0, \end{aligned} \quad (2.6.5)$$

where the dimensionless parameters m and β are given by

$$m = \frac{\mu_2}{\mu_1}, \quad \beta = \frac{\lambda_2}{\lambda_1}. \quad (2.6.6)$$

In (2.6.5) the function h is defined by (2.1.30), while $\Gamma(r, t) = \gamma(r, t, 0)$ by (2.1.31). The relation (2.1.19) between γ and $\partial v/\partial r$ remains the same after scaling, and also holds for the dimensionless variables $\hat{\gamma}$ and $\partial \hat{v}/\partial \hat{r}$. By multiplying (2.6.5) by β/m we obtain

$$\begin{aligned} & \varepsilon^{-1} h(\Gamma(r, t))e^{-t} + \varepsilon^{-1} \int_0^t h(\gamma(r, t, \tau))e^{-(t-\tau)} d\tau + \beta h(\Gamma(r, t))e^{-\beta t} \\ & + \beta^2 \int_0^t h(\gamma(r, t, \tau))e^{-\beta(t-\tau)} d\tau = \frac{1}{2} \varepsilon^{-1} r f(t), \quad 0 \leq r \leq 1, \quad t > 0, \end{aligned} \quad (2.6.7)$$

in which $\varepsilon = m/\beta$.

The secondary relaxation time λ_2^{-1} is supposed to be much shorter than the dominant relaxation time λ_1^{-1} , so that $\beta \gg 1$. We shall now prove that the third and fourth terms in the left-hand side of (2.6.7) tend to $w(r, t) = -\partial v(r, t)/\partial r$ as $\beta \rightarrow \infty$.

Theorem 2.6.1 *Let the derivatives $w \equiv \partial \Gamma/\partial t$ and $\partial w/\partial t$ be bounded as functions of time t . Then for all $t > 0$,*

$$\lim_{\beta \rightarrow \infty} \left\{ \beta h(\Gamma(r, t))e^{-\beta t} + \beta^2 \int_0^t h(\Gamma(r, t) - \Gamma(r, \tau))e^{-\beta(t-\tau)} d\tau \right\} = w(r, t). \quad (2.6.8)$$

Proof: As the dependence on r is irrelevant for the proof, we suppress this variable and represent all functions as depending only on t . Thus, we need to prove that for all $t > 0$,

$$\lim_{\beta \rightarrow \infty} \left\{ \beta h(\Gamma(t))e^{-\beta t} + \beta^2 \int_0^t h(\Gamma(t) - \Gamma(t-s))e^{-\beta s} ds - w(t) \right\} = 0. \quad (2.6.9)$$

We start with some preliminaries. Let $\delta > 0$. Given the boundedness of $\partial w/\partial t$, there exists an $s_0 > 0$ such that

$$|\Gamma(t) - \Gamma(t-s) - sw(t)| \leq \delta s, \quad 0 \leq s < s_0, \quad t > 0. \quad (2.6.10)$$

For the function h defined by (2.1.30) we have the inequalities

$$|h(x)| \leq \frac{1}{2}, \quad |h(x+y) - h(y)| \leq |x|, \quad x, y \in \mathbb{R}, \quad (2.6.11)$$

while there exists an $x_0 > 0$ such that

$$|h(x) - x| \leq \delta|x|, \quad 0 \leq |x| < x_0. \quad (2.6.12)$$

For given $t_0 > 0$ there exists a $\beta_0 > 0$ such that

$$(1 + \beta t_0)e^{-\beta t_0} < \delta, \quad \beta e^{-\beta t_0} < \delta, \quad \beta > \beta_0. \quad (2.6.13)$$

Let $t > 0$ be fixed, and let $M := \sup_{t \geq 0} |w(t)|$. Choose t_0 such that $0 < t_0 < t$ and $t_0 < \min\{s_0, x_0/M\}$. Then by use of (2.6.11) and (2.6.13) we have the estimate

$$\begin{aligned} & |\beta h(\Gamma(t))e^{-\beta t} + \beta^2 \int_{t_0}^t h(\Gamma(t) - \Gamma(t-s))e^{-\beta s} ds| \\ & \leq \frac{1}{2}\beta(e^{-\beta t} + \beta \int_{t_0}^t e^{-\beta s} ds) = \frac{1}{2}\beta e^{-\beta t_0} < \frac{\delta}{2}, \quad \beta > \beta_0. \end{aligned} \quad (2.6.14)$$

Next, by use of (2.6.10)-(2.6.13), the remaining part of the expression on the left of (2.6.9) can be estimated by

$$\begin{aligned} & |\beta^2 \int_0^{t_0} h(\Gamma(t) - \Gamma(t-s))e^{-\beta s} ds - w(t)| \\ & = |\beta^2 \int_0^{t_0} [h(\Gamma(t) - \Gamma(t-s) - sw(t) + sw(t)) - h(sw(t))]e^{-\beta s} ds \\ & \quad + \beta^2 \int_0^{t_0} [h(sw(t)) - sw(t)]e^{-\beta s} ds + \beta^2 \int_0^{t_0} sw(t)e^{-\beta s} ds - w(t)| \\ & \leq \beta^2 \int_0^{t_0} |\Gamma(t) - \Gamma(t-s) - sw(t)|e^{-\beta s} ds \\ & \quad + \beta^2 \int_0^{t_0} \delta s |w(t)|e^{-\beta s} ds + |\beta^2 w(t) \int_0^{t_0} s e^{-\beta s} ds - w(t)| \\ & \leq \beta^2 \int_0^{t_0} \delta s e^{-\beta s} ds + M\delta + M(1 + \beta t_0)e^{-\beta t_0} < (1 + 2M)\delta, \quad \beta > \beta_0. \end{aligned} \quad (2.6.15)$$

This completes the proof. \square

Since $\beta \gg 1$, we approximate the third and fourth terms in the left-hand side of (2.6.7) by their limit $w(r, t)$ as $\beta \rightarrow \infty$. Then equation (2.6.7), multiplied by ε , reduces to

$$h(\Gamma(r, t))e^{-t} + \int_0^t h(\gamma(r, t, \tau))e^{-(t-\tau)} d\tau + \varepsilon w(r, t) = \frac{1}{2}rf(t), \quad 0 \leq r \leq 1, \quad t > 0. \quad (2.6.16)$$

The latter equation is identical to the previous equation (2.1.35), which was derived from the KBKZ-model with one relaxation rate and supplied with an extra Newtonian viscous term. In order that the present parameter $\varepsilon = m/\beta$ agrees with $\varepsilon = \eta_s \lambda / \mu$ from (2.1.28), we need to put $\eta_s = \mu_2 / \lambda_2$. Thus we have shown that equation (2.6.5) for a KBKZ-model with two relaxation rates $\lambda_1 \ll \lambda_2$, may be approximated by equation (2.1.35) for a KBKZ-model with one relaxation rate λ_1 and supplied with an extra Newtonian viscous term with a fictitious solvent viscosity $\eta_s = \mu_2 / \lambda_2$. The Newtonian viscous term accounts for the very fast relaxation rates of the polymeric melt.

The approximation of a KBKZ-model with two widely spaced relaxation rates by a KBKZ-model with one relaxation rate and a Newtonian viscous term can also be justified in a direct manner. To that end, we rewrite the second term in (2.6.1) as $\mu_2 \exp(-\lambda_2 t) = \varepsilon \mu_1 \beta \exp(-\lambda_1 \beta t)$. If $\beta \gg 1$, we may approximate this second term by its distribution limit

$$\lim_{\beta \rightarrow \infty} \varepsilon \mu_1 \beta \exp(-\lambda_1 \beta t) = \frac{\varepsilon \mu_1}{\lambda_1} \delta(t), \quad (2.6.17)$$

where δ denotes the delta-function of Dirac. Then the stress relaxation function becomes

$$G(t) = \mu_1 e^{-\lambda_1 t} + \frac{\varepsilon \mu_1}{\lambda_1} \delta(t), \quad (2.6.18)$$

which replaces (2.6.1). Again, the corresponding expression for $m(t) = -G'(t)$ and Papanastasiou's kernel K from (2.1.10) are inserted into (2.1.7). As a result we find that the extra stress tensor $S = S_p$ is given by

$$S = \mu_1 \lambda_1 \int_{-\infty}^t \frac{c}{c-3+I_{C^{-1}}} e^{-\lambda_1(t-\tau)} C^{-1} d\tau - \frac{\varepsilon \mu_1}{\lambda_1} \int_{-\infty}^t \frac{c}{c-3+I_{C^{-1}}} \delta'(t-\tau) C^{-1} d\tau. \quad (2.6.19)$$

The first integral in (2.6.19) is recognized as the polymer contribution S_p to the extra stress tensor, according to the KBKZ-model with one relaxation rate λ_1 ; see (2.1.11). The second integral in (2.6.19) is evaluated through an integration by parts yielding

$$\begin{aligned} \int_{-\infty}^t \frac{c}{c-3+I_{C^{-1}}} \delta'(t-\tau) C^{-1} d\tau &= \int_{-\infty}^t \frac{\partial}{\partial \tau} \left\{ \frac{c C^{-1}}{c-3+I_{C^{-1}}} \right\} \delta(t-\tau) d\tau \\ &= \frac{\partial}{\partial \tau} \left\{ \frac{c C^{-1}}{c-3+I_{C^{-1}}} \right\} \Big|_{\tau=t}. \end{aligned} \quad (2.6.20)$$

The latter derivative is determined by use of the expression (2.1.18) for C^{-1} and the special values $\gamma(r, t, \tau)|_{\tau=t} = 0$ and $\partial\gamma(r, t, \tau)/\partial\tau|_{\tau=t} = \partial v(r, t)/\partial r$, obtained from (2.1.19):

$$\begin{aligned} \left. \frac{\partial}{\partial\tau} \left\{ \frac{c C^{-1}}{c - 3 + I_{C^{-1}}} \right\} \right|_{\tau=t} &= \left[-\frac{2c\gamma}{(c + \gamma^2)^2} \frac{\partial\gamma}{\partial\tau} C^{-1} + \frac{c}{c + \gamma^2} \frac{\partial}{\partial\tau} \{C^{-1}\} \right]_{\tau=t} \\ &= \begin{pmatrix} 0 & 0 & -\frac{\partial v}{\partial r}(r, t) \\ 0 & 0 & 0 \\ -\frac{\partial v}{\partial r}(r, t) & 0 & 0 \end{pmatrix} = -2\mathcal{D}. \end{aligned} \quad (2.6.21)$$

Finally, by combining the previous results and by putting $\varepsilon = m/\beta = \eta_s \lambda_1 / \mu_1$, we find that the extra stress tensor \mathcal{S} of (2.6.19) can be expressed by

$$\mathcal{S} = \mathcal{S}_p + 2\eta_s \mathcal{D}, \quad (2.6.22)$$

in accordance with the relation (2.1.3) for the KBKZ-model with one relaxation rate λ_1 and supplied with a Newtonian viscous term. The present analysis shows that the Newtonian viscous term $2\eta_s \mathcal{D}$ follows from the constitutive Wagner integral, if the stress relaxation function G contains a delta-function as in (2.6.18).

2.7 Conclusions

Stability analysis and numerical calculations have been used to analyze the capillary flow of a polymeric melt. In order to find a theoretical explanation for the spurt phenomenon observed in the experiments of e.g. Vinogradov et al. [52], [53], a flow driven by a prescribed constant pressure gradient \bar{f} has been considered. The constitutive behaviour of the polymeric melt is described by Wagner's modification of the KBKZ-model, supplemented with an extra Newtonian viscous term. This extra term accounts for the effect of a small-molecule solvent with viscosity η_s . We used the kernel of Papanastasiou and restricted ourselves to one main relaxation rate λ . Thus, the KBKZ-model used here describes, by an integral relation, the characteristic behaviour of a viscoelastic concentrated polymer solution with fading memory. The addition of the extra Newtonian viscous term is essential in our analysis, since it leads to a nonmonotone relation between the steady state shear stress $F(r) = r\bar{f}/2$ and the steady state velocity gradient or shear strain-rate $\omega(r)$. We have shown that this nonmonotone relation provides an explanation for the spurt phenomenon. Hence, internal material properties of the fluid itself account for the spurt phenomenon, instead of a global external effect such as 'wall slip', because in our model the no-slip boundary condition at the wall of the capillary is maintained.

Our results for the pressure-driven flow of a KBKZ-fluid through a cylindrical capillary are very similar to those obtained by Malkus et al. [32], [33]. These authors employed the differential constitutive model of Johnson, Segalman and Oldroyd (JSO-model) in their analysis of the pressure-driven flow through a slit die. In addition, Malkus et al. studied the full governing JSO system of partial differential equations, whereas our analysis is restricted to

the case of inertialess flow governed by the integrodifferential equation (2.1.35) (which obtains by putting $\alpha = 0$ in equation (2.1.29) for the full flow problem).

For pure molten polymers, where the solvent is absent, we have shown that the KBKZ-model with two widely spaced relaxation rates can be approximated by a KBKZ-model with one relaxation rate and an extra Newtonian term viscous term. We have demonstrated that the stresses in a concentrated polymer solution, described by Wagner's integral with one relaxation rate λ and supplemented with the Newtonian viscous term with viscosity η_s , equal the stresses in a pure molten polymer with two widely spaced relaxation rates λ_1 and λ_2 , provided that $\lambda_2 \gg \lambda_1 = \lambda$ and $\eta_s = \mu_2/\lambda_2$, where μ_2 is the shear modulus corresponding to λ_2 . Hence, the Newtonian viscous term accounts for the unhindered polymer chain motions described by a very fast secondary relaxation rate. Thus, the KBKZ-model used here, describes the characteristic behaviour of both concentrated polymer solutions and pure molten polymers.

The description of the flow considered here, involves one dimensionless parameter ε , which is equal to the quotient of the solvent viscosity η_s and the shear viscosity μ/λ . In the case of no solvent viscosity ($\eta_s = 0$) and two widely spaced relaxation rates, the parameter ε is equal to the quotient of the two shear viscosities. We obtain a nonmonotone steady state relation, given by (2.2.10), between the steady state shear stress $F(r)$ and the steady state velocity gradient $\omega(r)$, if $0 < \varepsilon < \varepsilon_1 = 0.02886$. This nonmonotone relation gives rise to three distinct steady state solutions ω if $F_m < F < F_M$. We showed by analytical and numerical means that

- steady state solutions ω with $\omega_M < \omega < \omega_m$ are l -unstable (and conjectured to be unstable);
- steady state solutions ω with $0 \leq \omega < \omega_M$ or $\omega > \omega_m$ are asymptotically stable;
- if the stationary pressure gradient \bar{f} exceeds the critical value $\bar{f}_{crit} = 2F_M$, the steady state equation (2.2.10) has two distinct stable solutions for the steady state velocity gradient $\omega(r)$ for a certain range of the radial coordinate r ;
- as $t \rightarrow \infty$, the flow reaches a steady state.

The actual (stable) steady state attained by the fluid has to be determined by numerical calculations. Which steady state ω is attained depends on the radial position, the prescribed stationary pressure gradient \bar{f} and the deformation history of the fluid. Our calculations reveal that if the flow starts from rest under a prescribed subcritical pressure gradient $\bar{f} < \bar{f}_{crit} = 2F_M$, then the steady state velocity gradient $\omega(r)$ is a continuous function of the radial coordinate r . Consequently, the steady state velocity profile $\bar{v}(r)$ is a smooth function of r , and the flow is referred to as classical flow. If the stationary pressure gradient \bar{f} exceeds the critical value \bar{f}_{crit} (supercritical flow), one observes that for $r_M < r \leq 1$ near the wall and during a rather short time interval the velocity gradient increases from a value below ω_M to a value that exceeds $\tilde{\omega}_M$, after which the flow becomes gradually stationary; for $r \in [0, r_M)$, the velocity gradient tends to a steady state value $\omega(r) < \omega_M$. Hence, the steady state velocity gradient $\omega(r)$ is discontinuous at $r = r_M$, which leads to a kink in the steady state velocity

profile $\bar{v}(r)$ at $r = r_M$. The large values of $\omega(r)$ in the layer $r_M < r \leq 1$ near the wall (the so-called spurt layer) give rise to an overall raise of the velocity in the capillary, which provides an important contribution to the magnitude of the steady state volumetric flow rate \bar{Q} . As a result, if during a loading process the prescribed stationary pressure gradient is gradually increased from $\bar{f} = 0$ up to $\bar{f}_{max} > \bar{f}_{crit}$, a substantial increase of the volumetric flow rate \bar{Q} occurs at $\bar{f} = \bar{f}_{crit}$. This increase of \bar{Q} is known as the spurt phenomenon. Since in our analysis the no-slip boundary condition $\bar{v}(1) = 0$ is maintained (see Figure 2.2), wall slip cannot account for the spurt phenomenon.

In the unloading process where the prescribed stationary pressure gradient is gradually decreased from $\bar{f} = \bar{f}_{max}$ down to $\bar{f} = 0$, the following peculiarities are observed:

- When the unloading step $-\Delta\bar{f} = \bar{f}_{max} - \bar{f}$ is sufficiently small such that $\bar{f} > \bar{f}_{max} F_m / F_M$, the spurt layer remains fixed, which is referred to as shape memory;
- the velocity gradient first decreases rapidly, after which it gradually becomes stationary again (see the Figures 2.5 and 2.6);
- when the unloading step $-\Delta\bar{f} = \bar{f}_{max} - \bar{f}$ exceeds a certain value corresponding to $\bar{f} < \bar{f}_{max} F_m / F_M$, the spurt layer becomes thinner (loss of shape memory) as long as $\bar{f} > 2F_m$, and the layer disappears if $\bar{f} < 2F_m$;
- the loading and unloading paths in the plot of \bar{Q} versus \bar{f} do not coincide, which is characteristic for the occurrence of hysteresis (see Figure 2.10).

Hence, in case the steady state solution ω is not unique, it depends on the deformation history of the fluid which steady state is attained by the fluid. We found that if the flow starts from rest under a supercritical pressure gradient $\bar{f} > \bar{f}_{crit}$, top-jumping occurs. This means that, in terms of the steady state shear stress $F(r) = r\bar{f}/2$, the jump in the steady state velocity gradient $\omega(r)$ occurs at the local maximum $F = F_M$, corresponding to $r = r_M = 2F_M/\bar{f}$. During the unloading process, shape memory is observed as long as $\bar{f}_{max} > \bar{f} > \bar{f}_{max} F_m / F_M$, whereby the jump in $\omega(r)$ occurs at $F = F^* = F_m \bar{f} / \bar{f}_{max}$, corresponding to the fixed position $r = r^* = 2F_M / \bar{f}_{max}$. Shape memory is lost if $\bar{f}_{max} F_m / F_M > \bar{f} > 2F_m$, in which case bottom-jumping occurs: the jump in $\omega(r)$ occurs at the local minimum $F = F_m$, corresponding to $r = r_m = 2F_m / \bar{f}$. If $\bar{f} < 2F_m$, the jump in $\omega(r)$ has disappeared and the flow is classical again.

In the transient flow behaviour we distinguished different time phases. For a supercritical flow we observed, dependent on the radial coordinate r , two or three distinct time phases in the development of the velocity gradient $w(r, t)$. These time phases are characterized as follows:

- A Newtonian phase in which $w(r, t)$ decreases on an $O(\varepsilon)$ -time scale from its initial value $w(r, 0) = r\bar{f}/2\varepsilon$ to a value $w(r, t) = O(\varepsilon^0)$, $\varepsilon \rightarrow 0$.
- A latency phase in which $w(r, t) = O(\varepsilon^0)$, $\varepsilon \rightarrow 0$. If $r < r_M$, the latency phase is the final phase during which $w(r, t)$ tends to a steady state $\omega(r) < \omega_M$.
- If $r > r_M$, the latency phase is followed by a spurt phase during which $w(r, t)$ suddenly increases to a value larger than $\tilde{\omega}_M$, and then tends to a steady state $\omega(r) > \tilde{\omega}_M$.

These phases have also been analyzed in terms of the dimensionless stresses S and N , where S corresponds to the shear stress due to the polymer contribution, and N corresponds to the first normal stress difference. We observed that during the Newtonian phase the relationship between N and S is well approximated by $N = N_{New}(S)$, whereas during the latency phase S remains almost constant at $S = F + O(\varepsilon)$, $\varepsilon \rightarrow 0$. Moreover, we found that during loading the calculated (S, N) -plot lies inside the region bounded by the Newtonian curve $N = N_{New}(S)$ and the steady state curves $N = N_0(S)$ and $S = S_0(N)$.

By fitting the dimensionless parameter ε to the material parameters of the polymeric melt, the dimensional steady state volumetric flow rate \bar{Q} can be determined as a function of the dimensional driving pressure gradient \bar{f} . This flow rate is of great practical interest in polymer processing, since it determines the production rate of an extrusion process; a higher flow rate leads to more extrudate produced per unit of time. The dimensional critical pressure gradient \bar{f}_{crit} beyond which spurt ensues, can be estimated in terms of the material parameters η_s , λ , μ and c , and the radius R of the capillary. From this critical pressure gradient the associated dimensional critical volumetric flow rate \bar{Q}_{crit} can easily be derived, also in terms of η_s , λ , μ , c and R . In the experiments of Vinogradov et al. [52], [53], the extrudate becomes irregularly distorted at the onset of spurt. Thus, the critical flow rate \bar{Q}_{crit} determines the optimal production rate at which a classical steady state flow profile producing a smooth extrudate, can be established.

In Chapter 5 we fit the parameter ε to the material parameters of the polymeric samples used by Vinogradov et al. [52]. By comparison of our theoretical critical pressure gradient \bar{f}_{crit} at the onset of spurt, to the experimentally found critical pressure gradient, we are able to estimate the parameter c that occurs in Papanastasiou's kernel used in the KBKZ-model. Furthermore, we examine the critical conditions for the onset of spurt and hysteresis, in their dependence on the material properties of the polymeric fluid. The dependence predicted by our theory is next compared to the dependence observed in experiments of Vinogradov et al. [52], [53], and of El Kissi and Piau [12].

Chapter 3

Piston-driven shear flow of a JSO-fluid

In this chapter we analyze the flow of a polymeric melt through a cylindrical capillary. A piston, moving at constant speed, controls the flow by inducing a constant volumetric flow rate. The pressure gradient is then unknown and adjusts itself to maintain the desired flow rate. Since the polymeric melt is strongly viscous, the inertia forces may be neglected. The constitutive equation to describe the characteristic behaviour of the viscoelastic fluid with fading memory chosen here, is the Johnson-Segalman-Oldroyd (JSO) model supplied with an extra Newtonian viscous term. This extra term, which accounts for the unhindered motion of the polymer chains, is essential as it leads to a nonmonotone behaviour of the steady state shear stress as function of the steady state shear strain-rate or velocity gradient (see Figure 3.1).

3.1 Mathematical formulation

The flow of the incompressible melt is governed by the conservation of mass

$$\nabla \cdot \mathbf{v} = 0 \tag{3.1.1}$$

and the balance of linear momentum

$$\nabla \cdot \mathcal{T} + \rho \mathbf{b} = \rho \left(\frac{\partial \mathbf{v}}{\partial t} + (\mathbf{v} \cdot \nabla) \mathbf{v} \right). \tag{3.1.2}$$

Here, ρ is the (constant) fluid density, \mathbf{b} the body force per unit of mass, \mathbf{v} the fluid velocity and \mathcal{T} the total (symmetric) stress tensor. Later on we shall show that for strongly viscous fluids the inertia forces, represented by the right-hand side of (3.1.2), can be neglected.

The characteristic response of the material to a deformation is described by the constitutive equation for the stress. For viscoelastic fluids with fading memory, the stress depends on the deformation history. If a polymer solution contains a small-molecule solvent, this solvent will generally respond in a viscous manner to any applied force or deformation, separately from the elastic response due to the dissolved polymer; see Renardy et al. [48, p. 17]. Therefore, it is assumed that the extra stress tensor $\mathcal{S} := \mathcal{T} + pI$ in the fluid consists of a Newtonian viscous component and an isotropic elastic one, namely

$$\mathcal{S} = \mathcal{T} + pI = 2\eta_s \mathcal{D} + \mathcal{S}_p. \tag{3.1.3}$$

Here, p is the pressure, I the unit tensor, and \mathcal{D} is the rate-of-deformation tensor defined by

$$\mathcal{D} = \frac{1}{2}(\mathcal{L} + \mathcal{L}^T), \quad \mathcal{L} = \text{grad } \mathbf{v} = \frac{\partial \mathbf{v}}{\partial \mathbf{x}} (\equiv (\nabla \mathbf{v})^T). \quad (3.1.4)$$

Furthermore, η_s is the solvent viscosity, and the elastic part \mathcal{S}_p characterizes the polymer contribution.

In this chapter the elastic part \mathcal{S}_p is assumed to be described by the constitutive JSO-model, which can be derived from the Phan-Thien-Tanner (PTT) model by neglecting the extensional flow response. In the JSO-model, which is suitable in pure shear flows, \mathcal{S}_p is determined by the following nonlinear differential equation (see Tanner [50, p. 207]):

$$\frac{d\mathcal{S}_p}{dt} - \mathcal{L}\mathcal{S}_p - \mathcal{S}_p\mathcal{L}^T + (1-a)(\mathcal{D}\mathcal{S}_p + \mathcal{S}_p\mathcal{D}) + \lambda\mathcal{S}_p = 2\mu\mathcal{D}, \quad (3.1.5)$$

where d/dt denotes the material derivative. The relaxation rate λ , the slip parameter $a \in (-1, 1)$, and the shear modulus μ are material parameters. The special cases $a = 1$, $a = 0$ and $a = -1$ are known as the upper convected, the corotational and the lower convected Maxwell models, respectively; cf. Renardy et al. [48, p. 24].

In general, the constitutive equation involves a continuous spectrum of relaxation rates. Let this spectrum be approximated by choosing a set of $n \geq 1$ discrete relaxation rates λ_i , then the elastic part \mathcal{S}_p of the extra stress tensor \mathcal{S} is given by the multimode model

$$\mathcal{S}_p = \sum_{i=1}^n \mathcal{S}_p^{(i)}, \quad (3.1.6)$$

where each elastic part $\mathcal{S}_p^{(i)}$ is determined by (3.1.5) with $\mathcal{S}_p = \mathcal{S}_p^{(i)}$, $\lambda = \lambda_i$, $\mu = \mu_i$, and $a = a_i$, $i = 1, \dots, n$. Malkus et al. [33] have shown that the effects of two widely spaced relaxation rates λ_1 and λ_2 for a JSO-fluid with $a_2 = 1$ are correctly modelled by one main relaxation rate $\lambda = \lambda_1$ and a small Newtonian viscosity η_s , provided that $\lambda_2 \gg \lambda_1$ and $\eta_s = \mu_2/\lambda_2$. Thus, the extra Newtonian viscous term $2\eta_s\mathcal{D}$ accounts either for the response of a small-molecule solvent, or for the unhindered polymer chain motions described by a very fast relaxation rate.

We consider the axisymmetric shear flow in a cylindrical tube with radius R . Cylindrical coordinates (r, θ, z) are introduced with the z -axis along the centerline of the tube. With the flow aligned along the z -axis, the flow parameters are independent of the axial coordinate z and the azimuthal coordinate θ . Under the condition that the flow starts from rest at time $t = 0$, the velocity takes the form

$$\mathbf{v} = v(r, t)H(t)\mathbf{e}_z, \quad (3.1.7)$$

where H is the (Heaviside) step function and \mathbf{e}_z is a unit vector in the positive z -direction. The conservation of mass is now automatically satisfied, and the convective terms $\rho(\mathbf{v} \cdot \nabla)\mathbf{v}$ in (3.1.2) disappear. The no-slip boundary condition at the wall and the regularity of the velocity at the axis require

$$v(R, t) = 0, \quad (3.1.8)$$

and

$$\frac{\partial v}{\partial r}(0, t) = 0, \quad (3.1.9)$$

respectively.

With the velocity given by (3.1.7), $L_{rz} = \partial v / \partial r$ is the only non-zero component of \mathcal{L} and the components S_{ij} of \mathcal{S}_p are functions of r and t only. As a result, the material derivative dS_p/dt is equal to the partial time derivative $\partial S_p / \partial t$, and the JSO-model (3.1.5) transforms into the following equations:

$$\begin{aligned}
 \frac{\partial S_{rr}}{\partial t} + (1-a)S_{rz} \frac{\partial v}{\partial r} + \lambda S_{rr} &= 0, \\
 \frac{\partial S_{zz}}{\partial t} - (1+a)S_{rz} \frac{\partial v}{\partial r} + \lambda S_{zz} &= 0, \\
 \frac{\partial S_{rz}}{\partial t} - \frac{1}{2}(1+a)S_{rr} \frac{\partial v}{\partial r} + \frac{1}{2}(1-a)S_{zz} \frac{\partial v}{\partial r} + \lambda S_{rz} &= \mu \frac{\partial v}{\partial r}, \\
 \frac{\partial S_{r\theta}}{\partial t} + \lambda S_{r\theta} &= 0, \\
 \frac{\partial S_{\theta\theta}}{\partial t} + \lambda S_{\theta\theta} &= 0, \\
 \frac{\partial S_{\theta z}}{\partial t} + \lambda S_{\theta z} &= 0.
 \end{aligned} \tag{3.1.10}$$

Under the initial condition $\mathcal{S}_p = 0$ at $t = 0$, the solutions of (3.1.10)^{4,5,6} are $S_{r\theta} = S_{\theta\theta} = S_{\theta z} = 0$.

Introduction of the new variables

$$\begin{aligned}
 S &:= -S_{rz}, & W &:= -\frac{1}{2}(1+a)S_{rr} - \frac{1}{2}(1-a)S_{zz}, \\
 Z &:= \frac{1}{2}(1+a)S_{rr} - \frac{1}{2}(1-a)S_{zz},
 \end{aligned} \tag{3.1.11}$$

in (3.1.10) yields for S , Z and W the differential equations

$$\begin{aligned}
 \frac{\partial Z}{\partial t} - (1-a^2)S \frac{\partial v}{\partial r} + \lambda Z &= 0, \\
 \frac{\partial W}{\partial t} + \lambda W &= 0, \\
 \frac{\partial S}{\partial t} + Z \frac{\partial v}{\partial r} + \lambda S &= -\mu \frac{\partial v}{\partial r}.
 \end{aligned} \tag{3.1.12}$$

The solution of the second equation of (3.1.12), with $W(r, 0) = 0$, is $W = 0$, implying that

$$Z = (1+a)S_{rr} = -(1-a)S_{zz}. \tag{3.1.13}$$

In terms of S and Z , the stress components T_{ij} of \mathcal{T} according to (3.1.3) become

$$\begin{aligned}
 T_{rr} &= -p + \frac{1}{1+a}Z(r, t), & T_{\theta\theta} &= -p, \\
 T_{zz} &= -p - \frac{1}{1-a}Z(r, t), & T_{rz} &= \eta_s \frac{\partial v}{\partial r}(r, t) - S(r, t), \\
 T_{r\theta} &= T_{\theta z} = 0,
 \end{aligned} \tag{3.1.14}$$

where $p = p(r, z, t)$. The first and second normal stress differences $N_1 := T_{zz} - T_{rr}$ and $N_2 := -T_{\theta\theta} + T_{rr}$ are determined by

$$N_1 = -\frac{2}{1-a^2}Z(r, t), \quad \frac{N_2}{N_1} = -\frac{1-a}{2}. \quad (3.1.15)$$

Hence, Z is related to the first normal stress difference, and the ratio of the two normal stress differences is constant.

The balance of linear momentum (3.1.2), with $\rho \mathbf{b} = \mathbf{0}$, is satisfied if the stress components T_{ij} , given by (3.1.14), solve the equations

$$\frac{\partial T_{rr}}{\partial r} + \frac{1}{r}(T_{rr} - T_{\theta\theta}) = 0, \quad \frac{\partial T_{rz}}{\partial r} + \frac{T_{rz}}{r} - \frac{\partial p}{\partial z} = \rho \frac{\partial v}{\partial t}. \quad (3.1.16)$$

Since T_{rz} and v are independent of z , the solution for the pressure p takes the form

$$p(r, z, t) = -f(t)z + p_0(r, t), \quad (3.1.17)$$

with

$$p_0(r, t) = \frac{1}{1+a}Z(r, t) + \frac{1}{1+a} \int_0^r \frac{Z(y, t)}{y} dy + P_0(t), \quad (3.1.18)$$

while the shear stress T_{rz} equals

$$T_{rz} = -\frac{1}{2}rf(t) + \frac{\rho}{r} \int_0^r y \frac{\partial v}{\partial t}(y, t) dy. \quad (3.1.19)$$

Here, f is the pressure gradient driving the flow, and P_0 is a further irrelevant pressure term. Substitution of (3.1.17) and (3.1.18) into (3.1.14)^{1,2,3} yields

$$\begin{aligned} T_{rr} &= f(t)z - \frac{1}{1+a} \int_0^r \frac{Z(y, t)}{y} dy - P_0(t), \\ T_{\theta\theta} &= f(t)z - \frac{1}{1+a} \int_0^r \frac{Z(y, t)}{y} dy - \frac{Z(r, t)}{1+a} - P_0(t), \\ T_{zz} &= f(t)z - \frac{1}{1+a} \int_0^r \frac{Z(y, t)}{y} dy - \frac{2Z(r, t)}{1-a^2} - P_0(t). \end{aligned} \quad (3.1.20)$$

By equating the expressions (3.1.14)⁴ and (3.1.19) for T_{rz} , we are led to the following relation between the velocity gradient and the pressure gradient:

$$-\eta_s \frac{\partial v(r, t)}{\partial r} + S(r, t) = \frac{1}{2}rf(t) - \frac{\rho}{r} \int_0^r y \frac{\partial v}{\partial t}(y, t) dy, \quad 0 \leq r \leq R, \quad t > 0. \quad (3.1.21)$$

Finally, the volumetric flow rate Q is defined by

$$Q(t) = 2\pi \int_0^R v(r, t) r dr. \quad (3.1.22)$$

The equations are made dimensionless by scaling length by R and time by λ^{-1} . Furthermore, we introduce the dimensionless variables \hat{v} , \hat{f} , \hat{Z} and \hat{S} by writing $v = \lambda R \hat{v} / \sqrt{1-a^2}$,

$f = \mu \hat{f}/R\sqrt{1-a^2}$, $Z = \mu \hat{Z}$ and $S = \mu \hat{S}/\sqrt{1-a^2}$, and the two dimensionless parameters ε and α given by

$$\varepsilon = \frac{\eta_s \lambda}{\mu}, \quad \alpha = \frac{\rho R^2 \lambda^2}{\mu}. \quad (3.1.23)$$

Then equation (3.1.21) turns into its dimensionless form, reading (since no confusion will arise we omit the caret)

$$\varepsilon w(r, t) + S(r, t) = \frac{1}{2} r f(t) - \frac{\alpha}{r} \int_0^r y \frac{\partial v}{\partial t}(y, t) dy, \quad 0 \leq r \leq 1, \quad t > 0, \quad (3.1.24)$$

and equations (3.1.12)^{1,3} transform into

$$\frac{\partial Z}{\partial t} = -Z - wS, \quad \frac{\partial S}{\partial t} = -S + w(1 + Z), \quad 0 \leq r \leq 1, \quad t > 0. \quad (3.1.25)$$

Here, the velocity gradient, or shear strain-rate, w is defined by

$$w(r, t) = -\frac{\partial v}{\partial r}(r, t). \quad (3.1.26)$$

Notice that Malkus et al. [32], [33] obtain the same dimensionless equations (3.1.25) for the flow of a JSO-fluid through a slit die. The parameter ε represents the ratio of the Newtonian viscosity η_s and the shear viscosity μ/λ , and the quotient α/ε corresponds to the Reynolds number. For the strongly viscous polymers we consider, $\alpha \ll 1$. Thus, the last term in the right-hand side of (3.1.24) may be neglected, which amounts to the neglect of the inertia forces in (3.1.2). By putting $\alpha = 0$, equation (3.1.24) reduces to

$$\varepsilon w(r, t) + S(r, t) = \frac{1}{2} r f(t), \quad 0 \leq r \leq 1, \quad t \geq 0. \quad (3.1.27)$$

The boundary conditions pertinent to (3.1.27) read in dimensionless form

$$v(1, t) = 0, \quad w(0, t) = 0, \quad t > 0. \quad (3.1.28)$$

By writing $Q = \pi \lambda R^3 \hat{Q}/\sqrt{1-a^2}$, the expression (3.1.22) passes into the dimensionless form (omitting the carets)

$$Q(t) = 2 \int_0^1 v(r, t) r dr. \quad (3.1.29)$$

After one integration by parts with the aid of the no-slip boundary condition (3.1.28)¹ at the wall, the volumetric flow rate Q can be expressed in terms of the velocity gradient w by

$$Q(t) = \int_0^1 r^2 w(r, t) dr. \quad (3.1.30)$$

Elimination of w by means of (3.1.27), transforms (3.1.30) into the following (implicit) relation between the pressure gradient f and the volumetric flow rate Q :

$$f(t) = 8\varepsilon Q(t) + 8 \int_0^1 r^2 S(r, t) dr. \quad (3.1.31)$$

For the piston-driven flow considered here, it is understood that the volumetric flow rate has a prescribed constant value \bar{Q} for $t \geq 0$. Thus, after substitution of $Q(t) = \bar{Q}$ into (3.1.31), we obtain for the four unknowns f , w , S , and Z , the following system that describes the piston-driven flow:

$$\begin{aligned} \varepsilon w(r, t) + S(r, t) &= \frac{1}{2} r f(t), & f(t) &= 8\varepsilon \bar{Q} + 8 \int_0^1 r^2 S(r, t) dr, & t \geq 0, \\ \frac{\partial S}{\partial t} &= -S + w(1 + Z), & \frac{\partial Z}{\partial t} &= -Z - wS, & 0 \leq r \leq 1, \quad t > 0. \end{aligned} \quad (3.1.32)$$

For $t < 0$ the fluid is at rest, and at $t = 0$ the flow is suddenly started up by imposing the constant flow rate \bar{Q} . Thus, the initial conditions for S and Z which are supposed to be continuous at $t = 0$, are given by

$$S(r, 0) = 0, \quad Z(r, 0) = 0, \quad 0 \leq r \leq 1. \quad (3.1.33)$$

Substitution of (3.1.33) into (3.1.32)^{1,2} then yields the initial values

$$f(0) = 8\varepsilon \bar{Q}, \quad w(r, 0) = 4\bar{Q}r, \quad 0 \leq r \leq 1. \quad (3.1.34)$$

Notice that, in contrast to Chapter 2 where $w(r, 0) = O(1/\varepsilon)$, the initial velocity gradient of the piston-driven flow considered here is of order ε^0 , $\varepsilon \rightarrow 0$. By integration with respect to r and by use of the boundary condition at the wall, we find that the initial velocity profile $v(r, 0) = 2\bar{Q}(1 - r^2)$ is parabolic in r . The equations (3.1.32) governing the piston-driven flow can be viewed as a continuous family of quadratic ordinary differential equations coupled by a non-local constraint that fixes the volumetric flow rate \bar{Q} . Malkus et al. [35, Sec. 3] have shown that the system (3.1.32) for the inertialess piston-driven flow is globally well-posed in time. Following Malkus et al. [35], [36], we establish the Lyapunov-type identity

$$\frac{\partial}{\partial t} \left\{ S^2 + (Z + 1)^2 \right\} = -2 \left[S^2 + \left(Z + \frac{1}{2} \right)^2 - \frac{1}{4} \right], \quad (3.1.35)$$

which readily follows from (3.1.32)^{3,4}. This identity can be used to prove global existence and boundedness of solutions of the system (3.1.32), in much the same manner as in [35], [36]. However, we will not pursue this point.

3.2 Steady state flow

In this section we investigate the steady state reached by the flow as $t \rightarrow \infty$. The steady state flow, driven by the constant volumetric flow rate \bar{Q} , is described in terms of the steady state variables

$$\begin{aligned} \omega(r) &= \lim_{t \rightarrow \infty} w(r, t), & \bar{f} &= \lim_{t \rightarrow \infty} f(t), \\ \bar{S}(r) &= \lim_{t \rightarrow \infty} S(r, t), & \bar{Z}(r) &= \lim_{t \rightarrow \infty} Z(r, t), \end{aligned} \quad (3.2.1)$$

under the assumption that these limits exist. In (3.2.1), ω is the steady state velocity gradient, \bar{f} is the steady state pressure gradient, and \bar{S} and \bar{Z} are the steady state extra stresses. For $t \rightarrow \infty$, the equations (3.1.32) reduce to

$$\begin{aligned} \varepsilon\omega(r) + \bar{S}(r) &= \frac{1}{2}r\bar{f}, & \bar{f} &= 8\varepsilon\bar{Q} + 8 \int_0^1 r^2\bar{S}(r)dr, \\ 0 &= -\bar{S} + \omega(1 + \bar{Z}), & 0 &= -\bar{Z} - \omega\bar{S}. \end{aligned} \quad (3.2.2)$$

The solutions of (3.2.2)^{3,4} expressed in terms of ω read

$$\bar{S}(r) = \frac{\omega(r)}{1 + \omega^2(r)}, \quad \bar{Z}(r) = -\frac{\omega^2(r)}{1 + \omega^2(r)}. \quad (3.2.3)$$

On substitution of (3.2.3)¹ into (3.2.2)¹, we find that the steady state velocity gradient can be determined for each $r \in [0, 1]$ by solving $\omega = \omega(r)$ from the equation

$$\mathcal{F}(\omega(r)) = F(r), \quad (3.2.4)$$

where the steady state shear stress F is defined by

$$F(r) = r\bar{f}/2, \quad (3.2.5)$$

and the function \mathcal{F} is defined by

$$\mathcal{F}(\omega) = \varepsilon\omega + \frac{\omega}{1 + \omega^2}. \quad (3.2.6)$$

Notice that the same function \mathcal{F} appears in Malkus et al. [32], [33]. For a given volumetric flow rate \bar{Q} , the velocity gradient ω must satisfy the constraint

$$\bar{Q} = \int_0^1 r^2\omega(r)dr, \quad (3.2.7)$$

obtained by letting $t \rightarrow \infty$ in (3.1.30). The steady state velocity profile $\bar{v}(r) = \lim_{t \rightarrow \infty} v(r, t)$ is obtained by integration of $\bar{v}'(r) = -\omega(r)$ using the boundary condition $\bar{v}(1) = 0$ at the wall.

For $\varepsilon < 1/8$ the function \mathcal{F} is nonmonotone in ω . In Figure 3.1 the function $\mathcal{F}(\omega)$ is plotted for a specific value of ε with $0 < \varepsilon < 1/8$. Since the Newtonian viscosity η_s is small in comparison to the shear viscosity μ/λ , we will henceforth assume that $0 < \varepsilon < 1/8$. Then the function $\mathcal{F}(\omega)$ has two extreme values, a maximum $F_M = \mathcal{F}(\omega_M)$ at $\omega = \omega_M = [(1 - 2\varepsilon - \sqrt{1 - 8\varepsilon})/2\varepsilon]^{1/2}$ and a minimum $F_m = \mathcal{F}(\omega_m)$ at $\omega = \omega_m = [(1 - 2\varepsilon + \sqrt{1 - 8\varepsilon})/2\varepsilon]^{1/2}$; see Figure 3.1. In addition to $\omega = \omega_M$ and $\omega = \omega_m$, both equations $\mathcal{F}(\omega) = F_M$ and $\mathcal{F}(\omega) = F_m$ have a second solution $\omega = \tilde{\omega}_M$ and $\omega = \tilde{\omega}_m$, respectively; see Figure 3.1. For small values of ε the following expansions can be derived:

$$\begin{aligned} \omega_M &= 1 + 2\varepsilon + 6\varepsilon^2 + O(\varepsilon^3), & \omega_m &= \frac{1}{\sqrt{\varepsilon}} \left[1 - \frac{3}{2}\varepsilon - \frac{25}{8}\varepsilon^2 + O(\varepsilon^3) \right], \\ \tilde{\omega}_M &= \frac{1}{\varepsilon} \left[\frac{1}{2} - \varepsilon - 3\varepsilon^2 + O(\varepsilon^3) \right], & \tilde{\omega}_m &= \sqrt{\varepsilon} [2 + 5\varepsilon + O(\varepsilon^2)], \\ F_M &= \frac{1}{2} + \varepsilon + \varepsilon^2 + O(\varepsilon^3), & F_m &= \sqrt{\varepsilon} \left[2 - \varepsilon - \frac{5}{4}\varepsilon^2 + O(\varepsilon^3) \right]. \end{aligned} \quad (3.2.8)$$

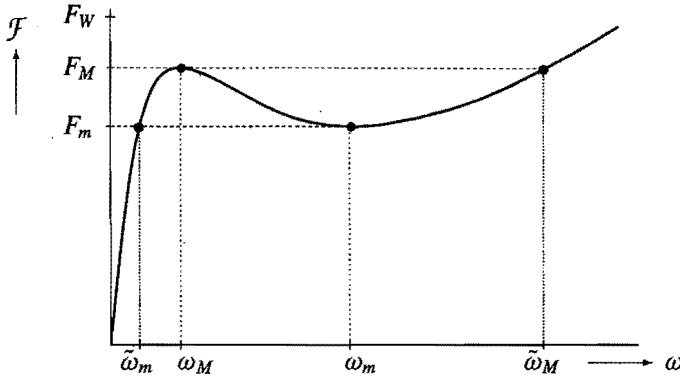


Figure 3.1 The function $\mathcal{F}(\omega) = \varepsilon\omega + \omega/(1 + \omega^2)$, when $0 < \varepsilon < 1/8$. In steady state flow the velocity gradient ω satisfies $\mathcal{F}(\omega) = F$, where $F = r\bar{f}/2$ is the steady state shear stress.

The steady state shear stress F is linear in r and has its maximum at the wall $r = 1$. If this maximum, denoted by $F_W = \bar{f}/2$, remains below the minimum F_m , then equation (3.2.4) has a unique solution $\omega(r) < \tilde{\omega}_m$ for each radial coordinate r . Clearly, $\omega(r)$ is continuous in r , leading to a smooth steady state velocity profile $\bar{v}(r)$, and the flow is referred to as classical flow. If the maximum $F_W = \bar{f}/2$ exceeds the minimum F_m , equation (3.2.4) has three distinct solutions if $F_m < F < F_M$. Malkus et al. [33, Sec. 3] have shown by a phase-plane analysis of the critical points of the system (3.1.32), that the solution ω with $\omega_M < \omega < \omega_m$ corresponds to a saddle point. Hence, this ω -solution is unstable and is therefore not attained. If $F(1) > F_M$, i.e. if $\bar{f} > 2F_M =: \bar{f}_{crit}$ (supercritical flow), the steady state velocity gradient $\omega(r)$ has at least one jump at some radial coordinate r . In case of exactly one jump we denote the radial coordinate at which the jump occurs by r^* ($r^* < 1$), and we refer to the flow as spurt flow. Hence, in spurt flow $\omega(r) < \omega_-^*$ for $0 \leq r < r^*$, whereas $\omega(r) > \omega_+^*$ for $r^* < r \leq 1$, where

$$\omega_-^* = \lim_{r \uparrow r^*} \omega(r) < \lim_{r \downarrow r^*} \omega(r) = \omega_+^*, \quad (3.2.9)$$

with $\omega_-^* \leq \omega_M$ and $\omega_+^* \geq \omega_m$. From (3.2.3) it follows that in spurt flow $\bar{S}(r)$ and $\bar{Z}(r)$ are also discontinuous at $r = r^*$. The jump in ω results in a kink in the steady state velocity profile $\bar{v}(r)$ at $r = r^*$, and a spurt layer with large velocity gradients forms near the wall; see Figure 2.2. For small ε , we can express the steady state values in this spurt layer in terms of the shear stress $F(r) = r\bar{f}/2$, $r^* < r \leq 1$, by

$$\begin{aligned} \omega &= \frac{F}{\varepsilon} - \frac{1}{F} - \frac{\varepsilon}{F^3} + O(\varepsilon^2), & \bar{S} &= \frac{\varepsilon}{F} + \frac{\varepsilon^2}{F^3} + O(\varepsilon^3), \\ \bar{Z} &= -1 + \frac{\varepsilon^2}{F^2} + \frac{2\varepsilon^3}{F^4} + O(\varepsilon^4), & \varepsilon &\rightarrow 0. \end{aligned} \quad (3.2.10)$$

To obtain an expression for the constant volumetric flow rate \bar{Q} in terms of the steady state pressure gradient \bar{f} , we change the variable of integration in (3.2.7) from r to ω , by

using the steady state equation (3.2.4) written as $r = 2\mathcal{F}(\omega)/\bar{f}$. This transforms the relation (3.2.7) into

$$\bar{Q} = \frac{8}{\bar{f}^3} \int_{\mathcal{W}} \mathcal{F}^2(\omega) \mathcal{F}'(\omega) \omega d\omega. \quad (3.2.11)$$

Here, \mathcal{W} is the set of attained velocity gradients $\omega(r)$, $0 \leq r \leq 1$, which we shall specify below for classical flow and for spurt flow. The primitive function \mathcal{P} of the integrand in (3.2.11) can be calculated by analytical means, yielding

$$\begin{aligned} \mathcal{P}(\omega) = & \frac{1}{4}\varepsilon^3\omega^4 + \frac{1}{2}\varepsilon^2\omega^2 - \frac{1}{2}\varepsilon(1-\varepsilon)\ln(1+\omega^2) + \frac{1-5\varepsilon+2\varepsilon^2}{2(1+\omega^2)} \\ & - \frac{3-4\varepsilon}{4(1+\omega^2)^2} + \frac{1}{3(1+\omega^2)^3}. \end{aligned} \quad (3.2.12)$$

For classical flow, the set \mathcal{W} is given by $\mathcal{W} = [0, \omega_{wall}]$ where $\omega_{wall} := \omega(1) \leq \omega_M$, implying that (3.2.11) can be evaluated as

$$\bar{Q} = \frac{8}{\bar{f}^3} [\mathcal{P}(\omega_{wall}) - \mathcal{P}(0)], \quad 0 \leq \omega_{wall} \leq \omega_M. \quad (3.2.13)$$

In classical flow one has $0 \leq \omega(r) \leq \omega_{wall} \leq \omega_M$ for $0 \leq r \leq 1$, and $\omega(r)$ is found as the smallest solution of the steady state equation $\mathcal{F}(\omega(r)) = r\bar{f}/2$. By means of Figure 3.1 it is readily seen that for fixed r , the velocity gradient $\omega(r)$ increases with increasing \bar{f} . Thus it follows from (3.2.7) that \bar{Q} , as given by (3.2.13), is an increasing function of \bar{f} . The inverse of this function exists and is denoted by $\bar{f} = f_{clas}(\bar{Q})$, which is an increasing function of \bar{Q} . The maximum value of \bar{Q} for which classical flow can be achieved, occurs if $\bar{f} = \bar{f}_{crit} = 2F_M$ and $\omega_{wall} = \omega_M$. Denote this value by \bar{Q}_{crit} , then $\bar{Q}_{crit} = [\mathcal{P}(\omega_M) - \mathcal{P}(0)]/F_M^3$ by (3.2.13). By use of (3.2.12) and the expansions (3.2.8) we establish the following approximations:

$$\bar{f}_{crit} = 1 + 2\varepsilon + O(\varepsilon^2), \quad \bar{Q}_{crit} = \frac{1}{6} + (3 - 4\ln 2)\varepsilon + O(\varepsilon^2), \quad \varepsilon \rightarrow 0. \quad (3.2.14)$$

In classical flow the steady state velocity gradient can be approximated by

$$\omega(r) = \frac{1 - \sqrt{1 - r^2 \bar{f}^2}}{r\bar{f}} + O(\varepsilon), \quad 0 \leq r \leq 1, \quad \varepsilon \rightarrow 0, \quad (3.2.15)$$

provided that $\bar{f} \leq 1$. Likewise, the volumetric flow rate \bar{Q} as given by (3.2.13) can be approximated by

$$\bar{Q} = \frac{1}{\bar{f}} \left[\frac{1}{2} + \frac{1}{3\bar{f}^2} (1 - \bar{f}^2)^{3/2} - \frac{1}{3\bar{f}^2} \right] + O(\varepsilon), \quad \bar{f} \leq 1, \quad \varepsilon \rightarrow 0. \quad (3.2.16)$$

In spurt flow the steady state velocity gradient $\omega(r)$ is discontinuous at some radial coordinate $r = r^*$, where ω jumps from a value $\omega_-^* < \omega_M$ to a value $\omega_+^* > \omega_m$; cf. Figure 2.7b.

Hence, for spurt flow the set \mathcal{W} is given by $\mathcal{W} = [0, \omega_-^*] \cup [\omega_+^*, \omega_{wall}]$ where $\omega_{wall} = \omega(1)$, implying that (3.2.11) can be evaluated as

$$\bar{Q} = \frac{8}{\bar{f}^3} [\mathcal{P}(\omega_-^*) - \mathcal{P}(0) + \mathcal{P}(\omega_{wall}) - \mathcal{P}(\omega_+^*)], \quad 0 \leq \omega_-^* < \omega_+^* \leq \omega_{wall}. \quad (3.2.17)$$

Here, $\omega = \omega_{wall}$ is found as the largest solution of the steady state equation $\mathcal{F}(\omega) = \bar{f}/2$, while $\omega = \omega_-^*$ and $\omega = \omega_+^*$ are the smallest and largest solutions of the equation $\mathcal{F}(\omega) = r^* \bar{f}/2$. Thus the volumetric flow rate \bar{Q} is uniquely determined by the values of \bar{f} and r^* , and we shortly rewrite (3.2.17) as

$$\bar{Q} = Q(r^*, \bar{f}). \quad (3.2.18)$$

Next we examine the monotony of the function Q with respect to \bar{f} and r^* . In spurt flow the steady state velocity gradient $\omega(r)$ is found as the smallest or the largest solution of the steady state equation $\mathcal{F}(\omega(r)) = r\bar{f}/2$, dependent on whether $0 \leq r < r^*$ or $r^* < r \leq 1$, respectively. By use of Figure 3.1 we observe that for fixed r and r^* , $\omega(r)$ increases with increasing \bar{f} , while for fixed r and \bar{f} , $\omega(r)$ decreases with increasing r^* . Then it follows from (3.2.7) that $\bar{Q} = Q(r^*, \bar{f})$ is an increasing function of \bar{f} and a decreasing function of r^* . Hence, for a given flow rate \bar{Q} and radial coordinate r^* , there exists a unique steady state pressure gradient \bar{f} such that $\bar{Q} = Q(r^*, \bar{f})$. Spurt flow can only occur if $\bar{f} \geq 2F_m$ and accordingly, the function $Q(r^*, \bar{f})$ is defined for $\bar{f} \geq 2F_m$, $r_m \leq r^* \leq \min\{1, r_M\}$. Here, the lower bound $r^* = r_m := 2F_m/\bar{f}$ corresponds to bottom-jumping, whereby $F^* = F(r^*) = F_m$ and ω jumps from $\omega_-^* = \tilde{\omega}_m$ to $\omega_+^* = \omega_m$; cf. Figure 2.7c. The upper bound $r^* = r_M := 2F_M/\bar{f}$ corresponds to top-jumping, whereby $F^* = F(r^*) = F_M$ and ω jumps from $\omega_-^* = \omega_M$ to $\omega_+^* = \tilde{\omega}_M$; cf. Figure 2.7a. For a fixed $\bar{f} \geq 2F_m$, the function $\bar{Q} = Q(r^*, \bar{f})$ has its maximum at $r^* = r_m$, corresponding to bottom-jumping, and this maximum is given by

$$\bar{Q} = Q_{max}(\bar{f}) = \frac{8}{\bar{f}^3} [\mathcal{P}(\tilde{\omega}_m) - \mathcal{P}(0) + \mathcal{P}(\omega_{wall}) - \mathcal{P}(\omega_m)], \quad \bar{f} \geq 2F_m. \quad (3.2.19)$$

Since $Q_{max}(\bar{f})$ is an increasing function of \bar{f} , the inverse of this function exists and is denoted by $\bar{f} = f_{bottom}(\bar{Q})$. Consequently, the lower bound $r^* = r_m$ can be represented as a function of \bar{Q} according to $r^* = r_{bottom}^*(\bar{Q}) := 2F_m/f_{bottom}(\bar{Q})$. The functions $f_{bottom}(\bar{Q})$ and $r_{bottom}^*(\bar{Q})$ are defined for $\bar{Q} \geq Q_{max}(2F_m) = [\mathcal{P}(\tilde{\omega}_m) - \mathcal{P}(0)]/F_m^3 =: \bar{Q}_0$. Use of the expansions (3.2.8) yields the approximation

$$\bar{Q}_0 = \sqrt{\varepsilon}/2 + O(\varepsilon^{3/2}), \quad \varepsilon \rightarrow 0. \quad (3.2.20)$$

For a fixed $\bar{f} \geq 2F_m$, the function $\bar{Q} = Q(r^*, \bar{f})$ has its minimum at $r^* = r_M$, corresponding to top-jumping, and this minimum is given by

$$\bar{Q} = Q_{min}(\bar{f}) = \frac{8}{\bar{f}^3} [\mathcal{P}(\omega_M) - \mathcal{P}(0) + \mathcal{P}(\omega_{wall}) - \mathcal{P}(\tilde{\omega}_M)], \quad \bar{f} \geq 2F_m. \quad (3.2.21)$$

Since $Q_{min}(\bar{f})$ is an increasing function of \bar{f} , the inverse of this function exists and is denoted by $\bar{f} = f_{top}(\bar{Q})$. Consequently, the upper bound $r^* = r_M$ can be represented as a function

of \bar{Q} according to $r^* = r_{top}^*(\bar{Q}) := 2F_M/f_{top}(\bar{Q})$. The functions $f_{top}(\bar{Q})$ and $r_{top}^*(\bar{Q})$ are defined for $\bar{Q} \geq Q_{min}(2F_M) = [\mathcal{P}(\omega_M) - \mathcal{P}(0)]/F_M^3 = \bar{Q}_{crit}$. Finally, $Q_{min}(\bar{f}) \leq Q(r^*, \bar{f}) \leq Q_{max}(\bar{f})$ holds, which implies that

$$f_{bottom}(\bar{Q}) \leq \bar{f} \leq f_{top}(\bar{Q}). \quad (3.2.22)$$

Plots of the functions $f_{clas}(\bar{Q})$, $f_{bottom}(\bar{Q})$, and $f_{top}(\bar{Q})$, are shown as dashed curves in Figure 3.5, while plots of the functions $1 - r_{bottom}^*(\bar{Q})$ and $1 - r_{top}^*(\bar{Q})$, are shown as dashed curves in Figure 3.6. In Table 3.1 the values of ω_M , ω_m , F_M , F_m , $\tilde{\omega}_M$, $\tilde{\omega}_m$, \bar{Q}_{crit} and \bar{Q}_0 , are given for $\varepsilon = 0.02, 0.01$ and 0.005 .

ε	ω_M	ω_m	F_M	F_m	$\tilde{\omega}_M$	$\tilde{\omega}_m$	\bar{Q}_{crit}	\bar{Q}_0
0.02	1.0427	6.8493	0.5204	0.2799	23.9356	0.2984	0.1714	0.0724
0.01	1.0206	9.8467	0.5101	0.1990	48.9689	0.2052	0.1690	0.0506
0.005	1.0102	14.0349	0.5050	0.1411	98.9847	0.1432	0.1678	0.0356

Table 3.1 The values of ω_M , ω_m , F_M , F_m , $\tilde{\omega}_M$, $\tilde{\omega}_m$, \bar{Q}_{crit} and \bar{Q}_0 , for $\varepsilon = 0.02, 0.01$ and 0.005 .

In conclusion, for a prescribed constant flow rate \bar{Q} we have for a possible steady state:

- If $0 \leq \bar{Q} \leq \bar{Q}_0$, the steady state is unique; classical flow occurs with $\bar{f} = f_{clas}(\bar{Q})$.
- If $\bar{Q}_0 < \bar{Q} \leq \bar{Q}_{crit}$, the steady state is not unique; either classical flow or spurt flow occurs with $f_{bottom}(\bar{Q}) \leq \bar{f} \leq f_{clas}(\bar{Q})$.
- If $\bar{Q} > \bar{Q}_{crit}$, the steady state is not unique; spurt flow occurs with $f_{bottom}(\bar{Q}) \leq \bar{f} \leq f_{top}(\bar{Q})$.

Notice that the results derived in this section are only valid in case the steady state does indeed exist. Numerical computations as carried out in the next section will show whether or not the flow tends to a steady state as $t \rightarrow \infty$. It will turn out that for $\bar{Q} \leq \bar{Q}_{crit}$ there is no jump in the steady state velocity gradient, so that the flow is classical.

3.3 Transient flow behaviour

In this section we compute for $t > 0$ the transient flow, starting from rest at time $t = 0$ and driven by the constant volumetric flow rate $Q(t) = \bar{Q}$, $t \geq 0$. The flow is governed by the system of equations (3.1.32), with initial conditions (3.1.33) and (3.1.34). From the numerical results we infer whether the flow reaches a steady state, and we determine the steady state variables. The main interest goes to the relationship between \bar{Q} and the steady state pressure gradient $\bar{f} = \lim_{t \rightarrow \infty} f(t)$. In the case of a classical steady state this relationship is one-to-one: $\bar{f} = f_{clas}(\bar{Q})$, obtainable as the inverse of (3.2.13). In the case of a spurt steady state, \bar{f} is not uniquely determined by just \bar{Q} , as discussed below (3.2.18). Whether the flow tends to a steady state, is found to depend on the values of \bar{Q} and the dimensionless parameter ε . In the first part of this section we take $\varepsilon = 0.02$ and compute the transient flow for several

values of \bar{Q} . It turns out that a steady state is reached for all values of \bar{Q} considered. Furthermore, the steady state velocity gradient $\omega(r) = \lim_{t \rightarrow \infty} w(r, t)$ is either continuous in r , corresponding to classical flow, or $\omega(r)$ has one jump at $r = r^*$, corresponding to spurt flow. In the latter case, the radial coordinate r^* is related to \bar{Q} and \bar{f} by (3.2.18). Next, we present some analytical approximations for $f(t)$, $w(r, t)$, $S(r, t)$ and $Z(r, t)$, that are valid during the initial phase of the flow. Finally, we investigate the dependence of the transient flow on the parameter ε , by taking $\varepsilon = 0.01$ and $\varepsilon = 0.005$. The numerical calculations for $\varepsilon = 0.01$ reveal that a steady state is reached for all values of \bar{Q} considered. However, in case $\varepsilon = 0.005$ we find a range of \bar{Q} -values for which the flow shows so-called persistent oscillations that do not die out, so that no steady state is attained.

The equations (3.1.32) for f , w , S and Z , are solved by numerical integration. Let the discretisation time step be denoted by Δt . Divide the interval $0 \leq r \leq 1$ into M subintervals of equal length $\Delta r = 1/M$. The numerical discretisation scheme used below for the computation of S , Z and w , has been adopted from Malkus et al. [32], [34], [35]; see [34] for a detailed analysis of the stability of the algorithm. For $k = 0, 1, \dots, M$, $n = 1, 2, 3, \dots$, the stresses $S(r, t)$ and $Z(r, t)$ at $t = t_n := n\Delta t$ and $r = r_k := k\Delta r$ are computed according to the following first-order scheme:

$$\begin{aligned} S(r_k, t_n) &= [1 - \Delta t]S(r_k, t_{n-1}) + \Delta t w(r_k, t_{n-1})[1 + Z(r_k, t_{n-1})], \\ Z(r_k, t_n) &= [1 - \Delta t]Z(r_k, t_{n-1}) - \Delta t w(r_k, t_{n-1})S(r_k, t_n), \end{aligned} \quad (3.3.1)$$

with initial values $S(r_k, 0) = 0$, $Z(r_k, 0) = 0$, $w(r_k, 0) = 4r_k\bar{Q}$. Hence, S is treated explicitly (Euler forward), whereas (the nonlinear term in) Z is treated semi-implicitly. Next we compute the pressure gradient $f(t_n)$ by approximating the integral in (3.1.32)² by the trapezoidal rule, to obtain

$$f(t_n) = 8\varepsilon\bar{Q} + 8\Delta r \sum_{k=1}^{M-1} r_k^2 S(r_k, t_n) + 4\Delta r S(1, t_n). \quad (3.3.2)$$

Subsequently, for $k = 0, 1, \dots, M$, the velocity gradient $w(r_k, t_n)$ is computed according to

$$w(r_k, t_n) = \frac{r_k f(t_n)/2 - S(r_k, t_n)}{\varepsilon}. \quad (3.3.3)$$

System (3.1.32) is thus treated explicitly, and for given \bar{Q} and ε we obtain the numerically computed values $f(t_n)$, $w(r_k, t_n)$, $S(r_k, t_n)$ and $Z(r_k, t_n)$, $k = 1, 2, \dots, M$, $n = 1, 2, \dots$.

In Figure 3.2 the pressure gradient $f(t)$, the velocity gradient $w(1, t)$ at the wall, and the stresses $S(1, t)$ and $Z(1, t)$ at the wall are plotted as functions of time t , for $\varepsilon = 0.02$ and $\bar{Q} = 0.1$; the plots are drawn as solid curves. We observe that $f(t)$, $w(1, t)$, $S(1, t)$ and $Z(1, t)$ are monotone and smooth functions of t . After sufficient time a steady state is reached. From the numerical results that underlie Figure 3.2, we determine the steady state values \bar{f} , $\omega(1)$, $\bar{S}(1)$ and $\bar{Z}(1)$, as listed in Table 3.2. It has been checked that these values do satisfy (3.2.3) and the steady state equation $\mathcal{F}(\omega(1)) = \bar{f}/2$; cf. (3.2.4). Since $\bar{Q} = 0.1 \in (\bar{Q}_0, \bar{Q}_{crit})$ for $\varepsilon = 0.02$ (see Table 3.1), the steady state pressure gradient \bar{f} is not uniquely determined by just the given flow rate \bar{Q} ; either a classical steady state or a spurt

steady state with a discontinuous velocity gradient occurs. The computations for $\bar{Q} = 0.1$ reveal that $\omega(1) < \omega_M$, implying that the flow reaches a classical steady state with a continuous steady state velocity gradient. As a further check it has been verified that the relation (3.2.13) for classical flow is satisfied.

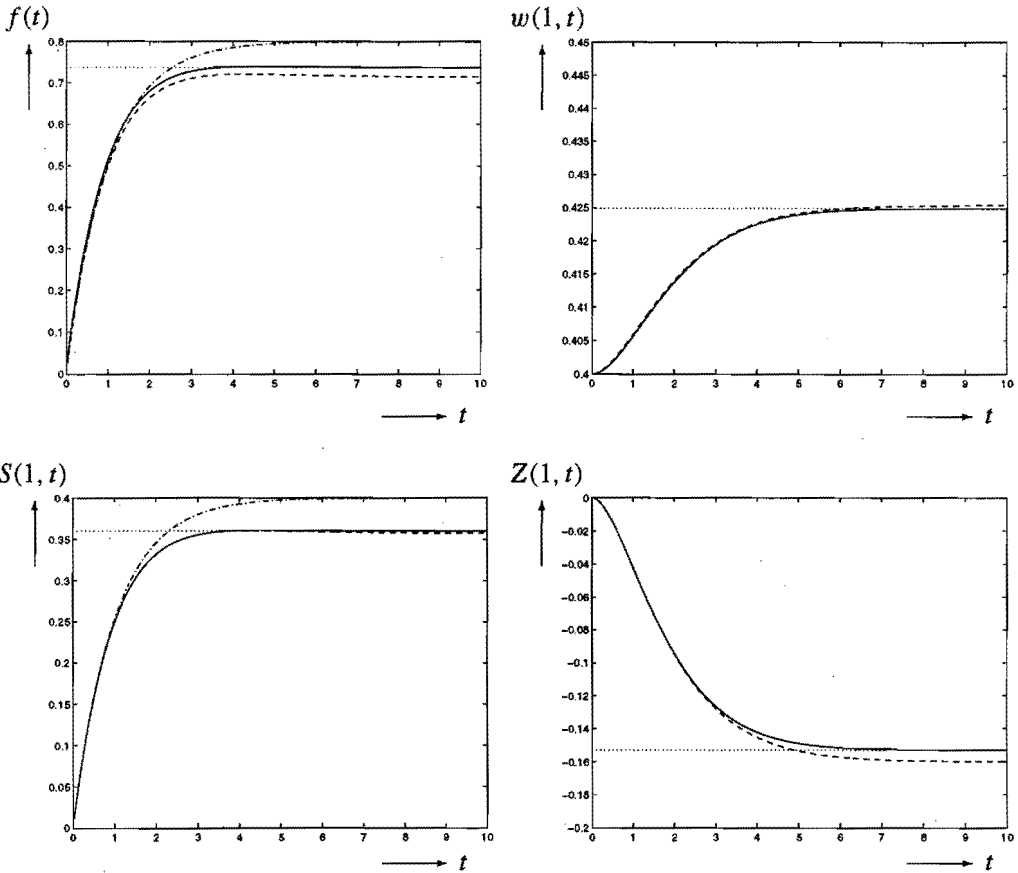


Figure 3.2 The pressure gradient $f(t)$, the velocity gradient $w(1, t)$, and the stresses $S(1, t)$ and $Z(1, t)$ as functions of time t , for $\varepsilon = 0.02$ and $Q(t) = \bar{Q} = 0.1$, $t \geq 0$, computed according to (3.3.1)-(3.3.3) with $\Delta t = 0.0005$ and $\Delta r = 0.0004$, and plotted as solid curves. The approximations $f_0(t)$ and $S_0(1, t)$ are plotted as dashed-dotted curves, and the approximations $f_1(t)$, $w_1(1, t)$, $S_1(1, t)$ and $Z_1(1, t)$ as dashed curves. The dotted lines correspond to the steady state values of Table 3.2.

To investigate supercritical flow ($\bar{Q} > \bar{Q}_{crit} = 0.1714$) for $\varepsilon = 0.02$, we take successively $\bar{Q} = 0.2$ and $\bar{Q} = 1.0$. In the Figures 3.3 and 3.4, the pressure gradient $f(t)$, the velocity gradient $w(1, t)$ at the wall, and the stresses $S(1, t)$ and $Z(1, t)$ at the wall are plotted as functions of time t , and the plots are drawn as solid curves. We observe for both flow rates that in the beginning $f(t)$ shows an overshoot. After sufficient time this overshoot disappears and

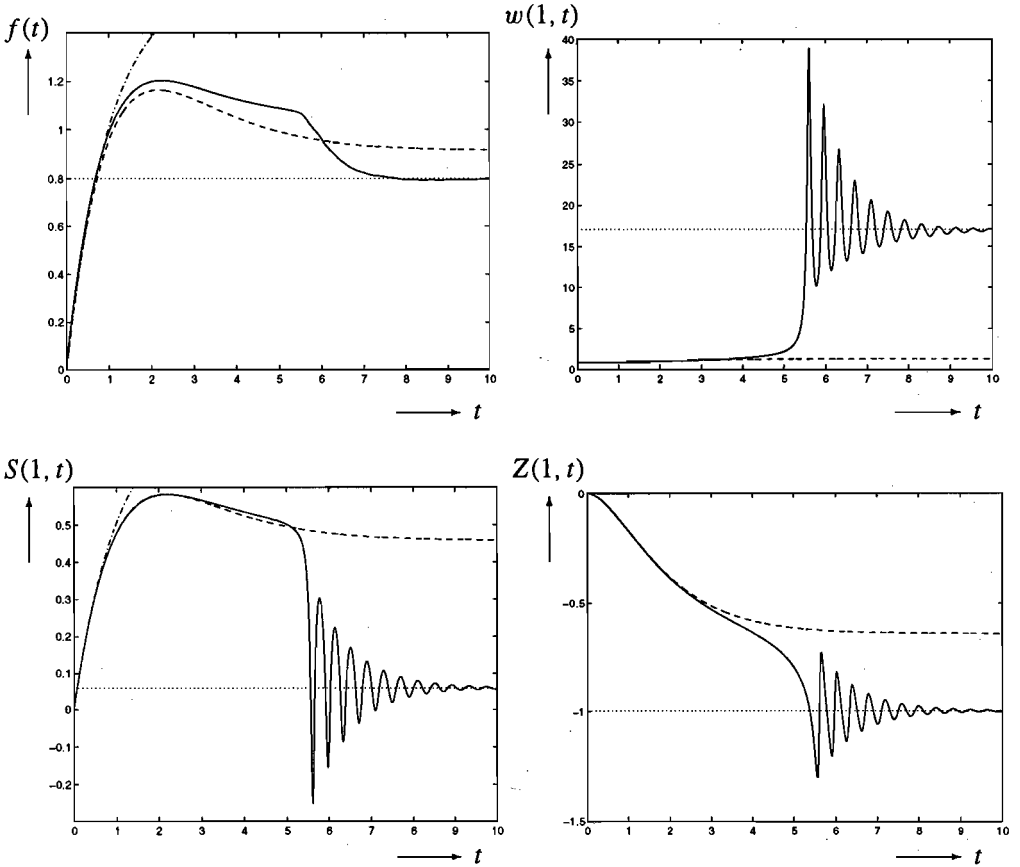


Figure 3.3 The pressure gradient $f(t)$, the velocity gradient $w(1, t)$, and the stresses $S(1, t)$ and $Z(1, t)$ as functions of time t , for $\varepsilon = 0.02$ and $Q(t) = \bar{Q} = 0.2$, $t \geq 0$, computed according to (3.3.1)-(3.3.3) with $\Delta t = 0.0005$ and $\Delta r = 0.0004$, and plotted as solid curves. The approximations $f_0(t)$ and $S_0(1, t)$ are plotted as dashed-dotted curves, and the approximations $f_1(t)$, $w_1(1, t)$, $S_1(1, t)$ and $Z_1(1, t)$ as dashed curves. The dotted lines correspond to the steady state values of Table 3.2.

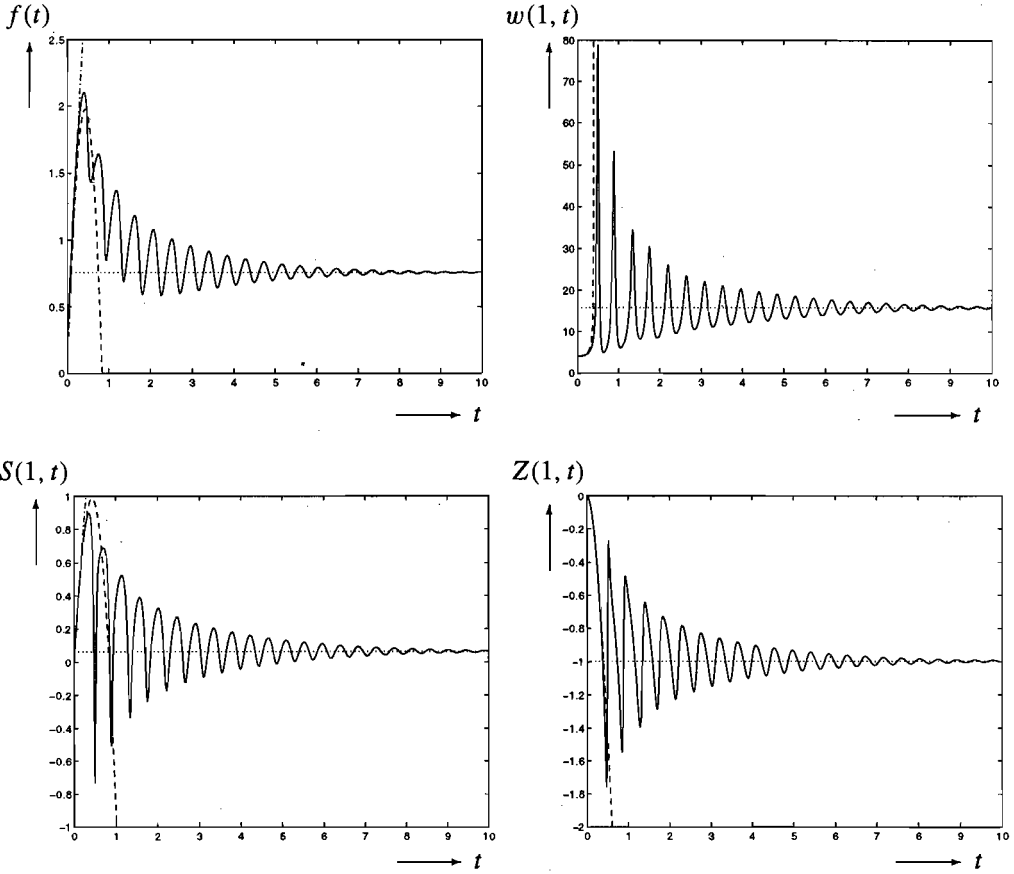


Figure 3.4 The pressure gradient $f(t)$, the velocity gradient $w(1, t)$, and the stresses $S(1, t)$ and $Z(1, t)$ as functions of time t , for $\varepsilon = 0.02$ and $Q(t) = \bar{Q} = 1.0$, $t \geq 0$, computed according to (3.3.1)-(3.3.3) with $\Delta t = 0.0005$ and $\Delta r = 0.0004$, and plotted as solid curves. The approximations $f_0(t)$ and $S_0(1, t)$ are plotted as dashed-dotted curves, and the approximations $f_1(t)$, $w_1(1, t)$, $S_1(1, t)$ and $Z_1(1, t)$ as dashed curves. The dotted lines correspond to the steady state values of Table 3.2.

\bar{Q}	\bar{f}	r^*	ω_-^*	ω_+^*	$\omega(1)$	$\bar{S}(1)$	$\bar{Z}(1)$
0.1	0.7369	-	-	-	0.4249	0.3599	-0.1530
0.2	0.8001	0.9946	0.4766	16.96	17.09	0.0583	-0.9966
1.0	0.7591	0.9346	0.4030	14.24	15.83	0.0629	-0.9960

Table 3.2 The computed steady state values \bar{f} , r^* , ω_-^* , ω_+^* , $\omega(1)$, $\bar{S}(1)$ and $\bar{Z}(1)$, for a flow driven by the constant volumetric flow rate $Q(t) = \bar{Q}$, $t \geq 0$, with $\bar{Q} = 0.1, 0.2$ and 1.0, for $\varepsilon = 0.02$.

oscillations in $w(1, t)$, $S(1, t)$ and $Z(1, t)$ appear. For $\bar{Q} = 1.0$, also $f(t)$ starts to oscillate. The numerical computations disclose that oscillations in $w(r, t)$, $S(r, t)$ and $Z(r, t)$ occur for each radial coordinate r . All these oscillations die out and after sufficient time a steady state is reached. From the numerical results that underlie Figures 3.3 and 3.4, we determine the steady state values \bar{f} , $\omega(1)$, $\bar{S}(1)$ and $\bar{Z}(1)$, as listed in Table 3.2. Again it has been checked that these values satisfy (3.2.3) and the steady state equation $\mathcal{F}(\omega(1)) = \bar{f}/2$. The computations for $\bar{Q} = 0.2$ and $\bar{Q} = 1.0$ reveal that both steady states show a discontinuous velocity gradient $\omega(r)$ with exactly one jump from $\omega_-^* < \omega_M$ to $\omega_+^* > \omega_m$ at some radial coordinate $r = r^*$. Furthermore, $\bar{S}(r)$ and $\bar{Z}(r)$ are also discontinuous at $r = r^*$. Recall that $\omega = \omega_-^*$ and $\omega = \omega_+^*$ are the smallest and largest solutions of the equation $\mathcal{F}(\omega) = r^* \bar{f}/2$. Then the values of r^* , ω_-^* and ω_+^* are found by numerical solution of equation (3.2.17), and the values computed are listed in Table 3.2. The functions $\bar{f} = f_{bottom}(\bar{Q})$ and $\bar{f} = f_{top}(\bar{Q})$ were introduced as the inverses of the functions (3.2.19) and (3.2.21). By a simple calculation we have $f_{bottom}(\bar{Q}) = 0.5696$, $f_{top}(\bar{Q}) = 1.0421$, for $\bar{Q} = 0.2$, so that $f_{bottom}(\bar{Q}) < \bar{f} < f_{top}(\bar{Q})$. It has been checked that the latter inequality also holds for $\bar{Q} = 1.0$. Hence, the two steady states for $\bar{Q} = 0.2$ and $\bar{Q} = 1.0$, correspond neither to top-jumping nor to bottom-jumping.

To investigate whether for $\varepsilon = 0.02$ and a given flow rate \bar{Q} the flow starting from rest reaches a steady state, we compute the transient flow for several flow rates, varying from $\bar{Q} = 0$ to $\bar{Q} = 5.0$. The result is that for all values of \bar{Q} considered, a steady state is reached. In Figure 3.5 the steady state pressure gradient \bar{f} attained is plotted versus the flow rate \bar{Q} , for $\varepsilon = 0.02$; the \bar{f} versus \bar{Q} curve (solid curve) is called the flow curve. The functions $\bar{f} = f_{clas}(\bar{Q})$, $\bar{f} = f_{bottom}(\bar{Q})$ and $\bar{f} = f_{top}(\bar{Q})$, which are the inverse functions of (3.2.13), (3.2.19) and (3.2.21), respectively, are represented by the dashed curves in Figure 3.5, and correspond to classical flow, bottom-jumping and top-jumping, respectively. We observe that for $0 \leq \bar{Q} \leq \bar{Q}_{crit}$, the flow curve coincides with the curve $\bar{f} = f_{clas}(\bar{Q})$, which demonstrates that the (subcritical) flow tends to a classical steady state. If the flow becomes supercritical ($\bar{Q} > \bar{Q}_{crit}$), the computations disclose that the steady state velocity gradient $\omega(r)$ is discontinuous at some radial coordinate $r = r^*$. The steady state pressure gradient \bar{f} attained satisfies $f_{bottom}(\bar{Q}) < \bar{f} < f_{top}(\bar{Q})$ for $\bar{Q} > \bar{Q}_{crit}$, implying that neither top-jumping nor bottom-jumping takes place. The flow curve shows a kink at $\bar{Q} = \bar{Q}_{crit}$ and is S-shaped, with a local maximum $\bar{f} = \bar{f}_{crit}$ at $\bar{Q} = \bar{Q}_{crit}$ and a local minimum $\bar{f} \approx 0.6423$ at $\bar{Q} \approx 0.35$. Furthermore, the flow curve tends to the curve $\bar{f} = f_{top}(\bar{Q})$ for \bar{Q} sufficiently large. In Figure 3.6 the thickness $1 - r^*$ of the spurt layer is plotted versus the flow rate \bar{Q} for supercritical flow, and $\varepsilon = 0.02$; the plot is drawn as a solid curve. The value of r^* follows either from the place of the discontinuity in the computed steady state velocity gradient $\omega(r)$, or, more ac-

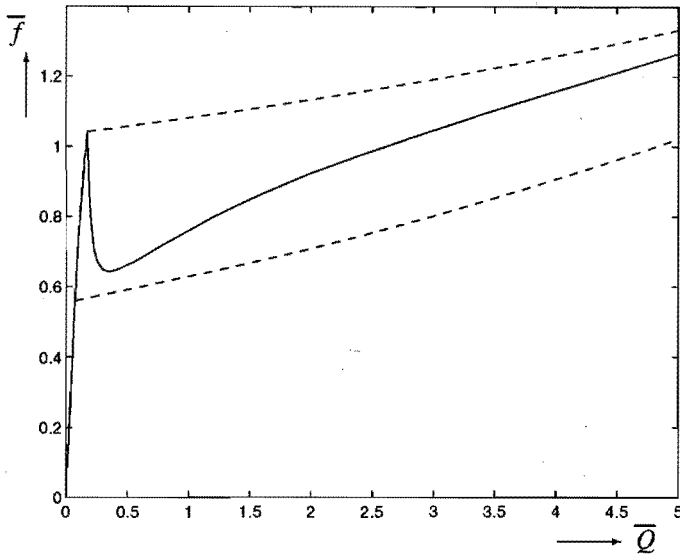


Figure 3.5 The flow curve of the steady state pressure gradient $\bar{f} = \lim_{t \rightarrow \infty} f(t)$ versus the volumetric flow rate \bar{Q} , for $\varepsilon = 0.02$, plotted as a solid curve. The dashed curves correspond to $\bar{f} = f_{clas}(\bar{Q})$ (classical flow), $\bar{f} = f_{bottom}(\bar{Q})$ (bottom-jumping) and $\bar{f} = f_{top}(\bar{Q})$ (top-jumping). The flow curve shows a kink at $\bar{Q} = \bar{Q}_{crit} = 0.1714$.

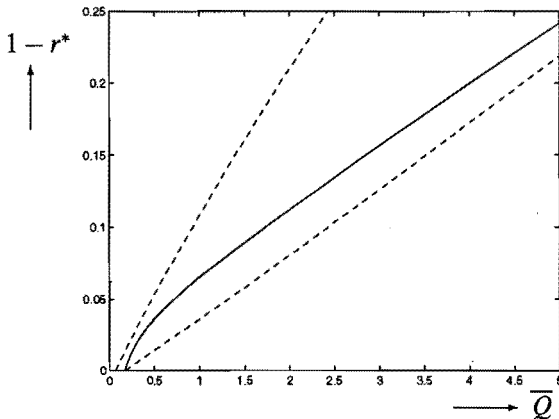


Figure 3.6 The thickness $1 - r^*$ of the spurt layer versus the volumetric flow rate \bar{Q} , for $\varepsilon = 0.02$ and $\bar{Q} > \bar{Q}_{crit} = 0.1714$ (supercritical flow), plotted as a solid curve. The dashed curves correspond to $1 - r^* = 1 - r_{bottom}^*(\bar{Q})$ (bottom-jumping) and $1 - r^* = 1 - r_{top}^*(\bar{Q})$ (top-jumping).

curately, by numerical solution of equation (3.2.17) with known \bar{Q} and \bar{f} . We observe that the spurt layer becomes thicker with increasing \bar{Q} . The functions $1 - r^* = 1 - r_{bottom}^*(\bar{Q})$ and $1 - r^* = 1 - r_{top}^*(\bar{Q})$ are represented by the dashed curves in Figure 3.6, and correspond to bottom-jumping and top-jumping, respectively.

One of the differences between supercritical transient flow ($\bar{Q} > \bar{Q}_{crit}$; see the Figures 3.3 and 3.4) and subcritical transient flow ($\bar{Q} < \bar{Q}_{crit}$; see Figure 3.2), concerns the occurrence of damped oscillations during the period in which the flow settles to a steady state. For $\bar{Q} = 0.2$ (see Figure 3.3) the oscillations in $f(t)$ are still negligible, but the oscillations in $S(1, t)$, $w(1, t)$ and $Z(1, t)$ are clearly visible. For $\bar{Q} = 1.0$ (see Figure 3.4) also the oscillations in $f(t)$ become manifest. The instant at which these oscillations start is preceded by a time phase in which $f(t)$, $w(1, t)$, $S(1, t)$ and $Z(1, t)$ behave smoothly in t . Therefore, in supercritical flow we distinguish two time phases, characterized as follows:

1. a so-called latency phase, $0 \leq t < t_s$, in which $w(r, t) = O(\varepsilon^0)$, $\varepsilon \rightarrow 0$, and $f(t)$, $w(r, t)$, $Z(r, t)$ and $S(r, t)$ are smooth functions of t ;
2. a so-called spurt phase, $t > t_s$, during which $w(r, t)$, $f(t)$, $S(r, t)$ and $Z(r, t)$ oscillate as functions of t .

The time $t = t_s$ is taken as the instant at which the normal stress difference $Z(1, t)$ at the wall assumes the value -1 for the first time. From the Figures 3.3 and 3.4 we observe that $Z = -1$ at $t = t_s$ indeed corresponds to the onset of oscillations.

We shall now derive some analytical approximations for the functions f , w , S and Z , that are valid during the latency phase, provided that $\varepsilon \ll 1$. During the latency phase $w(r, t) = O(\varepsilon^0)$, $\varepsilon \rightarrow 0$, holds for $0 \leq r \leq 1$. Neglecting the $O(\varepsilon)$ -terms, we put $\varepsilon = 0$ in the governing equations (3.1.32) to obtain the following system:

$$\begin{aligned} \frac{\partial S}{\partial t} &= -S + w(1 + Z), & \frac{\partial Z}{\partial t} &= -Z - wS, & 0 \leq r \leq 1, & t > 0, \\ S(r, t) &= rf(t)/2, & f(t) &= 8 \int_0^1 r^2 S(r, t) dr. \end{aligned} \quad (3.3.4)$$

Substitution of the third equation of (3.3.4) into the fourth equation yields an identity. Therefore, the fourth equation is omitted and replaced by the original equation (3.1.30) with $Q(t) = \bar{Q}$, viz.

$$\bar{Q} = \int_0^1 r^2 w(r, t) dr. \quad (3.3.5)$$

For $\varepsilon = 0$ the initial values (3.1.33) and (3.1.34) reduce to

$$S(r, 0) = 0, \quad Z(r, 0) = 0, \quad f(0) = 0, \quad w(r, 0) = 4\bar{Q}r, \quad 0 \leq r \leq 1. \quad (3.3.6)$$

Equations (3.3.4)^{1,3} are solved for S and w expressed in terms of f and Z , with the result

$$S(r, t) = \frac{1}{2}rf(t), \quad (3.3.7)$$

$$w(r, t) = \frac{r[f'(t) + f(t)]}{2[1 + Z(r, t)]}, \quad (3.3.8)$$

where $f'(t)$ is the derivative of $f(t)$. On substitution of (3.3.8) into (3.3.5), we find for $f(t)$ the differential equation

$$f'(t) + f(t) = 2\bar{Q} \left[\int_0^1 \frac{r^3}{1 + Z(r, t)} dr \right]^{-1}, \quad t > 0. \quad (3.3.9)$$

By use of (3.3.9), the solution (3.3.8) for $w(r, t)$ is rewritten as

$$w(r, t) = \frac{\bar{Q}r}{1 + Z(r, t)} \left[\int_0^1 \frac{y^3}{1 + Z(y, t)} dy \right]^{-1}. \quad (3.3.10)$$

Finally, by substitution of (3.3.7) and (3.3.10) into equation (3.3.4)², we find for $Z(r, t)$ the differential equation

$$\frac{\partial Z}{\partial t}(r, t) + Z(r, t) = -\frac{\bar{Q}r^2 f(t)}{2[1 + Z(r, t)]} \left[\int_0^1 \frac{y^3}{1 + Z(y, t)} dy \right]^{-1}, \quad (3.3.11)$$

valid for $0 \leq r \leq 1$, $t > 0$. Thus, the functions $f(t)$ and $Z(r, t)$ are found as solutions of the system of equations (3.3.9) and (3.3.11), subject to the initial conditions $f(0) = 0$ and $Z(r, 0) = 0$. Next, the functions $S(r, t)$ and $w(r, t)$ are given by (3.3.7) and (3.3.10), expressed in terms of f and Z .

The equations (3.3.9) and (3.3.11) are now solved by a kind of iteration procedure, leading to analytical approximations f_n and Z_n ($n = 0, 1$) for the functions f and Z . The corresponding approximations for the functions S and w are denoted by S_n and w_n , and are determined by (3.3.7) and (3.3.10). Since $|Z| \ll 1$ in the beginning of the latency phase (see e.g. Figure 3.3), we take $Z_0 = 0$ as zeroth approximation for the function Z . By putting $Z = Z_0 = 0$ in the right-hand side of (3.3.9), we find for f_0 the differential equation

$$f_0'(t) + f_0(t) = 8\bar{Q}, \quad t > 0, \quad (3.3.12)$$

with initial condition $f_0(0) = 0$. The solution for f_0 is given by

$$f_0(t) = 8\bar{Q}(1 - e^{-t}), \quad (3.3.13)$$

whereupon the approximations S_0 and w_0 follow as

$$S_0(r, t) = \frac{1}{2}rf_0(t) = 4\bar{Q}r(1 - e^{-t}), \quad w_0(r, t) = 4\bar{Q}r. \quad (3.3.14)$$

The next approximation Z_1 must satisfy the differential equation

$$\frac{\partial Z_1}{\partial t}(r, t) + Z_1(r, t) = -16\bar{Q}^2 r^2(1 - e^{-t}), \quad 0 \leq r \leq 1, \quad t > 0, \quad (3.3.15)$$

obtained from (3.3.11) by putting $f = f_0$ and $Z = Z_0 = 0$ in the right-hand side. The solution of (3.3.15) with initial value $Z_1(r, 0) = 0$ reads

$$Z_1(r, t) = -16\bar{Q}^2 r^2(1 - e^{-t} - te^{-t}) =: -r^2 z_1(t). \quad (3.3.16)$$

We now establish the auxiliary result

$$\left[\int_0^1 \frac{r^3}{1 + Z_1(r, t)} dr \right]^{-1} = \left[\int_0^1 r^3 [1 + r^2 z_1(t) + O(z_1^2)] dr \right]^{-1} \quad (3.3.17)$$

$$= 4 \left[1 - \frac{2}{3} z_1(t) + O(z_1^2) \right], \quad z_1 \rightarrow 0,$$

which is used in the right-hand sides of (3.3.9) and (3.3.10), whereby the $O(z_1^2)$ -terms are neglected. Thus we find from (3.3.10) that the approximation w_1 is given by

$$w_1(r, t) = \frac{4\bar{Q}r}{1 - r^2 z_1(t)} \left(1 - \frac{2}{3} z_1(t) \right) = \frac{4\bar{Q}r [1 - \frac{32}{3}\bar{Q}^2(1 - e^{-t} - te^{-t})]}{1 - 16\bar{Q}^2 r^2 (1 - e^{-t} - te^{-t})}. \quad (3.3.18)$$

From (3.3.9) we find that the approximation f_1 satisfies the differential equation

$$f_1'(t) + f_1(t) = 8\bar{Q} \left(1 - \frac{2}{3} z_1(t) \right) = 8\bar{Q} \left[1 - \frac{32}{3}\bar{Q}^2(1 - e^{-t} - te^{-t}) \right], \quad t > 0, \quad (3.3.19)$$

with initial condition $f_1(0) = 0$. The solution for f_1 is given by

$$f_1(t) = 8\bar{Q} \left[1 - e^{-t} - \frac{32}{3}\bar{Q}^2(1 - e^{-t} - te^{-t}) - \frac{1}{2}t^2 e^{-t} \right], \quad (3.3.20)$$

whereupon the approximation S_1 follows as

$$S_1(r, t) = \frac{1}{2} r f_1(t) = 4\bar{Q}r \left[1 - e^{-t} - \frac{32}{3}\bar{Q}^2(1 - e^{-t} - te^{-t}) - \frac{1}{2}t^2 e^{-t} \right]. \quad (3.3.21)$$

The approximations f_0 , f_1 , w_0 , w_1 , S_0 , S_1 and Z_1 are compared with the numerical solutions for f , w , S and Z , presented in the Figures 3.2-3.4 and in the Figures 3.7-3.9. In the Figures 3.2, 3.3 and 3.4, the approximations $f_0(t)$ and $S_0(1, t)$ are plotted as dashed-dotted curves, while $f_1(t)$, $w_1(1, t)$, $S_1(1, t)$ and $Z_1(1, t)$ are plotted as dashed curves, for $\bar{Q} = 0.1$, $\bar{Q} = 0.2$ and $\bar{Q} = 1.0$, respectively. In the Figures 3.7, 3.8 and 3.9, the calculated functions $S(r, t)$, $Z(r, t)$ and $w(r, t)$ are plotted as functions of the radial coordinate r at times $t = 1, 2, 3, 4$ and 5 , during the latency phase, for $\varepsilon = 0.02$ and $\bar{Q} = 0.2$; the plots are drawn as solid curves. Also in the Figures 3.7, 3.8 and 3.9, the approximations $S_1(r, t)$, $Z_1(r, t)$, $w_0(r, t)$ and $w_1(r, t)$ are plotted as functions of r at $t = 1, 2, 3, 4, 5$; the plots are drawn as dashed curves.

For $\varepsilon = 0.02$ and $\bar{Q} = 0.1$ (subcritical flow) we observe in Figure 3.2 that the approximations f_1 , w_1 , S_1 and Z_1 are very close to the numerical solutions for all $t \geq 0$. For $\bar{Q} = 0.2$, we observe in Figure 3.3 and in the Figures 3.7-3.9, that the approximations f_1 , w_1 , S_1 and Z_1 are rather close to the numerical solutions during the beginning $0 \leq t < t_0$ of the latency phase. Furthermore, the upper-left Figure 3.3 shows that the time $t = t_0$ at which the approximation f_1 for f starts to fail, corresponds to the time at which the derivative $f'(t)$ becomes zero. Using the approximation $f \approx f_1$, we find that $f_1'(t_0) = 0$ for $t_0 = \sqrt{3/4\bar{Q}}$; note that $t_0 = \sqrt{3/4\bar{Q}} = 2.165$ for $\bar{Q} = 0.2$. In Figure 3.3 we observe that $w_1(1, t)$ and $S_1(1, t)$ approximate $w(1, t)$ and $S(1, t)$ quite well even beyond $t = t_0$. For $\bar{Q} = 1.0$, we observe in

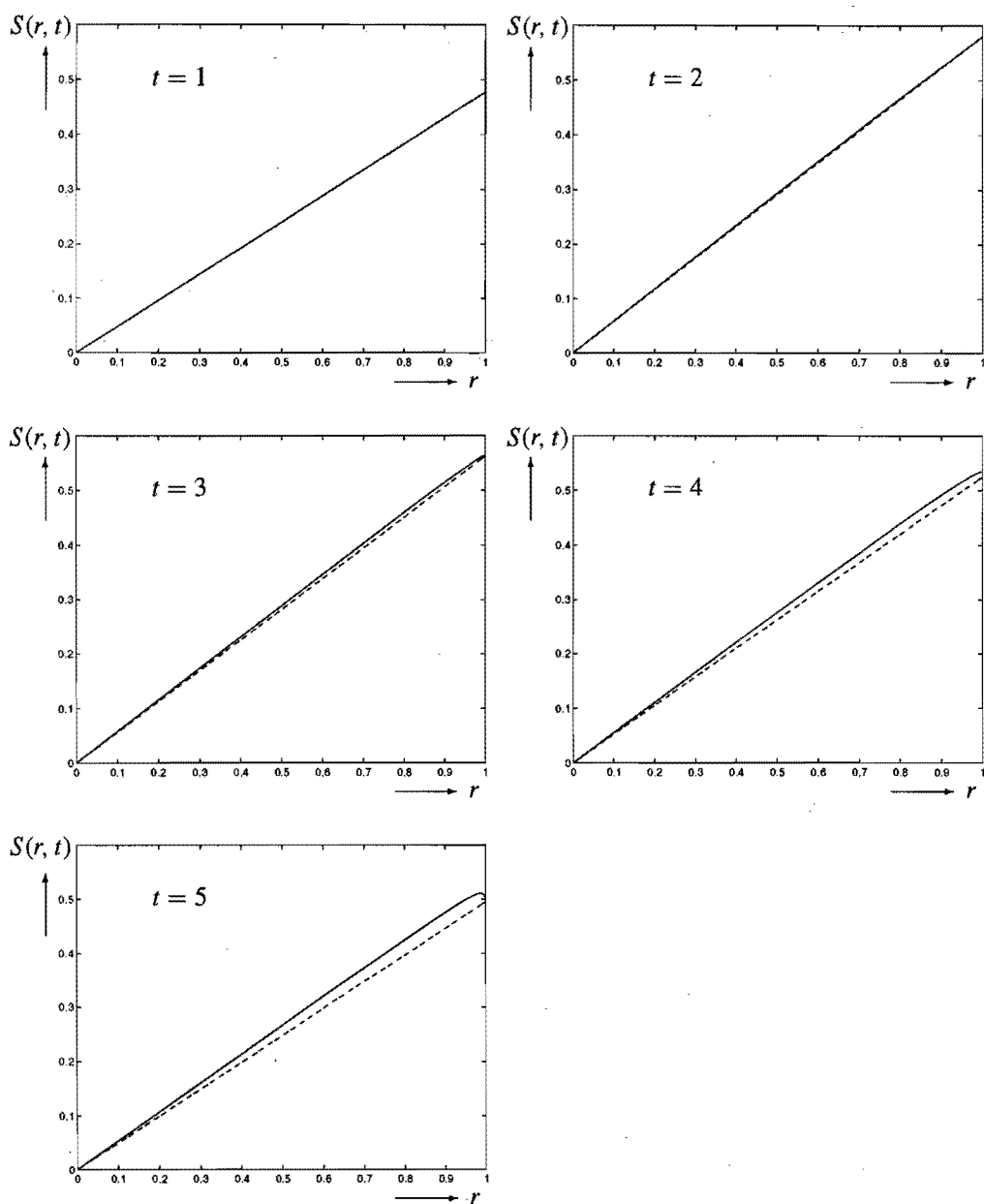


Figure 3.7 The stress $S(r, t)$ as function of the radial coordinate r at times $t = 1, 2, 3, 4$ and 5 , during the latency phase $0 \leq t < t_s \approx 5.4$, for $\varepsilon = 0.02$ and $\bar{Q} = 0.2$, plotted as solid curves. The approximation $S_1(r, t)$, given by (3.3.21), is plotted as a dashed curve.

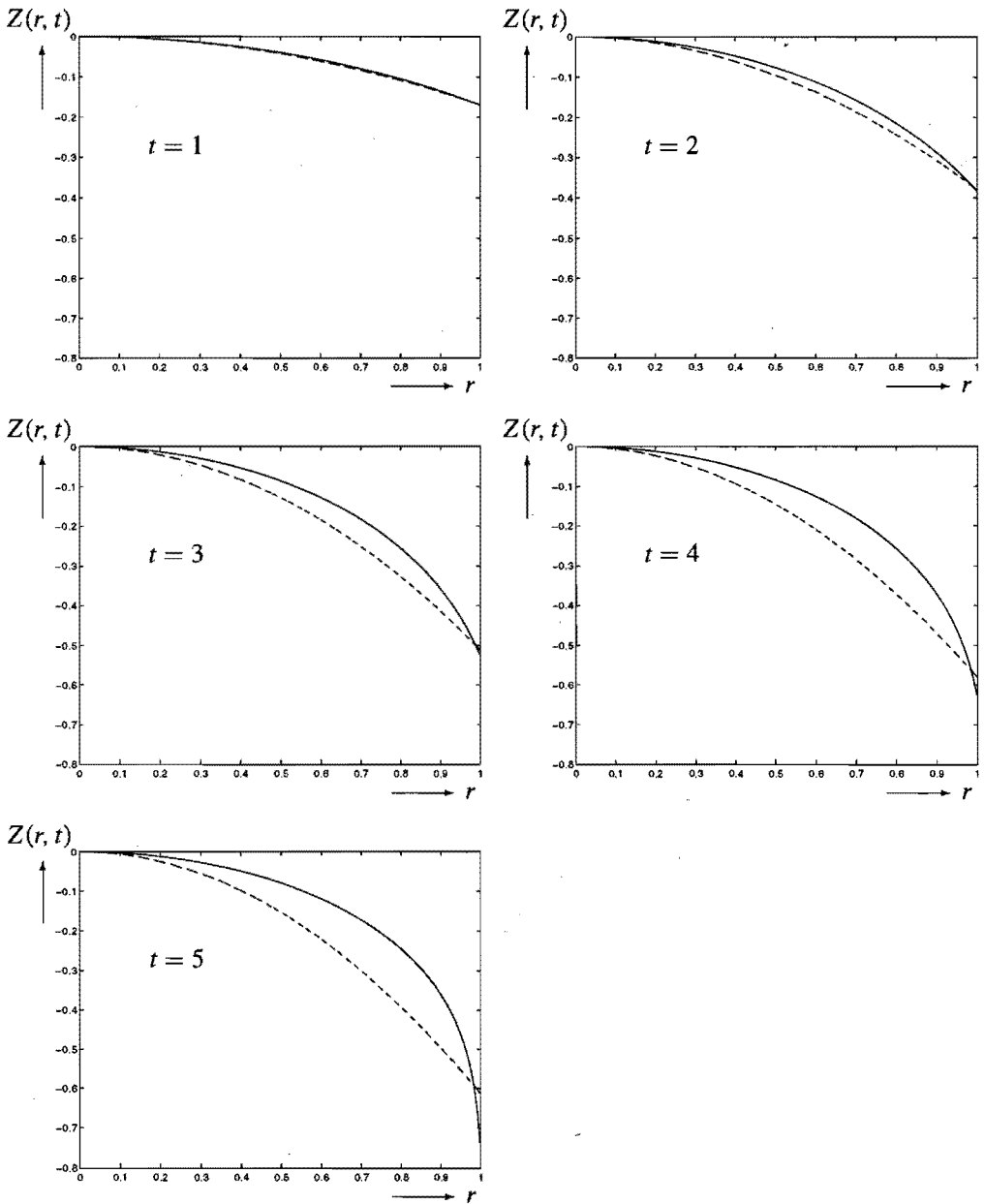


Figure 3.8 The stress difference $Z(r, t)$ as function of the radial coordinate r at times $t = 1, 2, 3, 4$ and 5 , during the latency phase $0 \leq t < t_s \approx 5.4$, for $\varepsilon = 0.02$ and $\bar{Q} = 0.2$, plotted as solid curves. The approximation $Z_1(r, t)$, given by (3.3.16), is plotted as a dashed curve.

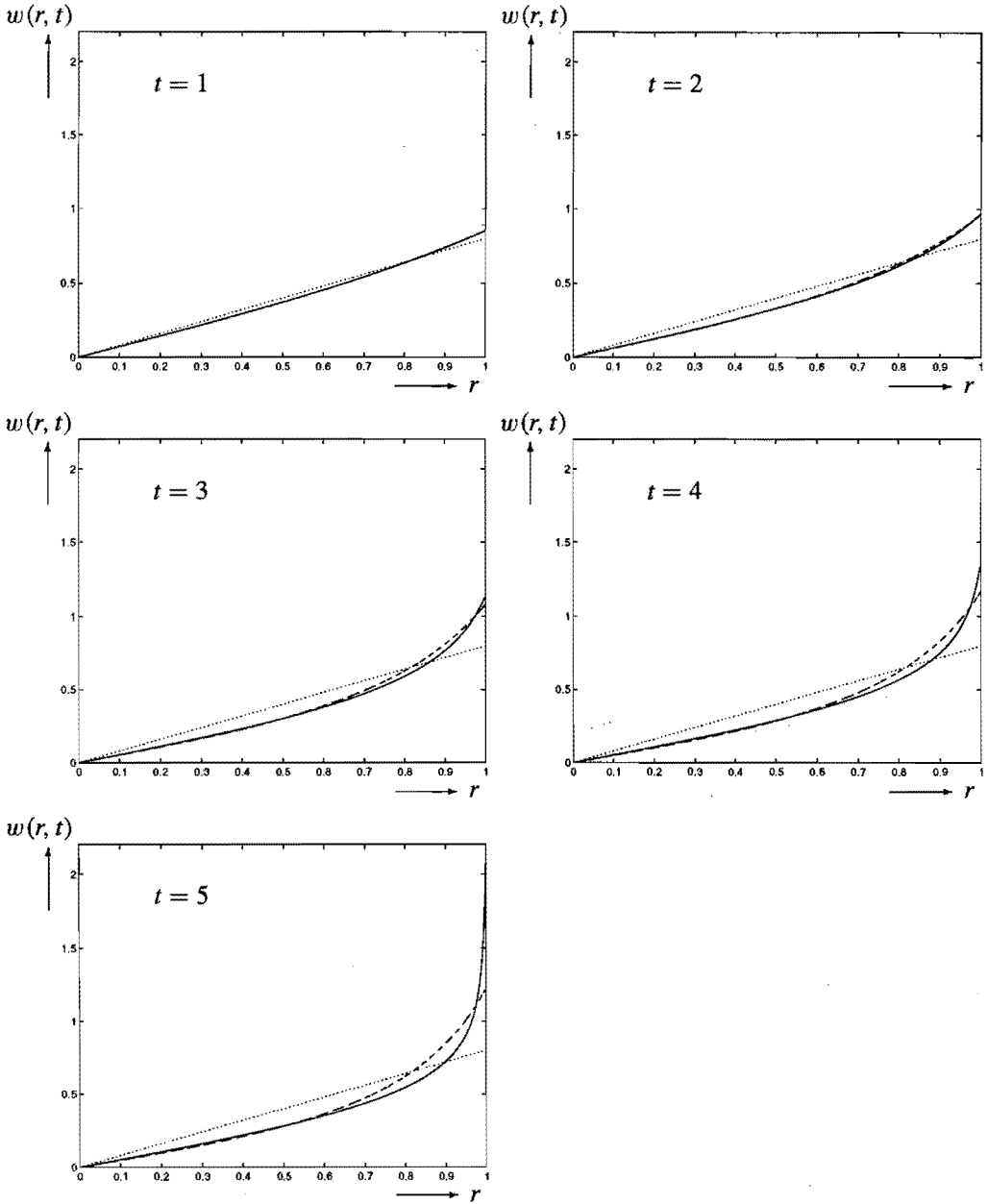


Figure 3.9 The velocity gradient $w(r, t)$ as function of the radial coordinate r at times $t = 1, 2, 3, 4$ and 5 , during the latency phase $0 \leq t < t_s \approx 5.4$, for $\varepsilon = 0.02$ and $\bar{Q} = 0.2$, plotted as solid curves. The approximations $w_0(r, t)$ and $w_1(r, t)$, given by (3.3.14)² and (3.3.18), are plotted as dotted and dashed curves, respectively.

Figure 3.4 that $Z_1(1, t)$ is rather close to the numerical solution $Z(1, t)$ during the whole latency phase $0 \leq t < t_s$. Using the approximation $Z \approx Z_1$ we find, by solving $Z_1(1, t_s) = -1$, that $t_s = 0.40$ for $\bar{Q} = 1.0$. We observe in Figure 3.4 that also the approximations $f_1(t)$, $w_1(1, t)$ and $S_1(1, t)$ are rather close to the numerical solutions for $f(t)$, $w(1, t)$ and $S(1, t)$, during the whole latency phase $0 \leq t < t_s$. Furthermore, at $t = t_s = 0.40$ the approximations f_1 , w_1 , S_1 and Z_1 start to fail, and oscillations appear.

Finally, we investigate the influence of the parameter ε on the transient flow behaviour and the steady state values attained. As we may infer from the previous analysis, the influence of ε on the transient flow behaviour during the latency phase is negligible, provided that $\varepsilon \ll 1$. During the spurt phase, however, the transient flow is clearly affected by the value of ε . For example, the dependence on ε of the steady state velocity gradient $\omega(r) = r\bar{f}/2\varepsilon + O(\varepsilon^0)$, $\varepsilon \rightarrow 0$, is striking. To demonstrate the influence of ε , we compute the transient flow for several values of the constant flow rate \bar{Q} , in the two cases $\varepsilon = 0.01$ and $\varepsilon = 0.005$, and we compare the numerical results to those obtained in the case $\varepsilon = 0.02$.

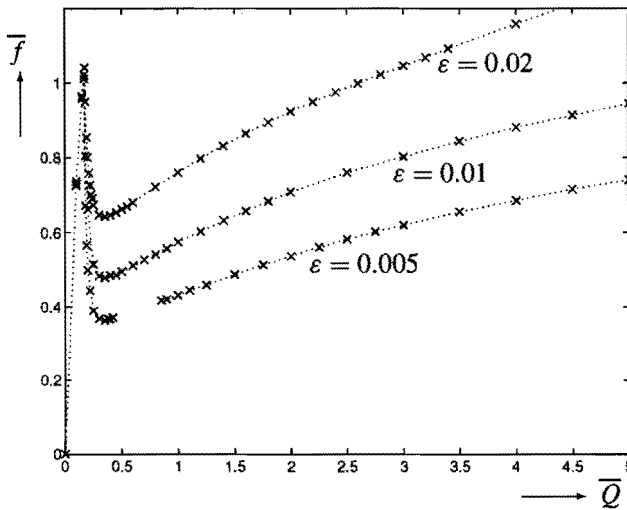


Figure 3.10 The flow curve of the steady state pressure gradient $\bar{f} = \lim_{t \rightarrow \infty} f(t)$ versus the volumetric flow rate \bar{Q} , for $\varepsilon = 0.02, 0.01$ and 0.005 . The points (\bar{Q}, \bar{f}) marked by the crosses (\times) correspond to computed steady states. The gap in the flow curve for $\varepsilon = 0.005$ corresponds to flow rates \bar{Q} for which persistent oscillations occur.

The numerical computations for $\varepsilon = 0.01$ disclose that the transient flow behaviour is similar to the flow behaviour observed when $\varepsilon = 0.02$. For $\bar{Q} < \bar{Q}_{crit} = 0.1690$ (see Table 3.1), it is found that the functions f , w , S and Z behave smoothly in time and after sufficient time a steady state is reached that is classical. For $\bar{Q} > \bar{Q}_{crit}$, damped oscillations occur and after sufficient time a steady state is reached. This steady state exhibits a discontinuous steady state velocity gradient $\omega(r)$ with exactly one jump from $\omega_-^* < \omega_M$ to $\omega_+^* > \omega_m$ at some radial

coordinate $r = r^*$. Also $\bar{S}(r)$ and $\bar{Z}(r)$ are discontinuous at $r = r^*$. In Figure 3.10 the flow curve of the steady state pressure gradient $\bar{f} = \lim_{t \rightarrow \infty} f(t)$ versus the volumetric flow rate \bar{Q} is plotted for $\varepsilon = 0.01$. The computed points (\bar{Q}, \bar{f}) are marked by a cross (\times). We observe that the flow curve for $\varepsilon = 0.01$ is S-shaped just like the flow curve for $\varepsilon = 0.02$ which has been included in Figure 3.10 (see also Figure 3.5). In Figure 3.11 the thickness $1 - r^*$ of the spurt layer is plotted versus the volumetric flow rate \bar{Q} , for $\varepsilon = 0.01$. The computed points $(\bar{Q}, 1 - r^*)$ are marked by a cross (\times). We observe that also for $\varepsilon = 0.01$ the spurt layer becomes thicker with increasing \bar{Q} .

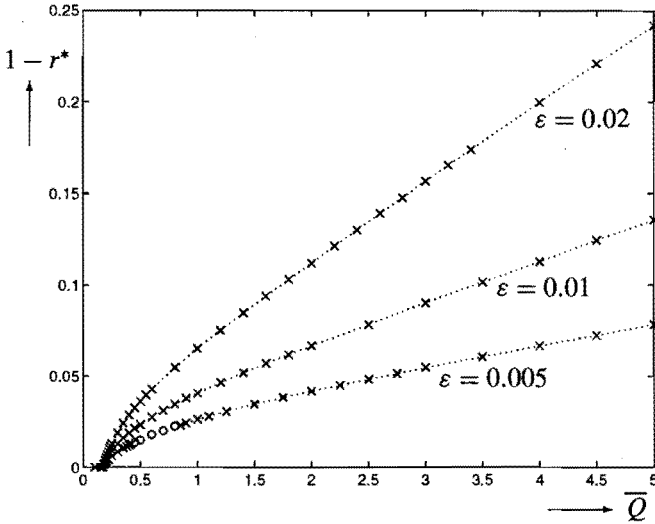


Figure 3.11 The thickness $1 - r^*$ of the spurt layer versus the volumetric flow rate \bar{Q} , for $\varepsilon = 0.02, 0.01$ and 0.005 . The points $(\bar{Q}, 1 - r^*)$ marked by the crosses (\times) correspond to computed steady states; the points $(\bar{Q}, 1 - r^*)$ marked by the dots (\circ) correspond to flows for which persistent oscillations occur.

For $\varepsilon = 0.005$, the transient flow behaviour is essentially different for a certain range of flow rates \bar{Q} . In Figure 3.12 the computed pressure gradient $f(t)$ is plotted as function of time t , for $\varepsilon = 0.005$ and $\bar{Q} = 0.1, 0.2, 0.6$ and 1.0 . We observe that for $\bar{Q} = 0.1 (< \bar{Q}_{crit} = 0.1678$ at $\varepsilon = 0.005$; see Table 3.1) $f(t)$ is a smooth increasing function of t and after sufficient time a steady state is attained with $\bar{f} = \lim_{t \rightarrow \infty} f(t) = 0.7248$. The computations disclose that the steady state variables $\omega(r)$, $\bar{S}(r)$ and $\bar{Z}(r)$ attained are continuous in r , implying that the steady state corresponds to classical flow. As a further check it has been verified that the relation (3.2.13) for classical flow is satisfied. For $\bar{Q} = 0.2 (> \bar{Q}_{crit})$, the pressure gradient $f(t)$ shows oscillations with a very small amplitude. The oscillations decay and after sufficient time a steady state is reached with $\bar{f} = 0.4991$. The computations reveal that the steady state variables $\omega(r)$, $\bar{S}(r)$ and $\bar{Z}(r)$ attained are discontinuous with one jump at $r = r^* = 0.9970$. The value of r^* has been determined by numerical solution of equation (3.2.17). For $\bar{Q} = 0.6$ and $\bar{Q} = 1.0$, the oscillations in $f(t)$ are clearly visible. For $\bar{Q} = 1.0$, we observe that the amplitude of the oscillation decays. The numerical computations show

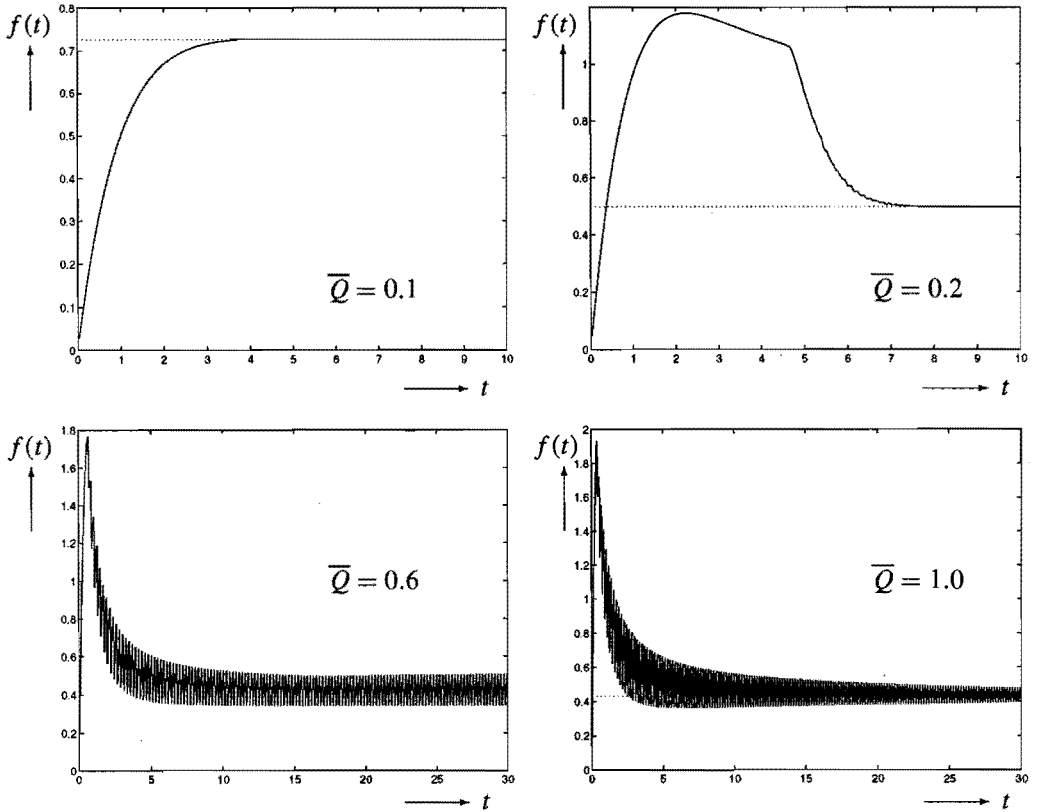


Figure 3.12 The pressure gradient $f(t)$ as function of time t , for $\varepsilon = 0.005$ and $Q(t) = \bar{Q}$, $t \geq 0$, with $\bar{Q} = 0.1, 0.2, 0.6$ and 1.0 , computed according to (3.3.1)-(3.3.3) with $\Delta t = 0.00025$ and $\Delta r = 0.0004$. The dotted lines correspond to the steady state pressure gradient $\bar{f} = \lim_{t \rightarrow \infty} f(t)$.

that the oscillations are sufficiently damped out at $t = 80$, and that a steady state is reached with $\bar{f} = 0.4316$ and a jump in $\omega(r)$ at $r = r^* = 0.9738$. Again, the latter value has been found by numerical solution of equation (3.2.17). For $\bar{Q} = 0.6$, however, we observe that the amplitude of the oscillations in $f(t)$ fails to decay and remains constant after a certain instant. We computed the transient flow up to $t = 320$, at which time the amplitude of the oscillations is still the same as at $t = 30$. Hence, for $\bar{Q} = 0.6$, the pressure gradient $f(t)$ does not settle to a stationary value within the time interval of computation, indicating that no steady state pressure gradient \bar{f} is attained. Instead, $f(t)$ shows so-called persistent oscillations about a certain value. The numerical computations for $\bar{Q} = 0.6$ reveal that persistent oscillations also appear in the velocity gradient $w(r, t)$, the stress $S(r, t)$ and the stress difference $Z(r, t)$ for each value of the radial coordinate r . These oscillations have a larger amplitude near the wall $r = 1$. Although no steady state is attained for $\bar{Q} = 0.6$, the computations show that the oscillating functions $w(r, t)$, $S(r, t)$ and $Z(r, t)$ tend to become discontinuous in r at some

radial coordinate $r = r^*$. Recalling the notation $r_k = k\Delta r$, we find that the plots of $w(r_k, t)$ and $w(r_{k+1}, t)$ start to deviate significantly after sufficient time, for a specific index k . Next, the value of r^* is taken as $r^* = (r_k + r_{k+1})/2$, which might be in error by at most $\Delta r/2$. In the computations for $\bar{Q} = 0.6$, the numerical discontinuity appears between $r_k = 0.9820$ and $r_{k+1} = 0.9824$, and we set $r^* = 0.9822$.

To establish for which \bar{Q} a steady state is attained (within the time interval of computation) when $\varepsilon = 0.005$, we compute the transient flow for several flow rates, varying from $\bar{Q} = 0$ to $\bar{Q} = 5.0$. The outcome of the computations is that a steady state is reached for $\bar{Q} \leq 0.42$ and for $\bar{Q} \geq 0.85$. This steady state is classical when $\bar{Q} \leq \bar{Q}_{crit} = 0.1678$, and corresponds to spurt flow when $\bar{Q}_{crit} < \bar{Q} \leq 0.42$ or $\bar{Q} \geq 0.85$. For values of \bar{Q} close to 0.42 or 0.85, the time interval within which the flow settles to a steady state, becomes very large. For $0.45 \leq \bar{Q} \leq 0.80$, however, the functions $f(t)$, $w(r, t)$, $S(r, t)$ and $Z(r, t)$ show persistent oscillations and fail to settle to stationary values within the time interval of computation. Thus, for $\varepsilon = 0.005$, four different flow regimes can be distinguished, corresponding to different ranges for the prescribed flow rate \bar{Q} . For $\bar{Q} > \bar{Q}_{crit}$ (supercritical flow), we find that the (steady state) velocity gradient is discontinuous at some radial coordinate $r = r^*$.

In Figure 3.10 the flow curve of the steady state pressure gradient $\bar{f} = \lim_{t \rightarrow \infty} f(t)$ versus the volumetric flow rate \bar{Q} is plotted for $\varepsilon = 0.005$. The computed points (\bar{Q}, \bar{f}) are marked by a cross (\times). We observe that the flow curve for $\varepsilon = 0.005$ is again S-shaped. Furthermore, we observe that for $\bar{Q} < \bar{Q}_{crit}$ the three flow curves for $\varepsilon = 0.02, 0.01$ and 0.005 almost coincide, whereas for $\bar{Q} > \bar{Q}_{crit}$ the flow curve for $\varepsilon = 0.005$ lies below the one for $\varepsilon = 0.01$, which in its turn lies below the flow curve for $\varepsilon = 0.02$. Hence, at a fixed supercritical flow rate $\bar{Q} > \bar{Q}_{crit}$, the steady state pressure gradient \bar{f} becomes smaller if ε is changed from $\varepsilon = 0.02$ to the smaller values $\varepsilon = 0.01$ or $\varepsilon = 0.005$. The gap in the flow curve for $\varepsilon = 0.005$ corresponds to flow rates \bar{Q} for which persistent oscillations occur and no steady state is attained. In Figure 3.11 the thickness $1 - r^*$ of the spurt layer is plotted versus the volumetric flow rate \bar{Q} , for $\varepsilon = 0.005$. In case the flow tends to a steady state the computed points $(\bar{Q}, 1 - r^*)$ are marked by a cross (\times); in case persistent oscillations occur the computed points $(\bar{Q}, 1 - r^*)$ are marked by a dot (\circ). We observe that also for $\varepsilon = 0.005$ the spurt layer becomes thicker with increasing \bar{Q} . On the other hand, at a fixed supercritical flow rate $\bar{Q} > \bar{Q}_{crit}$, the spurt layer becomes thinner if ε is changed from $\varepsilon = 0.02$ to the smaller values $\varepsilon = 0.01$ or $\varepsilon = 0.005$.

From the numerical results presented in this section we infer that a bounded range $\mathcal{R} = (\bar{Q}_m, \bar{Q}_M)$ of flow rates \bar{Q} exists, for which persistent oscillations occur and no steady state is attained. At $\bar{Q} = \bar{Q}_m$ and $\bar{Q} = \bar{Q}_M$, the transition from a steady state to a state of persistent oscillations and vice versa takes place. The size of \mathcal{R} depends on the value of ε : for $\varepsilon = 0.02$ and $\varepsilon = 0.01$, the range \mathcal{R} is empty, whereas for $\varepsilon = 0.005$, the range $\mathcal{R} = (\bar{Q}_m, \bar{Q}_M)$ is not empty and has transition points \bar{Q}_m between 0.42 and 0.45, and \bar{Q}_M between 0.80 and 0.85. In the next section we provide an explanation for the occurrence of persistent oscillations.

3.4 Stability analysis

In this section we provide an explanation for the occurrence of persistent oscillations, as observed in Section 3.3, by means of a linearized stability analysis of the steady state solution. It will turn out that the transient flow showing persistent oscillations corresponds precisely to the steady state solution being unstable. Likewise, if the transient flow tends to a steady state, then correspondingly the steady state solution is found to be stable. In Section 3.3 the range \mathcal{R} of flow rates \bar{Q} for which persistent oscillations occur, was found to depend on the parameter ε . In this section we further investigate the dependence of \mathcal{R} on ε by additional numerical computations of the transient flow.

From the results of Section 3.3 we infer that the prescribed flow rate $Q(t) = \bar{Q}$, $t \geq 0$, completely determines the transient flow behaviour. For $\bar{Q} > \bar{Q}_{crit}$, the transient flow is found to either tend to a spurt steady state or to show persistent oscillations. If a spurt steady state is attained, the numerical results yield the values of the steady state pressure gradient $\bar{f} = \lim_{t \rightarrow \infty} f(t)$ and of the steady state velocity gradient $\omega(r) = \lim_{t \rightarrow \infty} w(r, t)$. This velocity gradient is discontinuous with one jump from $\omega_-^* < \omega_M$ to $\omega_+^* > \omega_m$ at $r = r^* (< 1)$. The steady state values \bar{f} and r^* satisfy the relation (3.2.17), while $\omega(r)$ is the smallest or the largest solution of the steady state equation $\mathcal{F}(\omega(r)) = r\bar{f}/2$, dependent on whether $0 \leq r < r^*$ or $r^* < r \leq 1$, respectively. If persistent oscillations occur, however, no steady state is attained. In that case the velocity gradient $w(r, t)$, calculated at $r = r_k = k\Delta r$, is found to show after sufficient time a numerical discontinuity between r_k and r_{k+1} for some specific index k . By taking $r^* = (r_k + r_{k+1})/2$, we assign a value to the radial coordinate r^* at which $w(r, t)$ is discontinuous. The fictitious steady state solution corresponding to persistent oscillations, is then determined as follows: the fictitious steady state pressure gradient \bar{f} is determined from \bar{Q} and r^* such that (3.2.17) is satisfied, while the fictitious steady state velocity gradient $\omega(r)$ is the smallest or the largest root of $\mathcal{F}(\omega(r)) = r\bar{f}/2$, dependent on whether $0 \leq r < r^*$ or $r^* < r \leq 1$, respectively. Thus, in case of a spurt steady state as well as in case of persistent oscillations, the (fictitious) steady state solution satisfies the equations of Section 3.2.

We now proceed with the stability analysis of the (fictitious) steady state solution. Analogous to Malkus et al. [36, Sec. 5], we consider the solution of the system (3.1.32) to consist of a stationary part plus a dynamic part:

$$\begin{aligned} f(t) &= \bar{f} + \varphi(t), & w(r, t) &= \omega(r) + \xi(r, t), \\ S(r, t) &= \bar{S}(r) + X(r, t), & Z(r, t) &= \bar{Z}(r) + Y(r, t), \end{aligned} \quad (3.4.1)$$

where φ , ξ , X and Y are dynamic perturbations. Substitution of (3.4.1) into (3.1.32) yields, with the use of (3.2.2),

$$\begin{aligned} \varepsilon \xi(r, t) + X(r, t) &= \frac{1}{2} r \varphi(t), & \varphi(t) &= 8 \int_0^1 r^2 X(r, t) dr, \\ \frac{\partial X}{\partial t} &= -X + (1 + \bar{Z})\xi + \omega Y + \xi Y, & \frac{\partial Y}{\partial t} &= -Y - \bar{S}\xi - \omega X - \xi X. \end{aligned} \quad (3.4.2)$$

Eliminating ξ by means of (3.4.2)¹, we obtain the following two ordinary differential equations for X and Y :

$$\begin{pmatrix} \frac{\partial X}{\partial t} \\ \frac{\partial Y}{\partial t} \end{pmatrix} = \begin{pmatrix} -1 - \frac{1 + \bar{Z}}{\varepsilon} & \omega \\ \frac{\bar{S}}{\varepsilon} - \omega & -1 \end{pmatrix} \begin{pmatrix} X \\ Y \end{pmatrix} + \frac{r\varphi}{2\varepsilon} \begin{pmatrix} 1 + \bar{Z} \\ -\bar{S} \end{pmatrix} + \frac{r\varphi/2 - X}{\varepsilon} \begin{pmatrix} Y \\ -X \end{pmatrix}. \quad (3.4.3)$$

Expressing \bar{S} and \bar{Z} in terms of ω according to (3.2.3), we rewrite (3.4.3) as

$$\frac{\partial}{\partial t} \begin{pmatrix} X(r, t) \\ Y(r, t) \end{pmatrix} = \mathcal{A}(\omega(r)) \begin{pmatrix} X(r, t) \\ Y(r, t) \end{pmatrix} + \frac{r\varphi(t)}{2\varepsilon} \mathbf{a}(\omega(r)) + \mathbf{G}(X, Y, \varphi), \quad (3.4.4)$$

where the matrix \mathcal{A} and the vector \mathbf{a} are given by

$$\mathcal{A}(\omega) = \begin{pmatrix} -1 - \frac{1}{\varepsilon(1 + \omega^2)} & \omega \\ \frac{\omega}{\varepsilon(1 + \omega^2)} - \omega & -1 \end{pmatrix}, \quad \mathbf{a}(\omega) = \begin{pmatrix} \frac{1}{1 + \omega^2} \\ \frac{\omega}{-1 + \omega^2} \end{pmatrix}, \quad (3.4.5)$$

and the vector \mathbf{G} consists of terms of second order in the perturbations.

Next, we consider the linearized form of the system of equations (3.4.4) and (3.4.2)². In order to determine the stability properties of the solution of the linearized system, we look for a non-trivial solution of the form

$$X(r, t) = \bar{X}(r)e^{zt}, \quad Y(r, t) = \bar{Y}(r)e^{zt}, \quad \varphi(t) = \bar{\varphi}e^{zt}, \quad (3.4.6)$$

where z is the eigenvalue parameter. Substitution of (3.4.6) into (3.4.4) with $\mathbf{G} = \mathbf{0}$ yields

$$z \begin{pmatrix} \bar{X} \\ \bar{Y} \end{pmatrix} = \mathcal{A} \begin{pmatrix} \bar{X} \\ \bar{Y} \end{pmatrix} + \frac{r\bar{\varphi}}{2\varepsilon} \mathbf{a}, \quad (3.4.7)$$

while substitution of (3.4.6) into (3.4.2)² leads to

$$\bar{\varphi} = 8 \int_0^1 r^2 \bar{X}(r) dr. \quad (3.4.8)$$

Provided that the matrix $zI - \mathcal{A}$ is non-singular, the solution of (3.4.7) expressed in terms of $\bar{\varphi}$ reads

$$\bar{X}(r) = ra(r, z)\bar{\varphi}/2, \quad \bar{Y}(r) = rb(r, z)\bar{\varphi}/2, \quad (3.4.9)$$

where the functions a and b are given by

$$a(r, z) = \frac{z + 1 - \omega^2(r)}{(z + 1)(1 + \varepsilon(z + 1)) - (1 - \varepsilon - \varepsilon(z + 1)^2)\omega^2(r) + \varepsilon\omega^4(r)}, \quad (3.4.10)$$

$$b(r, z) = -\frac{(z + 2)\omega(r)}{(z + 1)(1 + \varepsilon(z + 1)) - (1 - \varepsilon - \varepsilon(z + 1)^2)\omega^2(r) + \varepsilon\omega^4(r)}. \quad (3.4.11)$$

Finally, by using (3.4.9)¹ in (3.4.8) we are led to the eigenvalue equation

$$1 = 4 \int_0^1 a(r, z) r^3 dr. \quad (3.4.12)$$

Changing in the integral the variable of integration from r to ω by writing $r = 2\mathcal{F}(\omega)/\bar{f}$, we transform equation (3.4.12) into

$$\Phi(z, \bar{Q}) := 1 - \frac{64}{\bar{f}^4} \left(\int_0^{\omega_*} + \int_{\omega_*}^{\omega_{wall}} \right) \bar{a}(\omega, z) \mathcal{F}^3(\omega) \mathcal{F}'(\omega) d\omega = 0, \quad (3.4.13)$$

where $\bar{a}(\omega(r), z) := a(r, z)$. Hence, for the steady state solution determined by \bar{Q} , the eigenvalues z are the roots of equation (3.4.13). Analogous to the stability theory of ordinary differential equations, the following stability criteria apply: The steady state solution is unstable if there is at least one eigenvalue z with a positive real part ($\text{Re } z > 0$), whereas the steady state solution is stable if all eigenvalues z have a negative real part ($\text{Re } z < 0$).

To find the eigenvalues z we set $z = x + iy$ with $x, y \in \mathbb{R}$ in (3.4.13), and solve numerically

$$\text{Re} \{ \Phi(x + iy, \bar{Q}) \} = 0, \quad \text{Im} \{ \Phi(x + iy, \bar{Q}) \} = 0, \quad (3.4.14)$$

by means of a program package for solving nonlinear equations. Since $\Phi(\bar{z}, \bar{Q}) = \overline{\Phi(z, \bar{Q})}$, the eigenvalues are either real or appear as complex conjugate pairs. The numerical computations reveal that, for the range of flow rates \bar{Q} we explored, equation (3.4.13) has three eigenvalues z : one real eigenvalue $z = x_0 < 0$, and two complex conjugate eigenvalues $z = z_0^\pm := \lambda_0 \pm i\Omega$.

In Table 3.3 the computed eigenvalues $z = x_0$ and $z = z_0^\pm = \lambda_0 \pm i\Omega$ are presented for flows driven by a constant flow rate \bar{Q} , varying from $\bar{Q} = 0.18 > \bar{Q}_{crit}$ to $\bar{Q} = 5.0$, in case $\varepsilon = 0.02$. In this table also the radial coordinate r^* at which the steady state velocity gradient $\omega(r)$ is discontinuous, and the steady state pressure gradient $\bar{f} = \lim_{t \rightarrow \infty} f(t)$ are listed; cf. Figures 3.5 and 3.6. We observe that all eigenvalues have a negative real part ($x_0 < 0$ and $\text{Re } z_0^\pm < 0$). Hence, the steady state solution is stable for each value of \bar{Q} . This stability result corresponds precisely to the result of Section 3.3, where we found that for $\varepsilon = 0.02$ the transient flow shows damped oscillations and tends to a steady state for each value of \bar{Q} .

Similarly, we have calculated the three eigenvalues $z = x_0$ and $z = z_0^\pm = \lambda_0 \pm i\Omega$ for flows driven by a constant flow rate \bar{Q} , for several values of \bar{Q} , in case $\varepsilon = 0.01$. The calculations (of which no details are given here) disclose that all eigenvalues have a negative real part ($x_0 < 0$ and $\text{Re } z_0^\pm < 0$). Hence, the steady state solution is stable for each flow rate \bar{Q} considered. Again there is agreement with the result of Section 3.3, where we found that for $\varepsilon = 0.01$ the transient flow shows damped oscillations and tends to a steady state for each value of \bar{Q} .

\bar{Q}	r^*	\bar{f}	x_0	z_0^\pm
0.18	0.9982	0.9496	-0.750	$-1.147 \pm 0.353i$
0.20	0.9946	0.8001	-2.151	$-1.004 \pm 15.531i$
0.25	0.9870	0.6736	-4.289	$-0.723 \pm 10.981i$
0.30	0.9810	0.6478	-5.889	$-0.493 \pm 9.993i$
0.35	0.9758	0.6423	-7.061	$-0.376 \pm 9.854i$
0.40	0.9714	0.6462	-7.891	$-0.340 \pm 10.094i$
0.50	0.9638	0.6619	-9.137	$-0.346 \pm 10.083i$
0.60	0.9570	0.6801	-10.156	$-0.381 \pm 11.588i$
0.80	0.9454	0.7214	-11.740	$-0.475 \pm 13.114i$
1.00	0.9346	0.7591	-13.154	$-0.560 \pm 14.397i$
2.00	0.8882	0.9230	-18.417	$-0.870 \pm 19.440i$
3.00	0.8434	1.0456	-22.586	$-0.992 \pm 23.001i$
4.00	0.8002	1.1572	-25.744	$-1.023 \pm 26.148i$
5.00	0.7582	1.2659	-28.050	$-1.026 \pm 29.136i$

Table 3.3 The computed eigenvalues $z = x_0$ and $z = z_0^\pm$, which are the roots of the eigenvalue equation $\Phi(z, \bar{Q}) = 0$, for flows driven by a constant flow rate $Q(t) = \bar{Q}$, $t \geq 0$, and $\varepsilon = 0.02$. The radial coordinate r^* signifies the position of the discontinuity in the steady state velocity gradient $\omega(r)$, and $\bar{f} = \lim_{t \rightarrow \infty} f(t)$ is the steady state pressure gradient.

In Table 3.4 the computed eigenvalues $z = x_0$ and $z = z_0^\pm = \lambda_0 \pm i\Omega$ are presented for flows driven by a constant flow rate \bar{Q} , varying from $\bar{Q} = 0.18 > \bar{Q}_{crit}$ to $\bar{Q} = 5.0$, and $\varepsilon = 0.005$. In case a steady state is attained, also the radial coordinate r^* at which the steady state velocity gradient $\omega(r)$ is discontinuous, and the steady state pressure gradient $\lim_{t \rightarrow \infty} f(t) = \bar{f}$ are listed in Table 3.4. In case persistent oscillations occur, however, only the radial coordinate r^* at which the velocity gradient $w(r, t)$ shows a numerical discontinuity is listed in Table 3.4. The numerical values of \bar{f} and r^* versus \bar{Q} are in accordance with Figures 3.10 and 3.11. We observe that for $\bar{Q} \leq 0.42$ and $\bar{Q} \geq 0.85$ all eigenvalues have a negative real part ($x_0 < 0$ and $\text{Re } z_0^\pm < 0$), whereas for $0.45 \leq \bar{Q} \leq 0.80$ the eigenvalues $z = z_0^\pm$ have a positive real part ($\text{Re } z_0^\pm > 0$). Hence, the steady state solution is stable for $0 \leq \bar{Q} \leq 0.42$ and $\bar{Q} \geq 0.85$, whereas the (fictitious) steady state solution is unstable for $0.45 \leq \bar{Q} \leq 0.80$. For comparison we quote the result of Section 3.3 in case $\varepsilon = 0.005$: The transient flow shows damped oscillations and tends to a steady state for $0 \leq \bar{Q} \leq 0.42$ and $\bar{Q} \geq 0.85$, whereas persistent oscillations occur and no steady state is attained for $0.45 \leq \bar{Q} \leq 0.80$. Thus we conclude that stability of the steady state solution corresponds precisely to the transient flow tending to a steady state, whereas instability of the steady state solution agrees with the occurrence of persistent oscillations. The gap in the flow curve of Figure 3.10 and the dots (\circ) in Figure 3.11 correspond to steady state solutions that are unstable.

The transition from a spurt steady state to a state of persistent oscillations and vice versa takes place at the flow rates $\bar{Q} = \bar{Q}_m$ and $\bar{Q} = \bar{Q}_M$. Using the results of the linearized stability analysis, we now determine \bar{Q}_m and \bar{Q}_M as the flow rates at which the transition from a stable steady state solution to an unstable fictitious steady state solution and vice versa takes

\bar{Q}	r^*	\bar{f}	x_0	z_0^\pm
0.18	0.9986	0.6717	-2.084	$-1.024 \pm 62.440i$
0.20	0.9970	0.4991	-3.554	$-0.947 \pm 43.220i$
0.25	0.9938	0.3894	-6.844	$-0.590 \pm 29.664i$
0.30	0.9914	0.3673	-9.343	$-0.284 \pm 26.693i$
0.35	0.9894	0.3621	-11.260	$-0.096 \pm 26.035i$
0.40	0.9878	0.3651	-12.612	$-0.024 \pm 26.538i$
0.42	0.9874	0.3702	-12.856	$-0.047 \pm 27.251i$
0.45	0.9862	-	-13.938	$0.038 \pm 26.965i$
0.50	0.9650	-	-14.790	$0.022 \pm 28.091i$
0.60	0.9822	-	-16.939	$0.059 \pm 29.245i$
0.70	0.9802	-	-18.406	$0.012 \pm 31.137i$
0.80	0.9778	-	-19.990	$0.002 \pm 32.338i$
0.85	0.9770	0.4174	-20.475	$-0.053 \pm 33.636i$
0.90	0.9758	0.4209	-21.341	$-0.055 \pm 34.089i$
1.00	0.9738	0.4316	-22.699	$-0.090 \pm 35.418i$
1.50	0.9654	0.4871	-28.139	$-0.308 \pm 41.934i$
2.00	0.9582	0.5366	-32.606	$-0.514 \pm 47.517i$
3.00	0.9454	0.6197	-40.151	$-0.840 \pm 56.672i$
4.00	0.9334	0.6852	-46.825	$-0.993 \pm 63.830i$
5.00	0.9218	0.7395	-52.920	$-1.020 \pm 69.688i$

Table 3.4 The computed eigenvalues $z = x_0$ and $z = z_0^\pm$, which are the roots of the eigenvalue equation $\Phi(z, \bar{Q}) = 0$, for flows driven by a constant flow rate $Q(t) = \bar{Q}$, $t \geq 0$, and $\varepsilon = 0.005$. The radial coordinate r^* signifies the position of the discontinuity in the (steady state) velocity gradient, and $\bar{f} = \lim_{t \rightarrow \infty} f(t)$ is the steady state pressure gradient.

place. That is, we estimate by numerical computations of the transient flow for several flow rates \bar{Q} , the radial coordinate r^* at which the (steady state) velocity gradient shows a numerical discontinuity. Subsequently, we calculate \bar{Q}_m and \bar{Q}_M as the values of \bar{Q} for which the eigenvalue equation $\Phi(z, \bar{Q}) = 0$ has two purely imaginary roots $z = \pm i\Omega$. In this way we find that $\bar{Q}_m \approx 0.43$ and $\bar{Q}_M \approx 0.82$, if $\varepsilon = 0.005$.

The range \mathcal{R} of flow rates \bar{Q} for which persistent oscillations occur depends on the parameter ε . We have computed the transient flow for a set of input parameters (ε, \bar{Q}) . From the transient flow behaviour we estimate, for given ε , the range $\mathcal{R} = (\bar{Q}_m, \bar{Q}_M)$ for which persistent oscillations occur. Subsequently, we use the linearized stability analysis to determine $\bar{Q} = \bar{Q}_m$ and $\bar{Q} = \bar{Q}_M$ as the values of \bar{Q} for which the eigenvalue equation $\Phi(z, \bar{Q}) = 0$ has two purely imaginary roots $z = \pm i\Omega$. In Figure 3.13 the range \mathcal{R} obtained is plotted for $\varepsilon = 0.006, 0.005, 0.004, 0.003, 0.002$ and 0.001 . The dotted curve corresponds to $\bar{Q} = \bar{Q}_{crit}$, and the transition points \bar{Q}_m and \bar{Q}_M of \mathcal{R} are marked by dots (\circ). The dots lie on the boundary of a region in the (ε, \bar{Q}) -plane. For parameters (ε, \bar{Q}) inside this region the flow shows persistent oscillations, whereas for (ε, \bar{Q}) outside this region the flow tends to a (stable) steady state. We observe that $\bar{Q}_m \approx 0.4$, whereas \bar{Q}_M strongly depends on ε . Further-

more, \mathcal{R} becomes smaller with increasing ε . The numerical computations reveal that $\mathcal{R} = \emptyset$, for $\varepsilon = 0.007$. Hence, a critical value ε_{crit} exists below which persistent oscillations may occur. In conclusion, if $\varepsilon \geq \varepsilon_{crit} = 0.007$, the flow driven by a constant flow rate \bar{Q} tends to a steady state for each value of \bar{Q} ; if $\varepsilon < \varepsilon_{crit} = 0.007$, the flow tends to a steady state if $\bar{Q} \notin \mathcal{R}$, whereas the flow shows persistent oscillations if $\bar{Q} \in \mathcal{R}$.

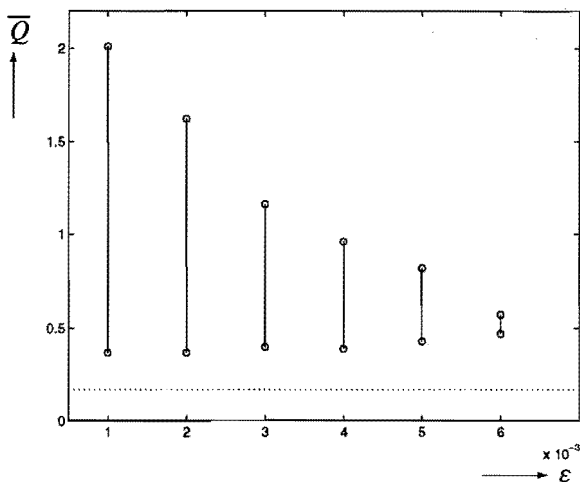


Figure 3.13 The range $\mathcal{R} = (\bar{Q}_m, \bar{Q}_M)$ of flow rates \bar{Q} for which persistent oscillations occur, for $\varepsilon = 0.001, 0.002, 0.003, 0.004, 0.005$ and 0.006 ; $\mathcal{R} = \emptyset$ for $\varepsilon = 0.007$. The transition points $\bar{Q} = \bar{Q}_m$ and $\bar{Q} = \bar{Q}_M$ are marked by a dot (\circ). The dotted curve corresponds to $\bar{Q} = \bar{Q}_{crit}$.

3.5 Conclusions

Stability analysis and numerical calculations have been used to analyze the flow of a polymeric melt through a cylindrical capillary. In order to find a theoretical explanation for the phenomenon of persistent oscillations, as observed in the experiments of e.g. Kalika and Denn [23], Lim and Schowalter [31], and El Kissi and Piau [12], a flow driven by a prescribed constant volumetric flow rate \bar{Q} has been considered. The pressure gradient $f(t)$ is unknown and adjusts itself to maintain the desired flow rate \bar{Q} . The constitutive behaviour of the polymeric melt is described by the JSO-model supplemented with an extra Newtonian viscous term. This extra term accounts either for the response of a small-molecule solvent, or for the unhindered motion of the polymer chains, described by a very fast relaxation rate (cf. Malkus et al. [33]). The JSO-model used here describes the characteristic behaviour of viscoelastic concentrated polymer solutions and pure molten polymers with fading memory, by a differential equation. The additional Newtonian viscous term leads to a nonmonotone relation between the steady state shear stress $F(r)$ and the steady state velocity gradient or shear strain-rate $\omega(r)$. We have shown by numerical computations of the transient flow that persistent oscillations in the pressure gradient may occur, as observed in experiments. Hence,

internal material properties of the fluid itself account for persistent oscillations, instead of a global external effect such as 'wall slip', because in our model the no-slip boundary condition at the wall of the capillary is maintained.

A theoretical explanation for the occurrence of persistent oscillations has been given before by Malkus et al. [35], [36], in the piston-driven flow of a JSO-fluid through a slit die. In fact, this chapter deals with the analogous problem of a piston-driven flow of a JSO-fluid through a cylindrical capillary. By numerical computations of the transient flow we have found critical conditions for the onset of persistent oscillations in terms of the volumetric flow rate \bar{Q} and the material parameters of the polymeric melt.

In the description of the piston-driven flow considered here, the material parameters of the polymeric melt are included in one dimensionless parameter ε , which is equal to the quotient of the solvent viscosity η_s and the shear viscosity μ/λ . In the case of no solvent viscosity ($\eta_s = 0$) and two widely spaced relaxation rates, the parameter ε is equal to the quotient of the two shear viscosities (see Malkus et al. [33]). The equations (3.1.32) governing the piston-driven flow can be viewed as a continuous family of quadratic ordinary differential equations coupled by the non-local constraint that fixes the volumetric flow rate \bar{Q} . The non-local constraint expresses the pressure gradient $f(t)$ in terms of \bar{Q} and an integral of the extra shear stress $S(r, t)$ over the cross-section of the capillary. The quadratic ordinary differential equations relate the stresses $S(r, t)$ and $Z(r, t)$ to the pressure gradient $f(t)$ and the velocity gradient $w(r, t)$ for each radial coordinate r , whereby w is determined in terms of S and f by the balance of linear momentum.

The steady state flow is described by a nonmonotone relation between the steady state shear stress $F(r)$ and the steady state velocity gradient $\omega(r)$, if $0 < \varepsilon < 1/8$. This nonmonotone relation gives rise to three distinct steady state solutions ω if $F_m < F < F_M$. As shown by Malkus et al. [33, Sec. 3], the solution ω with $\omega_M < \omega < \omega_m$ is unstable, whereas the solutions ω with $\omega < \omega_M$ or $\omega > \omega_m$ are stable. The steady state pressure gradient $\bar{f} = \lim_{t \rightarrow \infty} f(t)$ and the steady state velocity gradient $\omega(r)$ depend on the flow rate \bar{Q} in the following manner:

- If $0 \leq \bar{Q} \leq \bar{Q}_0$, \bar{f} is unique and $\omega(r)$ is continuous in r ; the flow is referred to as classical flow.
- If $\bar{Q}_0 < \bar{Q} \leq \bar{Q}_{crit}$, \bar{f} is not unique, and $\omega(r)$ is either continuous in r (classical flow) or $\omega(r)$ is discontinuous with a jump from $\omega_-^* < \omega_M$ to $\omega_+^* > \omega_m$ at some radial coordinate $r = r^*$; the latter case is referred to as spurt flow.
- If $\bar{Q} > \bar{Q}_{crit}$, \bar{f} is not unique and $\omega(r)$ is discontinuous at $r = r^*$, corresponding to spurt flow.

In the case of classical flow, \bar{f} is uniquely determined by \bar{Q} only, as expressed by (3.2.13). In the case of spurt flow, \bar{f} is uniquely determined by \bar{Q} and r^* , as expressed by (3.2.17). In spurt flow, the jump in $\omega(r)$ results in a kink in the steady state velocity profile $\bar{v}(r)$ at $r = r^*$, and a spurt layer, of thickness $1 - r^*$, with large shear velocity gradients forms near the wall.

By numerical computations we have examined whether or not the transient flow tends to a steady state. If a steady state is attained, the computations yield the value of \bar{f} and, in the case of spurt flow, the value of r^* where $\omega(r)$ is discontinuous. For $\varepsilon = 0.02$ and $\varepsilon = 0.01$, the

calculations of the transient flow revealed that for each flow rate \bar{Q} a steady state is attained, showing the following characteristics:

- If $\bar{Q} < \bar{Q}_{crit}$ (subcritical flow), the flow tends to a classical steady state with $\bar{f} = f_{clas}(\bar{Q})$.
- If $\bar{Q} > \bar{Q}_{crit}$ (supercritical flow), the flow tends to a spurt steady state with $f_{bottom}(\bar{Q}) \leq \bar{f} \leq f_{top}(\bar{Q})$.
- The flow curve of \bar{f} versus \bar{Q} is S-shaped, shows a kink at $\bar{Q} = \bar{Q}_{crit}$, and tends to the curve $\bar{f} = f_{top}(\bar{Q})$ for \bar{Q} sufficiently large.
- The spurt layer becomes thicker with increasing $\bar{Q} > \bar{Q}_{crit}$.

The transient flow behaviour was found to crucially depend on the values of ε and \bar{Q} . For $\varepsilon = 0.005$ we observed that for a certain bounded range $\mathcal{R} = (\bar{Q}_m, \bar{Q}_M)$ of supercritical flow rates \bar{Q} , persistent oscillations in $f(t)$, $w(r, t)$, $S(r, t)$ and $Z(r, t)$ occur, for each value of the radial coordinate r . These persistent oscillations do not die out and have constant amplitude after a certain instant. For $\bar{Q} \notin \mathcal{R}$, a steady state is reached after sufficient time. At $\bar{Q} = \bar{Q}_m$ and $\bar{Q} = \bar{Q}_M$, the transition from a steady state to a state of persistent oscillations and vice versa takes place. From additional computations we conclude that

- if $0 < \varepsilon < \varepsilon_{crit} = 0.007$, a bounded range $\mathcal{R} = (\bar{Q}_m, \bar{Q}_M)$ of flow rates \bar{Q} exists for which persistent oscillations occur;
- if $\varepsilon \geq \varepsilon_{crit} = 0.007$, the flow tends to a steady state for each flow rate \bar{Q} ;
- the range \mathcal{R} becomes smaller with increasing ε .

In the case of persistent oscillations we have found that after sufficient time the velocity gradient $w(r, t)$, calculated at $r = r_k = k\Delta r$, shows a numerical discontinuity between $r = r_k$ and $r = r_{k+1}$ for some specific index k . Then the value of r^* is taken as $r^* = (r_k + r_{k+1})/2$. In this manner, we have been able to assign a value to the radial coordinate r^* at which the (steady state) velocity gradient is discontinuous, for each flow rate \bar{Q} .

The occurrence of persistent oscillations has been explained by means of a linearized stability analysis of the steady state solution. By numerical computations we have verified that the transient flow tending to a steady state for some value of \bar{Q} , corresponds precisely to the steady state solution being stable. Likewise, if the transient flow shows persistent oscillations for some value of \bar{Q} , then correspondingly the steady state solution is found to be unstable.

By fitting the dimensionless parameter ε to the material parameters of the polymeric melt, the dimensional steady state pressure gradient attained can be determined as a function of the dimensional driving flow rate \bar{Q} . This flow rate is of great practical interest in polymer processing, since it determines the production rate of an extrusion process; a higher flow rate leads to more extrudate produced per unit of time. The dimensional critical flow rate \bar{Q}_{crit} beyond which spurt flow ensues, and the range $\mathcal{R} = (\bar{Q}_m, \bar{Q}_M)$ of dimensional flow rates for which persistent oscillations occur, can be estimated in terms of the material parameters η_s , μ , λ , a , and the radius R of the capillary. Furthermore, the value ε_{crit} determines directly the critical quotient $\eta_s \lambda / \mu$ of material parameters below which persistent oscillations occur,

dependent on whether $\bar{Q} \in \mathcal{R}$. Thus, for a polymeric fluid with material properties such that $\varepsilon \geq \varepsilon_{crit}$, no persistent oscillations occur and the transient flow tends to a steady state for each flow rate \bar{Q} . In Chapter 5 we will compare the critical conditions for the onset of persistent oscillations predicted by our theory, to the critical conditions found in the experiments of Kalika and Denn [23], Lim and Schowalter [31], and of El Kissi and Piau [12].

Chapter 4

Extrusion of a JSO-fluid, combined with compression

In this chapter we consider the extrusion process for a polymeric melt, combined with compression. The extruder consists of a wide barrel connected to a narrow cylindrical capillary. The melt in the barrel is compressed by a plunger, moving at constant speed, and the melt is thus forced to flow into the capillary. The flow in the capillary is shear dominated, whereas the flow in the barrel is mainly a uniform compression flow. A global relation between the pressure in the barrel and the volumetric flow rate in the capillary is derived in terms of the melt compressibility and the plunger speed. Since the polymeric melt is strongly viscous, the inertia forces may be neglected. The constitutive equation to describe the characteristic behaviour of the viscoelastic melt with fading memory chosen here, is the Johnson-Segalman-Oldroyd (JSO)-model supplied with an extra Newtonian viscous term. This extra term, which accounts for the unhindered motion of the polymer chains, is essential as it leads to a nonmonotone behaviour of the steady state shear stress as function of the steady state shear strain-rate or velocity gradient (see Figure 4.2).

4.1 Mathematical formulation

This section deals with the modelling of the extrusion process. The extruder consists of a wide cylindrical barrel connected to a narrow cylindrical capillary; see Figure 4.1. Thus, the radius R of the capillary is small compared to the radius R_b of the barrel. The centerlines of the barrel and the capillary coincide. Cylindrical coordinates (r, θ, z) are introduced with the z -axis along the centerline of the extruder, and $z = 0$ corresponding to the position where the barrel is connected to the capillary; see Figure 4.1. The polymeric melt in the barrel is compressed by a plunger, moving at constant speed V_0 in the positive z -direction. Consequently, the length l of the barrel equals $l(t) = l_0 - V_0 t$, where $l_0 = l(0)$ denotes the initial length. Due to the plunger movement a pressure P is built up inside the barrel, and the melt is forced to leave the barrel at $z = 0$ and to flow into the capillary, with volumetric flow rate Q . At the end of the capillary, i.e. at $z = L$ where L denotes the capillary length, the melt leaves the capillary and the extrudate is formed. In the main part of the barrel the flow is aligned along the z -axis, and the flow is a uniform compression flow; only near $z = 0$ a strong contraction

flow exists; see Figure 1.1. Thus, the compressibility of the melt inside the barrel must be taken into account, and the melt density ρ is variable. Since the flow in the barrel is uniform, P and ρ are only time-dependent, i.e. $P = P(t)$ and $\rho = \rho(t)$. The melt flowing through the capillary is incompressible, and the flow inside the capillary is a pure shear flow. Hence, the melt flows through the whole capillary with volumetric flow rate $Q = Q(t)$.

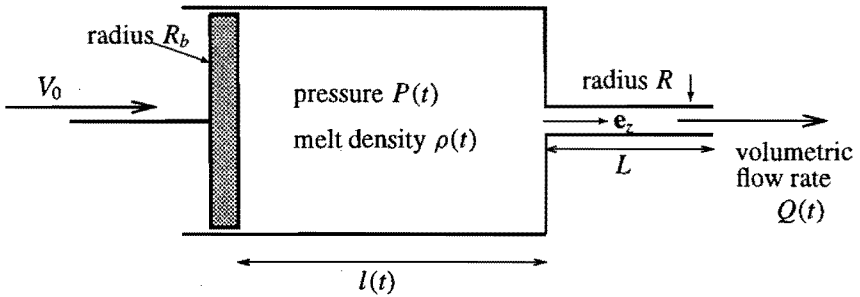


Figure 4.1. The extruder which consists of a wide barrel and a narrow cylindrical capillary. The melt in the barrel is compressed by a plunger moving with constant speed V_0 in the positive z -direction.

We first consider the flow inside the barrel, where the polymeric melt is compressible. This flow is governed by the conservation of mass

$$\frac{d\rho}{dt} = -\rho(\nabla \cdot \mathbf{v}) \quad (4.1.1)$$

and the balance of linear momentum

$$\nabla \cdot \mathcal{T} + \rho \mathbf{b} = \rho \left(\frac{\partial \mathbf{v}}{\partial t} + (\mathbf{v} \cdot \nabla) \mathbf{v} \right). \quad (4.1.2)$$

Here, ρ is the fluid density, \mathbf{b} the body force per unit of mass, \mathbf{v} the fluid velocity and \mathcal{T} the total (symmetric) stress tensor. The rate-of-deformation tensor \mathcal{D} is defined by

$$\mathcal{D} = \frac{1}{2}(\mathcal{L} + \mathcal{L}^T), \quad \mathcal{L} = \text{grad } \mathbf{v} = \frac{\partial \mathbf{v}}{\partial \mathbf{x}} (\equiv (\nabla \mathbf{v})^T). \quad (4.1.3)$$

With the flow aligned along the z -axis, the flow parameters in the barrel are independent of the azimuthal coordinate θ and the radial coordinate r . Under the condition that the flow starts from rest at time $t = 0$, and that the compression flow in the barrel is uniform, the velocity takes the form

$$\mathbf{v} = [W(t)z + V(t)]H(t)\mathbf{e}_z, \quad (4.1.4)$$

where H is the (Heaviside) step function and \mathbf{e}_z is a unit vector in the positive z -direction. Consequently,

$$\nabla \cdot \mathbf{v} \equiv \text{tr } \mathcal{D} = D_{zz} = W(t) \quad (4.1.5)$$

and D_{zz} is the only non-zero component of \mathcal{D} . The conservation of mass (4.1.1) then becomes

$$\frac{d\rho(t)}{dt} = -\rho(t)W(t). \quad (4.1.6)$$

The global balance of mass, expressing that the total change of mass of the melt in the barrel equals the mass flowing out of the barrel into the capillary, is formulated by

$$\frac{d}{dt} \{ Al(t)\rho(t) \} = -\rho(t)Q(t), \quad (4.1.7)$$

where $A := \pi R_b^2$ denotes the area of the cross-section of the barrel. By using $l'(t) = -V_0$ we rewrite (4.1.7) as

$$\frac{d\rho(t)}{dt} = \frac{\rho(t)}{Al(t)} [Q_i - Q(t)], \quad (4.1.8)$$

where $Q_i := AV_0$ denotes the constant (prescribed) inlet flow rate due to the plunger movement. The inlet flow rate Q_i is driving the flow inside the extruder. Combination of (4.1.6) and (4.1.8) yields

$$W(t) = \frac{Q(t) - Q_i}{Al(t)}. \quad (4.1.9)$$

Since the compression flow in the barrel is uniform, the stress tensor \mathcal{T} only depends on time t . Thus, the balance of linear momentum (4.1.2), with the body force $\rho\mathbf{b}$ and the inertia forces $\rho(\partial\mathbf{v}/\partial t + (\mathbf{v} \cdot \nabla)\mathbf{v})$ neglected, is automatically satisfied.

The characteristic response of the material to a deformation is described by the constitutive equation for the stress. For viscoelastic fluids with fading memory, the stress depends on the deformation history. If a polymer solution contains a small-molecule solvent, this solvent will generally respond in a viscous manner to any applied force or deformation, separately from the elastic response due to the dissolved polymer; see Renardy et al. [48, p. 17]. Therefore, it is assumed that the extra stress tensor $\mathcal{S} := \mathcal{T} + pI$ in the fluid consists of a Newtonian viscous component and an isotropic elastic one, namely

$$\mathcal{S} = \mathcal{T} + pI = 2\eta_s\mathcal{D} + \mathcal{S}_p. \quad (4.1.10)$$

Here, p is the pressure, I the unit tensor, η_s the solvent viscosity, and the elastic part \mathcal{S}_p characterizes the polymer contribution. As in Chapter 3, the elastic part \mathcal{S}_p is assumed to be described by the constitutive JSO-model. In the JSO-model, \mathcal{S}_p is determined by the following nonlinear differential equation (see Tanner [50, p. 207]):

$$\frac{d\mathcal{S}_p}{dt} - \mathcal{L}\mathcal{S}_p - \mathcal{S}_p\mathcal{L}^T + (1-a)(\mathcal{D}\mathcal{S}_p + \mathcal{S}_p\mathcal{D}) + \lambda\mathcal{S}_p = 2\mu\mathcal{D}, \quad (4.1.11)$$

where d/dt denotes the material derivative. The relaxation rate λ , the slip parameter $a \in (-1, 1)$, and the shear modulus μ are material parameters.

For the uniform compression flow in the barrel, the elastic part S_p only depends on time t . With L_{zz} the only non-zero component of \mathcal{L} , the JSO-model (4.1.11) transforms into the following equations for the components S_{ij} of S_p :

$$\begin{aligned} \frac{dS_{rr}}{dt} + \lambda S_{rr} &= 0, & \frac{dS_{\theta\theta}}{dt} + \lambda S_{\theta\theta} &= 0, \\ \frac{dS_{zz}}{dt} - 2aD_{zz}S_{zz} + \lambda S_{zz} &= 2\mu D_{zz}, & \frac{dS_{r\theta}}{dt} + \lambda S_{r\theta} &= 0, \\ \frac{dS_{\theta z}}{dt} + \lambda S_{\theta z} &= 0, & \frac{dS_{rz}}{dt} + \lambda S_{rz} &= 0. \end{aligned} \quad (4.1.12)$$

Under the initial condition $S_p = 0$ at $t = 0$, it follows that $S_{rr} = S_{\theta\theta} = S_{r\theta} = S_{\theta z} = S_{rz} = 0$. Hence,

$$\text{tr } S_p = S_{zz}, \quad (4.1.13)$$

and the stress components T_{ij} of \mathcal{T} in the barrel reduce to

$$T_{rr} = T_{\theta\theta} = -p, \quad T_{zz} = -p + 2\eta_s D_{zz} + S_{zz}, \quad T_{r\theta} = T_{\theta\theta} = T_{rz} = 0. \quad (4.1.14)$$

The pressure P in the barrel is measured as the opposite $-T_{rr}$ of the normal stress at the wall of the barrel. Hence, according to (4.1.14),

$$p = P(t). \quad (4.1.15)$$

By substitution of $D_{zz} = W(t)$ from (4.1.9) into (4.1.12)³ for S_{zz} , we are led to the following differential equation:

$$\frac{dS_{zz}(t)}{dt} = -\lambda S_{zz}(t) + \frac{2\mu[Q(t) - Q_i]}{Al(t)} + \frac{2a[Q(t) - Q_i]S_{zz}(t)}{Al(t)}, \quad t > 0. \quad (4.1.16)$$

The characteristic response of the material to a compression is described by the constitutive equation for the hydrostatic pressure $p_{hydr} := -(\text{tr } \mathcal{T})/3$. Here, it is assumed that the compression in the barrel is purely elastic, which means that p_{hydr} satisfies the constitutive equation

$$\frac{dp_{hydr}}{dt} = -K \text{tr } \mathcal{D}, \quad (4.1.17)$$

where K is the compression or bulk modulus of the polymeric melt. With

$$p_{hydr} = -\frac{1}{3}\text{tr } \mathcal{T} = P(t) - \frac{2\eta_s[Q(t) - Q_i]}{3Al(t)} - \frac{1}{3}S_{zz}(t), \quad (4.1.18)$$

equation (4.1.17) reduces to

$$\frac{dP(t)}{dt} = -\frac{K[Q(t) - Q_i]}{Al(t)} + \frac{2\eta_s}{3A} \frac{d}{dt} \left\{ \frac{Q(t) - Q_i}{l(t)} \right\} + \frac{1}{3} \frac{dS_{zz}(t)}{dt}, \quad t > 0. \quad (4.1.19)$$

The equations (4.1.16) and (4.1.19) provide one coupling between the pressure $P(t)$ in the barrel and the volumetric flow rate $Q(t)$ in the capillary. In these equations $l(t) = l_0 - V_0 t$.

is the length of the barrel. Later on we will show that for a low plunger speed V_0 , the length $l(t)$ may be replaced by the initial length l_0 .

Next we consider the flow in the capillary, where the polymeric melt is incompressible. This flow is governed by the balance of linear momentum (4.1.2) and the conservation of mass (4.1.1) with $d\rho/dt = 0$, i.e.

$$\nabla \cdot \mathbf{v} = 0. \quad (4.1.20)$$

With the flow aligned along the z -axis, the flow parameters in the capillary are independent of the axial coordinate z and the azimuthal coordinate θ . Under the condition that the flow starts from rest at time $t = 0$, the velocity takes the form

$$\mathbf{v} = v(r, t)H(t)\mathbf{e}_z, \quad (4.1.21)$$

where H is the (Heaviside) step function and \mathbf{e}_z is a unit vector in the positive z -direction. The conservation of mass is now automatically satisfied, and the convective terms $\rho(\mathbf{v} \cdot \nabla)\mathbf{v}$ in (4.1.2) disappear. The no-slip boundary condition at the wall of the capillary and the regularity of the velocity at the axis require

$$v(R, t) = 0, \quad (4.1.22)$$

and

$$\frac{\partial v}{\partial r}(0, t) = 0, \quad (4.1.23)$$

respectively.

To further describe the pure shear flow in the capillary, we use the results of Chapter 3. With the stress tensor \mathcal{T} given by (4.1.10) and the constitutive JSO-model (4.1.11) used for the elastic part \mathcal{S}_p , under the initial condition $\mathcal{S}_p = 0$ at $t = 0$, we found in (3.1.14) that the stress components T_{ij} of \mathcal{T} are given by

$$\begin{aligned} T_{rr} &= -p + \frac{1}{1+a}Z(r, t), & T_{\theta\theta} &= -p, \\ T_{zz} &= -p - \frac{1}{1-a}Z(r, t), & T_{rz} &= \eta_s \frac{\partial v}{\partial r}(r, t) - S(r, t), \\ T_{r\theta} &= T_{\theta z} = 0. \end{aligned} \quad (4.1.24)$$

Here, $p = p(r, z, t)$ is the pressure inside the capillary, and the variables S and Z , introduced in (3.1.11), satisfy

$$\begin{aligned} \frac{\partial Z}{\partial t} - (1-a^2)S \frac{\partial v}{\partial r} + \lambda Z &= 0, \\ \frac{\partial S}{\partial t} + Z \frac{\partial v}{\partial r} + \lambda S &= -\mu \frac{\partial v}{\partial r}, \end{aligned} \quad 0 \leq r \leq R, \quad t > 0; \quad (4.1.25)$$

see (3.1.12). According to (3.1.15), the variable Z is related to the first and second normal stress differences $N_1 := T_{zz} - T_{rr}$ and $N_2 := -T_{\theta\theta} + T_{rr}$, while $S = -S_{rz}$ by (3.1.11). In

(3.1.17)-(3.1.19) we found that the balance of linear momentum (4.1.2), with $\rho \mathbf{b} = \mathbf{0}$, is satisfied if the pressure p takes the form

$$p(r, z, t) = -f(t)z + p_0(r, t), \quad (4.1.26)$$

with

$$p_0(r, t) = \frac{1}{1+a}Z(r, t) + \frac{1}{1+a} \int_0^r \frac{Z(y, t)}{y} dy + P_0(t), \quad (4.1.27)$$

while the shear stress T_{rz} equals

$$T_{rz} = -\frac{1}{2}rf(t) + \frac{\rho}{r} \int_0^r y \frac{\partial v}{\partial t}(y, t) dy. \quad (4.1.28)$$

Here, f is the pressure gradient in the capillary, and P_0 is a pressure term determined by the boundary condition at the end $z = L$ of the capillary. We assume that the pressure outside the capillary is at level zero, so that $p(0, L, t) = 0$. Then it follows that

$$P_0(t) = Lf(t). \quad (4.1.29)$$

By equating the expressions (4.1.28) and (4.1.24)⁴ for T_{rz} , we are led to the following relation between the velocity gradient and the pressure gradient:

$$-\eta_s \frac{\partial v}{\partial r}(r, t) + S(r, t) = \frac{1}{2}rf(t) - \frac{\rho}{r} \int_0^r y \frac{\partial v}{\partial t}(y, t) dy, \quad 0 \leq r \leq R, \quad t > 0. \quad (4.1.30)$$

The volumetric flow rate Q in the capillary is defined by

$$Q(t) = 2\pi \int_0^R v(r, t) r dr. \quad (4.1.31)$$

The second coupling between the flow in the capillary and the flow in the barrel is achieved by equating the pressure terms in the barrel and in the capillary at $r = 0, z = 0$. From (4.1.15) and (4.1.26) it follows that $P_0 = P$, or equivalently,

$$P(t) = Lf(t). \quad (4.1.32)$$

Equation (4.1.32) can be used to replace f in (4.1.30) by P/L .

The equations describing the extrusion process are made dimensionless by appropriate scaling. We use the same scaling as in Section 3.1, that is, we put $Q = \pi \lambda R^3 \hat{Q}/\sqrt{1-a^2}$, $r = R\hat{r}$, $t = \hat{t}/\lambda$, $v = \lambda R \hat{v}/\sqrt{1-a^2}$, $f = \mu \hat{f}/R\sqrt{1-a^2}$, $S = \mu \hat{S}/\sqrt{1-a^2}$, and $Z = \mu \hat{Z}$. Furthermore, we introduce dimensionless variables \hat{l} , \hat{Q}_i , \hat{P} and \hat{S}_{zz} , by writing $l = l_0 \hat{l}$, $Q_i = \pi \lambda R^3 \hat{Q}_i/\sqrt{1-a^2}$, $P = 8\mu L \hat{P}/R\sqrt{1-a^2}$ and $S_{zz} = \mu \hat{S}_{zz}/\sqrt{1-a^2}$. Then equations (4.1.19) and (4.1.16), governing the flow in the barrel, transform into their dimensionless forms, reading (since no confusion will arise we omit the carets)

$$\begin{aligned} \frac{dP(t)}{dt} &= -\frac{1}{\chi} \frac{Q(t) - Q_i}{l(t)} + \zeta \frac{d}{dt} \left\{ \frac{Q(t) - Q_i}{l(t)} \right\} + \kappa \frac{dS_{zz}(t)}{dt}, \quad t > 0, \\ \frac{dS_{zz}(t)}{dt} &= -S_{zz}(t) + \sigma \frac{Q(t) - Q_i}{l(t)} + \frac{\alpha \sigma}{\sqrt{1-a^2}} \frac{Q(t) - Q_i}{l(t)} S_{zz}(t), \quad t > 0, \end{aligned} \quad (4.1.33)$$

where the dimensionless inlet flow rate Q_i and length l are given by

$$Q_i = \frac{AV_0\sqrt{1-a^2}}{\pi\lambda R^3}, \quad l(t) = 1 - \frac{V_0}{\lambda l_0}t, \quad (4.1.34)$$

and the dimensionless parameters χ , ζ , κ and σ are given by

$$\chi = \frac{8Al_0\mu L}{K\pi R^4}, \quad \zeta = \frac{\eta_s\lambda\pi R^4}{12Al_0\mu L}, \quad \kappa = \frac{R}{24L}, \quad \sigma = \frac{2\pi R^3}{Al_0}. \quad (4.1.35)$$

Furthermore, equation (4.1.32) transforms into its dimensionless form

$$f(t) = 8P(t). \quad (4.1.36)$$

Equations (4.1.25) and (4.1.30), governing the flow in the capillary, transform into

$$\frac{\partial S}{\partial t} = -S + w(1 + Z), \quad \frac{\partial Z}{\partial t} = -Z - wS, \quad 0 \leq r \leq 1, \quad t > 0, \quad (4.1.37)$$

and

$$\varepsilon w(r, t) + S(r, t) = \frac{1}{2}rf(t) - \frac{\alpha}{r} \int_0^r y \frac{\partial v}{\partial t}(y, t) dy, \quad 0 \leq r \leq 1, \quad t \geq 0. \quad (4.1.38)$$

Here, the velocity gradient, or shear strain-rate, w is defined by

$$w(r, t) = -\frac{\partial v}{\partial r}(r, t), \quad (4.1.39)$$

and the dimensionless parameters ε and α are given by

$$\varepsilon = \frac{\eta_s\lambda}{\mu}, \quad \alpha = \frac{\rho R^2\lambda^2}{\mu}. \quad (4.1.40)$$

Finally, the volumetric flow rate passes into its dimensionless form

$$Q(t) = 2 \int_0^1 v(r, t) r dr. \quad (4.1.41)$$

The boundary conditions pertinent to (4.1.38) read in dimensionless form

$$v(1, t) = 0, \quad w(0, t) = 0, \quad t > 0. \quad (4.1.42)$$

The parameter ε represents the ratio of the solvent viscosity η_s and the shear viscosity μ/λ , and the quotient α/ε corresponds to the Reynolds number. In Table 4.1 the order of magnitude is given of the various parameters of the polymeric melt and the extruder. For the strongly viscous polymers we consider, $\alpha \ll 1$; see Table 4.1. Thus, the last term in the right-hand side of (4.1.38) may be neglected, which amounts to the neglect of the inertia forces in (4.1.2). By putting $\alpha = 0$, and with the use of (4.1.36), equation (4.1.38) reduces to

$$\varepsilon w(r, t) + S(r, t) = 4rP(t), \quad 0 \leq r \leq 1, \quad t \geq 0. \quad (4.1.43)$$

After one integration by parts with the aid of the no-slip boundary condition (4.1.42)¹ at the wall, the volumetric flow rate Q can be expressed in terms of the velocity gradient w by

$$Q(t) = \int_0^1 r^2 w(r, t) dr. \quad (4.1.44)$$

Elimination of w by means of (4.1.43), transforms (4.1.44) into the following (implicit) relation between the pressure P and the volumetric flow rate Q :

$$P(t) = \varepsilon Q(t) + \int_0^1 r^2 S(r, t) dr. \quad (4.1.45)$$

From Table 4.1 we find that $V_0/\lambda l_0 \approx 10^{-3} \ll 1$. Hence, we may replace $l(t)$ in (4.1.33) by $l(0) = 1$, which is valid as long as $t \ll \lambda l_0/V_0$; see (4.1.34)². Considering (4.1.33)² we observe that S_{zz} is proportional to σ , so that the derivative $\kappa dS_{zz}(t)/dt$ is proportional to $\kappa\sigma$. For the strongly viscous polymers we consider, one has $\kappa\sigma\chi = 2\mu/3K \ll 1$ and $\zeta\chi = 2\eta_s\lambda/3K \ll 1$; see Table 4.1. Thus the last two terms in the right-hand side of (4.1.33)¹ may be neglected. In the original expression (4.1.14)² this amounts to the neglect of the extra stress component $2\eta_s D_{zz} + S_{zz}$ in the stress T_{zz} . Consequently, for the compression flow in the barrel also T_{zz} equals $-p$. By putting $l(t) = 1$, $\zeta = 0$ and $\kappa = 0$, equations (4.1.33) reduce to

$$\frac{dP(t)}{dt} = -\frac{1}{\chi} [Q(t) - Q_i]. \quad (4.1.46)$$

Notice that Molenaar and Koopmans [39] obtained the same differential equation.

symbol	order of magnitude	unit	symbol	order of magnitude	unit
R	10^{-3}	m	K	10^9	Nm^{-2}
L	10^{-2}	m	μ	10^5	Nm^{-2}
V_0	10^{-4}	ms^{-1}	λ	10^0	s^{-1}
l_0	10^{-1}	m	η_s	10^3	Nsm^{-2}
R_b	10^{-2}	m	a	0.9	-
$A = \pi R_b^2$	10^{-4}	m^2	ρ	10^3	kgm^{-3}

Table 4.1 The order of magnitude of the various parameters of the extruder and the polymeric melt.

Thus, the extrusion process driven by a plunger moving at constant speed is described by the following system of equations:

$$\begin{aligned} \frac{\partial S}{\partial t} &= -S + w(1 + Z), & \frac{\partial Z}{\partial t} &= -Z - wS, \\ \varepsilon w(r, t) + S(r, t) &= 4rP(t), & P(t) &= \varepsilon Q(t) + \int_0^1 r^2 S(r, t) dr, \\ \frac{dP(t)}{dt} &= -\frac{1}{\chi} [Q(t) - Q_i], & 0 \leq r \leq 1, \quad t > 0. \end{aligned} \quad (4.1.47)$$

For $t < 0$ the fluid is at rest, and at $t = 0$ the flow is suddenly started up by letting the plunger move at constant speed V_0 . The plunger movement induces the constant inlet flow rate Q_i . The initial conditions for P , S and Z , which are supposed to be continuous at $t = 0$, are given by

$$P(0) = 0, \quad S(r, 0) = 0, \quad Z(r, 0) = 0, \quad 0 \leq r \leq 1. \quad (4.1.48)$$

Substitution of (4.1.48) into (4.1.47)^{3,4} yields the initial values

$$Q(0) = 0, \quad w(r, 0) = 0, \quad 0 \leq r \leq 1. \quad (4.1.49)$$

The equations (4.1.47) governing the flow in the extruder can be viewed as a continuous family of quadratic ordinary differential equations coupled by the non-local constraint that determines the flow rate, and the non-local ordinary differential equation that describes the compression in the barrel. The material parameters of the polymeric melt, the plunger speed V_0 , and the dimensions of the extruder are included in the three dimensionless parameters ε , χ and Q_i . Notice that ε contains only the material parameters of the polymeric melt, whereas Q_i and χ depend on both the material parameters and the geometry of the extruder. The parameter χ is proportional to the melt compressibility $1/K$.

4.2 Steady state flow

In this section we investigate the steady state reached by the flow as $t \rightarrow \infty$. The steady state flow, driven by the constant inlet flow rate Q_i , is described in terms of the steady state variables

$$\begin{aligned} \bar{P} &= \lim_{t \rightarrow \infty} P(t), & \bar{f} &= \lim_{t \rightarrow \infty} f(t), & \bar{Q} &= \lim_{t \rightarrow \infty} Q(t), \\ \omega(r) &= \lim_{t \rightarrow \infty} w(r, t), & \bar{S}(r) &= \lim_{t \rightarrow \infty} S(r, t), & \bar{Z}(r) &= \lim_{t \rightarrow \infty} Z(r, t), \end{aligned} \quad (4.2.1)$$

under the assumption that these limits exist. In (4.2.1), \bar{P} is the steady state pressure, \bar{f} is the steady state pressure gradient, \bar{Q} is the steady state volumetric flow rate, ω is the steady state velocity gradient, and \bar{S} and \bar{Z} are the steady state extra stresses. For $t \rightarrow \infty$, the equations (4.1.36) and (4.1.47) reduce to

$$\begin{aligned} 0 &= -\bar{S} + \omega(1 + \bar{Z}), & 0 &= -\bar{Z} - \omega\bar{S}, & \bar{Q} - Q_i &= 0, \\ \varepsilon\omega(r) + \bar{S}(r) &= 4r\bar{P}, & \bar{P} &= \varepsilon\bar{Q} + \int_0^1 r^2\bar{S}(r)dr, & \bar{f} &= 8\bar{P}. \end{aligned} \quad (4.2.2)$$

Hence, $\bar{Q} = Q_i$ and $\bar{f} = 8\bar{P}$, and the solutions of (4.2.2)^{1,2} expressed in terms of ω read

$$\bar{S}(r) = \frac{\omega(r)}{1 + \omega^2(r)}, \quad \bar{Z}(r) = -\frac{\omega^2(r)}{1 + \omega^2(r)}. \quad (4.2.3)$$

On substitution of (4.2.3)¹ into (4.2.2)⁴, we find that the steady state velocity gradient can be determined for each $r \in [0, 1]$ by solving $\omega = \omega(r)$ from the equation

$$\mathcal{F}(\omega(r)) = F(r), \quad (4.2.4)$$

where the steady state shear stress F is defined by

$$F(r) = 4r\bar{P} = \frac{1}{2}r\bar{f}, \quad (4.2.5)$$

and the function \mathcal{F} is defined by

$$\mathcal{F}(\omega) = \varepsilon\omega + \frac{\omega}{1 + \omega^2}. \quad (4.2.6)$$

For a given inlet flow rate Q_i , the velocity gradient ω must satisfy the constraint

$$Q_i = \int_0^1 r^2 \omega(r) dr, \quad (4.2.7)$$

obtained by letting $t \rightarrow \infty$ in (4.1.44). The steady state velocity profile $\bar{v}(r) = \lim_{t \rightarrow \infty} v(r, t)$ is obtained by integration of $\bar{v}'(r) = -\omega(r)$ using the boundary condition $\bar{v}(1) = 0$ at the wall. Notice that the equations (4.2.3)-(4.2.7) with $\bar{f} = 8\bar{P}$ and $\bar{Q} = Q_i$ are identical to the equations (3.2.3)-(3.2.7) describing the steady state of a piston-driven flow controlled by a constant volumetric flow rate \bar{Q} ; see Section 3.2.

For $\varepsilon < 1/8$ the function \mathcal{F} is nonmonotone in ω . In Figure 4.2 the function $\mathcal{F}(\omega)$ is plotted for a specific value of ε with $0 < \varepsilon < 1/8$. Since the Newtonian viscosity η_s is small in comparison to the shear viscosity μ/λ , we will henceforth assume that $0 < \varepsilon < 1/8$. Then the function $\mathcal{F}(\omega)$ has two extreme values, a maximum $F_M = \mathcal{F}(\omega_M)$ at $\omega = \omega_M = [(1 - 2\varepsilon - \sqrt{1 - 8\varepsilon})/2\varepsilon]^{1/2}$ and a minimum $F_m = \mathcal{F}(\omega_m)$ at $\omega = \omega_m = [(1 - 2\varepsilon + \sqrt{1 - 8\varepsilon})/2\varepsilon]^{1/2}$; see Figure 4.2. In addition to $\omega = \omega_M$ and $\omega = \omega_m$, both equations $\mathcal{F}(\omega) = F_M$ and $\mathcal{F}(\omega) = F_m$ have a second solution $\omega = \tilde{\omega}_M$ and $\omega = \tilde{\omega}_m$, respectively; see Figure 4.2.

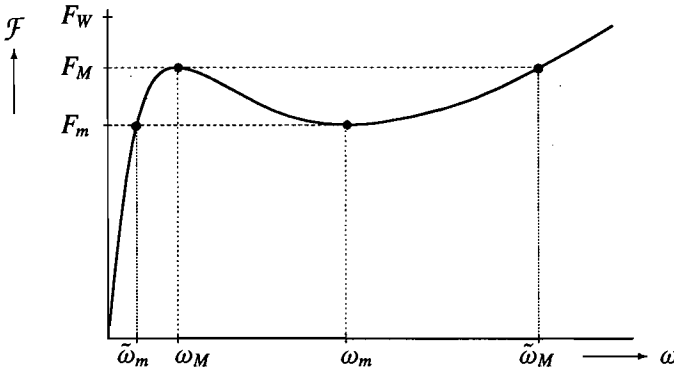


Figure 4.2 The function $\mathcal{F}(\omega) = \varepsilon\omega + \omega/(1 + \omega^2)$, when $0 < \varepsilon < 1/8$. In steady state flow the velocity gradient ω satisfies $\mathcal{F}(\omega) = F$, where $F = 4r\bar{P}$ is the steady state shear stress.

The steady state shear stress F is linear in r and has its maximum at the wall $r = 1$. If this maximum, denoted by $F_W = 4\bar{P}$, remains below the minimum F_m , then equation (4.2.4) has a unique solution $\omega(r) < \tilde{\omega}_m$ for each radial coordinate r . Clearly, $\omega(r)$ is continuous in r , leading to a smooth steady state velocity profile $\bar{v}(r)$, and the flow is referred to as classical flow. If the maximum $F_W = 4\bar{P}$ exceeds the minimum F_m , equation (4.2.4) has

- one solution if $0 \leq F < F_m$;
- three solutions if $F_m < F < F_M$;
- one solution if $F_M < F \leq F_w$.

Malkus et al. [33, Sec. 3] have shown by a phase-plane analysis of the critical points of the system (4.1.47), that the solution ω with $\omega_M < \omega < \omega_m$ corresponds to a saddle point. Hence, this ω -solution is unstable and is therefore not attained. If $F(1) > F_M$, i.e. if $\bar{P} > F_M/4 =: \bar{P}_{crit}$ (supercritical flow), the steady state velocity gradient $\omega(r)$ has at least one jump at some radial coordinate r . In case of exactly one jump we denote the radial coordinate at which the jump occurs by r^* ($r^* < 1$), and we refer to the flow as spurt flow. Hence, in spurt flow $\omega(r) < \omega_-^*$ for $0 \leq r < r^*$, whereas $\omega(r) > \omega_+^*$ for $r^* < r \leq 1$, where

$$\omega_-^* := \lim_{r \uparrow r^*} \omega(r) < \lim_{r \downarrow r^*} \omega(r) =: \omega_+^*, \quad (4.2.8)$$

with $\omega_-^* \leq \omega_M$ and $\omega_+^* \geq \omega_m$. From (4.2.3) it follows that in spurt flow $\bar{\omega}(r)$ and $\bar{Z}(r)$ are also discontinuous at $r = r^*$. The jump in ω results in a kink in the steady state velocity profile $\bar{v}(r)$ at $r = r^*$, and a spurt layer with large velocity gradients forms near the wall; see Figure 2.2. If the velocity gradient jumps from $\omega_-^* = \omega_M$ to $\omega_+^* = \tilde{\omega}_M$, i.e. if $F(r^*) = F_M$, we call this top-jumping. If the velocity gradient jumps from $\omega_-^* = \tilde{\omega}_m$ to $\omega_+^* = \omega_m$, i.e. if $F(r^*) = F_m$, we call this bottom-jumping.

For classical flow, we infer from (3.2.13) with $\bar{f} = 8\bar{P}$ and $\bar{Q} = Q_i$, the following relation between the inlet flow rate and the velocity gradient at the wall:

$$Q_i = \frac{1}{64\bar{P}^3} [\mathcal{P}(\omega_{wall}) - \mathcal{P}(0)], \quad 0 \leq \omega_{wall} \leq \omega_M, \quad (4.2.9)$$

where $\omega_{wall} := \omega(1) \leq \omega_M$ and the function \mathcal{P} is given by (3.2.12). The inverse of (4.2.9) is known to exist and is denoted by $\bar{P} = P_{clas}(Q_i)$. The maximum value of Q_i for which classical flow can be achieved, equals $Q_i = \bar{Q}_{crit} := [\mathcal{P}(\omega_M) - \mathcal{P}(0)]/F_M^3$. For spurt flow with $\omega(r)$ being discontinuous at $r = r^*$, we infer from (3.2.17) and (3.2.18) with $\bar{Q} = Q_i$ and $\bar{f} = 8\bar{P}$, the following relationship:

$$Q_i = Q(r^*, 8\bar{P}) := \frac{1}{64\bar{P}^3} [\mathcal{P}(\omega_-^*) - \mathcal{P}(0) + \mathcal{P}(\omega_{wall}) - \mathcal{P}(\omega_+^*)], \quad (4.2.10)$$

$$0 \leq \omega_-^* < \omega_+^* \leq \omega_{wall}.$$

Here, $\omega = \omega_{wall}$ is found as the largest solution of the steady state equation $\mathcal{F}(\omega) = 4\bar{P}$, while $\omega = \omega_-^*$ and $\omega = \omega_+^*$ are the smallest and largest solutions of the equation $\mathcal{F}(\omega) = 4r^*\bar{P}$. Bottom-jumping occurs when $F(r^*) = F_m$, or equivalently, when $r^* = r_m := F_m/4\bar{P}$; see Figure 2.7c. The steady state pressure for bottom-jumping is given by $\bar{P} = P_{bottom}(Q_i)$, where the function P_{bottom} is the inverse of (4.2.10) with $\omega_-^* = \tilde{\omega}_m$ and $\omega_+^* = \omega_m$. This inverse exists for $Q_i \geq \bar{Q}_0 := [\mathcal{P}(\tilde{\omega}_m) - \mathcal{P}(0)]/F_m^3$. The lower bound $r^* = r_m$ can be represented as a function of Q_i according to $r^* = r_{bottom}^*(Q_i) := F_m/4P_{bottom}(Q_i)$. Top-jumping occurs when $F(r^*) = F_M$, or equivalently, when $r^* = r_M := F_M/4\bar{P}$; see Figure 2.7a. The steady state pressure for top-jumping is given by $\bar{P} = P_{top}(Q_i)$, where the function P_{top} is the inverse of

(4.2.10) with $\omega_-^* = \omega_M$ and $\omega_+^* = \tilde{\omega}_M$. The inverse exists for $Q_i \geq \bar{Q}_{crit} = [\mathcal{P}(\omega_M) - \mathcal{P}(0)]/F_M^3$ (supercritical flow). The upper bound $r^* = r_M$ can be represented as a function of Q_i according to $r^* = r_{top}^*(Q_i) = F_M/4P_{top}(Q_i)$. Plots of the functions $P_{clas}(Q_i)$, $P_{bottom}(Q_i)$, and $P_{top}(Q_i)$, are shown as dotted curves in Figure 4.6, while plots of the functions $1 - r_{bottom}^*(Q_i)$ and $1 - r_{top}^*(Q_i)$, are shown as dotted curves in Figure 4.7. In Table 3.1 of Chapter 3 the values of ω_M , ω_m , F_M , F_m , $\tilde{\omega}_M$, $\tilde{\omega}_m$, \bar{Q}_{crit} and \bar{Q}_0 , are given for $\varepsilon = 0.02, 0.01$ and 0.005 .

In conclusion, for a prescribed constant inlet flow rate Q_i we have for a possible steady state:

- If $0 \leq Q_i \leq \bar{Q}_0$, the steady state is unique; classical flow occurs with $\bar{P} = P_{clas}(Q_i)$.
- If $\bar{Q}_0 < Q_i \leq \bar{Q}_{crit}$, the steady state is not unique; either classical flow or spurt flow occurs with $P_{bottom}(Q_i) \leq \bar{P} \leq P_{clas}(Q_i)$.
- If $Q_i > \bar{Q}_{crit}$, the steady state is not unique; spurt flow occurs with $P_{bottom}(Q_i) \leq \bar{P} \leq P_{top}(Q_i)$.

Notice that the results derived in this section are only valid in case the steady state does indeed exist. Numerical computations as carried out in the next section will show whether or not the flow tends to a steady state as $t \rightarrow \infty$. It will turn out that for $Q_i \leq \bar{Q}_{crit}$ there is no jump in the steady state velocity gradient, so that the flow is classical.

4.3 Transient flow behaviour

In this section we compute for $t > 0$ the transient flow, starting from rest at time $t = 0$ and driven by the constant inlet flow rate Q_i due to the plunger movement. The flow is governed by the system of equations (4.1.47), with initial conditions (4.1.48) and (4.1.49). From the numerical results we infer whether the flow reaches a steady state, and we determine the steady state variables. The main interest goes to the relationship between Q_i and the steady state pressure $\bar{P} = \lim_{t \rightarrow \infty} P(t)$. In the case of a classical steady state this relationship is one-to-one: $\bar{P} = P_{clas}(Q_i)$, obtainable as the inverse of (4.2.9). In the case of a spurt steady state, \bar{P} is not uniquely determined by just Q_i , as discussed in Section 3.2 below (3.2.18). Whether the flow tends to a steady state, is found to depend on the values of Q_i and the dimensionless parameters ε and χ . In the first part of this section we take $\varepsilon = 0.02$ and $\chi = 1, 2, 4$, and compute the transient flow for several values of Q_i . It turns out that a steady state is reached for all values of Q_i considered. Furthermore, the steady state velocity gradient $\omega(r) = \lim_{t \rightarrow \infty} \omega(r, t)$ is either continuous in r , corresponding to classical flow, or $\omega(r)$ has one jump at $r = r^*$, corresponding to spurt flow. In the latter case, the radial coordinate r^* is related to Q_i and \bar{P} by (4.2.10). Next, we investigate the dependence of the transient flow on the parameters ε and χ , by taking $\varepsilon = 0.005$ and $\chi = 1, 2, 6$. The numerical calculations for $\varepsilon = 0.005$ and $\chi = 6$ reveal that a steady state is reached for all values of Q_i considered. However, in case $\chi = 1$ or $\chi = 2$ we find a range of Q_i -values for which the flow shows so-called persistent oscillations that do not die out, so that no steady state is attained. Finally, we calculate the frequency of the persistent oscillations by means of a Fourier spectral analysis.

The equations (4.1.47) for P , Q , w , S and Z , are solved by numerical integration. Let the discretisation time step be denoted by Δt . Divide the interval $0 \leq r \leq 1$ into M subintervals of equal length $\Delta r = 1/M$. The numerical discretisation scheme used below for the computation of S , Z and w , has been adopted from Malkus et al. [32], [34], [35]; see [34] for a detailed analysis of the stability of the algorithm. For $k = 0, 1, \dots, M, n = 1, 2, 3, \dots$, the stresses $S(r, t)$ and $Z(r, t)$ at $t = t_n := n\Delta t$ and $r = r_k := k\Delta r$ are computed according to the following first-order scheme:

$$\begin{aligned} S(r_k, t_n) &= [1 - \Delta t]S(r_k, t_{n-1}) + \Delta t w(r_k, t_{n-1})[1 + Z(r_k, t_{n-1})], \\ Z(r_k, t_n) &= [1 - \Delta t]Z(r_k, t_{n-1}) - \Delta t w(r_k, t_{n-1})S(r_k, t_n), \end{aligned} \quad (4.3.1)$$

with initial values $S(r_k, 0) = 0$, $Z(r_k, 0) = 0$, $w(r_k, 0) = 0$. Hence, S is treated explicitly (Euler forward), whereas (the nonlinear term in) Z is treated semi-implicitly. Next we compute the pressure $P(t_n)$ by using Euler's forward discretisation method, i.e.

$$P(t_n) = P(t_{n-1}) - \frac{\Delta t}{\chi} [Q(t_{n-1}) - Q_i], \quad (4.3.2)$$

with initial values $P(0) = 0$ and $Q(0) = 0$. Subsequently, for $k = 0, 1, \dots, M$, the velocity gradient $w(r_k, t_n)$ is computed according to

$$w(r_k, t_n) = \frac{4r_k P(t_n) - S(r_k, t_n)}{\varepsilon}. \quad (4.3.3)$$

Finally, we compute the volumetric flow rate $Q(t_n)$ by approximating the integral in (4.1.47)⁴ by the trapezoidal rule, to obtain

$$Q(t_n) = \frac{1}{\varepsilon} \left[P(t_n) - \Delta r \sum_{k=1}^{M-1} r_k^2 S(r_k, t_n) - \frac{1}{2} \Delta r S(1, t_n) \right]. \quad (4.3.4)$$

System (4.1.47) is thus treated explicitly, and for given Q_i , ε and χ we obtain the numerically computed values $P(t_n)$, $Q(t_n)$, $w(r_k, t_n)$, $S(r_k, t_n)$ and $Z(r_k, t_n)$, $k = 1, 2, \dots, M, n = 1, 2, \dots$.

In Figure 4.3 the pressure $P(t)$ and the volumetric flow rate $Q(t)$ are plotted as functions of time t , for $\varepsilon = 0.02$, $\chi = 1$ and $Q_i = 0.1$ (subcritical flow). We observe that $P(t)$ and $Q(t)$ are monotone and smooth functions of t . The numerical computations disclose that also $S(r, t)$, $Z(r, t)$ and $w(r, t)$ are monotone and smooth functions of t , for each value of the radial coordinate r . After sufficient time a steady state is reached. From the numerical results that underlie Figure 4.3, we determine the steady state values \bar{P} , \bar{Q} , $\bar{\omega}(1)$, $\bar{S}(1)$ and $\bar{Z}(1)$, as listed in Table 4.2. It has been checked that these values do satisfy (4.2.3) and the steady state equation $\mathcal{F}(\bar{\omega}(1)) = 4\bar{P}$; cf. (4.2.4). Since $Q_i = 0.1 \in (\bar{Q}_0, \bar{Q}_{crit})$ for $\varepsilon = 0.02$ (see Table 3.1), the steady state pressure \bar{P} is not uniquely determined by just the given inlet flow rate Q_i ; either a classical steady state or a spurt steady state with a discontinuous velocity gradient occurs. The computations for $Q_i = 0.1$ reveal that $\bar{\omega}(1) < \bar{\omega}_M$, implying that the flow reaches a classical steady state with a continuous steady state velocity gradient. As a further check it has been verified that the relation (4.2.9) for classical flow is satisfied. Notice that $\bar{f} = 8\bar{P} = 0.7369$ is equal to the steady state pressure gradient \bar{f} attained in a piston-driven capillary flow with $Q(t) = \bar{Q} = 0.1$, $t \geq 0$; see Table 3.2.

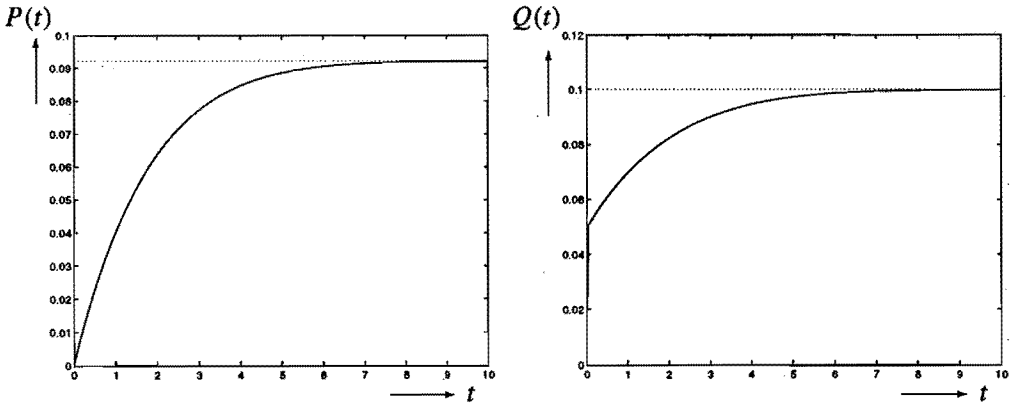


Figure 4.3 The pressure $P(t)$ and the volumetric flow rate $Q(t)$ as functions of time t , for $\varepsilon = 0.02$, $\chi = 1$ and $Q_i = 0.1$, computed according to (4.3.1)-(4.3.4) with $\Delta t = 0.0005$ and $\Delta r = 0.0004$. The dotted lines correspond to the steady state values of Table 4.2.

Q_i	\bar{Q}	\bar{P}	r^*	ω_-^*	ω_+^*	$\omega(1)$	$\bar{S}(1)$	$\bar{Z}(1)$
0.1	0.1	0.09211	-	-	-	0.4249	0.3599	-0.1530
0.6	0.6	0.07933	0.9486	0.3258	10.19	11.58	0.0857	-0.9926
2.0	2.0	0.10845	0.8750	0.4436	15.83	19.08	0.0523	-0.9973

Table 4.2 The computed steady state values \bar{Q} , \bar{P} , r^* , ω_-^* , ω_+^* , $\omega(1)$, $\bar{S}(1)$ and $\bar{Z}(1)$, for a flow driven by the constant inlet flow rate Q_i , with $Q_i = 0.1, 0.6$ and 2.0 , for $\varepsilon = 0.02$ and $\chi = 1$.

To investigate supercritical flow ($Q_i > \bar{Q}_{crit} = 0.1714$) for $\varepsilon = 0.02$ and $\chi = 1$, we take successively $Q_i = 0.6$ and $Q_i = 2.0$. In the Figures 4.4 and 4.5, the pressure $P(t)$ and the volumetric flow rate $Q(t)$ are plotted as functions of time t . We observe for both values of Q_i that in the beginning $P(t)$ shows an overshoot. After sufficient time this overshoot disappears and oscillations in $P(t)$ and $Q(t)$ appear. The numerical computations disclose that also oscillations occur in $S(r, t)$, $Z(r, t)$ and $w(r, t)$ for each radial coordinate r . All these oscillations die out and after sufficient time a steady state is reached. From the numerical results that underlie Figures 4.4 and 4.5, we determine the steady state values \bar{P} , \bar{Q} , $\omega(1)$, $\bar{S}(1)$ and $\bar{Z}(1)$, as listed in Table 4.2. Again it has been checked that these values satisfy (4.2.3) and the steady state equation $\mathcal{F}(\omega(1)) = 4\bar{P}$. The computations for $Q_i = 0.6$ and $Q_i = 2.0$ reveal that both steady states show a discontinuous velocity gradient $\omega(r)$ with exactly one jump from $\omega_-^* < \omega_M$ to $\omega_+^* > \omega_m$ at some radial coordinate $r = r^*$. Furthermore, $\bar{S}(r)$ and $\bar{Z}(r)$ are also discontinuous at $r = r^*$. Recall that $\omega = \omega_-^*$ and $\omega = \omega_+^*$ are the smallest and largest solutions of the equation $\mathcal{F}(\omega) = 4r^*\bar{P}$. Then the values of r^* , ω_-^* and ω_+^* are found by numerical solution of equation (4.2.10), and the values computed are listed in Table 4.2.

To investigate whether for $\varepsilon = 0.02$, $\chi = 1$ and a given flow rate Q_i the flow starting from rest reaches a steady state, we compute the transient flow for several flow rates, varying from $Q_i = 0$ to $Q_i = 4.0$. The result is that for all values of Q_i considered, a steady state is reached.

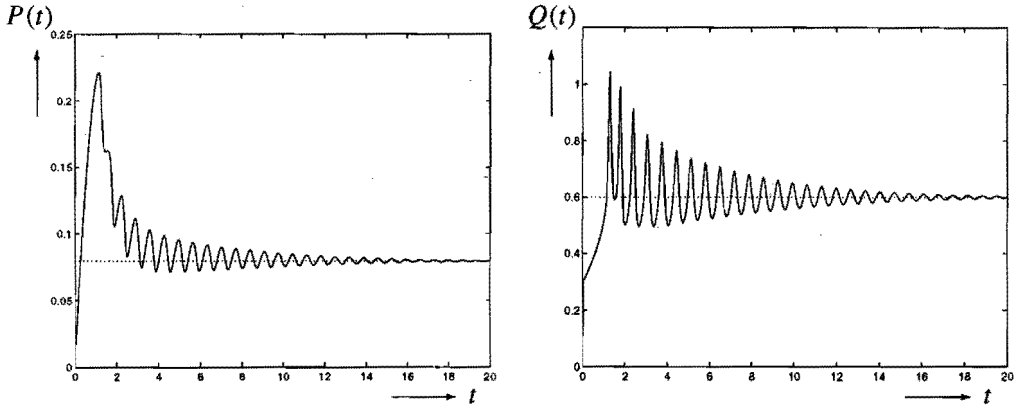


Figure 4.4 The pressure $P(t)$ and the volumetric flow rate $Q(t)$ as functions of time t , for $\varepsilon = 0.02$, $\chi = 1$ and $Q_i = 0.6$, computed according to (4.3.1)-(4.3.4) with $\Delta t = 0.0005$ and $\Delta r = 0.0004$. The dotted lines correspond to the steady state values of Table 4.2.

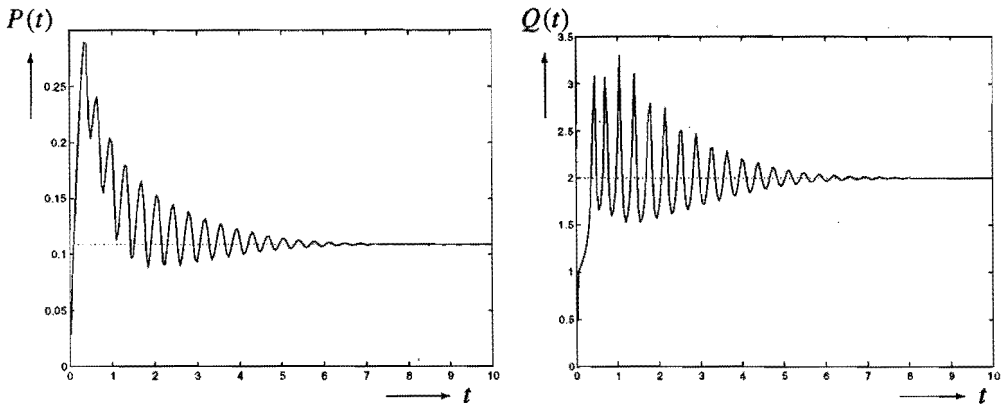


Figure 4.5 The pressure $P(t)$ and the volumetric flow rate $Q(t)$ as functions of time t , for $\varepsilon = 0.02$, $\chi = 1$ and $Q_i = 2.0$, computed according to (4.3.1)-(4.3.4) with $\Delta t = 0.0005$ and $\Delta r = 0.0004$. The dotted lines correspond to the steady state values of Table 4.2.

In Figure 4.6 the steady state pressure \bar{P} attained is plotted versus the inlet flow rate Q_i , for $\varepsilon = 0.02$ and $\chi = 1$; the plot is drawn as a solid curve. The \bar{P} versus Q_i curve is called the flow curve. The functions $\bar{P} = P_{clas}(Q_i)$, $\bar{P} = P_{bottom}(Q_i)$ and $\bar{P} = P_{top}(Q_i)$ are represented by the dotted curves in Figure 4.6, and correspond to classical flow, bottom-jumping and top-jumping, respectively. We observe that for $0 \leq Q_i \leq \bar{Q}_{crit}$, the flow curve coincides with the curve $\bar{P} = P_{clas}(Q_i)$, which demonstrates that the subcritical flow tends to a classical steady state. If the flow becomes supercritical ($Q_i > \bar{Q}_{crit}$), the computations disclose that the steady state velocity gradient $\omega(r)$ is discontinuous at some radial coordinate $r = r^*$. The steady state pressure \bar{P} attained satisfies $P_{bottom}(Q_i) < \bar{P} < P_{top}(Q_i)$ for $Q_i > \bar{Q}_{crit}$, implying that neither top-jumping nor bottom-jumping takes place. The flow curve shows a kink at $Q_i = \bar{Q}_{crit}$ and is S-shaped. Furthermore, the flow curve tends to the curve $\bar{P} = P_{top}(Q_i)$ for Q_i sufficiently large. In Figure 4.7 the thickness $1 - r^*$ of the spurt layer is plotted versus the inlet flow rate Q_i for supercritical flow, and $\varepsilon = 0.02$, $\chi = 1$; the plot is drawn as a solid curve. The functions $1 - r^* = 1 - r_{bottom}^*(Q_i)$ and $1 - r^* = 1 - r_{top}^*(Q_i)$ are represented by the dotted curves in Figure 4.7, and correspond to bottom-jumping and top-jumping, respectively. The value of r^* follows either from the place of the discontinuity in the computed steady state velocity gradient $\omega(r)$, or, more accurately, by numerical solution of equation (4.2.10) with known Q_i and \bar{P} . We observe that the spurt layer becomes thicker with increasing Q_i .

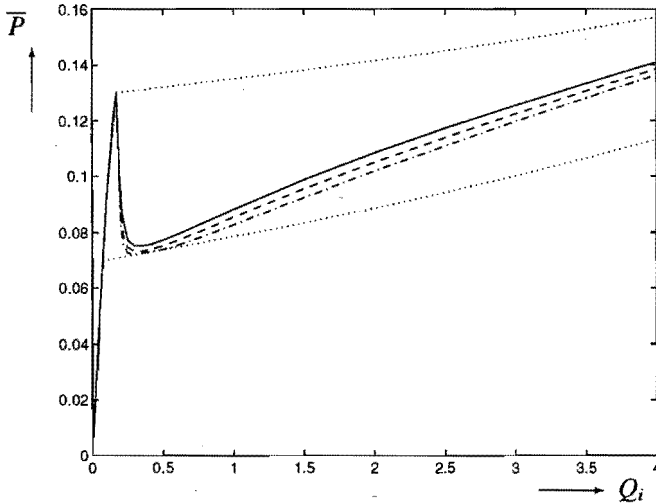


Figure 4.6 The flow curves of the steady state pressure $\bar{P} = \lim_{t \rightarrow \infty} P(t)$ versus the inlet flow rate Q_i , for $\varepsilon = 0.02$ and $\chi = 1$ (solid curve), $\chi = 2$ (dashed curve) and $\chi = 4$ (dashed-dotted curve). The dotted curves correspond to $\bar{P} = P_{clas}(Q_i)$ (classical flow), $\bar{P} = P_{bottom}(Q_i)$ (bottom-jumping) and $\bar{P} = P_{top}(Q_i)$ (top-jumping). The flow curves show a kink at $Q_i = \bar{Q}_{crit} = 0.1714$.

To investigate the influence of the parameter χ , we compute the transient flow for $\chi = 2$ and $\chi = 4$, keeping $\varepsilon = 0.02$, and we compare the numerical results to those obtained in the case $\chi = 1$, $\varepsilon = 0.02$. The numerical computations disclose that for all values of Q_i considered, a steady state is reached. In Figure 4.6 the flow curves are plotted for $\varepsilon = 0.02$ and $\chi = 2$

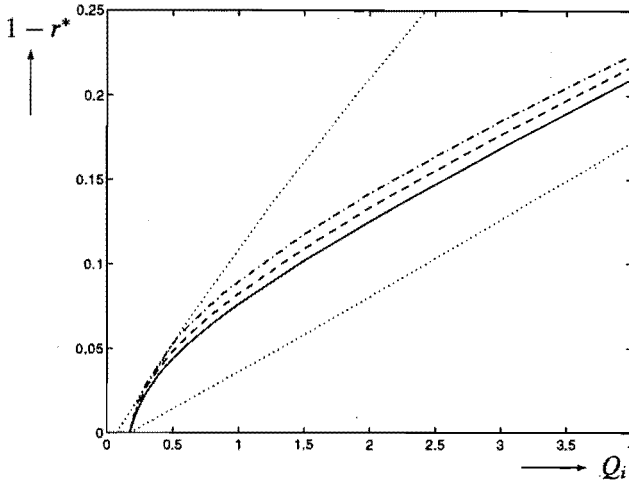


Figure 4.7 The thickness $1 - r^*$ of the spurt layer versus the inlet flow rate Q_i , for $\varepsilon = 0.02$, $Q_i > \bar{Q}_{crit} = 0.1714$ (supercritical flow), and $\chi = 1$ (solid curve), $\chi = 2$ (dashed curve) and $\chi = 4$ (dashed-dotted curve). The dotted curves correspond to $1 - r^* = 1 - r^*_{bottom}(Q_i)$ (bottom-jumping) and $1 - r^* = 1 - r^*_{top}(Q_i)$ (top-jumping).

(dashed curve), and for $\varepsilon = 0.02$ and $\chi = 4$ (dashed-dotted curve). We observe that the flow curves for $\chi = 2$ and $\chi = 4$ are S-shaped, just like the flow curve for $\chi = 1$. Furthermore, the flow curves show a kink at $Q_i = \bar{Q}_{crit}$ independent of χ . Notice that for $Q_i < \bar{Q}_{crit}$ the three flow curves for $\chi = 1, 2$ and 4 coincide, whereas for $Q_i > \bar{Q}_{crit}$ the flow curve for $\chi = 4$ lies below the one for $\chi = 2$, which in its turn lies below the flow curve for $\chi = 1$. Hence, at a fixed supercritical flow rate $Q_i > \bar{Q}_{crit}$, the steady state pressure \bar{P} becomes smaller if χ is changed from $\chi = 1$ to the larger values $\chi = 2$ or $\chi = 4$. In Figure 4.7 the thickness $1 - r^*$ of the spurt layer is plotted versus the inlet flow rate Q_i , for $\varepsilon = 0.02$ and $\chi = 2$ (dashed curve), and for $\varepsilon = 0.02$ and $\chi = 4$ (dashed-dotted curve). We observe that also for $\chi = 2$ and $\chi = 4$ the spurt layer becomes thicker with increasing Q_i . In addition, at a fixed supercritical flow rate $Q_i > \bar{Q}_{crit}$, the spurt layer also becomes thicker if χ is changed from $\chi = 1$ to the larger values $\chi = 2$ or $\chi = 4$.

Next, we investigate the influence of the parameters ε and χ on the transient flow behaviour and the steady state values attained. To that end, we compute the transient flow for several values of the inlet flow rate Q_i , when $\varepsilon = 0.005$ and $\chi = 1, 2$ and 6 . In the Figures 4.8, 4.9 and 4.10 the pressure $P(t)$ and the volumetric flow rate $Q(t)$ are plotted as functions of time t , for $\varepsilon = 0.005$, $\chi = 1$, and $Q_i = 0.2, 0.6$ and 2.0 , respectively. We observe that in the beginning $P(t)$ shows an overshoot, for all the three inlet flow rates. After some time this overshoot disappears and oscillations in $Q(t)$ appear. For $Q_i = 0.6$ and $Q_i = 2.0$, also oscillations in $P(t)$ appear. For $Q_i = 0.2$ and $Q_i = 2.0$, the amplitudes of these oscillations decay, and the oscillations are sufficiently damped out at $t = 20$. Hence, after sufficient time a steady state is reached, if $Q_i = 0.2$ or $Q_i = 2.0$. The computations yield the steady

state values $\bar{P} = 0.05446$, $\bar{Q} = 0.2$ for $Q_i = 0.2$, and $\bar{P} = 0.06002$, $\bar{Q} = 2.0$ for $Q_i = 2.0$. Furthermore, the steady state variables $\omega(r)$, $\bar{S}(r)$ and $\bar{Z}(r)$ are found to be discontinuous at $r = r^*$, with $r^* = 0.9962$ for $Q_i = 0.2$, and $r^* = 0.9514$ for $Q_i = 2.0$. Again the value of r^* follows either from the place of the discontinuity in the computed steady state velocity gradient $\omega(r)$, or, more accurately, by numerical solution of equation (4.2.10) with known Q_i and \bar{P} .

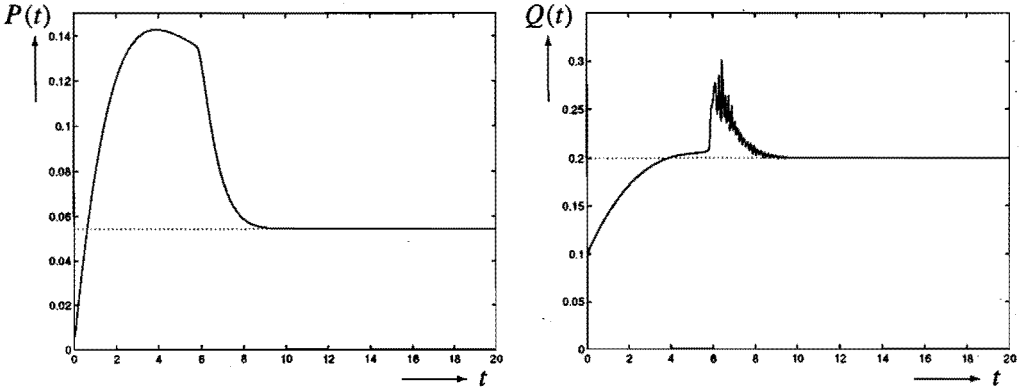


Figure 4.8 The pressure $P(t)$ and the volumetric flow rate $Q(t)$ as functions of time t , for $\varepsilon = 0.005$, $\chi = 1$ and $Q_i = 0.2$, computed according to (4.3.1)-(4.3.4) with $\Delta t = 0.00025$ and $\Delta r = 0.0004$. The dotted lines correspond to the steady state values $\bar{P} = \lim_{t \rightarrow \infty} P(t)$ and $\bar{Q} = \lim_{t \rightarrow \infty} Q(t)$.

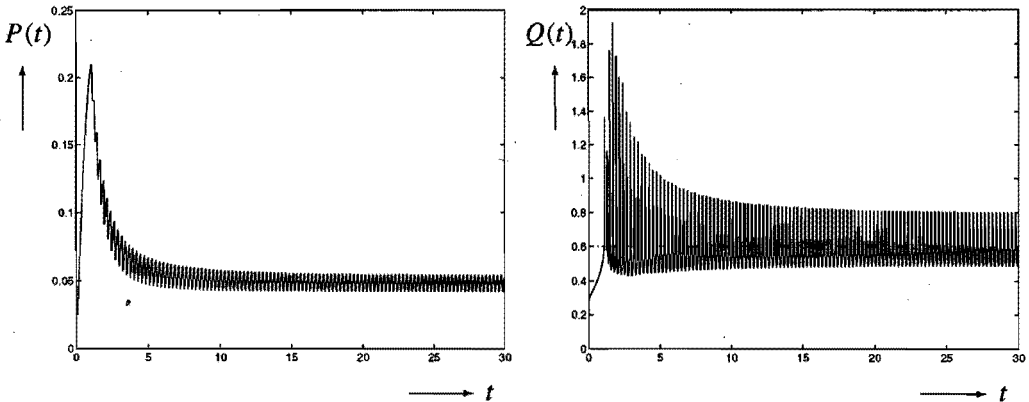


Figure 4.9 The pressure $P(t)$ and the volumetric flow rate $Q(t)$ as functions of time t , for $\varepsilon = 0.005$, $\chi = 1$ and $Q_i = 0.6$, computed according to (4.3.1)-(4.3.4) with $\Delta t = 0.00025$ and $\Delta r = 0.0002$.

For $Q_i = 0.6$, however, we observe in Figure 4.9 that the amplitude of the oscillations in $P(t)$ and $Q(t)$ fails to decay and remains constant after a certain instant. We compute the

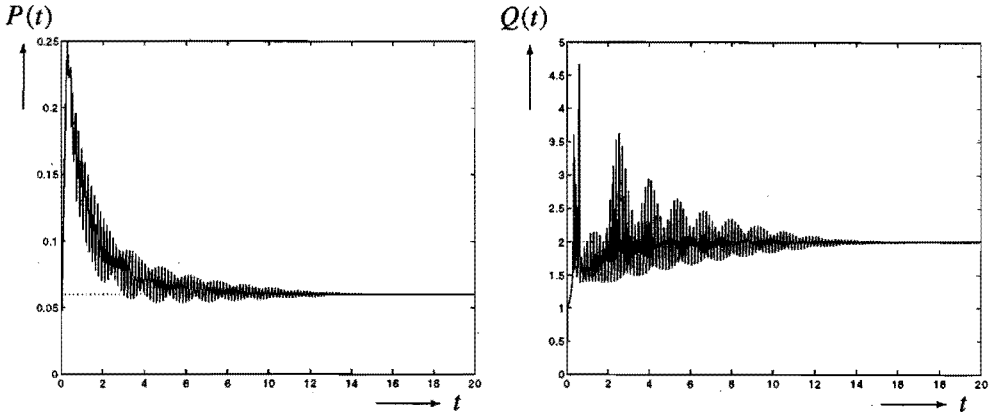


Figure 4.10 The pressure $P(t)$ and the volumetric flow rate $Q(t)$ as functions of time t , for $\varepsilon = 0.005$, $\chi = 1$ and $Q_i = 2.0$, computed according to (4.3.1)-(4.3.4) with $\Delta t = 0.00025$ and $\Delta r = 0.0004$. The dotted lines correspond to the steady state values $\bar{P} = \lim_{t \rightarrow \infty} P(t)$ and $\bar{Q} = \lim_{t \rightarrow \infty} Q(t)$.

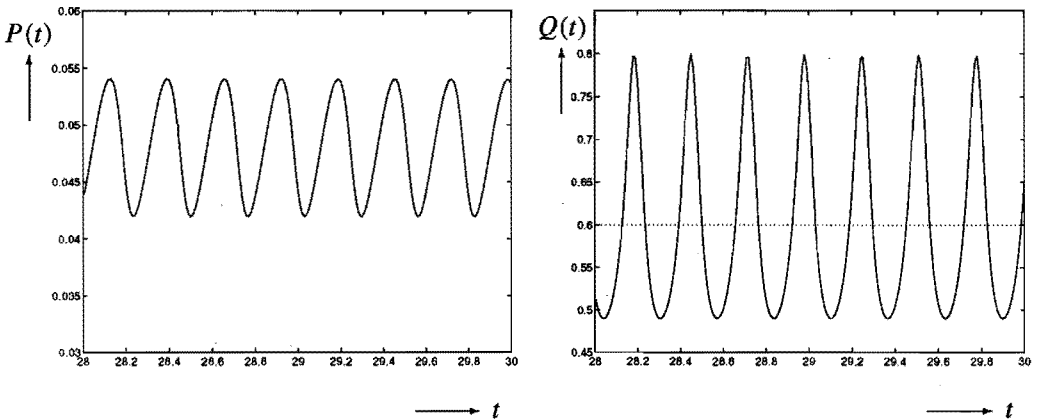


Figure 4.11 The pressure $P(t)$ and the volumetric flow rate $Q(t)$ as functions of time t , for $\varepsilon = 0.005$, $\chi = 1$ and $Q_i = 0.6$, computed according to (4.3.1)-(4.3.4) with $\Delta t = 0.00025$ and $\Delta r = 0.0002$; enlarged detail of Figure 4.9. The dotted line in the right picture corresponds to the inlet flow rate $Q_i = 0.6$.

transient flow up to $t = 200$, at which time the amplitude of the oscillations is still the same as at $t = 30$. Hence, for $Q_i = 0.6$, the functions $P(t)$ and $Q(t)$ do not settle to a stationary value within the time interval of computation, indicating that no steady state is attained. Instead, $P(t)$ and $Q(t)$ show so-called persistent oscillations. The numerical computations for $Q_i = 0.6$ reveal that persistent oscillations also appear in $w(r, t)$, $S(r, t)$ and $Z(r, t)$ for each value of the radial coordinate r . In Figure 4.11 a more detailed plot of the persistent oscillations in $P(t)$ and $Q(t)$ is given. We observe that the amplitude of the persistent oscillations is constant. Furthermore, the span of the oscillations in $P(t)$ is approximately 25 percent of the mean value of $P(t)$, whereas the span of the oscillations in $Q(t)$ is about half the fictitious steady state value $\bar{Q} = Q_i = 0.6$. Finally, we observe that the oscillations in $P(t)$ and $Q(t)$ differ in phase. Although no steady state is attained for $Q_i = 0.6$, the computations show that the oscillating functions $w(r, t)$, $S(r, t)$ and $Z(r, t)$ tend to become discontinuous in r at some radial coordinate $r = r^*$; see Figure 4.12. Recalling the notation $r_k = k\Delta r$, we find that the plots of $w(r_k, t)$ and $w(r_{k+1}, t)$ start to deviate significantly after sufficient time, for a specific index k . Next, the value of r^* is taken as $r^* = (r_k + r_{k+1})/2$, which might be in error by at most $\Delta r/2$. In the computations for $Q_i = 0.6$, the numerical discontinuity appears between $r_k = 0.9788$ and $r_{k+1} = 0.9790$, and we set $r^* = 0.9789$. In Figure 4.12 the stress $S(r, t)$ is plotted as function of the radial coordinate r at the times $t = 28.18$ and $t = 28.30$, for $\varepsilon = 0.005$, $\chi = 1$ and $Q_i = 0.6$. At these times the flow rate $Q(t)$ reaches its maximum and its minimum, respectively. We observe that $S(r, t)$ is discontinuous in r at $t = 28.18$ and $t = 28.30$, so that a spurt layer has formed near the wall. Outside the spurt layer, i.e. for $0 \leq r < r^*$, $S(r, t) \approx 4rP(t)$ is approximately linear in r .

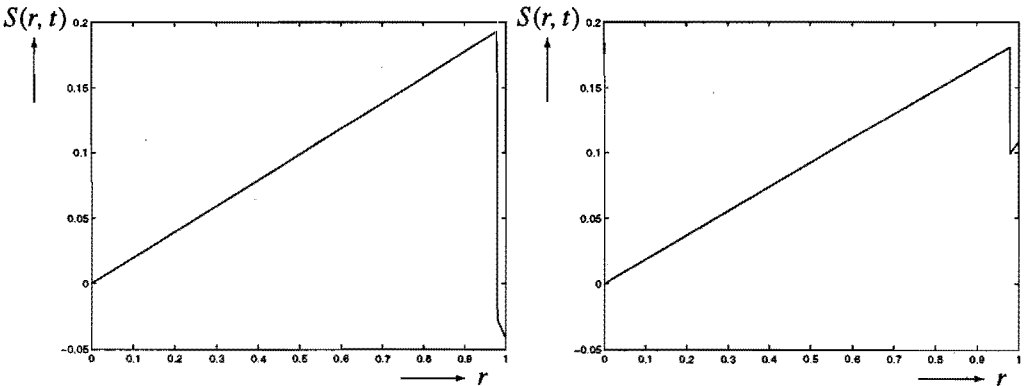


Figure 4.12 The stress $S(r, t)$ as function of the radial coordinate r at the times $t = 28.18$ and $t = 28.30$, at which the flow rate $Q(t)$ reaches its maximum and its minimum, respectively, for $\varepsilon = 0.005$, $\chi = 1$ and $Q_i = 0.6$.

To establish for which inlet flow rates Q_i a steady state is attained (within the time interval of computation) when $\varepsilon = 0.005$ and $\chi = 1, 2, 6$, we compute the transient flow for several flow rates, varying from $Q_i = 0$ to $Q_i = 3.0$. The outcome of the computations for $\chi = 1$ is that a steady state is reached for $Q_i \leq 0.35$ and for $Q_i \geq 0.90$. This steady state is classical when $Q_i \leq \bar{Q}_{crit} = 0.1678$, and corresponds to spurt flow when $\bar{Q}_{crit} < Q_i \leq 0.35$.

or $Q_i \geq 0.90$. For values of Q_i close to 0.35 or 0.90, the time interval within which the flow settles to a steady state, becomes very large. For $0.40 \leq Q_i \leq 0.80$, however, the functions $P(t)$, $Q(t)$, $w(r, t)$, $S(r, t)$ and $Z(r, t)$ show persistent oscillations and fail to settle to stationary values within the time interval of computation. Thus, four different flow regimes can be distinguished, corresponding to different ranges for the inlet flow rate Q_i . For $Q_i > \bar{Q}_{crit}$ (supercritical flow), we find that the (steady state) velocity gradient is discontinuous at some radial coordinate r . The computations for $\varepsilon = 0.005$ and $\chi = 2$ disclose that the transient flow behaviour is similar to that observed when $\varepsilon = 0.005$ and $\chi = 1$. For $Q_i \leq 0.35$ or $Q_i \geq 0.70$, it is found that after sufficient time a steady state is reached. This steady state is classical when $Q_i \leq \bar{Q}_{crit} = 0.1678$, and corresponds to spurt flow when $\bar{Q}_{crit} < Q_i \leq 0.35$ or $Q_i \geq 0.70$. For $0.40 \leq Q_i \leq 0.65$, however, persistent oscillations occur, and the flow fails to settle to a steady state. For $\varepsilon = 0.005$ and $\chi = 6$, the numerical computations reveal that a steady state is reached after sufficient time, for each value of the inlet flow rate Q_i considered.

In Figure 4.13 the flow curve of the steady state pressure $\bar{P} = \lim_{t \rightarrow \infty} P(t)$ versus the inlet flow rate Q_i is plotted for $\varepsilon = 0.005$ and $\chi = 1, 2, 6$. The computed points (Q_i, \bar{P}) are marked by a cross (\times). Notice that the three flow curves are S-shaped. The gaps in the flow curves for $\chi = 1$ and $\chi = 2$ correspond to flow rates Q_i for which persistent oscillations occur and no steady state is attained. We observe that the gap becomes smaller if χ is changed from $\chi = 1$ to the larger value $\chi = 2$, and has disappeared when $\chi = 6$.

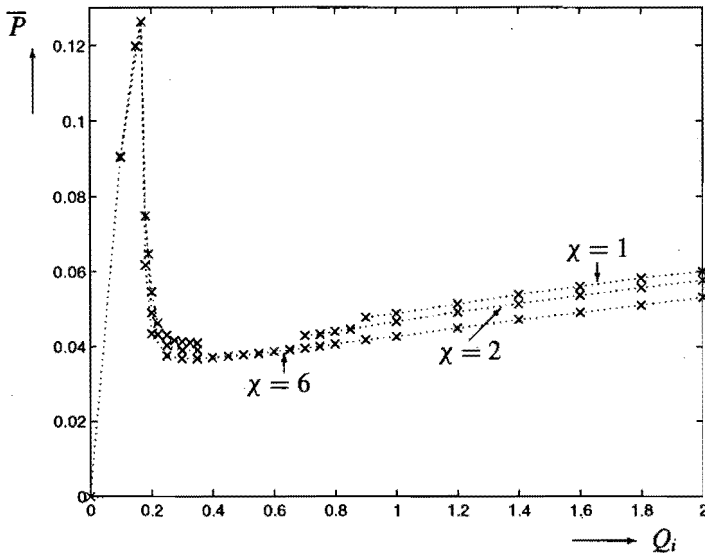


Figure 4.13 The flow curve of the steady state pressure $\bar{P} = \lim_{t \rightarrow \infty} P(t)$ versus the inlet flow rate Q_i , for $\varepsilon = 0.005$ and $\chi = 1, 2, 6$. The points (Q_i, \bar{P}) marked by the crosses (\times) correspond to computed steady states. The gaps in the flow curves for $\chi = 1$ and $\chi = 2$ correspond to flow rates Q_i for which persistent oscillations occur.

In Figure 4.14 the thickness $1 - r^*$ of the spurt layer is plotted versus the inlet flow rate Q_i , for $\varepsilon = 0.005$ and $\chi = 1, 2, 6$. In case the flow tends to a steady state, the computed points $(Q_i, 1 - r^*)$ are marked by a cross (\times); in case persistent oscillations occur the computed

points $(Q_i, 1 - r^*)$ are marked by a dot (\circ). We observe that the spurt layer becomes thicker with increasing Q_i . In addition, at a fixed supercritical flow rate $Q_i > \bar{Q}_{crit}$, the spurt layer also becomes thicker if χ is changed from $\chi = 1$ to the larger values $\chi = 2$ or $\chi = 6$.

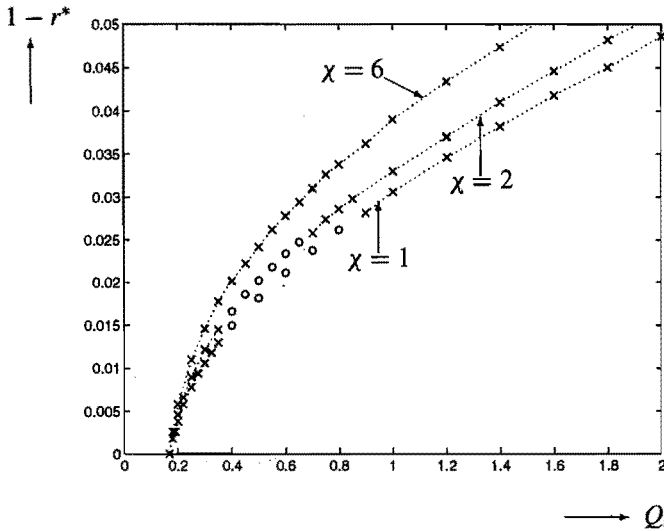


Figure 4.14 The thickness $1 - r^*$ of the spurt layer versus the inlet flow rate Q_i , for $\varepsilon = 0.005$, $Q_i > \bar{Q}_{crit} = 0.1678$, and $\chi = 1, 2, 6$. The points $(Q_i, 1 - r^*)$ marked by the crosses (\times) correspond to computed steady states; the points $(Q_i, 1 - r^*)$ marked by the dots (\circ) correspond to flows for which persistent oscillations occur.

From the numerical results presented in this section we infer that a bounded range $\mathcal{R} = (\bar{Q}_m, \bar{Q}_M)$ of inlet flow rates Q_i exists, for which persistent oscillations occur and no steady state is attained. At $Q_i = \bar{Q}_m$ and $Q_i = \bar{Q}_M$, the transition from a steady state to a state of persistent oscillations and vice versa takes place. The size of \mathcal{R} depends on the value of ε as well as on the value of χ : for $\varepsilon = 0.02$ and $\chi = 1, 2, 4$, and for $\varepsilon = 0.005$ and $\chi = 6$, the range \mathcal{R} is empty, whereas for $\varepsilon = 0.005$ and $\chi = 1, 2$, the range $\mathcal{R} = (\bar{Q}_m, \bar{Q}_M)$ is not empty. For $\varepsilon = 0.005$ and $\chi = 1$, the range \mathcal{R} has transition points \bar{Q}_m between 0.35 and 0.40, and \bar{Q}_M between 0.80 and 0.90. For $\varepsilon = 0.005$ and $\chi = 2$, the range \mathcal{R} has transition points \bar{Q}_m between 0.35 and 0.40, and \bar{Q}_M between 0.65 and 0.70. In the next section we provide an explanation for the occurrence of persistent oscillations.

Finally, we determine the frequency of the computed persistent oscillations by means of a Fourier spectral analysis. We consider the persistent oscillations in the pressure $P(t)$. The function $P(t)$ is taken as a time dependent signal that has been computed over a time interval $t_0 \leq t \leq t_0 + T$ of length T . Then $P(t)$ is expanded in a complex Fourier series, viz.

$$P(t + t_0) = \sum_{k=-\infty}^{\infty} c_k e^{2\pi i k t / T}, \quad 0 \leq t \leq T, \quad (4.3.5)$$

where the Fourier coefficients c_k are given by

$$c_k = \frac{1}{T} \int_0^T P(t + t_0) e^{-2\pi i k t / T} dt. \tag{4.3.6}$$

In (4.3.5) the Fourier component $c_k e^{2\pi i k t / T}$ has frequency $\nu_k = k/T$ and amplitude $|c_k|$. To determine c_k , the signal $P(t)$ is sampled N times at equidistant points $t = t_0 + jT/N$, $j = 0, 1, \dots, N - 1$. Next the integral (4.3.6) is approximated by the discrete Fourier transform

$$c_k = \frac{1}{N} \sum_{j=0}^{N-1} P(t_0 + jT/N) e^{-2\pi i k j / N}, \quad k = 0, 1, \dots, N - 1, \tag{4.3.7}$$

which is conveniently evaluated by means of a fast Fourier transform (FFT) algorithm. For a survey of discrete Fourier transforms and FFT algorithms, see the books by Brigham [7], and Elliot and Rao [11].

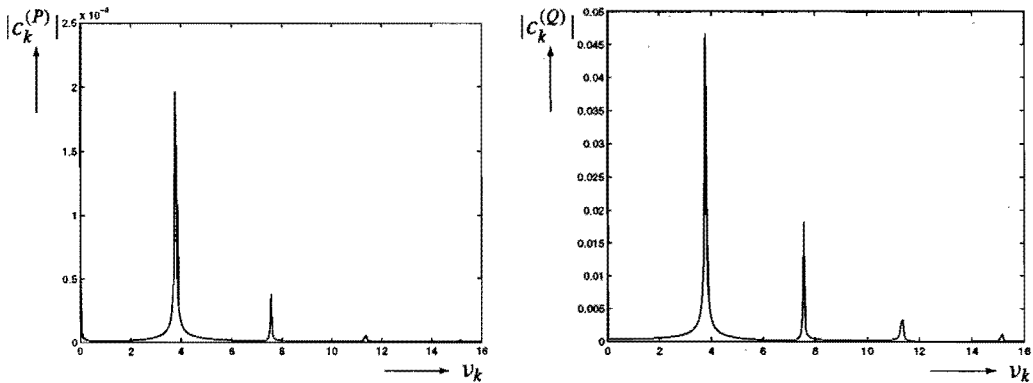


Figure 4.15 The amplitude spectra $|c_k^{(P)}|$ and $|c_k^{(Q)}|$ of the pressure $P(t)$ and the volumetric flow rate $Q(t)$, respectively, as function of the frequency $\nu_k = k/30$, $k = 0, \dots, 480$, for $\varepsilon = 0.005$, $\chi = 1$ and $Q_i = 0.6$. The signals $P(t)$ and $Q(t)$ computed for $10 \leq t \leq 40$, are sampled at intervals 0.01.

As an example we consider the persistent oscillations in the pressure $P(t)$ and the volumetric flow rate $Q(t)$, shown in Figures 4.9 and 4.11, and occurring in the transient flow for $\varepsilon = 0.005$, $\chi = 1$ and $Q_i = 0.6$. The signals $P(t)$ and $Q(t)$, computed over the time interval $10 \leq t \leq 40$ of length $T = 30$, are sampled at intervals $T/N = 0.01$, so that $N = 3000$ samples are taken. By use of the FFT algorithm of 'Matlab' applied to (4.3.7), we compute the Fourier coefficients $c_k^{(P)}$ and $c_k^{(Q)}$ of $P(t)$ and $Q(t)$, respectively. In Figure 4.15 the amplitude spectra $|c_k^{(P)}|$ and $|c_k^{(Q)}|$ are plotted as functions of the frequency $\nu_k = k/T$, $k = 0, \dots, 480$. In this figure we distinguish five peaks in both $|c_k^{(P)}|$ and $|c_k^{(Q)}|$. The computations show that in both spectra the peaks are located at $\nu_0 = 0$, $\nu_{113} = 3.77$, $\nu_{227} = 7.57$, $\nu_{341} = 11.37$ and $\nu_{455} = 15.17$. These locations correspond to the so-called dominant frequencies. We observe that the dominant frequencies are approximately integral multiples of $\nu_{113} = 3.77$. The latter value is called the main frequency of the signal, to be denoted by ν . Thus we have $\nu = 3.77$

as the frequency of the persistent oscillations in the transient flow for $\varepsilon = 0.005$, $\chi = 1$ and $Q_i = 0.6$. The value $\nu = 3.77$ agrees very well with the frequency 3.75, determined from Figure 4.11 by counting the number of oscillations per unit of time. As a further check we have verified that a spectral analysis of the signal $w(r, t)$ for several values of r , produces the same main frequency $\nu = 3.77$. Our computations also show that $c_0^{(Q)} \approx Q_i = 0.6$, suggesting that the average value of $Q(t)$ is equal to the fictitious steady state value $\bar{Q} = Q_i$.

Q_i	χ	ν	Q_i	χ	ν
0.4	1	3.23	0.4	2	2.81
0.5	1	3.50	0.5	2	3.06
0.6	1	3.77	0.6	2	3.30
0.7	1	4.00			
0.8	1	4.27			

Table 4.3 The main frequency ν of persistent oscillations, for $\varepsilon = 0.005$, $\chi = 1$, $Q_i = 0.4, 0.5, 0.6, 0.7, 0.8$ ($\in \mathcal{R}$), and $\varepsilon = 0.005$, $\chi = 2$, $Q_i = 0.4, 0.5, 0.6$ ($\in \mathcal{R}$).

The same spectral analysis has been carried out for several other flows showing persistent oscillations. Thus the amplitude spectra $|c_k^{(P)}|$ and $|c_k^{(Q)}|$ of the signals $P(t)$ and $Q(t)$ have been computed by means of the discrete Fourier transform (4.3.7), for transient flows at given ε , χ and $Q_i \in \mathcal{R}$. In all cases considered the computations show that the signals $P(t)$ and $Q(t)$ have the same main frequency ν . In Table 4.3, the frequency ν of the persistent oscillations is given for $\varepsilon = 0.005$, $\chi = 1$, $Q_i = 0.4, 0.5, 0.6, 0.7, 0.8$, and for $\varepsilon = 0.005$, $\chi = 2$, $Q_i = 0.4, 0.5, 0.6$. We observe that ν increases with increasing $Q_i \in \mathcal{R}$. On the other hand, at a given $Q_i \in \mathcal{R}$, the frequency ν decreases if χ is changed from $\chi = 1$ to the larger value $\chi = 2$.

ε	r^*	ν
0.005	0.9789	3.77
0.004	0.9818	4.37
0.003	0.9849	5.37
0.002	0.9883	7.10
0.001	0.9927	11.42

Table 4.4 The radial coordinate r^* at which $w(r, t)$ is discontinuous, and the main frequency ν for flows showing persistent oscillations, for $\chi = 1$, $Q_i = 0.6$ and $\varepsilon = 0.005, 0.004, 0.003, 0.002$ and 0.001 .

To investigate the dependence of the frequency ν on ε , we compute the transient flow for $\chi = 1$, $Q_i = 0.6$ and $\varepsilon = 0.005, 0.004, 0.003, 0.002, 0.001$. The computations reveal for the values of ε considered, that the flow shows persistent oscillations. Furthermore, the velocity gradient $w(r, t)$ tends to become discontinuous in r at some radial coordinate $r = r^*$. Again, we calculate the amplitude spectra $|c_k^{(P)}|$ and $|c_k^{(Q)}|$ of the signals $P(t)$ and $Q(t)$ by means of the discrete Fourier transform. The outcome of the calculations is that, for given ε , the signals $P(t)$ and $Q(t)$ have the same main frequency ν . In Table 4.4, the values of ν and r^*

are given for $\chi = 1$, $Q_i = 0.6$ and $\varepsilon = 0.005, 0.004, 0.003, 0.002, 0.001$. We observe that ν strongly depends on ε , in such a way that ν increases with decreasing ε . Furthermore, we see that the spurt layer becomes thinner with decreasing ε . In the next section it is found, just by comparison of numerical values, that $\nu \approx \Omega/2\pi$, where Ω is the imaginary part of the complex eigenvalue that comes up in the stability analysis of the steady state solution.

4.4 Stability analysis

In this section we provide an explanation for the occurrence of persistent oscillations, as observed in Section 4.3, by means of a linearized stability analysis of the steady state solution. It will turn out that the transient flow showing persistent oscillations corresponds precisely to the steady state solution being unstable. Likewise, if the transient flow tends to a steady state, then correspondingly the steady state solution is found to be stable. In Section 4.3 the range \mathcal{R} of flow rates Q_i for which persistent oscillations occur, was found to depend on the parameters ε and χ . In this section we further investigate the dependence of \mathcal{R} on ε and χ by additional numerical computations of the transient flow.

From the results of Section 4.3 we infer that the prescribed inlet flow rate Q_i completely determines the transient flow behaviour. For $Q_i > \bar{Q}_{crit}$, the transient flow is found to either tend to a spurt steady state or to show persistent oscillations. If a spurt steady state is attained, the numerical results yield the values of the steady state pressure $\bar{P} = \lim_{t \rightarrow \infty} P(t)$, the steady state flow rate $\bar{Q} = \lim_{t \rightarrow \infty} Q(t) = Q_i$, and of the steady state velocity gradient $\omega(r) = \lim_{t \rightarrow \infty} w(r, t)$. This velocity gradient is discontinuous with one jump from $\omega_-^* < \omega_M$ to $\omega_+^* > \omega_m$ at $r = r^* (< 1)$. The steady state values \bar{P} and r^* satisfy the relation (4.2.10), while $\omega(r)$ is the smallest or the largest solution of the steady state equation $\mathcal{F}(\omega(r)) = 4r\bar{P}$, dependent on whether $0 \leq r < r^*$ or $r^* < r \leq 1$, respectively. If persistent oscillations occur, however, no steady state is attained. In that case the velocity gradient $w(r, t)$, calculated at $r = r_k = k\Delta r$, is found to show after sufficient time a numerical discontinuity between r_k and r_{k+1} for some specific index k . By taking $r^* = (r_k + r_{k+1})/2$, we assign a value to the radial coordinate r^* at which $w(r, t)$ is discontinuous. The fictitious steady state solution corresponding to persistent oscillations is then determined as follows: the fictitious steady state pressure \bar{P} is determined from Q_i and r^* such that (4.2.10) is satisfied, while the fictitious steady state velocity gradient $\omega(r)$ is the smallest or the largest root of $\mathcal{F}(\omega(r)) = 4r\bar{P}$, dependent on whether $0 \leq r < r^*$ or $r^* < r \leq 1$, respectively. Thus, in case of a spurt steady state as well as in case of persistent oscillations, the (fictitious) steady state solution satisfies the equations of Section 4.2.

We now proceed with the stability analysis of the (fictitious) steady state solution. Analogous to Malkus et al. [36, Sec. 5], we consider the solution of the system (4.1.47) to consist of a stationary part plus a dynamic part:

$$\begin{aligned} P(t) &= \bar{P} + \psi(t), & S(r, t) &= \bar{S}(r) + X(r, t), & w(r, t) &= \omega(r) + \xi(r, t), \\ Q(t) &= \bar{Q} + q(t), & Z(r, t) &= \bar{Z}(r) + Y(r, t), \end{aligned} \quad (4.4.1)$$

where ψ, q, ξ, X and Y are dynamic perturbations. Substitution of (4.4.1) into (4.1.47) yields,

with the use of (4.2.2),

$$\begin{aligned} \varepsilon\xi(r, t) + X(r, t) &= 4r\psi(t), & \psi(t) &= \varepsilon q(t) + \int_0^1 r^2 X(r, t) dr, \\ \frac{\partial X}{\partial t} &= -X + (1 + \bar{Z})\xi + \omega Y + \xi Y, & \frac{\partial Y}{\partial t} &= -Y - \bar{S}\xi - \omega X - \xi X, \\ \frac{d\psi(t)}{dt} &= -\frac{1}{\chi}q(t). \end{aligned} \quad (4.4.2)$$

Eliminating ξ by means of (4.4.2)¹, we obtain the following two ordinary differential equations for X and Y :

$$\begin{aligned} \begin{pmatrix} \frac{\partial X}{\partial t} \\ \frac{\partial Y}{\partial t} \end{pmatrix} &= \begin{pmatrix} -1 - \frac{1 + \bar{Z}}{\varepsilon} & \omega \\ \frac{\bar{S}}{\varepsilon} - \omega & -1 \end{pmatrix} \begin{pmatrix} X \\ Y \end{pmatrix} + \frac{4r\psi}{\varepsilon} \begin{pmatrix} 1 + \bar{Z} \\ -\bar{S} \end{pmatrix} \\ &\quad + \frac{4r\psi - X}{\varepsilon} \begin{pmatrix} Y \\ -X \end{pmatrix}. \end{aligned} \quad (4.4.3)$$

Expressing \bar{S} and \bar{Z} in terms of ω according to (4.2.3), we rewrite (4.4.3) as

$$\frac{\partial}{\partial t} \begin{pmatrix} X(r, t) \\ Y(r, t) \end{pmatrix} = \mathcal{A}(\omega(r)) \begin{pmatrix} X(r, t) \\ Y(r, t) \end{pmatrix} + \frac{4r\psi(t)}{\varepsilon} \mathbf{a}(\omega(r)) + \mathbf{G}(X, Y, \psi), \quad (4.4.4)$$

where the matrix \mathcal{A} and the vector \mathbf{a} are given by

$$\mathcal{A}(\omega) = \begin{pmatrix} -1 - \frac{1}{\varepsilon(1 + \omega^2)} & \omega \\ \frac{\omega}{\varepsilon(1 + \omega^2)} - \omega & -1 \end{pmatrix}, \quad \mathbf{a}(\omega) = \begin{pmatrix} \frac{1}{1 + \omega^2} \\ -\frac{\omega}{1 + \omega^2} \end{pmatrix}, \quad (4.4.5)$$

and the vector \mathbf{G} consists of terms of second order in the perturbations.

Next, we consider the linearized form of the system of equations (4.4.4) and (4.4.2)^{2,5}. In order to determine the stability properties of the solution of the linearized system, we look for a non-trivial solution of the form

$$X(r, t) = \bar{X}(r)e^{zt}, \quad Y(r, t) = \bar{Y}(r)e^{zt}, \quad \psi(t) = \bar{\psi}e^{zt}, \quad q(t) = \bar{q}e^{zt}, \quad (4.4.6)$$

where z is the eigenvalue parameter. Substitution of (4.4.6) into (4.4.4) with $\mathbf{G} = \mathbf{0}$ yields

$$z \begin{pmatrix} \bar{X} \\ \bar{Y} \end{pmatrix} = \mathcal{A} \begin{pmatrix} \bar{X} \\ \bar{Y} \end{pmatrix} + \frac{4r\bar{\psi}}{\varepsilon} \mathbf{a}, \quad (4.4.7)$$

while substitution of (4.4.6) into (4.4.2)^{2,5} leads to

$$\bar{\psi} = \varepsilon\bar{q} + \int_0^1 r^2 \bar{X}(r) dr, \quad z\bar{\psi} = -\frac{1}{\chi}\bar{q}. \quad (4.4.8)$$

Provided that the matrix $zI - \mathcal{A}$ is non-singular, the solution of (4.4.7) expressed in terms of $\bar{\psi}$ reads

$$\bar{X}(r) = 4ra(r, z)\bar{\psi}, \quad \bar{Y}(r) = 4rb(r, z)\bar{\psi}, \quad (4.4.9)$$

where the functions a and b are given by

$$a(r, z) = \frac{z + 1 - \omega^2(r)}{(z + 1)(1 + \varepsilon(z + 1)) - (1 - \varepsilon - \varepsilon(z + 1)^2)\omega^2(r) + \varepsilon\omega^4(r)}, \quad (4.4.10)$$

$$b(r, z) = -\frac{(z + 2)\omega(r)}{(z + 1)(1 + \varepsilon(z + 1)) - (1 - \varepsilon - \varepsilon(z + 1)^2)\omega^2(r) + \varepsilon\omega^4(r)}. \quad (4.4.11)$$

Finally, by using (4.4.9)¹ in (4.4.8) we are led to the eigenvalue equation

$$1 = 4 \int_0^1 a(r, z)r^3 dr - \varepsilon\chi z. \quad (4.4.12)$$

Changing in the integral the variable of integration from r to ω by writing $r = \mathcal{F}(\omega)/4\bar{P}$, we transform equation (4.4.12) into

$$\Psi(z, Q_i) := 1 + \varepsilon\chi z - \frac{1}{64\bar{P}^4} \left(\int_0^{\omega_-^z} + \int_{\omega_+^*}^{\omega_{wall}} \right) \bar{a}(\omega, z) \mathcal{F}^3(\omega) \mathcal{F}'(\omega) d\omega = 0, \quad (4.4.13)$$

where $\bar{a}(\omega(r), z) := a(r, z)$. Notice that $\Psi(z, Q_i) = \Phi(z, Q_i) + \varepsilon\chi z$, where Φ is given by (3.4.13). Thus, for the steady state solution determined by Q_i , the eigenvalues z are the roots of equation (4.4.13). Analogous to the stability theory of ordinary differential equations, the following stability criteria apply: The steady state solution is unstable if there is at least one eigenvalue z with a positive real part ($\text{Re } z > 0$), whereas the steady state solution is stable if all eigenvalues z have a negative real part ($\text{Re } z < 0$).

To find the eigenvalues z we set $z = x + iy$ with $x, y \in \mathbb{R}$ in (4.4.13), and solve numerically

$$\text{Re} \{ \Psi(x + iy, Q_i) \} = 0, \quad \text{Im} \{ \Psi(x + iy, Q_i) \} = 0, \quad (4.4.14)$$

by means of a program package for solving nonlinear equations. Since $\Psi(\bar{z}, Q_i) = \overline{\Psi(z, Q_i)}$, the eigenvalues are either real or appear as complex conjugate pairs. The numerical computations reveal that, for the range of flow rates Q_i we explored, equation (4.4.13) has three eigenvalues z : one real eigenvalue $z = x_0 < 0$, and two complex conjugate eigenvalues $z = z_0^\pm := \lambda_0 \pm i\Omega$.

In Table 4.5 the computed eigenvalues $z = x_0$ and $z = z_0^\pm = \lambda_0 \pm i\Omega$ are presented for flows driven by a constant inlet flow rate Q_i , varying from $Q_i = 0.19 > \bar{Q}_{crit}$ to $Q_i = 3.0$, in case $\varepsilon = 0.02$, $\chi = 1$. In this table also the radial coordinate r^* at which the steady state velocity gradient $\omega(r)$ is discontinuous, and the steady state pressure $\bar{P} = \lim_{t \rightarrow \infty} P(t)$ are listed; cf. Figures 4.6 and 4.7. We observe that all eigenvalues have a negative real part ($x_0 < 0$ and $\text{Re } z_0^\pm < 0$). Hence, the steady state solution is stable for each value of Q_i . This stability result corresponds precisely to the result of Section 4.3, where we found that for $\varepsilon = 0.02$ and

Q_i	r^*	\bar{P}	x_0	z_0^\pm
0.19	0.9954	0.10122	-0.825	$-0.980 \pm 0.256i$
0.20	0.9934	0.09347	-0.859	$-1.126 \pm 0.070i$
0.25	0.9834	0.07725	-3.275	$-0.682 \pm 8.178i$
0.30	0.9762	0.07526	-4.724	$-0.360 \pm 7.314i$
0.40	0.9650	0.07562	-6.202	$-0.181 \pm 7.603i$
0.50	0.9562	0.07730	-6.972	$-0.197 \pm 8.381i$
0.60	0.9486	0.07933	-7.551	$-0.249 \pm 9.188i$
0.80	0.9354	0.08372	-8.509	$-0.371 \pm 10.694i$
1.00	0.9238	0.08818	-9.345	$-0.491 \pm 12.049i$
2.00	0.8750	0.10845	-11.209	$-0.770 \pm 14.961i$
3.00	0.8314	0.12546	-15.944	$-1.048 \pm 21.719i$

Table 4.5 The computed eigenvalues $z = x_0$ and $z = z_0^\pm$, which are the roots of the eigenvalue equation $\Psi(z, Q_i) = 0$, for flows driven by a constant inlet flow rate Q_i , and $\varepsilon = 0.02$, $\chi = 1$. The radial coordinate r^* signifies the position of the discontinuity in the steady state velocity gradient $\omega(r)$, and $\bar{P} = \lim_{t \rightarrow \infty} P(t)$ is the steady state pressure.

$\chi = 1$ the transient flow shows damped oscillations and tends to a steady state for each value of Q_i .

In Table 4.6 the computed eigenvalues $z = x_0$ and $z = z_0^\pm = \lambda_0 \pm i\Omega$ are presented for flows driven by a constant inlet flow rate Q_i , varying from $Q_i = 0.18 > \bar{Q}_{crit}$ to $Q_i = 3.0$, in case $\varepsilon = 0.005$, $\chi = 1$. In this table also the radial coordinate r^* at which the (steady state) velocity gradient is discontinuous, and the steady state pressure $\bar{P} = \lim_{t \rightarrow \infty} P(t)$ (if attained) are listed. The numerical values of \bar{P} and r^* versus Q_i are in accordance with Figures 4.13 and 4.14. We observe that for $Q_i \leq 0.35$ and $Q_i \geq 0.90$ all eigenvalues have a negative real part ($x_0 < 0$ and $\text{Re } z_0^\pm < 0$), whereas for $0.40 \leq Q_i \leq 0.80$ the eigenvalues $z = z_0^\pm$ have a positive real part ($\text{Re } z_0^\pm > 0$). Hence, the steady state solution is stable for $0 \leq Q_i \leq 0.35$ and $Q_i \geq 0.90$, whereas the (fictitious) steady state solution is unstable for $0.40 \leq Q_i \leq 0.80$. For comparison we quote the result of Section 4.3 in case $\varepsilon = 0.005$, $\chi = 1$: The transient flow shows damped oscillations and tends to steady state for $0 \leq Q_i \leq 0.35$ and $Q_i \geq 0.90$, whereas persistent oscillations occur and no steady state is attained for $0.40 \leq Q_i \leq 0.80$. Thus we conclude that stability of the steady state solution corresponds precisely to the transient flow tending to a steady state, whereas instability of the steady state solution agrees with the occurrence of persistent oscillations. The gap in the flow curve of Figure 4.13 and the dots (o) in Figure 4.14 correspond to steady state solutions that are unstable.

The transition from a spurt steady state to a state of persistent oscillations and vice versa takes place at the flow rates $Q_i = \bar{Q}_m$ and $Q_i = \bar{Q}_M$. Using the results of the linearized stability analysis, we now determine \bar{Q}_m and \bar{Q}_M as the flow rates at which the transition from a stable steady state solution to an unstable fictitious steady state solution and vice versa takes place. To that end the following procedure is adopted. Starting from a numerical computation of the transient flow for given values of Q_i , ε and χ , we determine the radial coordinate r^* at which the (steady state) velocity gradient shows a numerical discontinuity. Next, we

Q_i	r^*	\bar{P}	x_0	z_0^\pm
0.18	0.9982	0.07482	-0.916	$-1.110 \pm 62.641i$
0.20	0.9962	0.05446	-2.238	$-0.980 \pm 35.571i$
0.25	0.9922	0.04301	-4.737	$-0.588 \pm 22.915i$
0.30	0.9894	0.04127	-6.564	$-0.254 \pm 20.612i$
0.35	0.9870	0.04084	-7.981	$-0.029 \pm 20.067i$
0.40	0.9850	-	-8.974	$0.073 \pm 20.413i$
0.50	0.9818	-	-10.249	$0.093 \pm 22.084i$
0.60	0.9789	-	-11.342	$0.078 \pm 23.696i$
0.70	0.9762	-	-12.336	$0.051 \pm 25.194i$
0.80	0.9738	-	-13.172	$0.001 \pm 26.747i$
0.90	0.9718	0.04772	-13.802	$-0.076 \pm 28.487i$
1.00	0.9694	0.04877	-14.697	$-0.102 \pm 29.603i$
1.40	0.9618	0.05381	-17.306	$-0.322 \pm 34.677i$
2.00	0.9514	0.06002	-20.959	$-0.632 \pm 40.578i$
3.00	0.9366	0.06909	-26.072	$-1.038 \pm 49.010i$

Table 4.6 The computed eigenvalues $z = x_0$ and $z = z_0^\pm$, which are the roots of the eigenvalue equation $\Psi(z, Q_i) = 0$, for flows driven by a constant inlet flow rate Q_i , and $\varepsilon = 0.005$, $\chi = 1$. The radial coordinate r^* signifies the position of the discontinuity in the (steady state) velocity gradient, and $\bar{P} = \lim_{t \rightarrow \infty} P(t)$ is the steady state pressure.

calculate \bar{Q}_m and \bar{Q}_M as the values of Q_i for which the eigenvalue equation $\Psi(z, Q_i) = 0$ has two purely imaginary roots $z = \pm i\Omega$. In this way we find, for example, that $\bar{Q}_m \approx 0.36$ and $\bar{Q}_M \approx 0.81$, if $\varepsilon = 0.005$ and $\chi = 1$.

The range $\mathcal{R} = (\bar{Q}_m, \bar{Q}_M)$ of inlet flow rates Q_i for which persistent oscillations occur depends on the parameters ε and χ . Starting from numerical computations of the transient flow for various values of Q_i , ε and χ , we determine the transition points \bar{Q}_m and \bar{Q}_M by the procedure described above. In Figure 4.16 the range \mathcal{R} obtained is plotted for $\varepsilon = 0.005$, and $\chi = 1, 2, 3, 4, 5, 6$. The dotted line corresponds to $Q_i = \bar{Q}_{crit} = 0.1678$, and the transition points \bar{Q}_m and \bar{Q}_M of \mathcal{R} are marked by dots (\circ). The dots lie on the boundary of a region in the (χ, Q_i) -plane. For parameters (χ, Q_i) inside this region the flow shows persistent oscillations, whereas for (χ, Q_i) outside this region the flow tends to a (stable) steady state. We observe that $\bar{Q}_m \approx 0.35$, whereas \bar{Q}_M strongly depends on χ . Furthermore, \mathcal{R} becomes smaller with increasing χ . The numerical computations reveal that $\mathcal{R} = \emptyset$, for $\chi = 6$. Hence, a critical value χ_{crit} , dependent on the value of ε , exists below which persistent oscillations may occur. In conclusion, if $\chi \geq \chi_{crit} = 6$ and $\varepsilon = 0.005$, the flow driven by a constant inlet flow rate Q_i tends to a steady state for each value of Q_i ; if $\chi < \chi_{crit} = 6$, the flow tends to a steady state if $Q_i \notin \mathcal{R}$, whereas the flow shows persistent oscillations if $Q_i \in \mathcal{R}$.

In Figure 4.17 the range \mathcal{R} obtained from the numerical computations is plotted for $\chi = 1$, and $\varepsilon = 0.001$ (0.001) 0.010. The dotted curve corresponds to $Q_i = \bar{Q}_{crit}$, and the transition points \bar{Q}_m and \bar{Q}_M of \mathcal{R} are marked by dots (\circ). The dots lie on the boundary of a region in the (ε, Q_i) -plane. For parameters (ε, Q_i) inside this region the flow shows persistent oscillations, whereas for (ε, Q_i) outside this region the flow tends to a (stable) steady state.

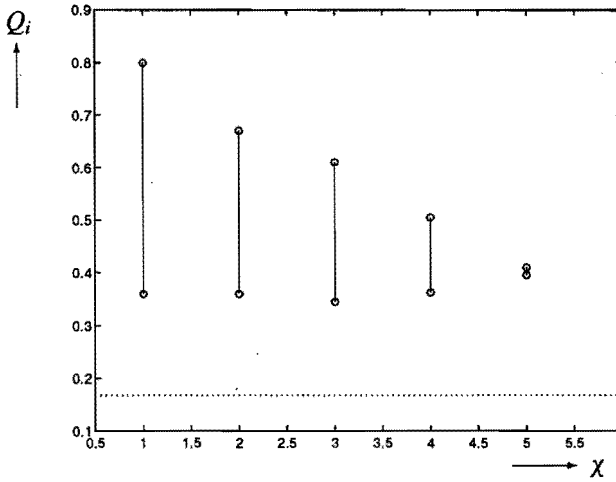


Figure 4.16 The range $\mathcal{R} = (\bar{Q}_m, \bar{Q}_M)$ of inlet flow rates Q_i for which persistent oscillations occur, for $\varepsilon = 0.005$ and $\chi = 1, 2, 3, 4, 5$; $\mathcal{R} = \emptyset$ for $\chi = 6$. The transition points $Q_i = \bar{Q}_m$ and $Q_i = \bar{Q}_M$ are marked by dots (\circ). The dotted line corresponds to $Q_i = \bar{Q}_{crit} = 0.1678$.

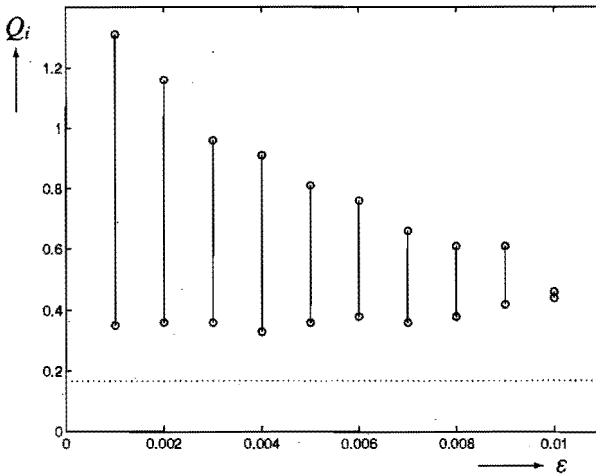


Figure 4.17 The range $\mathcal{R} = (\bar{Q}_m, \bar{Q}_M)$ of inlet flow rates Q_i for which persistent oscillations occur, for $\chi = 1$ and $\varepsilon = 0.001$ (0.001) 0.010; $\mathcal{R} = \emptyset$ for $\varepsilon = 0.011$. The transition points $Q_i = \bar{Q}_m$ and $Q_i = \bar{Q}_M$ are marked by dots (\circ). The dotted curve corresponds to $Q_i = \bar{Q}_{crit}$.

We observe that $\bar{Q}_m \approx 0.35$, whereas \bar{Q}_M strongly depends on ε . Furthermore, \mathcal{R} becomes smaller with increasing ε . The numerical computations reveal that $\mathcal{R} = \emptyset$, for $\varepsilon = 0.011$. Hence, a critical value ε_{crit} , dependent on the value of χ , exists below which persistent oscillations may occur. In conclusion, if $\varepsilon \geq \varepsilon_{crit} = 0.011$ and $\chi = 1$, the flow driven by a constant inlet flow rate Q_i tends to a steady state for each value of Q_i ; if $\varepsilon < \varepsilon_{crit} = 0.011$, the flow tends to a steady state if $Q_i \notin \mathcal{R}$, whereas the flow shows persistent oscillations if $Q_i \in \mathcal{R}$.

ε	χ	Q_i	x_0	z_0^\pm	$\Omega/2\pi$	ν
0.005	1	0.4	-8.974	$0.073 \pm 20.413i$	3.25	3.23
0.005	1	0.5	-10.249	$0.093 \pm 22.084i$	3.51	3.50
0.005	1	0.6	-11.342	$0.078 \pm 23.696i$	3.77	3.77
0.005	1	0.7	-12.336	$0.051 \pm 25.194i$	4.01	4.00
0.005	1	0.8	-13.172	$0.001 \pm 26.747i$	4.26	4.27
0.005	2	0.4	-7.327	$0.046 \pm 17.573i$	2.80	2.81
0.005	2	0.5	-8.296	$0.066 \pm 19.078i$	3.04	3.06
0.005	2	0.6	-9.067	$0.039 \pm 20.614i$	3.28	3.30
0.005	1	0.6	-11.342	$0.078 \pm 23.696i$	3.77	3.77
0.004	1	0.6	-12.023	$0.098 \pm 27.772i$	4.42	4.37
0.003	1	0.6	-13.035	$0.130 \pm 33.918i$	5.40	5.37
0.002	1	0.6	-14.781	$0.197 \pm 44.502i$	7.08	7.10
0.001	1	0.6	-17.575	$0.160 \pm 73.459i$	11.69	11.42

Table 4.7 The eigenvalues $z = x_0$ and $z = z_0^\pm = \lambda_0 \pm i\Omega$, the frequency $\Omega/2\pi$, and the main frequency ν of the persistent oscillations, for several values of ε, χ and $Q_i \in \mathcal{R}$.

In all cases considered we found that the eigenvalue equation (4.4.13) has three solutions: one real eigenvalue $z = x_0 < 0$, and two complex conjugate eigenvalues $z = z_0^\pm = \lambda_0 \pm i\Omega$. If $\lambda_0 < 0$, the steady state solution is stable which was found to correspond precisely to the transient flow tending to a steady state. If $\lambda_0 > 0$, the (fictitious) steady state solution is unstable and correspondingly the transient flow shows persistent oscillations. The solution of the linearized system of equations (4.4.4) and (4.4.2)^{2,5} corresponding to the eigenvalues $z = z_0^\pm = \lambda_0 \pm i\Omega$ has a frequency $\Omega/2\pi$. In Table 4.7 the eigenvalues $z = x_0$ and $z = z_0^\pm$, and the associated frequency $\Omega/2\pi$ are listed for several flows showing persistent oscillations; part of the results have been taken from Table 4.6. In the final column of Table 4.7 we have listed the main frequency ν of the persistent oscillations, computed by the discrete Fourier transform; the results for ν have been taken from Tables 4.3 and 4.4. From Table 4.7 we conclude that $\Omega/2\pi \approx \nu$ for the flows considered.

4.5 Loading and unloading

In Section 4.3 we have computed the transient flow of the extrusion process, starting from rest at time $t = 0$ and driven by a constant inlet flow rate Q_i . In this section we consider experiments in which the flow is in a steady state corresponding to $Q_i = Q_i^{(0)}$, whereupon

at time $t = t_0$ the inlet flow rate is suddenly changed to $Q_i = Q_i^{(0)} + \Delta Q_i$. If $\Delta Q_i > 0$, we call this process loading, otherwise unloading. On the basis of numerical calculations of the transient flow we will demonstrate the influence of the deformation history in some loading and unloading processes. In the processes considered the flow starts from rest at time $t = 0$, and the parameters ε and χ have the values $\varepsilon = 0.005$ and $\chi = 1$.

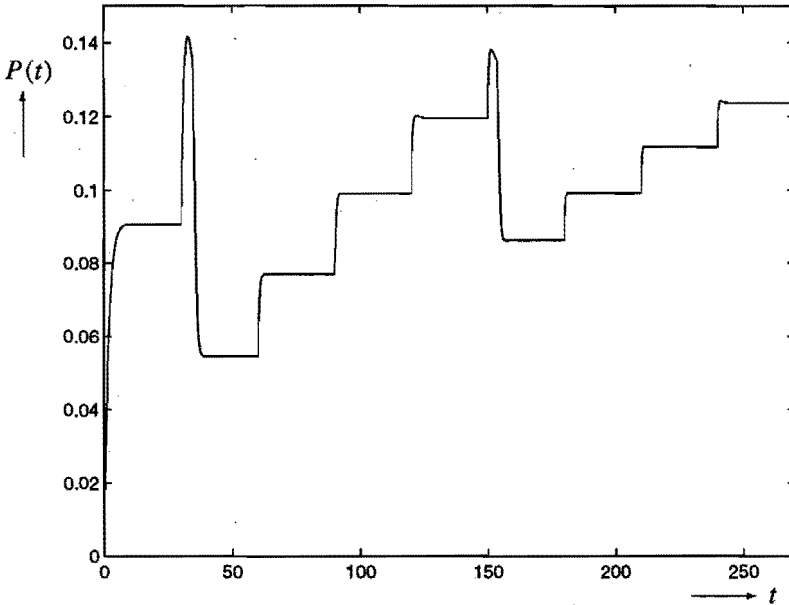


Figure 4.18 The pressure $P(t)$ as function of time t for a loading process, in which at times $t = 30j$, $j = 1, 2, \dots, 8$, the inlet flow rate is increased by a loading step $\Delta Q_i = 0.1$ from $Q_i = 0.1$ up to $Q_i = 0.9$; parameter values $\varepsilon = 0.005$ and $\chi = 1$.

We start with a loading process, in which at times $t = 30j$, $j = 1, 2, \dots, 8$, the inlet flow rate is successively increased by a loading step $\Delta Q_i = 0.1$ from $Q_i = 0.1$ up to $Q_i = 0.9$. In Figure 4.18 the computed pressure $P(t)$ is plotted as function of time t for this loading process. We observe that the time interval between successive loadings is sufficiently long for $P(t)$ to attain a steady state value. From the numerical results that underlie Figure 4.18 we determine the steady state pressure \bar{P} attained just before the next loading step is imposed; the values of \bar{P} are listed in Table 4.8. The computations reveal that the steady state attained is classical if $Q_i = 0.1$, whereas the steady states show a discontinuous velocity gradient $\omega(r)$ with exactly one jump at some radial coordinate $r = r^*$ if $Q_i \geq 0.2$. The values of r^* , found from the place of the discontinuity in the computed steady state velocity gradient $\omega(r)$, are listed in Table 4.8. It has been checked that the steady state values $\bar{Q} = Q_i$, \bar{P} and r^* satisfy equation (4.2.10). We observe that \bar{P} increases while r^* remains fixed, when Q_i increases from $Q_i = 0.2$ up to $Q_i = 0.5$. Hence, the boundary of the spurt layer remains fixed after loading, which is referred to as shape memory (cf. Section 2.5). For $Q_i = 0.6$, however, we observe that both r^* and \bar{P} have become smaller. Hence, the boundary of the spurt layer has moved further away from the wall, and the shape memory is lost. The reason for the loss of

shape memory is that no value of \bar{P} exists that satisfies equation (4.2.10) with $Q_i = 0.6$ and $r^* = r_0^* = 0.9962$. When Q_i increases from $Q_i = 0.6$ up to $Q_i = 0.9$, the radial coordinate r^* again remains fixed while \bar{P} increases, so that again shape memory occurs. From the numerical results presented in Table 4.8, we surmise that the occurrence of shape memory with fixed $r^* = r_0^*$ is inherent to the existence of a steady state pressure \bar{P} that satisfies equation (4.2.10) with $Q_i = Q_i^{(0)} + \Delta Q_i$ and $r^* = r_0^*$. Hence, the occurrence of shape memory depends on the initial flow rate $Q_i = Q_i^{(0)}$ and on the loading step ΔQ_i . Notice that under gradual increase of the inlet flow rate up to $Q_i = 0.6$, by loading steps $\Delta Q_i = 0.1$, the resulting transient flow tends to a steady state. This is in contrast to the case of Figure 4.9 where the flow starts from rest at $t = 0$ and is driven by the inlet flow rate $Q_i = 0.6$ suddenly imposed; then the transient flow shows persistent oscillations. Thus we conclude that the deformation history affects the transient flow behaviour and the steady state attained.

Q_i	\bar{P}	r^*	Q_i	\bar{P}	r^*
0.1	0.09060	-	0.6	0.08633	0.9922
0.2	0.05446	0.9962	0.7	0.09917	0.9922
0.3	0.07686	0.9962	0.8	0.11173	0.9922
0.4	0.09907	0.9962	0.9	0.12365	0.9922
0.5	0.11956	0.9962			

Table 4.8 The steady state pressure \bar{P} and the radial coordinate r^* at which $\omega(r)$ is discontinuous, for a loading process in which at times $t = 30j$, $j = 1, 2, \dots, 8$, the inlet flow rate is increased by a loading step $\Delta Q_i = 0.1$ from $Q_i = 0.1$ up to $Q_i = 0.9$; parameter values $\varepsilon = 0.005$ and $\chi = 1$.

Next, we consider a process of unloading where the flow is driven by a supercritical inlet flow rate $Q_i = Q_i^{(0)} = 0.3$, which at time $t = 40$ is suddenly lowered to the supercritical value $Q_i = Q_i^{(0)} + \Delta Q_i = 0.25$. Hence, $\Delta Q_i = -0.05$ (unloading). In Figure 4.19 the computed pressure $P(t)$ is plotted as function of time t . We observe that $P(t)$ has attained a steady state value at $t = 40$. From the numerical results that underlie Figure 4.19 we determine the steady state pressure $\bar{P} = 0.04127$ at $t = 40$. The computations disclose that the steady state at $t = 40$ shows a discontinuous velocity gradient $\omega(r)$ with exactly one jump at $r = r_0^* = 0.9894$. For $t > 40$, we observe that $P(t)$ slightly decreases and after some time oscillations appear. We computed the transient flow up to $t = 100$, at which time the amplitude of the oscillations in $P(t)$ is still the same as at $t = 80$. Thus, persistent oscillations occur and no steady state is attained after unloading to the supercritical value $Q_i = 0.25$. Furthermore, the computations reveal that for sufficiently large t (> 40) the velocity gradient $\omega(r, t)$ shows a numerical discontinuity also at $r = r_0^* = 0.9894$. Hence, the boundary of the spurt layer remains fixed after unloading, so that shape memory occurs. Shape memory is possible because of the existence of a fictitious steady state pressure $\bar{P} = 0.03789$ that satisfies equation (4.2.10) with $Q_i = 0.25$ and $r^* = r_0^* = 0.9894$. Thus, the occurrence of shape memory after unloading affects the transient flow behaviour, and persistent oscillations may occur.

An explanation for the occurrence of persistent oscillations after the unloading to $Q_i = 0.25$ can be given by means of the linearized stability analysis described in Section 4.4. For the fictitious steady state solution corresponding to $Q_i = 0.25$, the eigenvalue equation $\Psi(z, Q_i) = 0$

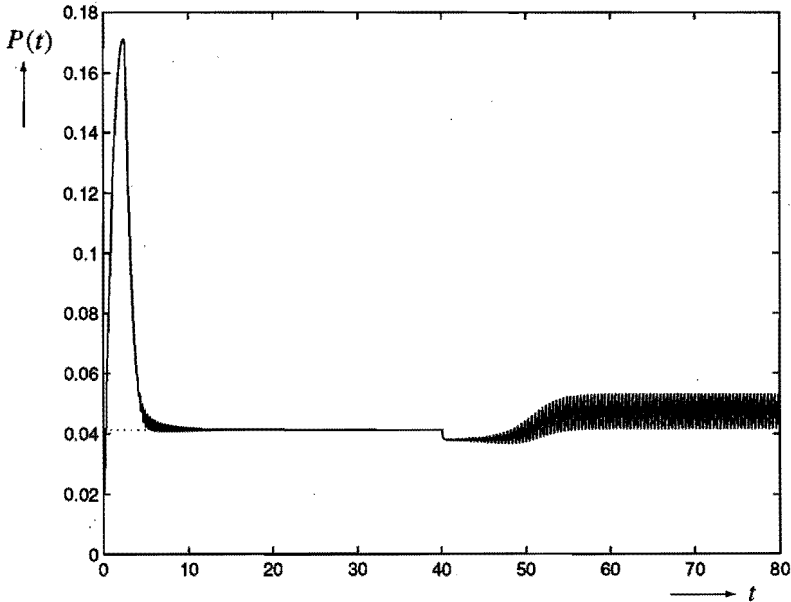


Figure 4.19 The pressure $P(t)$ as function of time t for an unloading process, in which at time $t = 40$ the inlet flow rate is lowered from $Q_i = Q_i^{(0)} = 0.3$ to $Q_i = Q_i^{(0)} + \Delta Q_i = 0.25 > \overline{Q}_{crit}$; parameter values $\varepsilon = 0.005$ and $\chi = 1$.

(see (4.4.13)) is found to have the solutions $z = x_0 = -7.924$ and $z = z_0^\pm = \lambda_0 \pm i\Omega = 0.347 \pm 15.279i$. Hence, the two eigenvalues $z = z_0^\pm$ have a positive real part ($\text{Re } z_0^\pm > 0$), implying that the fictitious steady state solution is unstable. This instability result corresponds precisely to the transient flow showing persistent oscillations. The main frequency ν of the persistent oscillations depicted in Figure 4.19, computed by the discrete Fourier transform, equals $\nu = 2.44$. Notice that $\Omega/2\pi = 2.43$, which agrees quite well with the value of ν .

Finally, we consider an unloading process where the flow is driven by a supercritical inlet flow rate $Q_i = Q_i^{(0)} = 0.22$, which at time $t = 40$ is suddenly lowered to the subcritical value $Q_i = Q_i^{(0)} + \Delta Q_i = 0.142$. Hence, $\Delta Q_i = -0.078$ (unloading). In Figure 4.20 the computed pressure $P(t)$ is plotted as function of time t . We observe that $P(t)$ has attained a steady state value at $t = 40$. From the numerical results that underlie Figure 4.20 we determine the steady state pressure $\overline{P} = 0.04614$ at $t = 40$. The computations disclose that the steady state at $t = 40$ shows a discontinuous velocity gradient $\omega(r)$ with exactly one jump at $r = r_0^* = 0.9942$. For $t > 40$, we observe that $P(t)$ first decreases and after some time oscillations appear. We computed the transient flow up to $t = 100$, at which time the amplitude of the oscillations in $P(t)$ is still the same as at $t = 80$. Thus, persistent oscillations occur and no steady state is attained after unloading to the subcritical value $Q_i = 0.142$. Furthermore, the computations reveal that for sufficiently large t (> 40) the velocity gradient $\omega(r, t)$ shows a numerical discontinuity also at $r = r_0^* = 0.9942$. Hence, the boundary of the spurt layer remains fixed after unloading, so that shape memory occurs. Shape memory is possible because of the existence of a fictitious steady state pressure $\overline{P} = 0.03663$ that satisfies equa-

tion (4.2.10) with $Q_i = 0.142$ and $r^* = r_0^* = 0.9942$. Thus, the occurrence of shape memory after unloading affects the transient flow behaviour, and persistent oscillations may occur, even for a subcritical flow rate $Q_i < \bar{Q}_{crit}$.

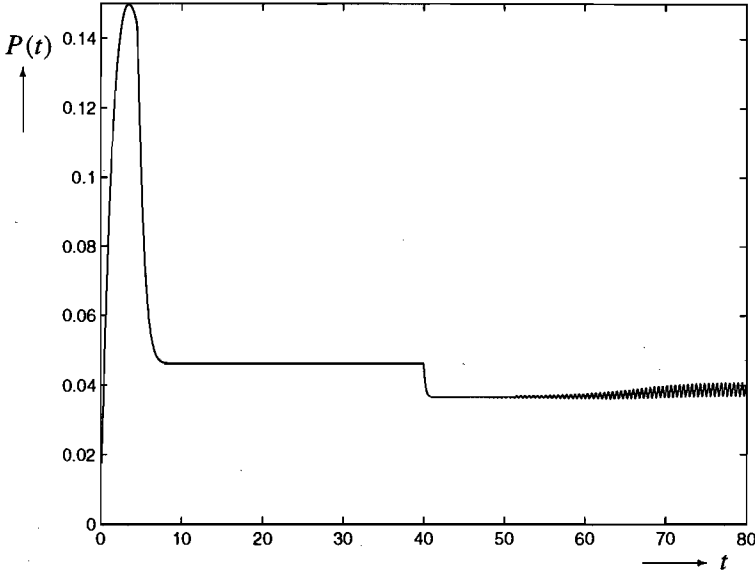


Figure 4.20 The pressure $P(t)$ as function of time t for an unloading process, in which at time $t = 40$ the inlet flow rate is lowered from $Q_i = Q_i^{(0)} = 0.22$ to $Q_i = Q_i^{(0)} + \Delta Q_i = 0.142 < \bar{Q}_{crit}$; parameter values $\varepsilon = 0.005$ and $\chi = 1$.

An explanation for the occurrence of persistent oscillations after the unloading to $Q_i = 0.142$ can be given by means of the linearized stability analysis described in Section 4.4. For the fictitious steady state solution corresponding to $Q_i = 0.142$, the eigenvalue equation $\Psi(z, Q_i) = 0$ is found to have the solutions $z = x_0 = -5.728$ and $z = z_0^\pm = 0.148 \pm 12.178i$. Hence, the two eigenvalues $z = z_0^\pm$ have a positive real part ($\text{Re } z_0^\pm > 0$), implying that the fictitious steady state solution is unstable. This corresponds precisely to the subcritical transient flow showing persistent oscillations.

4.6 Conclusions

Stability analysis and numerical calculations have been used to analyze the flow of a polymeric melt in an extrusion process. In order to find a theoretical explanation for the phenomenon of persistent oscillations, as observed in experiments of Kalika and Denn [23], Lim and Schowalter [31], and El Kissi and Piau [12], an extrusion flow combined with compression has been considered. The extruder consists of a wide cylindrical barrel connected to a narrow cylindrical capillary. The melt is compressed in the barrel by a plunger moving at

constant speed V_0 . Both the volumetric flow rate $Q(t)$ in the capillary and the pressure $P(t)$ in the barrel are unknown.

The constitutive behaviour of the polymeric melt is described by the JSO-model supplemented with an extra Newtonian viscous term. This extra term accounts either for the response of a small-molecule solvent, or for the unhindered motion of the polymer chains, described by a very fast relaxation rate (cf. Malkus et al. [33]). The JSO-model used here describes the characteristic behaviour of viscoelastic concentrated polymer solutions and pure molten polymers with fading memory, by a differential equation. The addition of the Newtonian viscous term is essential in our analysis, since it leads to a nonmonotone relation between the steady state shear stress $F(r)$ and the steady state velocity gradient or shear strain-rate $\omega(r)$. We have shown by numerical computations of the transient flow that persistent oscillations in the pressure as well as in the volumetric flow rate may occur, as observed in experiments. Recall that in the piston-driven shear flow considered in Chapter 3 persistent oscillations may occur in the pressure gradient only, and not in the volumetric flow rate. Hence, internal material properties of the fluid itself account for persistent oscillations, instead of a global external effect such as 'wall slip', because in our model the no-slip boundary condition at the wall of the capillary is maintained.

A theoretical explanation for the occurrence of persistent oscillations in the pressure has been given before by Malkus et al. [35], [36], in the piston-driven flow of a JSO-fluid through a slit die. In fact, this chapter deals with the analogous problem of the flow of a JSO-fluid through a cylindrical capillary combined with compression in a barrel. By taking into account the compression we obtain a model for the extrusion process that admits persistent oscillations both in the pressure and in the volumetric flow rate. By numerical computations of the transient flow we have found critical conditions for the onset of persistent oscillations, in terms of the plunger speed V_0 , the dimensions of the extruder, and the material parameters of the polymeric melt.

In the description of the flow considered here, the plunger speed, the dimensions of the extruder, and the material parameters of the polymeric melt are included in three dimensionless parameters ε , χ and Q_i . Here, ε is equal to the quotient of the solvent viscosity η_s and the shear viscosity μ/λ ; χ is proportional to the melt compressibility $1/K$; and Q_i is the dimensionless inlet flow rate, proportional to the plunger speed V_0 . The equations (4.1.47) governing the flow can be viewed as a continuous family of quadratic ordinary differential equations coupled by one non-local constraint and one non-local ordinary differential equation that describes the compression in the barrel. The non-local constraint expresses the pressure $P(t)$ in terms of the flow rate $Q(t)$ and an integral of the extra shear stress $S(r, t)$ over the cross-section of the capillary. The non-local ordinary differential equation couples $Q(t)$ to $P(t)$ and the coupling involves the parameters χ and Q_i . The quadratic ordinary differential equations relate the stresses $S(r, t)$ and $Z(r, t)$ to $P(t)$ and the velocity gradient $w(r, t)$ for each radial coordinate r , whereby w is determined in terms of S and P by the balance of linear momentum.

The steady state flow is described by a nonmonotone relation between the steady state shear stress $F(r)$ and the steady state velocity gradient $\omega(r)$, if $0 < \varepsilon < 1/8$. This nonmonotone relation gives rise to three distinct steady state solutions ω if $F_m < F < F_M$. As shown by Malkus et al. [33, Sec. 3], the solution ω with $\omega_M < \omega < \omega_m$ is unstable, whereas the

solutions ω with $\omega < \omega_M$ or $\omega > \omega_m$ are stable. The steady state pressure $\bar{P} = \lim_{t \rightarrow \infty} P(t)$ and the steady state velocity gradient $\omega(r)$ depend on the inlet flow rate Q_i in the following manner:

- If $0 \leq Q_i \leq \bar{Q}_0$, \bar{P} is unique and $\omega(r)$ is continuous in r ; the flow is referred to as classical flow.
- If $\bar{Q}_0 < Q_i \leq \bar{Q}_{crit}$, \bar{P} is not unique, and $\omega(r)$ is either continuous in r (classical flow) or $\omega(r)$ is discontinuous with a jump from $\omega_-^* < \omega_M$ to $\omega_+^* > \omega_m$ at some radial coordinate $r = r^*$; the latter case is referred to as spurt flow.
- If $Q_i > \bar{Q}_{crit}$, \bar{P} is not unique and $\omega(r)$ is discontinuous at $r = r^*$, corresponding to spurt flow.

In the case of classical flow, \bar{P} is uniquely determined by Q_i only, as expressed by (4.2.9). In the case of spurt flow, \bar{P} is uniquely determined by Q_i and r^* , as expressed by (4.2.10). In spurt flow, the jump in $\omega(r)$ results in a kink in the steady state velocity profile $\bar{v}(r)$ at $r = r^*$, and a spurt layer, of thickness $1 - r^*$, with large velocity gradients forms near the wall.

By numerical computations we have examined whether or not the transient flow tends to a steady state. If a steady state is attained, the computations yield the value of \bar{P} and, in the case of spurt flow, the value of r^* where $\omega(r)$ is discontinuous. For $\varepsilon = 0.02$ and $\chi = 1, 2, 4$, the calculations of the transient flow revealed that for each inlet flow rate Q_i a steady state is attained, showing the following characteristics:

- If $Q_i < \bar{Q}_{crit}$ (subcritical flow), the flow tends to a classical steady state with $\bar{P} = P_{clas}(Q_i)$.
- If $Q_i > \bar{Q}_{crit}$ (supercritical flow), the flow tends to a spurt steady state with $P_{bottom}(Q_i) \leq \bar{P} \leq P_{top}(Q_i)$.
- The flow curve of \bar{P} versus Q_i is S-shaped, shows a kink at $Q_i = \bar{Q}_{crit}$, and tends to the curve $\bar{P} = P_{top}(Q_i)$ for Q_i sufficiently large, independent of χ .
- The spurt layer becomes thicker with increasing $Q_i > \bar{Q}_{crit}$.
- The spurt layer becomes thicker with increasing χ .

The transient flow behaviour was found to crucially depend on the values of ε , χ and Q_i . For $\varepsilon = 0.005$ and $\chi = 1, 2$, we observed that for a certain bounded range $\mathcal{R} = (\bar{Q}_m, \bar{Q}_M)$ of supercritical inlet flow rates Q_i , persistent oscillations in $P(t)$, $Q(t)$, $w(r, t)$, $S(r, t)$ and $Z(r, t)$ occur, for each value of the radial coordinate r . These persistent oscillations do not die out and have constant amplitude after a certain instant. For $Q_i \notin \mathcal{R}$, a steady state is reached after sufficient time. At $Q_i = \bar{Q}_m$ and $Q_i = \bar{Q}_M$, the transition from a steady state to a state of persistent oscillations and vice versa takes place. From additional computations we conclude that

- if $\varepsilon = 0.005$ and $\chi < \chi_{crit} = 6$, a bounded range $\mathcal{R} = (\overline{Q}_m, \overline{Q}_M)$ of inlet flow rates Q_i exists for which persistent oscillations occur;
- if $\varepsilon = 0.005$ and $\chi \geq \chi_{crit} = 6$, the flow tends to a steady state for each inlet flow rate Q_i ;
- if $\chi = 1$ and $\varepsilon < \varepsilon_{crit} = 0.011$, a bounded range $\mathcal{R} = (\overline{Q}_m, \overline{Q}_M)$ of inlet flow rates Q_i exists for which persistent oscillations occur;
- if $\chi = 1$ and $\varepsilon \geq \varepsilon_{crit} = 0.011$, the flow tends to a steady state for each inlet flow rate Q_i ;
- the range \mathcal{R} becomes smaller with increasing χ ;
- the range \mathcal{R} becomes smaller with increasing ε .

In the case of persistent oscillations we have found that after sufficient time the velocity gradient $w(r, t)$, calculated at $r = r_k = k\Delta r$, shows a numerical discontinuity between $r = r_k$ and $r = r_{k+1}$ for some specific index k . Then the value of r^* is taken as $r^* = (r_k + r_{k+1})/2$. In this manner, we have been able to assign a value to the radial coordinate r^* at which the (steady state) velocity gradient is discontinuous, for each inlet flow rate Q_i .

The occurrence of persistent oscillations has been explained by means of a linearized stability analysis of the steady state solution. By numerical computations we have verified that the transient flow tending to a steady state for some value of Q_i , corresponds precisely to the steady state solution being stable. Likewise, if the transient flow shows persistent oscillations for some value of Q_i , then correspondingly the steady state solution is found to be unstable.

The frequency of the persistent oscillations has been determined by means of a Fourier spectral analysis of the functions $P(t)$ and $Q(t)$, considered as time-dependent signals. The actual calculation uses the discrete Fourier transform of the sampled signals $P(t)$ and $Q(t)$, which is conveniently evaluated by a fast Fourier transform algorithm. The main conclusions are that the frequency ν of the persistent oscillations increases with increasing flow rate $Q_i \in \mathcal{R}$, whereas ν decreases with increasing ε and/or χ . Furthermore, it has been verified that $\nu \approx \Omega/2\pi$, where Ω is the imaginary part of the complex eigenvalue that comes up as a solution of (4.4.13) in the stability analysis of the steady state solution.

The influence of the deformation history of the melt has been elucidated by some examples of loading and unloading processes. In the unloading process where the prescribed inlet flow rate is suddenly lowered from $Q_i = Q_i^{(0)}$ to $Q_i = Q_i^{(0)} + \Delta Q_i$ with $\Delta Q_i < 0$, the following peculiarities are observed:

- the boundary $r = r_0^*$ of the spurt layer remains fixed after unloading, which is referred to as shape memory;
- persistent oscillations may occur after unloading to supercritical as well as to subcritical flow rates Q_i .

It was found that the occurrence of shape memory depends on the initial flow rate $Q_i = Q_i^{(0)}$ and on the loading step ΔQ_i . The examples of loading and unloading processes considered

illustrate that the deformation history of the fluid affects the transient flow behaviour and the steady state attained.

By fitting the dimensionless parameters ε , χ and Q_i to the material parameters of the polymeric melt, the dimensions of the extruder, and to the plunger speed V_0 , the dimensional steady state pressure \bar{P} attained can be determined as a function of the plunger speed V_0 . The plunger speed is of great practical interest in polymer processing, since it determines the production rate of the extrusion process; a higher plunger speed leads to more extrudate produced per unit of time. The dimensional critical flow rate \bar{Q}_{crit} beyond which spurt flow ensues, and the range $\mathcal{R} = (\bar{Q}_m, \bar{Q}_M)$ of dimensional flow rates for which persistent oscillations occur, can be estimated in terms of the material parameters η_s , μ , λ , a , K , the radius R and the length L of the capillary, and the area A of the plunger. Furthermore, the values ε_{crit} and χ_{crit} determine directly the critical quotients $\eta_s \lambda / \mu$ and $8Al_0 \mu L / K \pi R^4$ of material parameters and extruder dimensions below which persistent oscillations occur, dependent on whether $Q_i \in \mathcal{R}$. Thus, for an extruder and a polymeric fluid with dimensions and material parameters such that $\varepsilon \geq \varepsilon_{crit}$ and $\chi \geq \chi_{crit}$, no persistent oscillations occur and the transient flow tends to a steady state for each inlet flow rate Q_i . In Chapter 5 we will compare the critical conditions for the onset of persistent oscillations predicted by our theory, to the critical conditions found in the experiments of Kalika and Denn [23], Lim and Schowalter [31], and of El Kissi and Piau [12].

Chapter 5

Validation and perspective

In the previous chapters we have analyzed the capillary flow of a polymeric melt under various driving mechanisms. The main goal was to provide a theoretical explanation for the occurrence of flow instabilities. In the present chapter we want to validate our theoretical analyses by a comparison with experimental results. More specifically, the phenomena of spurt and hysteresis occurring in a pressure-driven flow (Chapter 2) are compared to their counterparts as observed in experiments of Vinogradov et al. [52], [53], and El Kissi and Piau [12]. Spurt flow accompanied by persistent oscillations in the pressure was found to occur in a piston-driven flow (Chapter 3) and in an extrusion flow combined with compression (Chapter 4). These oscillations are compared to certain pressure oscillations as observed in experiments by Kalika and Denn [23], Lim and Schowalter [31], and El Kissi and Piau [12]. Likewise, we compare the critical conditions for the onset of flow instabilities predicted by our theory, to the critical conditions found in the experiments referred to. For a survey of experimental results we also refer to Section 1.5.

5.1 Validation of the models

We start with a validation of the theoretical analysis of Chapter 2 by a comparison with experimental results for pressure-driven flows, due to Vinogradov et al. [52], [53], and El Kissi and Piau [12]. In these experiments the spurt phenomenon shows up through a discontinuous increase of the volumetric flow rate at the slightest increase of the driving pressure gradient beyond a critical value. El Kissi and Piau [12] also observed the occurrence of hysteresis in an experiment in which the driving pressure gradient is successively raised and lowered. Characteristic for hysteresis is that the loading and unloading paths in the flow curve (plot of steady state flow rate versus steady state pressure gradient) do not coincide.

In Chapter 2 we have analyzed the flow of a polymeric melt through a cylindrical capillary of radius R , driven by a prescribed constant pressure gradient f . The characteristic behaviour of the polymeric melt was described by the KBKZ-model supplied with an extra Newtonian viscous term. This extra term accounts either for the response of a small-molecule solvent, or for the unhindered motion of the polymer chains. The extra term leads to a nonmonotone relationship between the steady state shear stress and the steady state velocity gradient. We have established that the KBKZ-model with one main relaxation rate and supplemented with

a Newtonian viscous term, is a good approximation to the KBKZ-model with two widely spaced relaxation rates. Under neglect of the inertia forces, the flow is governed by two dimensionless parameters, namely

$$\bar{f} = \frac{R}{\mu\sqrt{c}} f, \quad \varepsilon = \frac{\eta_s \lambda}{\mu}. \quad (5.1.1)$$

Here, \bar{f} is the dimensionless and f the dimensional pressure gradient; η_s (solvent viscosity), μ (shear modulus), λ (relaxation rate) and c are material parameters of the polymeric melt.

For the KBKZ-model considered, we have found that the spurt phenomenon can only occur if $0 < \varepsilon < \varepsilon_1 = 0.02886$. In that case, the dimensionless volumetric flow rate \bar{Q} is a continuous increasing function of the pressure gradient \bar{f} , for $\bar{f} < \bar{f}_{crit} = 2F_M$. For $\bar{f} > \bar{f}_{crit}$, the flow develops a spurt layer near the wall in which the velocity gradient is very large compared to the velocity gradient in the rest of the capillary. The occurrence of this spurt layer follows immediately from the nonmonotone relationship between the steady state shear stress and the steady state velocity gradient. When the spurt layer forms for $\bar{f} = \bar{f}_{crit}$, the flow becomes nearly plug-like and \bar{Q} increases substantially at a slight increase of \bar{f} . Furthermore, we have found that hysteresis in the flow curve occurs for a quasi-static loading-unloading cycle, and that the hysteresis loop is due to shape memory; see Section 2.5. We conclude that there is qualitative agreement between the theoretical results of Chapter 2, and the observed spurt phenomenon and hysteresis in the experiments of Vinogradov et al. [52], [53], and El Kissi and Piau [12]. Notice that the additional Newtonian viscous term plays a crucial role in the theoretical explanation of spurt. Furthermore, we have maintained the no-slip boundary condition at the wall of the capillary. In our approach the spurt phenomenon is referred to as a constitutive instability that is associated with internal properties of the polymeric melt. This is in contrast to the explanation of spurt as being due to wall slip, that is, the failure of the fluid to adhere to the wall.

To further validate the analysis of Chapter 2, we compare the critical conditions for the onset of spurt predicted by our theory, with the critical conditions found in experiments. Vinogradov et al. [52] report on the spurt phenomenon in the capillary flow of certain monodisperse polybutadienes and polyisoprenes at room temperature. To fit our material parameters η_s , μ , λ and c , to Vinogradov's experimental fluid samples PI-1 to PI-8 of polyisoprene of different molecular weights M (cf. Table 5.1), we use the following features of the fluid samples, taken from [52] and Malkus et al. [32]:

- The shear modulus μ is independent of the molecular weight M .
- The shear viscosity μ/λ depends on the molecular weight M according to the well-known empirical power law

$$\frac{\mu}{\lambda} = B M^{3.3}, \quad (5.1.2)$$

where B is independent of M .

- There is a critical molecular weight below which the material does not show the spurt phenomenon; the samples PI-1 and PI-2 do not exhibit spurt.

- For the samples PI-3 through PI-8 the critical wall shear stress $T_{rz,crit}$ at the onset of spurt is independent of the molecular weight M .
- For the samples PI-3 through PI-8 the critical wall shear strain-rate $\dot{\gamma}_{crit}$ at the onset of spurt depends on M according to

$$\dot{\gamma}_{crit} = \frac{\lambda}{\mu} T_{rz,crit} \propto M^{-3.3}. \quad (5.1.3)$$

Kolkka et al. [24] have fitted the power law (5.1.2) to the data of Vinogradov et al. [52], and they found that

$$B = 9.6 * 10^{-12} \text{ cgs units}, \quad \mu = 0.6 * 10^5 \text{ Nm}^{-2}. \quad (5.1.4)$$

The corresponding values of the shear viscosity μ/λ are presented in Table 5.1. Kolkka et al. [24] mention that their fit has a maximum error in relaxation rate λ of about 50 percent for fluids PI-2 and PI-3, whereas the error is less than 12 percent for fluids PI-4 through PI-8.

Next we determine the solvent viscosity η_s of Vinogradov's fluid samples within the KBKZ-model, by a calculation similar to that of Kolkka et al. [24] within the JSO-model. We assume that sample PI-2 is just subcritical for the onset of spurt, and that η_s does not vary with M , or equivalently, that the secondary (very fast) relaxation rate is independent of M . In the KBKZ-model the onset of spurt occurs at $\varepsilon = \eta_s \lambda / \mu = \varepsilon_1 = 0.0289$, while the fluid sample PI-2 has a shear viscosity $\mu/\lambda = 0.11 * 10^6 \text{ Nm}^{-2}\text{s}$ (see Table 5.1). Thus we find that

$$\eta_s = 3.2 * 10^3 \text{ Nm}^{-2}\text{s}. \quad (5.1.5)$$

By use of (5.1.5) and the values of μ/λ from Table 5.1, we calculate the dimensionless parameter $\varepsilon = \eta_s \lambda / \mu$ for the samples PI-1 through PI-8. The resulting values of ε are listed in Table 5.1. We observe that $\varepsilon \ll 1$ for each of the polyisoprene samples of Vinogradov et al. [52]. Obviously, the samples PI-1 and PI-2 have $\varepsilon \geq \varepsilon_1$, which corresponds to no spurt, whereas the samples PI-3 through PI-8 have $\varepsilon < \varepsilon_1$, which corresponds to spurt. Furthermore, we note that ε decreases with increasing M .

	unit	PI-1	PI-2	PI-3	PI-4	PI-5	PI-6	PI-7	PI-8
$M * 10^{-5}$	gram/mol	1.06	1.48	2.82	3.55	3.80	4.22	5.75	6.02
$\mu/\lambda * 10^{-6}$	Nm^{-2}s	0.037	0.11	0.93	2.0	2.5	3.5	9.8	11
$\varepsilon * 10^2$		8.7	2.9	0.34	0.16	0.13	0.091	0.033	0.028

Table 5.1 The shear viscosity μ/λ and the dimensionless parameter ε fitted to the polyisoprene samples of Vinogradov et al. [52] of different molecular weights M .

The key result in the observations of Vinogradov et al. [52], [53], is that the critical wall shear stress $T_{rz,crit}$ at the onset of spurt is independent of the molecular weight M , whereas the corresponding shear strain-rate $\dot{\gamma}_{crit}$ strongly depends on M . We compare the critical values as predicted by our analysis to these observations, under the assumption that the material parameter c is independent of M . In Section 2.2 we have found that the dimensionless critical

pressure gradient equals $\bar{f} = \bar{f}_{crit} = 2F_M$, so that the dimensional critical pressure gradient f_{crit} is given by

$$f_{crit} = \frac{\mu\sqrt{c}}{R} \bar{f}_{crit} = \frac{2\mu}{R} \sqrt{c} F_M. \quad (5.1.6)$$

From (2.1.34) and (5.1.6) the dimensional critical wall shear stress $T_{rz,crit}$ follows as

$$T_{rz,crit} = \frac{1}{2} R f_{crit} = \mu\sqrt{c} F_M. \quad (5.1.7)$$

By using the approximations (see (A.8) of Appendix A)

$$\omega_M = \omega^* + O(\varepsilon), \quad F_M = J(\omega^*) + O(\varepsilon), \quad \varepsilon \rightarrow 0, \quad (5.1.8)$$

with $\omega^* = 1.2979$ and $J(\omega^*) = 0.3479$, we find that

$$T_{rz,crit} = 0.3479 \mu\sqrt{c}, \quad (5.1.9)$$

under neglect of the $O(\varepsilon)$ -term. Since c and μ are independent of M , we conclude that $T_{rz,crit}$ is independent of M , which is in accordance with the observations of Vinogradov et al. [52], [53]. The independence of $T_{rz,crit}$ on M has also been found in experiments by El Kissi and Piau [12], and Ramamurthy [46]. From (5.1.9) with $\mu = 0.6 * 10^5 \text{ Nm}^{-2}$ by (5.1.4)², and Vinogradov's value $T_{rz,crit} = 0.151 * 10^6 \text{ Nm}^{-2}$ [52, Table II], we may determine the dimensionless material parameter c as $c = 52.3$. Alternatively, Kolkka et al. [24] have used Vinogradov's value of $T_{rz,crit}$ to determine the slip parameter a in the JSO-model as $a = 0.98$.

The dimensionless critical volumetric flow rate \bar{Q}_{crit} at the onset of spurt is computed by means of (3.2.11) with $\bar{f} = \bar{f}_{crit} = 2F_M$ and $\mathcal{W} = [0, \omega_M]$, that is

$$\bar{Q}_{crit} = \frac{1}{F_M^3} \int_0^{\omega_M} \mathcal{F}^2(\omega) \mathcal{F}'(\omega) \omega d\omega, \quad (5.1.10)$$

where $\mathcal{F}(\omega)$ is given by (2.2.11). By using (5.1.8) and the approximations (see (A.7) of Appendix A)

$$\mathcal{F}(\omega) = J(\omega) + O(\varepsilon), \quad \mathcal{F}'(\omega) = J'(\omega) + O(\varepsilon), \quad \varepsilon \rightarrow 0, \quad (5.1.11)$$

we find that

$$\bar{Q}_{crit} = I(\omega^*) + O(\varepsilon), \quad \varepsilon \rightarrow 0, \quad (5.1.12)$$

where $I(\omega^*)$ stands for the integral

$$I(\omega^*) = \frac{1}{J^3(\omega^*)} \int_0^{\omega^*} J^2(\omega) J'(\omega) \omega d\omega \quad (5.1.13)$$

and $J(\omega)$ is given by (2.2.9). The value of $I(\omega^*)$ is readily determined by numerical integration. Since $Q = \pi R^3 \lambda \sqrt{c} \bar{Q}$, where \bar{Q} denotes the dimensionless flow rate, the dimensional critical flow rate Q_{crit} is found to be

$$Q_{crit} = \pi R^3 \lambda \sqrt{c} I(\omega^*), \quad (5.1.14)$$

under neglect of the $O(\varepsilon)$ -term. In view of the power law (5.1.2) it follows that

$$Q_{crit} \propto M^{-3.3}, \quad (5.1.15)$$

since μ , B and c are independent of the molecular weight M . For a capillary flow, the critical wall shear strain-rate $\dot{\gamma}_{crit}$ is proportional to the critical volumetric flow rate Q_{crit} . Hence, $\dot{\gamma}_{crit}$ is proportional to $M^{-3.3}$, which is in accordance with the experimental result (5.1.3) of Vinogradov et al. [52]. Also El Kissi and Piau [12] found a strong dependence of the critical volumetric flow rate Q_{crit} on the molecular weight M . In particular, they observed that Q_{crit} is smaller for a fluid with larger M , which is in correspondence with (5.1.15).

In their experiments, El Kissi and Piau [12] observed that the hysteresis loop in the flow curve gets wider for larger values of the molecular weight M of the polymeric melt. In Figure 2.10 we have presented the theoretical flow curve as a plot of the dimensionless volumetric flow rate \bar{Q} versus the dimensionless pressure gradient \bar{f} , calculated for a quasi-static loading-unloading cycle. From this figure we derive that the hysteresis loop has a dimensionless width $\Delta \bar{f} = 2F_M - 2F_m$. Consequently, the dimensional width of the loop is found as

$$\Delta f = \frac{2\mu}{R} \sqrt{c} (F_M - F_m). \quad (5.1.16)$$

From (5.1.8) it follows that F_M is almost independent of ε , whereas Table A.1 of Appendix A indicates that F_m decreases with decreasing ε . The dependence of F_M and F_m on ε , together with the dependence of ε on M according to Table 5.1, demonstrate that F_M is almost independent of M , whereas F_m decreases strongly with increasing M . Thus we conclude from (5.1.16) that Δf increases with increasing M , which is in accordance with the observation of El Kissi and Piau [12].

We now recapitulate the main theoretical results bearing on the phenomena of spurt and hysteresis in a pressure-driven flow:

- The critical wall shear stress $T_{rz,crit}$ at the onset of spurt is independent of the molecular weight M .
- The critical volumetric flow rate Q_{crit} at the onset of spurt is proportional to $M^{-3.3}$.
- The width Δf of the hysteresis loop in the flow curve increases with increasing M .

These results agree quite well with the experimental results due to Vinogradov et al. [52], [53], El Kissi and Piau [12], and Ramamurthy [46]. The agreement observed supports our point of view that spurt is a constitutive instability.

Next we turn to a validation of the theoretical analysis of Chapter 3 by a comparison with experimental results for piston-driven flows, due to Kalika and Denn [23], Lim and Schowalter [31], and El Kissi and Piau [12]. In these experiments spurt flow is found to be accompanied by persistent oscillations in the pressure. These persistent oscillations show up for a bounded range of flow rates.

In Chapter 3 we have analyzed the flow of a polymeric melt through a cylindrical capillary of radius R , driven by a piston that moves at constant speed and induces a constant volumetric flow rate Q . The characteristic behaviour of the polymeric melt was described by the JSO-model supplied with an extra Newtonian viscous term. The inclusion of the Newtonian viscous term leads to a nonmonotone relationship between the steady state shear stress and the steady state velocity gradient. Under neglect of the inertia forces, the flow is governed by two dimensionless parameters, namely

$$\bar{Q} = \frac{\sqrt{1-a^2}}{\pi\lambda R^3} Q, \quad \varepsilon = \frac{\eta_s \lambda}{\mu}. \quad (5.1.17)$$

Here, \bar{Q} is the dimensionless and Q the dimensional flow rate; η_s (solvent viscosity), μ (shear modulus), λ (relaxation rate) and a (slip parameter) are material parameters of the polymeric melt.

For the piston-driven flow of a JSO-fluid considered, we have shown by numerical computations that there exists a bounded range \mathcal{R} of dimensionless flow rates \bar{Q} for which the pressure gradient f shows persistent oscillations. This theoretical result corresponds precisely to the observed spurt flow accompanied by pressure oscillations in the experiments of Kalika and Denn [23], Lim and Schowalter [31], and El Kissi and Piau [12]. Notice that the additional Newtonian viscous term is essential in the theoretical explanation of spurt. Furthermore, we have maintained the no-slip boundary condition at the wall of the capillary. Accordingly, spurt flow is associated with internal properties of the polymeric melt, and is therefore referred to as a constitutive instability.

To further validate the analysis of Chapter 3, we compare the critical conditions for the onset of spurt flow and persistent oscillations, predicted by our theory, to the critical conditions found in experiments. The experiments on piston-driven flows by El Kissi and Piau [12], and Lim and Schowalter [31], give rise to the following additional observations:

- The flow curve (i.e. the plot of steady state pressure gradient versus steady state flow rate) is S-shaped and shows a kink at a certain critical flow rate.
- The flow curve for a piston-driven flow is similar to the flow curve for a pressure-driven flow for sufficiently large flow rates.
- The critical flow rate at which the flow curve has a kink, is larger for a wider capillary.
- Persistent oscillations occur only for polymeric melts with a sufficiently large molecular weight M .
- Persistent oscillations are observed for a wider range of flow rates when the polymeric melt has a larger molecular weight M .

These observations are now compared with the theoretical results of Chapter 3 for a piston-driven flow. In the Figures 3.5 and 3.10 it is seen that the flow curve is indeed S-shaped with a kink at $\bar{Q} = \bar{Q}_{crit}$. Furthermore, we have found that the flow curve tends to the curve $\bar{f} = f_{top}(\bar{Q})$, corresponding to top-jumping, for \bar{Q} sufficiently large. Since in a pressure-driven flow always top-jumping occurs (cf. Figure 2.10, or Malkus et al. [33, Sec. 3]), the

curve $\bar{f} = f_{top}(\bar{Q})$ represents the flow curve for a pressure-driven flow. In conclusion, the flow curve based on our numerical computations shows qualitative agreement with the flow curve experimentally found by El Kissi and Piau [12]. As found in (3.2.14), the dimensionless critical flow rate \bar{Q}_{crit} equals $\bar{Q}_{crit} = 1/6 + O(\varepsilon)$, $\varepsilon \rightarrow 0$. Correspondingly, the dimensional critical flow rate Q_{crit} is given by

$$Q_{crit} = \frac{\pi\lambda R^3}{6\sqrt{1-a^2}}, \quad (5.1.18)$$

under neglect of the $O(\varepsilon)$ -term. Hence, Q_{crit} is proportional to R^3 . Thus, the critical flow rate Q_{crit} at which the flow curve shows a kink is larger for a wider capillary, which is in accordance with the observation of El Kissi and Piau [12].

Both in the KBKZ-model and in the JSO-model the parameter ε for Vinogradov's fluid samples decreases with increasing molecular weight M of the samples; see Table 5.1 and Malkus et al. [32, Table I]. In Section 3.4 we found that the bounded range \mathcal{R} of flow rates \bar{Q} for which persistent oscillations occur, is non-empty if $0 < \varepsilon < \varepsilon_{crit} = 0.007$. Thus, persistent oscillations occur only for polymeric melts with a sufficiently large molecular weight M , corresponding to ε sufficiently small. Furthermore, we observe in Figure 3.13 that \mathcal{R} becomes wider with decreasing ε . Hence, for a melt with larger molecular weight M , i.e. with smaller ε , the persistent oscillations occur for a wider range \mathcal{R} of flow rates \bar{Q} . In conclusion, our predictions about the dependence of the onset of persistent oscillations on the molecular weight M are in accordance with the observations of Lim and Schowalter [31] listed above.

This completes the reflection on Chapter 3: our theoretical model for piston-driven flow of a JSO-fluid fits quite well to the experiments considered. The agreement observed supports again our point of view that spurt flow is due to constitutive instabilities.

In Chapter 4 we have analyzed the extrusion flow of a polymeric melt that is compressed in a wide barrel by a plunger moving at constant speed V_0 . The barrel is connected to a narrow cylindrical capillary and the compression in the barrel forces the melt to flow through the capillary. The polymeric melt in the barrel is taken to be compressible according to an elastic constitutive model. The characteristic behaviour of the polymeric melt in the capillary is described by the JSO-model supplied with an extra Newtonian viscous term. This extra term leads to a nonmonotone relationship between the steady state shear stress and the steady state velocity gradient. Under neglect of the inertia forces, the flow is governed by three dimensionless parameters, namely

$$\varepsilon = \frac{\eta_s \lambda}{\mu}, \quad \chi = \frac{8Al_0\mu L}{K\pi R^4}, \quad Q_i = \frac{AV_0\sqrt{1-a^2}}{\pi\lambda R^3}. \quad (5.1.19)$$

Here, Q_i is the dimensionless inlet flow rate; K (compression modulus), η_s (solvent viscosity), μ (shear modulus), λ (relaxation rate) and a (slip parameter) are material parameters of the polymeric melt; while l_0 (initial length of the barrel), A (area of the plunger), R (radius of the capillary) and L (length of the capillary) are the dimensions of the extruder. Notice that χ contains material parameters as well as dimensions of the extruder, whereas Q_i is proportional to the plunger speed V_0 .

In Sections 4.3 and 4.4 we have shown that also the extrusion process combined with compression gives rise to the occurrence of spurt flow accompanied by persistent oscillations. More specifically, we have found by numerical computations that there exists a bounded range \mathcal{R} of inlet flow rates Q_i , for which the pressure P inside the barrel and the volumetric flow rate Q in the capillary show persistent oscillations. In the Figures 4.6 and 4.13 it is seen that the flow curves are S-shaped with a kink at $Q_i = \overline{Q}_{crit}$. These theoretical results agree quite well with experimental results for pressure oscillations and flow curves found for a piston-driven flow by Kalika and Denn [23], Lim and Schowalter [31], and El Kissi and Piau [12]. Notice again that the additional Newtonian viscous term plays a crucial role in the theoretical explanation of spurt flow accompanied by persistent oscillations. Accordingly, spurt flow is associated with internal properties of the polymeric melt (constitutive instability).

To further validate the analysis of Chapter 4, we make a comparison with the following additional experimental observations:

- The critical flow rate at which the flow curve shows a kink and beyond which spurt flow occurs, is independent of the length L of the capillary (El Kissi and Piau [12]).
- The amplitude of the persistent oscillations is constant in time (Kalika and Denn [23]).
- The span of the persistent oscillations goes through a maximum with increasing flow rate (Lim and Schowalter [31]).
- The frequency of the persistent oscillations increases with increasing flow rate (Kalika and Denn [23], Lim and Schowalter [31]).

The flow curves in Figures 4.6 and 4.13 show a kink at the critical flow rate $Q_i = \overline{Q}_{crit}$, independent of χ ; here $\overline{Q}_{crit} = 1/6 + O(\varepsilon)$ by (3.2.14). According to the definition of χ in (5.1.19)², independence of χ implies independence of $1/K$ and of L . Hence, the dimensional flow rate Q_{crit} , given by (5.1.18), is independent of $1/K$ and of L . The independence of L is in accordance with the observation of El Kissi and Piau [12]. From Figure 4.11 it is clear that the amplitudes of the persistent oscillations in the pressure P and in the volumetric flow rate Q are constant in time, which is in accordance with the observation of Kalika and Denn [23]. Furthermore, we have computed the span of the persistent oscillations for several values of $Q_i \in \mathcal{R}$, and given ε and χ . The computations (which are not included in Section 4.3) indicate that the span attains a maximum somewhere in the middle of the range \mathcal{R} , which corresponds to the observation of Lim and Schowalter [31]. Finally, looking at Table 4.3 we notice that the main frequency ν of the persistent oscillations increases with increasing Q_i , which is in accordance with the observations of Kalika and Denn [23], and Lim and Schowalter [31]. Thus, we conclude that there is qualitative agreement between the results predicted by our model and the experimental results listed above.

In the extruder shown in Figure 4.1 the entrance of the capillary forms a narrow contraction. The influence of the contraction on the capillary flow is ignored in the model of Chapter 4, so that this model is only valid for relatively long capillaries. Consequently, it does not make sense to compare the critical conditions for the onset of persistent oscillations predicted by our theory to the critical conditions found in experiments with a short capillary. The critical conditions predicted by our theory are that no persistent oscillations occur.

if the parameter χ exceeds the critical value $\chi_{crit} = 6$, or equivalently, if the length L of the capillary exceeds a critical value. This is in contrast to the observations of Kalika and Denn [23], and Durand [10], who experimentally found that no persistent oscillations occur for a relatively short capillary.

By comparing the results of Chapters 3 and 4, we may assess the influence of the melt compressibility $1/K$. In Figure 4.16 we observe that the range \mathcal{R} becomes smaller with increasing χ . As a consequence, the melt compressibility $1/K$ affects the onset of spurt flow accompanied by persistent oscillations. On the other hand, persistent oscillations also occur in the piston-driven flow discussed in Chapter 3, where no compression is taken into account. Thus, we conclude that polymer compressibility in the barrel is not crucial for the onset of spurt flow, although it has some effect. This is in harmony with a comment of Lim and Schowalter [31] that melt compressibility in the reservoir is not important in their experiments.

In this section we have provided a theoretical explanation for the occurrence of spurt and persistent oscillations as observed in various experiments involving both pressure-driven and piston-driven flows. In this explanation the flow instabilities are associated with internal properties of the melt (constitutive instabilities). We have examined the critical conditions for the onset of the flow instabilities in terms of both the material parameters of the melt and the dimensions of the extruder. The results predicted by our model are found to be consistent with the critical conditions observed in experiments. The agreement between theory and experiment supports the explanation of spurt in terms of constitutive instabilities. Notice that in our model spurt cannot be explained in terms of wall slip, because the no-slip boundary condition at the wall of the capillary is maintained.

5.2 Perspective

For more than 40 years it has been known that a polymeric melt passing through a capillary may exhibit flow instabilities leading to distortions of the extrudate. One would think that after these years of studying melt fracture in polymer melts and solutions, there would be at least some consensus among rheologists, polymer engineers, theoreticians, and others, on what is happening. The reason that no such consensus exists may be that different mechanisms are responsible for sharkskin, for spurt and for gross-melt fracture.

In this thesis we have explained spurt phenomena in terms of constitutive instabilities. Our model for extrusion does not involve wall slip, circulations in the barrel caused by the contraction, or singularities at the outlet edge of the capillary. By use of an appropriate constitutive model we demonstrated the occurrence of spurt by macroscopically observable phenomena, like a substantial increase of the steady state flow rate at a slight increase of the driving pressure gradient (see Chapter 2), or persistent oscillations in the pressure gradient for a certain range of flow rates (see Chapters 3 and 4). The relation between these phenomena and the extrudate distortions, however, is still not clear and remains a challenging subject for further research.

In the constitutive models used, the additional Newtonian viscous term accounts for the effect of a small-molecule solvent. In Section 2.6 we have shown that this term may also be interpreted as being due to a secondary (very fast) relaxation rate. The transient and steady state flow behaviour of a polymeric melt described by a constitutive equation involving two (or more) relaxation rates still needs to be investigated. By numerical computations the precise influence of two widely spaced relaxation rates on the transient and steady state flow can be examined, whereupon the effect on the onset of the flow instabilities can be clarified.

In the extrusion process considered in Chapter 4, the compression in the barrel has been taken into account. The melt is compressed in the barrel by a moving plunger. We have neglected the decrease of the length l of the barrel, by putting $l(t) = 1$ (i.e. $l(t) = l_0$ in dimensional form) in (4.1.34)². This decrease, however, can easily be incorporated in a modified model with (4.1.34)² left unchanged. We expect that also for the modified model persistent oscillations will occur, and that only the critical onset of the persistent oscillations might be affected.

In the model described in Chapter 4, also the effects of the contraction are neglected. By taking into account the contraction, the flow inside the extruder would be more accurately described. However, we expect that the influence of the contraction is only noticeable in the flow near the inlet of the capillary. We note that the computation of the flow through the contraction is very complicated. Thus, for rather short capillaries the contraction should be taken into account; for longer capillaries the model described in Chapter 4 is adequate.

In Section 5.1 we have validated our theoretical analyses by a qualitative comparison with experimental results. For a quantitative comparison, however, it will be necessary to incorporate sufficient relaxation rates in the constitutive equation, to render possible a satisfactory fit to experimental data. In this respect, we would like to emphasize the importance of correct and trustworthy constitutive equations which are also valid under extremely high shear-strain rates.

We conclude that many questions about the flow instabilities shown by polymeric melts and the related extrudate distortions are still open. Despite the agreement about the occurrence of flow instabilities, there remains substantial disagreement about the origin of these instabilities. This thesis contributes to the discussion about flow instabilities and, especially, provides a better insight into the constitutive instabilities. The ongoing research activities on the rheology of polymeric melts and concentrated solutions may build up within maybe another 40 years an integrated understanding of the origin of flow instabilities and the relation to extrudate distortions. The best way to obtain this understanding is to connect the experimental results to models that predict flow instabilities and extrudate distortions. Thus, following Kurtz [26], "old and new theories need to address what is known experimentally, both in terms of what fits and what does not fit".

Appendix A

Properties of $J(\omega)$ and $L(\omega)$

For convenience we repeat the definitions (2.2.9) and (2.4.10) of the functions $J(\omega)$ and $L(\omega)$, viz.

$$J(\omega) = \omega \int_0^{\infty} \frac{\tau e^{-\tau}}{1 + \omega^2 \tau^2} d\tau, \quad L(\omega) = \int_0^{\infty} \frac{e^{-\tau}}{1 + \omega^2 \tau^2} d\tau. \quad (\text{A.1})$$

These functions may be expressed in terms of the sine and cosine integrals, as

$$J(\omega) = g(1/\omega)/\omega, \quad L(\omega) = f(1/\omega)/\omega, \quad (\text{A.2})$$

where g and f are auxiliary functions defined by

$$\begin{aligned} g(z) &= -\text{Ci}(z) \cos z - \left(\text{Si}(z) - \frac{\pi}{2}\right) \sin z, \\ f(z) &= \text{Ci}(z) \sin z - \left(\text{Si}(z) - \frac{\pi}{2}\right) \cos z; \end{aligned} \quad (\text{A.3})$$

see Abramowitz and Stegun [3, p. 232]. By means of the latter reference we have the following expansions:

$$\begin{aligned} J(\omega) &= \frac{\ln \omega}{\omega} - \frac{C}{\omega} + \frac{\pi}{2\omega^2} - \frac{\ln \omega}{2\omega^3} + O\left(\frac{1}{\omega^3}\right), \quad \omega \rightarrow \infty, \\ L(\omega) &= \frac{\pi}{2\omega} - \frac{\ln \omega}{\omega^2} - \frac{1-C}{\omega^2} + O\left(\frac{1}{\omega^3}\right), \quad \omega \rightarrow \infty, \end{aligned} \quad (\text{A.4})$$

and

$$J(\omega) = \omega - 6\omega^3 + O(\omega^5), \quad L(\omega) = 1 - 2\omega^2 + O(\omega^4), \quad \omega \rightarrow 0. \quad (\text{A.5})$$

Here, $C = 0.57721\dots$ is Euler's constant. The derivative J' of the function J is determined by differentiation under the integral sign and integration by parts, yielding

$$J'(\omega) = \int_0^{\infty} \frac{\tau^2 - \tau}{1 + \omega^2 \tau^2} e^{-\tau} d\tau = \frac{1 - L(\omega)}{\omega^2} - \frac{J(\omega)}{\omega}. \quad (\text{A.6})$$

Numerical calculations reveal that on the interval $[0, \infty)$ the function J is non-negative with one maximum $J(\omega^*) = 0.34794$ at $\omega = \omega^* = 1.2979$. The derivative J' has one minimum

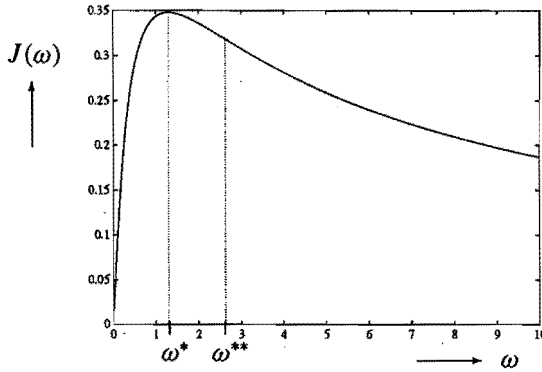


Figure A.1 The function $J(\omega)$ for $\omega \geq 0$.

$J'(\omega^{**}) = -0.02886$ at $\omega = \omega^{**} = 2.6255$. Hence, J' decreases strictly on the interval $[0, \omega^{**}]$ with $J'(0) = 1$, whereas on $[\omega^{**}, \infty)$ J' increases strictly to zero. In Figure A.1 the function $J(\omega)$ is plotted.

If $0 < \varepsilon < \varepsilon_1 := -J'(\omega^{**}) = 0.02886$, the function $\varepsilon + J'(\omega)$ has two zeros denoted by ω_M and ω_m . Let $\omega_M < \omega_m$, then $\omega^* < \omega_M < \omega^{**} < \omega_m$. Thus, if $0 < \varepsilon < \varepsilon_1$, the function $\mathcal{F}(\omega) = \varepsilon\omega + J(\omega)$ has two extreme values, a maximum $F_M = \varepsilon\omega_M + J(\omega_M)$ at $\omega = \omega_M$ and a minimum $F_m = \varepsilon\omega_m + J(\omega_m)$ at $\omega = \omega_m$. In addition to $\omega = \omega_M$ and $\omega = \omega_m$, both equations $\mathcal{F}(\omega) = F_M$ and $\mathcal{F}(\omega) = F_m$ have a second solution $\omega = \tilde{\omega}_M$ and $\omega = \tilde{\omega}_m$, respectively; see Figure 2.1. Numerical values of $\omega_M, F_M, \tilde{\omega}_M, \omega_m, F_m, \tilde{\omega}_m$ for $\varepsilon = 0.010, 0.020, 0.025$ are presented in Table A.1.

ε	ω_M	F_M ($= \varepsilon\omega_M + J(\omega_M)$)	$\tilde{\omega}_M$	ω_m	F_m ($= \varepsilon\omega_m + J(\omega_m)$)	$\tilde{\omega}_m$
0.010	1.4519	0.36164	25.4974	9.9609	0.28661	0.4703
0.020	1.7063	0.37730	9.0094	5.2439	0.35867	0.9242
0.025	1.9463	0.38637	5.5151	3.9248	0.38149	1.3454

Table A.1 The zeros ω_M and ω_m of the function $\mathcal{F}'(\omega)$ for different values of ε ($0 < \varepsilon < \varepsilon_1$), the maximum $F_M = \mathcal{F}(\omega_M)$ and the minimum $F_m = \mathcal{F}(\omega_m)$, and the zeros $\tilde{\omega}_M$ of $\mathcal{F}(\omega) - F_M$ and $\tilde{\omega}_m$ of $\mathcal{F}(\omega) - F_m$, where $\mathcal{F}(\omega) = \varepsilon\omega + J(\omega)$.

For small ε we may approximate the function $\mathcal{F}(\omega)$ and its derivative $\mathcal{F}'(\omega)$ according to

$$\mathcal{F}(\omega) = J(\omega) + O(\varepsilon), \quad \mathcal{F}'(\omega) = J'(\omega) + O(\varepsilon), \quad \varepsilon \rightarrow 0, \tag{A.7}$$

valid for $0 \leq \omega \leq \omega_M$. Consequently, we have the following approximations for the values ω_M and F_M :

$$\omega_M = \omega^* + O(\varepsilon), \quad F_M = J(\omega^*) + O(\varepsilon), \quad \varepsilon \rightarrow 0. \tag{A.8}$$

In Table A.1 we observe that ω_m and F_m strongly depend on ε , in such a way that ω_m decreases while F_m increases with increasing ε .

Bibliography

- [1] A.C.T. AARTS AND A.A.F. VAN DE VEN, Transient behaviour and stability points of the Poiseuille flow of a KBKZ-fluid, *Journal of Engineering Mathematics* **29** (1995), 371-392.
- [2] A.C.T. AARTS AND A.A.F. VAN DE VEN, Instabilities in the extrusion of polymers due to spurt, *Progress in Industrial Mathematics at ECMI 94*, H. Neunzert (Ed.), Wiley and Teubner, Chichester (1996), 216-223.
- [3] M. ABRAMOWITZ AND I.A. STEGUN (Eds.), *Handbook of Mathematical Functions, with Formulas, Graphs and Mathematical Tables*, Dover Publications, New York (1965).
- [4] B. BERNSTEIN, E.A. KEARSLY AND L.J. ZAPAS, A study of stress relaxation with finite strain, *Transactions of the Society of Rheology* **7** (1963), 391-410.
- [5] R.B. BIRD, R.C. ARMSTRONG AND O. HASSAGER, *Dynamics of Polymeric Liquids*, Volume 1, *Fluid Mechanics*, Second edition, Wiley, New York (1987).
- [6] J.M. BOWNS AND J.M. CUSHING, On preserving stability of Volterra integral equations under a general class of perturbations, *Mathematical Systems Theory* **9** (1975), 117-131.
- [7] E.O. BRIGHAM, *The Fast Fourier Transform*, Prentice-Hall, Englewood Cliffs (1974).
- [8] P. BRUNOVSKY AND D. SEVCOVIC, Explanation of spurt for a non-Newtonian fluid by a diffusion term, *Quarterly of Applied Mathematics* **52** (1994), 401-426.
- [9] M.M. DENN, Issues in viscoelastic fluid mechanics, *Annual Review of Fluid Mechanics* **22** (1990), 13-34.
- [10] V. DURAND, *Ecoulement et Instabilité Oscillante des Polyéthylènes Haute Densité*, Ph.D.Thesis, l'Ecole Nationale Supérieure des Mines de Paris (1993).
- [11] D.F. ELLIOTT AND K.R. RAO, *Fast Transforms: Algorithms, Analyses, Applications*, Academic Press, London (1982).
- [12] N. EL KISSI AND J.M. PIAU, The different capillary flow regimes of entangled polydimethylsiloxane polymers: macroscopic slip at the wall, hysteresis and cork flow, *Journal of Non-Newtonian Fluid Mechanics* **37** (1990), 55-94.

- [13] J.D. FERRY, *Viscoelastic Properties of Polymers*, Third edition, Wiley, Chichester (1980).
- [14] A. GOUBLomme, B. DRAILY AND M.J. CROCHET, Numerical prediction of extrudate swell of a high-density polyethylene, *Journal of Non-Newtonian Fluid Mechanics* **44** (1992), 171-195.
- [15] A. GOUBLomme AND M.J. CROCHET, Numerical prediction of extrudate swell of a high-density polyethylene: further results, *Journal of Non-Newtonian Fluid Mechanics* **47** (1993), 281-287.
- [16] J.M. GREENBERG AND Y. DEMAY, A simple model of the melt fracture instability, *European Journal of Applied Mathematics* **5** (1994), 337-358.
- [17] G. GRIPENBERG, S.-O. LONDEN AND O. STAFFANS, *Volterra Integral and Functional Equations*, Cambridge University Press, Cambridge (1990).
- [18] J.K. HUNTER AND M. SLEMMOD, Viscoelastic fluid flow exhibiting hysteretic phase changes, *Physics of Fluids* **26** (1983), 2345-2351.
- [19] T.W. HUSEBY, Hypothesis on a certain flow instability in polymer melts, *Transactions of the Society of Rheology* **10** (1966), 181-190.
- [20] G.S. JORDAN AND R.L. WHEELER, Structure of resolvents of Volterra integral and integrodifferential systems, *SIAM Journal on Mathematical Analysis* **11** (1980), 119-132.
- [21] D.D. JOSEPH, *Fluid Dynamics of Viscoelastic Liquids*, Springer, New York (1990).
- [22] D.D. JOSEPH AND Y. JOE LIU, Letter to the editor: Steep wave fronts on extrudates of polymer melts and solutions, *Journal of Rheology* **40** (1996), 317-319.
- [23] D.S. KALIKA AND M.M. DENN, Wall slip and extrudate distortion in linear low-density polyethylene, *Journal of Rheology* **31** (1987), 815-834.
- [24] R.W. KOLKKA, D.S. MALKUS, M.G. HANSEN, G.R. IERLEY AND R.A. WORTHING, Spurt phenomena of the Johnson-Segalman fluid and related models, *Journal of Non-Newtonian Fluid Mechanics* **29** (1988), 303-335.
- [25] E. KREYSZIG, *Introductory Functional Analysis with Applications*, Wiley, New York (1978).
- [26] S.J. KURTZ, Comment on: "Letter to the editor: Steep wave fronts on extrudates of polymer melts and solutions", *Journal of Rheology* **40** (1996), 319-320.
- [27] V. LAKSHMIKANTHAM, S. LEELA AND A.A. MARTYNYUK, *Stability Analysis of Nonlinear Systems*, Dekker, New York (1989).
- [28] R.G. LARSON, *Constitutive Equations for Polymer Melts and Solutions*, Butterworths, Boston (1988).

- [29] R.G. LARSON, Review: Instabilities in viscoelastic flows, *Rheologica Acta* **31** (1992), 213-263.
- [30] A.I. LEONOV, A linear model of the stick-slip phenomena in polymer flow in rheometers, *Rheologica Acta* **23** (1984), 591-600.
- [31] F.J. LIM AND W.R. SCHOWALTER, Wall slip of narrow molecular weight distribution polybutadienes, *Journal of Rheology* **33** (1989), 1359-1382.
- [32] D.S. MALKUS, J.A. NOHEL AND B.J. PLOHR, Dynamics of shear flow of a non-Newtonian fluid, *Journal of Computational Physics* **87** (1990), 464-487.
- [33] D.S. MALKUS, J.A. NOHEL AND B.J. PLOHR, Analysis of new phenomena in shear flow of non-Newtonian fluids, *SIAM Journal on Applied Mathematics* **51** (1991), 899-929.
- [34] D.S. MALKUS, Y.C. TSAI AND R.W. KOLKKA, New transient algorithms for non-Newtonian flow, *Finite Elements in Fluids* **8** (1992), 401-424.
- [35] D.S. MALKUS, J.A. NOHEL AND B.J. PLOHR, Approximating piston-driven flow of a non-Newtonian fluid, *Differential Equations, Dynamical Systems, and Control Science*, K.D. Elworthy, W. Norrie Everitt and E. Bruce Lee (Eds.), Dekker, New York (1994), 173-192.
- [36] D.S. MALKUS, J.A. NOHEL AND B.J. PLOHR, Oscillations in piston-driven shear flow of a non-Newtonian fluid, *IUTAM Symposium on Numerical Simulation of Non-isothermal Flow of Viscoelastic Liquids*, J.F. Dijksman and G.C.D. Kuiken (Eds.), Kluwer, Dordrecht (1994), 57-74.
- [37] J. MEISSNER, R.W. GARBELLA AND J. HOSTETTLER, Measuring normal stress differences in polymer melt shear flow, *Journal of Rheology* **33** (1989), 843-864.
- [38] R.K. MILLER, *Nonlinear Volterra Integral Equations*, W.A. Benjamin, Menlo Park (1971).
- [39] J. MOLENAAR AND R.J. KOOPMANS, Modeling polymer melt-flow instabilities, *Journal of Rheology* **38** (1994), 99-109.
- [40] Z. NEHARI, *Introduction to Complex Analysis*, Revised edition, Allyn and Bacon, Boston (1968).
- [41] J.A. NOHEL AND R.L. PEGO, Nonlinear stability and asymptotic behaviour of shearing motions of a non-Newtonian fluid, *SIAM Journal on Mathematical Analysis* **24** (1993), 911-942.
- [42] J.A. NOHEL AND R.L. PEGO, On the generation of discontinuous shearing motions of a non-Newtonian fluid, *Archive for Rational Mechanics and Analysis* (to appear).

- [43] J.M. PIAU AND N. EL KISSI, Measurement and modelling of friction in polymer melts during macroscopic slip at the wall, *Journal of Non-Newtonian Fluid Mechanics* **54** (1994), 121-142.
- [44] G. POMAR, S.J. MULLER AND M.M. DENN, Extrudate distortions in linear low-density polyethylene solutions and melts, *Journal of Non-Newtonian Fluid Mechanics* **54** (1994), 143-151.
- [45] V.F. PULYAEV AND Z.B. TSALYUK, Admissibility of certain pairs of spaces for linear operators and Volterra spaces, *Differential Equations* **19** (1983), 509-516.
- [46] A.V. RAMAMURTHY, Wall slip in viscous fluids and influence of materials of construction, *Journal of Rheology* **30** (1986), 337-357.
- [47] M. RENARDY, Short wave instabilities resulting from memory slip, *Journal of Non-Newtonian Fluid Mechanics* **35** (1990), 73-76.
- [48] M. RENARDY, W.J. HRUSA AND J.A. NOHEL, *Mathematical Problems in Viscoelasticity*, Longman, Essex (1987).
- [49] Y.Y. RENARDY, Spurt and instability in a two-layer Johnson-Segalman liquid, *Theoretical and Computational Fluid Dynamics* **7** (1995), 463-475.
- [50] R.I. TANNER, *Engineering Rheology*, Revised edition, Clarendon Press, Oxford (1988).
- [51] P.P. TAS, *Film Blowing, from Polymer to Product*, Ph.D.Thesis, Eindhoven University of Technology (1994).
- [52] G.V. VINOGRADOV, A.Y. MALKIN, Y.G. YANOVSKII, E.K. BORISENKOVA, B.V. YARLYKOV AND G.V. BEREZHNAJA, Viscoelastic properties and flow of narrow distribution polybutadienes and polyisoprenes, *Journal of Polymer Science Part A-2* **10** (1972), 1061-1084.
- [53] G.V. VINOGRADOV, V.P. PROTASOV AND V.E. DREVAL, The rheological behavior of flexible-chain polymers in the region of high shear rates and stresses, the critical process of spurling, and supercritical conditions of their movement at $T > T_g$, *Rheologica Acta* **23** (1984), 46-61.

List of symbols

Vectors are printed in bold-face type. Tensors and operators are printed in caligraphic type. An overbar ($\bar{}$) denotes the steady state value, or the complex conjugate. The Laplace transform is denoted by an asterisk (*). A caret (\wedge) over a symbol denotes the dimensionless form. The trace of a tensor \mathcal{A} is denoted by $\text{tr } \mathcal{A}$, and the transpose of \mathcal{A} by \mathcal{A}^T . Vectors and tensors are given both in direct (e.g. \mathbf{a}) and component (e.g. a_i) notation. Symbols which have more than one meaning are listed with a semi-colon separating the meanings.

Roman symbols

a	slip parameter
A	area πR_b^2 of the cross-section of the barrel
\mathbf{b} (b_i)	body force vector per unit mass
c	material parameter
C (C_{ij})	strain tensor $\mathcal{F}^T \mathcal{F}$
\mathcal{D} (D_{ij})	rate-of-deformation tensor $\frac{1}{2}(\mathcal{L} + \mathcal{L}^T)$
f	pressure gradient $-\partial p/\partial z$
F	steady state shear stress
\mathcal{F} (F_{ij})	deformation gradient tensor $\partial \bar{\mathbf{x}}/\partial \mathbf{x}$; functions defined by (2.2.11), (3.2.6) and (4.2.6)
G	stress relaxation function
H	Heaviside step function
I	unit tensor
K	compression modulus
l, l_0	length of the barrel
L	length of the capillary
\mathcal{L} (L_{ij})	velocity gradient tensor $\partial \mathbf{v}/\partial \mathbf{x}$
m	memory function; ratio of two shear moduli
M	molecular weight
N_1	first normal stress difference
N_2	second normal stress difference
p, p_0, P_0	pressure
P	pressure inside the barrel
p_{hydr}	hydrostatic pressure $-\frac{1}{3}\text{tr } \mathcal{T}$
Q	volumetric flow rate
Q_i	inlet flow rate AV_0 ; dimensionless inlet flow rate
r	radial coordinate
R	radius of the capillary
R_b	radius of the barrel
S	extra stress tensor $\mathcal{T} + pI$
S_p (S_{ij})	extra non-Newtonian stress tensor $\mathcal{T} + pI - 2\eta_s \mathcal{D}$
t	time
\mathcal{T} (T_{ij})	stress tensor
\mathbf{v} (v_i)	velocity vector

V_0	plunger speed
w	velocity gradient or shear strain-rate $-\partial v/\partial r = \partial\Gamma/\partial t$
$\mathbf{x}(x_i)$	position vector
z	axial coordinate; complex number

Greek symbols

α	ratio of the inertia forces to the elastic forces
β	ratio of two relaxation rates
γ, Γ	shear strain
$\dot{\gamma}$	wall shear strain-rate
$\delta(t)$	delta function of Dirac
ε	ratio of the solvent viscosity to the shear viscosity
η_s	solvent viscosity
λ	relaxation rate
μ	shear modulus
ν	frequency
ρ	fluid density
θ	azimuthal coordinate
χ	dimensionless parameter
ω	steady state velocity gradient

Special symbols

I_C	first invariant (trace) of tensor C
d/dt	material derivative $\partial/\partial t + v_j\partial/\partial x_j$
∇	gradient operator
$ $	norm

Function spaces

$C[0, T]$	continuous functions defined on $[0, T]$
BC	bounded continuous functions defined on \mathbb{R}^+ with sup-norm
BC_0	functions in BC that tend to zero at infinity
L^1	measurable functions defined on \mathbb{R}^+ with finite norm $\int_0^\infty \phi(t) dt$

Summary

Extrusion of polymeric melts is employed to produce, e.g., plastic wires, pipes and plates. The principle of extrusion is that the polymeric melt is forced to flow through a die, e.g., by the action of a driving pressure gradient or a moving piston. At high flow rates, often flow instabilities observed as surface distortions of the extrudate occur. Since the distortions make the product worthless, it is of great practical importance to know what causes the distortions and how they can be avoided. The aim of the research presented in this thesis is to get a better insight into the relation between the characteristic behaviour of polymeric melts and the flow instabilities. For three different flows of a strongly viscous non-Newtonian fluid, especially the flow instability 'spurt' is investigated. Spurt in pressure-driven flows is experimentally observed through a substantial increase of the volumetric flow rate at a slight increase of the pressure gradient beyond a critical value, while spurt in piston-driven flows is accompanied by persistent oscillations in the pressure. Specific questions are: What causes spurt, and how does spurt depend on the processing conditions and on the polymer used?

In this thesis spurt is explained in terms of constitutive instabilities (mechanical failure of the polymeric fluid itself), while the no-slip boundary condition at the wall of the die is maintained. This is in contrast to the explanation of spurt as being due to wall-slip (failure of the polymeric fluid to adhere to the wall of the die). The explanation is based on balance laws combined with either of two constitutive models: (1) the so-called KBKZ (Kaye, Bernstein, Kearsly and Zappas) integral model for the elastic part of the extra stress tensor, or (2) the JSO (Johnson, Segalman and Oldroyd) differential model for the evolution of the shear and normal stresses. To account for the response of a small-molecule solvent, an extra Newtonian viscous term is added to the constitutive model employed. This extra term leads to a nonmonotone relation between the steady state shear stress and the steady state velocity gradient or shear-strain rate. It is shown that the Newtonian viscous term may also be interpreted as accounting for the effect of a secondary (very fast) relaxation rate.

For a pressure-driven flow of a KBKZ-fluid through a cylindrical capillary, the occurrence of spurt is demonstrated. It is shown that the steady state solution is not unique if the steady state pressure gradient exceeds a critical value. The asymptotic stability of the possible steady states is established by means of a perturbation analysis of a nonlinear Volterra integral equation of non-convolution type. Numerical computations determine which specific steady state the fluid attains. The steady state attained is found to depend on the deformation history, and this explains phenomena like shape memory and hysteresis.

For a piston-driven flow of a JSO-fluid through a cylindrical capillary, spurt accompanied by persistent oscillations in the pressure gradient is found for a bounded range of prescribed flow rates. Numerical computations disclose that the onset of the persistent oscillations depends on the material parameters of the polymer. The occurrence of the persistent oscillations is explained by a linearized stability analysis.

The influence of compression on the onset of spurt is investigated for an extrusion process that is modelled by the flow of a JSO-fluid through a contraction from a wide barrel into a narrow cylindrical capillary. The fluid in the barrel is compressed by a moving plunger, and is thus forced to flow into the capillary. Numerical computations disclose that persistent oscillations in the pressure as well as in the volumetric flow rate occur for a bounded range of

prescribed plunger speeds. The onset of the persistent oscillations is found to depend on both the material parameters of the polymer and the dimensions of the barrel and the capillary. The frequency of the persistent oscillations is determined by a Fourier spectral analysis, while the occurrence of the persistent oscillations is explained by a linearized stability analysis. Numerical computations on loading and unloading processes, in which the plunger speed is gradually raised or lowered, clarify the influence of the deformation history.

Finally, the theory is validated by a qualitative comparison with experimental results.

Samenvatting

Extrusie van polymeersmelten wordt toegepast om bijvoorbeeld plastic draden, buizen en platen te produceren. Het principe van extrusie is dat de polymeersmelt geforceerd door een capillair stroomt, aangedreven door bijvoorbeeld een drukgradient of een bewegende zuiger. Bij hoge snelheden treden vaak instabiliteiten op in de stroming, die waargenomen worden als vervormingen van het oppervlak van het extrudaat. Omdat de vervormingen het produkt waardeloos maken, is het van groot praktisch belang te weten wat de vervormingen veroorzaakt en hoe ze vermeden kunnen worden. Het doel van het onderzoek beschreven in dit proefschrift is een beter inzicht te verkrijgen in de relatie tussen het karakteristiek gedrag van polymeersmelten en de instabiliteiten in de stroming. Voor drie verschillende stromingen van een sterk viskeuze, niet-Newtonse vloeistof wordt in het bijzonder de instabiliteit 'spurt' onderzocht. Spurt in een stroming aangedreven door een drukgradient wordt experimenteel waargenomen in de vorm van een enorme toename van het debiet bij een geringe toename van de drukgradient boven een kritische waarde, terwijl spurt in een stroming aangedreven door een bewegende zuiger gepaard gaat met persistente trillingen in de druk. Specifieke vragen zijn: Wat veroorzaakt spurt, en hoe hangt spurt af van de procescondities en het gebruikte polymeer?

In dit proefschrift wordt spurt verklaard in termen van constitutieve instabiliteiten (gereleerd aan de reologie van de polymere vloeistof), terwijl de 'no-slip' randvoorwaarde aan de wand van het capillair wordt aangehouden. Dit is in tegenstelling tot de verklaring van spurt als gevolg van 'wall-slip', d.i. het loslaten van de vloeistof aan de wand van het capillair. De verklaring is gebaseerd op balanswetten gecombineerd met één van de volgende constitutieve modellen: (1) het zogenoemde KBKZ (Kaye, Bernstein, Kearsly and Zappas) integraalmodel voor het elastische deel van de extra spanningstensor, en (2) het JSO (Johnson, Segalman en Oldroyd) differentiaal-model voor de evolutie van de afschuif- en normaalspanningen. Om de responsie van een laag-moleculair oplosmiddel in rekening te brengen wordt een extra Newtonse viskeuze term toegevoegd aan het gebruikte constitutieve model. Deze extra term leidt tot een niet-monotoon verband tussen de stationaire afschuifspanning en de stationaire snelheidsgradient of afschuifnelheid. Aangetoond is dat de Newtonse viskeuze term ook geïnterpreteerd mag worden als een beschrijving van het effect van een tweede (zeer hoge) relaxatiesnelheid.

Voor een stroming van een KBKZ-vloeistof door een cilindrisch capillair, aangedreven door een drukgradient, wordt het optreden van spurt aangetoond. Vastgesteld wordt dat de stationaire toestand van de stroming niet eenduidig is indien de stationaire drukgradient een kritische waarde overschrijdt. De asymptotische stabiliteit van de mogelijke stationaire toestanden wordt onderzocht met behulp van een storingsanalyse aan een niet-lineaire Volterra integraalvergelijking van niet-convolutie type. Numerieke berekeningen bepalen welke specifieke stationaire toestand de stroming bereikt. De bereikte stationaire toestand blijkt af te hangen van de vervormingsgeschiedenis, en dit verklaart verschijnselen als vormgeheugen en hysteresis.

Voor een stroming van een JSO-vloeistof door een cilindrisch capillair, aangedreven door een bewegende zuiger, wordt spurt gepaard gaand met persistente trillingen in de drukgradient gevonden voor een bepaald bereik van voorgeschreven waarden van het debiet. Nu-

merieke berekeningen tonen aan dat de aanvang van de persistente trillingen afhangt van de materiaalparameters van het polymeer. Het optreden van de persistente trillingen wordt verklaard aan de hand van een gelineariseerde stabiliteitsanalyse.

De invloed van compressie op de aanvang van spurt wordt onderzocht voor een extrusieproces dat gemodelleerd is als een stroming van een JSO-vloeistof door een contractie van een wijd vat in een nauw cilindrisch capillair. De vloeistof stroomt door het capillair, aangedreven door een bewegende zuiger die de vloeistof in het vat samendrukt. Numerieke berekeningen tonen aan dat persistente trillingen in de druk alsmede in het debiet optreden voor een bepaald bereik van voorgeschreven zuigersnelheden. De aanvang van de persistente trillingen blijkt af te hangen van zowel de materiaalparameters van het polymeer als van de afmetingen van het vat en het capillair. De frequentie van de persistente trillingen wordt bepaald met een Fourier spectraalanalyse, terwijl het optreden van de persistente trillingen verklaard wordt aan de hand van een gelineariseerde stabiliteitsanalyse. Numerieke berekeningen aan processen waarin de zuigersnelheid geleidelijk wordt verhoogd en verlaagd, maken de invloed van de vervormingsgeschiedenis duidelijk.

Tenslotte is de theorie gevalideerd door een kwalitatieve vergelijking met experimentele resultaten.

Curriculum Vitae

Annemarie Aarts was born on August 15, 1968, at Asten, the Netherlands. After her pre-university education (VWO) at the 'Sint Willibrord Gymnasium' in Deurne, she started in 1986 to study mathematics at the Eindhoven University of Technology. From September 1989 till June 1991 she worked as a teaching assistant in mathematical training services at the Eindhoven University of Technology. She graduated in June 1992 in applied mathematics and mechanics, on the subject of Cogswell flows of power-law fluids. Her Master's thesis was written under the supervision of dr. ir. A.A.F. van de Ven.

After her graduation, from September 1992 till August 1996, she worked as a trainee research assistant (AIO) in the group 'Toegepaste Analyse' at the faculty of Mathematics and Computing Science of the Eindhoven University of Technology. The research, in which she combined her interests in applied mathematics, mechanics, numerical computing and physics, resulted in this thesis. Since January 1994 Annemarie is an executive committee member of the 'Vereniging voor Wiskundig Ingenieurs Eindhoven' (WIRE).

Stellingen

behorende bij het proefschrift

Analysis of the Flow Instabilities in the Extrusion of Polymeric Melts

van

A.C.T. Aarts

1. In de beschrijving van het karakteristieke gedrag van een viscoëlastische smelt door een KBKZ-model, kan het KBKZ-model met twee ver uit elkaar liggende relaxatiesnelheden $\lambda_2 \gg \lambda_1$ benaderd worden door het KBKZ-model met de dominante relaxatiesnelheid λ_1 behouden en een Newtonse viskeuze term met viscositeit μ_2/λ_2 toegevoegd; hierbij is μ_2 de afschuifmodulus behorend bij λ_2 .
 - Hoofdstuk 2 van dit proefschrift.

2. Gegeven de niet-lineaire Volterra integraalvergelijking van niet-convolutie type

$$\xi(t) + \int_0^t k(t, \tau)\xi(\tau)d\tau = \Phi(t) + \mathcal{H}(\xi)(t), \quad t \geq 0, \quad (1)$$

waarin $k(t, \tau) = c(t) + b(t - \tau)$, $0 \leq \tau \leq t$. Veronderstel dat $b \in L^1$, $c \in L^1$,

$$\sup_{t \geq 0} t|c(t)| < \infty, \quad \lim_{T \rightarrow \infty} \sup_{t \geq T} (t - T)|c(t)| = 0$$

en dat b aan de Paley-Wiener voorwaarde

$$1 + \int_0^\infty b(t)e^{-z t} dt \neq 0, \quad \operatorname{Re} z \geq 0$$

voldoet. Veronderstel verder dat de operator $\mathcal{H} : BC_0 \cap L^1 \rightarrow BC_0 \cap L^1$ van hogere orde is en dat $\Phi \in BC_0 \cap L^1$. Dan bestaat er voor elke $\varepsilon > 0$ een $\delta > 0$ zo dat, indien $\|\Phi\| \leq \delta$, vergelijking (1) een unieke oplossing $\xi \in BC_0 \cap L^1$ heeft met $\|\xi\| \leq \varepsilon$.

- Hoofdstuk 2 van dit proefschrift.
3. Het extrusieproces voor een polymere smelt is te modelleren door een compressiestroming van een JSO-vloeistof in een wijd vat gekoppeld aan een afschuifstroming door een nauw cilindrisch capillair, waarbij de stroming wordt aangedreven door een bewegende zuiger. In deze stroming treden persistente trillingen op in de druk alsmede in het debiet, voor bepaalde waarden van de zuigersnelheid, de afmetingen van het vat en het capillair, en de materiaalparameters van de vloeistof.
 - Hoofdstuk 4 van dit proefschrift.

4. De frequenties van de persistente trillingen die optreden in een volgens Stelling 3 gemodelleerd extrusieproces voor een JSO-vloeistof, komen overeen met de eigenwaarden berekend door middel van een stabiliteitsanalyse van het rondom de stationaire toestand gelineariseerde model.

- Hoofdstuk 4 van dit proefschrift.

5. In hun extrusiemodel gaan Molenaar en Koopmans [1] uit van een gepostuleerd verband tussen druk en debiet, dat beschreven wordt door een stelsel autonome differentiaalvergelijkingen. In de oplossing van dit stelsel treden relaxatietrillingen op. Onder toepassing van het constitutieve JSO- of KBKZ-model blijkt dat het verband tussen druk en debiet beschreven wordt door een stelsel *niet*-autonome differentiaalvergelijkingen. In de numerieke oplossing van dit laatste stelsel treden *geen* relaxatietrillingen op.

[1] J. MOLENAAR AND R.J. KOOPMANS, Journal of Rheology **38** (1994), 99-109.

6. Een dunne cirkelvormige plaat met dikte $2h$ en straal R bevat een concentrisch cirkelvormig gat met straal α . De plaat is aan de buitenrand opgelegd en wordt aan de binnenrand in haar vlak belast door een uniforme druk p . Voor de knikdruk p_{knik} van deze plaat geldt

$$p_{knik} = \lambda^2 \frac{(1 - \nu) + \alpha^2(1 + \nu)}{3\alpha^2(1 - \nu)(1 + \nu)^2} E \left(\frac{h}{R} \right)^2,$$

waarbij E de elasticiteitsmodulus is, ν de dwarscontractiecoëfficiënt en $\alpha = a/R$. Voorts is $x = \lambda$ de kleinste wortel van de vergelijking

$$\begin{aligned} [xJ'_\mu(x) + \nu J_\mu(x)][\alpha x Y'_\mu(\alpha x) + \nu Y_\mu(\alpha x)] \\ - [xY'_\mu(x) + \nu Y_\mu(x)][\alpha x J'_\mu(\alpha x) + \nu J_\mu(\alpha x)] = 0, \end{aligned}$$

waarin $\mu = \sqrt{1 - (1 - \nu)x^2/(1 + \nu)}$, terwijl J_μ en Y_μ de Besselfuncties zijn van respectievelijk de eerste en tweede soort van orde μ .

7. Zij de rij $\{a_n\}$ monotoon stijgend met $a_n > 0$ en $\sum_{n=1}^{\infty} a_n^{-2}$ convergent; zij $\alpha > 0$. Dan geldt voor $\mathbf{x} = (x_1, x_2, x_3, \dots) \in l_2$,

$$\sum_{n=1}^{\infty} \frac{x_n^2}{a_n^2} + \frac{2}{\alpha} \left(\sum_{n=1}^{\infty} \frac{x_n}{a_n} \right)^2 \leq \frac{1}{\lambda_1^2} \sum_{n=1}^{\infty} x_n^2,$$

waarin $x = \lambda_1$ het kleinste positieve nulpunt is van de functie $xP'(x) + \alpha P(x)$, en $P(x) = \prod_{n=1}^{\infty} (1 - x^2/a_n^2)$. Gelijkheid treedt op indien $x_n = a_n/(\alpha^2 - \lambda_1^2)$.

8. Een conisch capillair met halve tophoek α heeft een instroomopening met straal R_1 en een uitstroomopening met straal R_2 ($< R_1$). Door het capillair stroomt een power-law vloeistof met een voorgeschreven debiet Q . De viscositeit van de vloeistof wordt gegeven door

$$\eta = C(|4\mathbb{I}_{\mathcal{D}}|)^{(n-1)/2},$$

waarin C en n constanten zijn, terwijl $\mathbb{I}_{\mathcal{D}}$ de tweede invariant is van de deformatiesnelheidstensor \mathcal{D} . Dan geeft de formule (ontleend aan [2, form. (4.110)] met daarin n vervangen door $(n + 1)/2$)

$$\Delta P = \frac{2C}{3n \sin \alpha} \left(\frac{3n+1}{n} \frac{Q}{\pi R_2^3} \right)^n \left(1 - \left(\frac{R_2}{R_1} \right)^{3n} \right)$$

een betere benadering voor de drukval over het capillair dan de oorspronkelijke formule van Cogswell [3].

[2] A.C.T. AARTS, Afstudeerverslag, TU Eindhoven (1992);

[3] F.N. COGSWELL, Polymer Engineering and Science **12** (1972), 64-73.

9. Met de 'Gelijke Kansen Studiefinancieringsmaatregel' riskeert de Technische Universiteit Twente dat vrouwelijke studenten niet volledig door hun omgeving worden geaccepteerd.
10. De herzieningen in de omschrijving van de sport volleybal in opeenvolgende drukken van 'Van Dale: Groot Woordenboek der Nederlandse Taal', duiden op een toegenomen populariteit van deze sport in de loop der jaren.